MULTI-FREQUENCY BIOIMPEDANCE VARIATIONS IN A SIMULATED HUMAN FOREARM

Gautam Anand

A thesis submitted to

Auckland University of Technology

in fulfilment of the requirements for the degree of

Doctor of Philosophy (PhD.)

Institute of Biomedical Technologies

School of Engineering

Faculty of Design and Creative Technologies

Supervisors: Dr. Andrew Lowe and Prof. Ahmed Al-Jumaily

June 2017

dedicated to

My guru

and

My family – Mom, Dad and Brother

Abstract

Bioimpedance analysis (BIA) is a popular technique used in the monitoring of various physiological parameters like arterial oscillation, blood volume flow rate and cardiac output. BIA is based on measuring the impedance of the tissue under test which reflects the dielectric behavior of the tissue along with the associated dynamics. This technique generally finds applications as single frequency BIA (SF-BIA) in the form of impedance cardiography (ICG) and impedance plethysmography (IPG), or multi-frequency BIA (MF-BIA) in the form of impedance spectroscopy and tomography.

Existing methods of hemodynamic monitoring employ SF-BIA (such as ICG) where a single frequency current is introduced into the tissue, and the obtained output is processed to estimate parameters like stroke volume, cardiac output, and pulse wave velocity (PWV). SF-BIA provides an approximate response of the volume changes and is unable to distinguish the impedance contributions of a single tissue domain from the overall measurements. This research aims at investigating the effect of blood flow-induced changes in the radial artery cross-section in the human forearm through MF-BIA. This offers a novel approach to analyze the multi-frequency impedance response related to blood flow in the peripheral arteries and relate the impedance changes to estimate the changes in the diameter.

The thesis presents a simulation model of the fat, muscle and artery tissue layers in a section of human forearm. The model, although assuming isotropic dielectric properties for each tissue, aims at simulating the dielectric response of the tissue layers within the major portion of β dispersion frequency range – 1 kHz to 2 MHz. The main aim of this analysis was to understand the effect of pulsatile blood flow on the MF-BIA response, which was realized by simulating impedance measurements at three radial arterial diameters – 2.3 mm, 2.35 mm, and 2.4 mm. The results indicated a non-linearly decreasing behavior of the impedance spectra with increasing artery diameters, and a Cole-type response.

Moreover, a human forearm phantom was developed, to mimic the dielectric properties of human tissues, with the same tissue layers as the simulation model. A coaxial cylindrical sensor was developed and calibrated to estimate the dielectric properties of liquid mixtures and the research identified blood can be simulated using 80% propylene glycol and 20% 4 M NaCl solution, muscle using 3.77% agar and 1.88% gelatine

suspended in 0.3% NaCl solution with 18.8% propylene glycol and fat using a suspension of 5% agar in 0.05% NaCl solution. The phantom was tested for the impedance response at the three arterial diameters within the same frequency range and agreed with the simulation response.

Analytical modeling was undertaken to investigate, parametrically, the behavior of the system. Two approaches were undertaken – a parametric Debye-type modeling to estimate the impedance contribution from different layers and a more realistic Cole model to fit the response in terms of Cole parameters. Moreover, a modified two dispersion Cole model was proposed to explain the contribution of the artery diameter to the impedance spectra. All models fitted the simulation and experimental data reasonably well and explained observed behavior with artery diameter changes.

Finally, a pilot study was performed to measure impedance from three human subjects and estimate the radial artery diameter changes from the measurements. The methodology was validated by comparing the results against ultrasound measurements, performed concurrently on the subjects along with the impedance measurements. The impedance derived diameters measured between 2.2 – 2.4 mm for the 10 frequencies between 3 kHz – 127 kHz with peak-to-peak changes of 0.05 – 0.15 mm. This was found to be in proportion with the ultrasound measurements which yielded diameters between 2.1 – 3 mm for the three subjects with 0.15 – 0.35 mm of peak-to-peak changes. The method exhibited expected behavior and showed promise for further development.

In summary, this research aims at investigating the potential of employing MF-BIA to target SF-BIA applications, one of which is hemodynamic monitoring in the human forearm. The objective is to investigate the potential of utilizing MF-BIA approach to overcome the drawbacks of SF-BIA, which is more of an approximated approach. This study has focussed on analyzing the contributions of forearm tissue composition and blood flow in the radial artery, validating the utility of multi-frequency impedance assessment of tissues for more accurate prediction of physiological changes.

Acknowledgement

I would like to begin by thanking the Almighty for blessing me with the opportunity of pursuing this research. The blessings of my *guru* and my parents have made it possible for me to complete this study.

Most importantly, I would like to express my appreciations to my primary supervisor, Dr. Andrew Lowe. He has been instrumental in helping me with his continued guidance, support, and criticism. It has been his expertise and patience throughout that has helped me finish this research.

Next, I would like to thank my secondary supervisor, Prof. Ahmed Al-Jumaily, for his continued moral and financial support and guidance throughout the period of this study. He has been like a father figure to all of us at the Institute of Biomedical Technologies (IBTec). His experience and knowledge have helped me understand important aspects of this research.

I would like to thank the technicians – Stephen Hartley (Electrical department) and Thomas Jones (Mechanical department) for helping me with the experimental setup.

I would like to specially thank two of my colleagues - Anubha Kalra for supporting me throughout my thesis tenure, and Parn Jones for helping me with the phantom mold preparations.

Finally, I would like to thank my friends and colleagues from IBTec for their constant support and motivation.

Table of Contents

List of Figures

List of Tables

Attestation of Authorship

"I hereby declare that this submission is my own work and that, to the best of my knowledge and belief, it contains no material previously published or written by another person (except where explicitly defined in the acknowledgements), nor material which to a substantial extent has been submitted for the award of any other degree or diploma of a university or other institution of higher learning."

…….. *(signed)*

…….. *(date)*

List of Units, Symbols and Abbreviations

Units

Symbol	Unit
F	Farad
g/cc	gram per cubic centimetres
Hz	Hertz
mA	milli-Ampere
mPa-s	milli-Pascal second
mV	milli-Volt
Pa	Pascal
S	Siemens
s^{-1}	per-second
Ω	Ohm

Symbols

Symbol	Quantity	Unit
C	Capacitance	F
D	Electric Flux Density	C m^{-2}
E	Electric Field Strength	V m^{-1}
G	Conductance	S
H	Magnetic Field Intensity	A/m
I	Current	A or mA

J	Electric Current Density	A m^{-2}
V	Voltage	V
Z	Impedance	Ω
ε	Permittivity	F/m
ε_o	Permittivity of free space (8.85×10^{-12})	F/m
ε_r	Relative Permittivity	
μ	Dynamic Viscosity	Pa-s
ρ	Resistivity	Ω-m
σ	Conductivity	S/m
τ	Time constant	seconds
ω	Frequency	rad s^{-1}

Abbreviations

BIA	Bioimpedance Analysis
CI	Confidence Intervals
DVT	Deep Vein Thrombosis
ECF	Extra-cellular Fluid
ECG	Electrocardiogram
EEG	Electroencephalogram
EIT	Electrical Impedance Tomography
EMG	Electromyogram
ICF	Intra-cellular Fluid

ICG	Impedance Cardiography
IPG	Impedance Plethysmography
MF-BIA	Multi-Frequency – Bioimpedance Analysis
PWV	Pulse Wave Velocity
RMSE	Root Mean Squared Error
SF-BIA	Single Frequency – Bioimpedance Analysis
SSE	Sum of Squared Errors

Chapter 1 BACKGROUND

1.1 Introduction

Bioelectrical impedance analysis or bioimpedance analysis (BIA) is a non-invasive procedure originating in the early 1930s and 1940s ([1], [2]) that involves the measurement of the electrical impedance of a region of tissue. Bioimpedance measurements provide information about the physical and electrochemical processes in the tissue region and hence can be used for monitoring physiological properties and variations. For example, BIA is commonly employed to estimate body fat or water composition as a measure of general health [3]–[7]. BIA has been implemented in diagnostic techniques such as electrical impedance cardiography (ICG) [8]–[11] which can be used for estimating cardiac output, electrical impedance tomography (EIT) [12]–[15] which can be used as an imaging modality to detect, for example, breast cancer, and electrical impedance spectroscopy (EIS) [16]–[18] which is used for multi-frequency analysis of materials with different electrical domains such as cellular membranes and tissues.

Another implementation of BIA which is particularly relevant to this work is bio-impedance plethysmography (IPG), which is widely used to determine changes in body fluid composition, for example, due to cardiac and lung function. This technique serves as a diagnostic measure for disorders like deep vein thrombosis (DVT) and measurement of cerebral blood flow, intra-thoracic fluid volume and peripheral arterial flow [19]. IPG can be employed to estimate hemodynamic parameters from which the cardiac flow can be derived [20]. The implication of IPG to diagnose DVT is quite established and is based on the change in the blood volume ejection through the impedance measurements at a single frequency. However, the choice of frequency and venous blood flow often contribute as confounders in the method as compared to ultrasound, which remains the gold standard for DVT diagnosis.

In contrast to medical diagnostic techniques such as electrocardiogram (ECG), electroencephalogram (EEG) and electromyogram (EMG) which rely on endogenic bioelectric signals, i.e. internally generated electricity within tissues, bioimpedance is an exogenic bioelectric response, i.e. the response obtained through an external electrical

stimulation. BIA employs the measurement of electrical impedance of the tissues by applying a known current excitation and typically recording the resultant potential difference using pairs of electrodes which are attached in particular configurations to measure the impedance of the region. Hence the measured bioimpedance is essentially a *transfer impedance* obtained as a ratio of the output voltage to the input current. The current input can be applied through a pair of electrodes, and the voltage measurement can be obtained through the same or a different pair of electrodes (Figure 1.1).

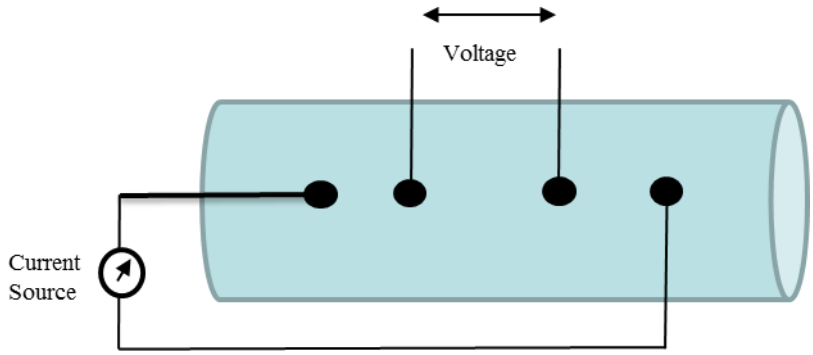

Figure 1.1: Bioimpedance measurement principle

The measurement is based on the assumption that the tissue in the region is an isotropic capacitor with the fluid inside it forming the medium or the dielectric. This leads to measurement of impedance at a single frequency (SF-BIA) or over a spectrum (MF-BIA) which changes as the volume or distribution of fluid in the region changes. The measurements also depend on many other factors such as electrode polarization, skin impedance, and coupling of the patient to the ground or other electrical potentials.

This research investigates the potential for the measurement of the diameters of peripheral arteries using bioimpedance. Arterial diameters are known to change due to transmural pressure fluctuations associated with the pulsatile flow. Ultrasound imaging techniques can measure the change in the diameter. However, ultrasound equipment is expensive, relatively bulky and requires significant skill on the part of the operator. Nevertheless, if arterial diameters can be measured accurately, they could provide clinically useful information about atherosclerosis, pulse wave mechanics and cardiovascular risk [21].

The forthcoming sections of this chapter discuss in more detail the applications of bioimpedance for measurement of vascular geometry, electrical properties of human tissue and the operating principles for such measurements.

1.2 Measurement of Volume using Bioimpedance

The principle of bioimpedance can be utilized in different ways to measure clinically relevant anatomical volumes. Three important applications utilizing different working principles include impedance plethysmography (IPG), impedance cardiography (ICG) and electrical impedance tomography (EIT). The measurement principle of the volumetric changes is common among all the applications. The changes in the volume of the tissues or body fluids change the electrical impedance of that region, which is reflected as the changing impedance measurements during the procedure. The body fluids and blood are comparatively more conductive than the other tissues and hence contribute mainly to the impedance changes due to their flow.

1.2.1 Impedance Plethysmography (IPG)

Impedance plethysmography is the general term for a procedure to use impedance measurements to estimate tissue volumes or volumetric changes within the human body. One common consumer application of IPG is the determination of body fat/water composition. This is based on the measurement of the resistive and reactive electrical response of the body and using it to calculate several parameters such as fat-free mass, total body water and cell mass. A low alternating current is applied, and the response is measured using a set of two or four electrodes [22]–[25]. The injected current is typically applied at a single frequency between 20kHz – 100kHz [26]. For measurement of body composition, the electrodes are normally placed so that the current passes through most of the body (for example, by using contralateral limb electrodes). Other applications of IPG are to measure lung water volumes [27]–[31] using thoracic electrodes, and deep vein thrombosis [32]–[35], where it is used to diagnose venous obstruction through volume changes in blood flow.

1.2.2 Impedance Cardiography (ICG)

ICG is a specialization of IPG which monitors real-time impedance changes occurring in the thorax to determine cardiovascular parameters like stroke volume (SV) and cardiac output (CO). ICG was one of the earlier clinical applications of BIA and popularized by Patterson, Kinnen and Kubicek in carrying out thoracic impedance measurements for the

estimation of the cardiac output ([36]) along with the thoracic measurements to determine the tissue resistivity in vivo ([37]).

ICG normally involves the application of a low alternating current at a single frequency to the thoracic cavity and measurement of the impedance changes as a result of thoracic hemodynamics. The measurement setup comprises two or four pairs of electrodes placed at the neck and the diaphragm to establish the conduction path of the current in the direction of the blood flow (Figure 1.2). As the current is applied, it traverses through a path of least resistance, i.e. blood in the heart, aorta and the vena cavae. The major output signals obtained are the change in impedance (dZ) and the first time derivative of impedance (dZ/dt). As blood is ejected during the cardiac cycle, the volume of blood in the thorax changes and is reflected in corresponding impedance changes. The impedance output signal is used, along with ECG and statistical covariates such as the patient's age, sex, height, and weight to calculate related physiological parameters like stroke volume (SV), cardiac output (CO), heart rate (HR), ventricular ejection time (VET) and pre-ejection period. However, existing techniques do not allow accurate reconstruction of the entire flow waveform, which carries important clinical information.

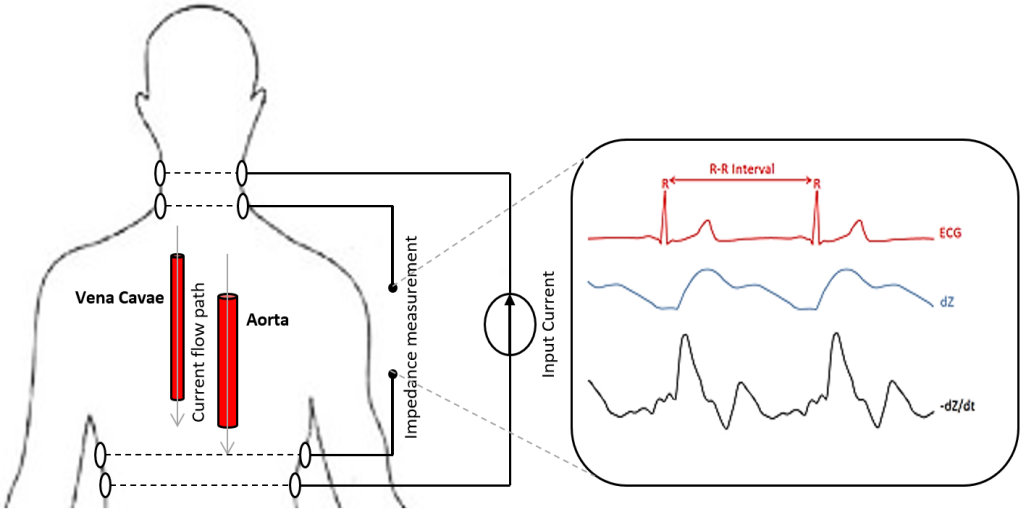

Figure 1.2: ICG measurement setup and obtained signals

ICG has advantages for this application as it is non-invasive and relatively easy to operate, and is marketed as an effective tool for assessing conditions like hypertension, heart failure, and dyspnoea. However, significant diversity exists in the reported accuracy of ICG when compared to techniques for cardiac measurement such as thermodilution. Previously reported correlation coefficients between these two techniques range between 0.83 and 0.88 for normal and heart patients [38]–[43]. Some of these reported no meaningful difference, whereas others depicted overestimation or underestimation of

stroke volume by ICG measurement. Comparison between ICG and the direct Fick method, along with dye dilution has also been done. A high correlation was reported in healthy subjects in some subjects [44]–[47]. Contrarily, no particular agreement between the direct Fick method and ICG for SV estimation was shown [48].

One recent work on the estimation of stroke volume from brachial artery bioimpedance [49] employed electrical impedance velocimetry (TBEV). It involved the introduction of a constant magnitude, high-frequency current from the upper arm to the antecubital fossa and was based on slight region-specific modifications in Kubicek's equation for ICG. To optimize the accuracy, the SV measurement was calibrated with that obtained from a commercial ICG device to determine the constant of proportionality between the two. Also, the result was statistically validated with the results of Doppler/echocardiography SV estimation and was found to meet accuracy criteria.

A recent variation on ICG is known as bioreactance [50]–[53], [54]. In contrast with other ICG systems, bioreactance is based on analyzing the relative phase shifts occurring in an oscillating current flow as it traverses through the thoracic cavity. (The changing blood volume is not only a contributor to the blood resistivity change but also to the capacitances and the intra-thoracic inductances and therefore signal phase.) The main advantage of this technique is that the electrode spacing is removed as a decisive factor since the phase shifts do not change with distance.

Nevertheless, commercially available ICG systems continue to utilize proprietary algorithms and relationships to estimate cardiac function from bioimpedance measurements in the face of a range of complicating factors such as differences in body size, lung volume, arterial and venous volumes and electrode spacing.

1.2.3 Electrical Impedance Tomography (EIT)

EIT is a fundamentally different technique for measuring anatomical volumes employing a multi-frequency BIA (MF-BIA). The basis of EIT is to use the frequency dependent dielectric properties of human tissues to characterize their behavior in response to an applied electric field induced by the low current at multiple frequencies. It is a non-invasive medical imaging tool which uses multiple pairs of surface electrodes for permittivity or conductivity calculations. The application of the current to the electrodes generates equipotential regions, which are measured by other electrodes. The surface

electrodes are used in various configurations to result in a conductivity scan or a tomogram of the area. After measurement, image reconstruction algorithms are used to develop volumetric images defining the conductivity patterns within a region. The significant variations in conductivities of different tissues are observed as contrasting profiles in the reconstructed image. EIT finds use in monitoring lung function and targeting other organs such as brain, breast, cervix, etc [55]–[59]. EIT can also be used to identify any abnormalities in tissues such as for cancer detection [60]–[62] and can also be used to analyze the perfusion of tissues within a region such as lungs and thorax.

One of the aims of this research is to investigate whether MF-BIA techniques (impedance spectroscopy) can be applied to traditionally SF-BIA target applications to provide a better understanding of the contributions of tissue layers in determining blood flow induced impedance variations. To avoid the complexity and number of confounding factors found in the thorax, for example, this research examines the forearm as the target region.

1.3 Electrical Properties of Human Tissues

Tissue can be considered as a suspension of cells from which the living being is composed. There are many types of tissues, each responsible for a specific set of tasks, with their specific composition and functionality. Each type of tissue can be considered a biomaterial exhibiting an electrical impedance. From an electrical perspective, tissues contain cells, which are composed of resistive fluids, with the cells having membranes that are very poor conductors of electricity and hence capacitive, from which it follows that bioimpedance should be frequency dependent. In 1957, Schwan [63] studied the dielectric properties of the tissues and defined the electrical behavior through three different dispersion regions - α, β, and γ (Figure 1.3), which will be explained later. This provided an insight into the tissue immittivity variation with frequency and the amount of permittivity or conductivity offered within a range of operation.

The physical properties of the tissue layers distinguish the electrical response of one type of tissue from another and indicate how tissue is both conductive, dielectric as well as inhomogeneous and anisotropic in structure. The structures can be considered as cell suspensions having compartments of fluids (extracellular and intracellular) bounded by insulating membranes. Following a theoretical approach, there is no conduction across the cell membranes at zero frequency or D.C., and the impedance is purely resistive being

a function of the extracellular fluid (ECF) (R_0 or R_E). For an alternating current within 0.1-100 MHz, the membrane capacitance, C_M, plays its role and the effect of intracellular fluid (ICF) increases. At very high frequencies, the capacitive effect becomes insignificant, and the overall impedance is resistive (R_∞), accounting for both the ECF and the ICF resistances [64]. This mechanism is shown in Figure 1.4.

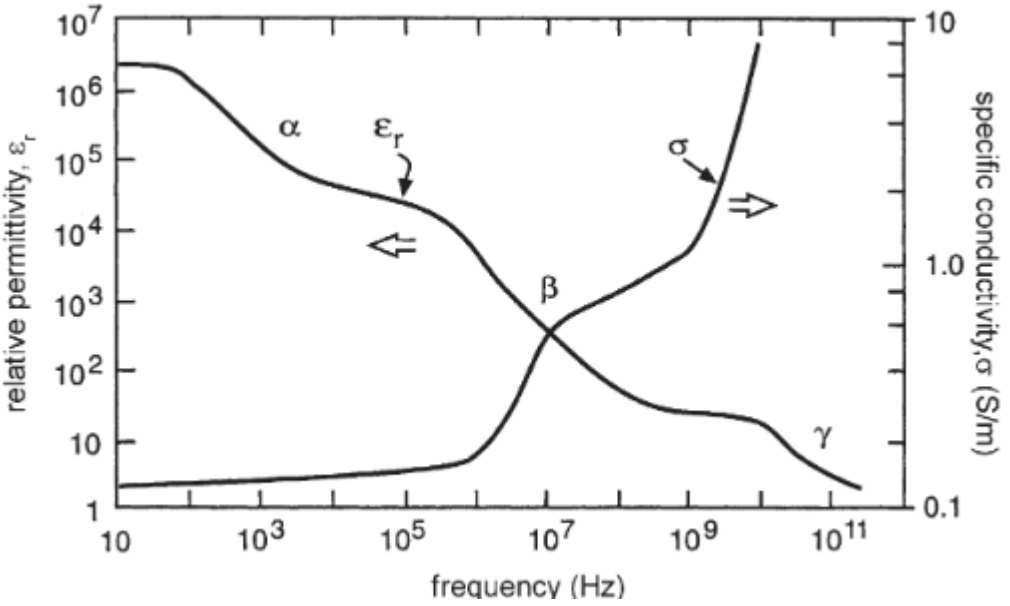

Figure 1.3: Frequency dependence of the complex permittivity and conductivity of biological tissues [63]

The measure of the capacitive reactance offered by the cell membrane (C_M) is sometimes characterised at a mid or characteristic frequency (F_C), that can be defined as a frequency of maximum reactance, X.

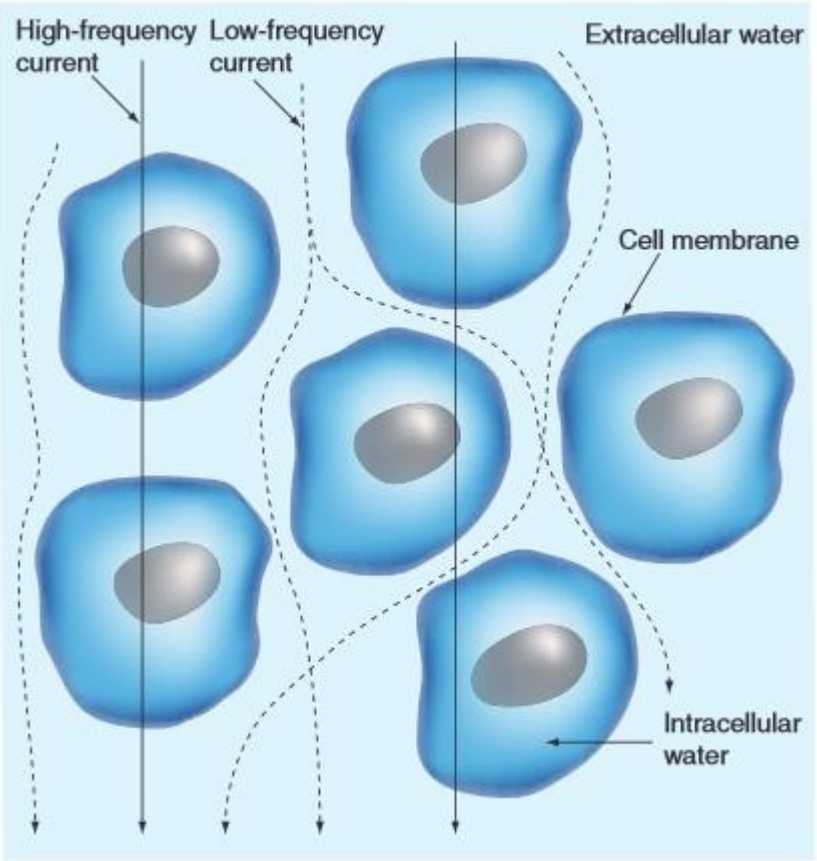

Figure 1.4: High and Low-frequency current distributions in cell suspensions [65]

1.4 Bioimpedance Theories

In analyzing bioimpedance measurement, three underpinning perspectives are helpful. These are:

- Lead Field Theory, which informs an understanding of the distribution of the electric fields and current within the tissue volume and is discussed further in section 1.4.1.
- An analytical model representing the complex dielectricity of materials discussed further in section 1.4.2, and
- Empirical models of the dielectric relaxation phenomena observed in tissue explained in section 1.4.3.

1.4.1 Lead Field Theory

The concept of bioelectrical signal determination can be understood through the quantitative analysis of the distribution of the electric fields within the tissue volume.

This is explained through the lead field theory which can be used to deduce optimal configurations for endogenic and exogenic measurements.

Lead field theory is conceptualized to understand the distribution of the electrical stimulation applied through a pair of electrodes, referred to as a lead, within the volume of the underlying tissue. It follows from an assumption of the existence of dipoles (point current source and sink of the same magnitude) spread uniformly as a function of position over a surface lying within a volume conductor. This surface is known as a double layer which generates an electric field that can be quantified using Gauss' theorem. According to this theory, the electric field at any point within or at the surface of the conductor can be evaluated using a lead vector that describes the influence of electric potential generated by any dipole within the volume at a point within or on the surface of that volume. This electric field generates a lead potential which equals the sum of the products of the dipole moment and the lead vector of each element within the volume. For an applied unit current through the electrode pair, the electric current field generates a lead voltage that equals the scalar product of the lead field current density and the volume source element divided by conductivity. The lead field analysis has been used to explain the Einthoven, Frank, and Burger triangles [66].

Lead field analysis in the measurement of bioelectric and biomagnetic sources leads to the conclusion that there is a significant change in the impedance of a region due to the conductivity change of the enclosed volume which is proportional to the amount of current through it. This directly relates to a more generalized relation of Ohm's law ($V = I^* Z$). Geselowitz (1971) [67] devised a mathematical formulation which can be used in impedance plethysmography to mathematically estimate impedance changes, for example resulting from changes in electrode configuration. Based on this analysis, if the current is introduced using the same electrodes as for voltage measurement, the lead fields due to the current and the voltage would mathematically be the same. However, it is a convention to avoid this due to imperfections in electrode impedance and hence using different electrodes provides better results [66]. Moreover, several other factors affect the best electrode performance and measurement sensitivity distribution.

1.4.2 Complex dielectricity of tissues – Complex conductivity and permittivity

A lossy, dielectric material exhibits both conductive and dielectric properties. For an electric field (E), the associated flux density (D) can be defined as:

$$\vec{D} = \varepsilon\vec{E} \tag{1.1}$$

where ε is called the permittivity of the material. Additionally, this electric field polarizes the material leading to an additional polarization vector ($\vec{P} = \varepsilon_0\chi\vec{E}$). Hence, the above expression modifies to:

$$\vec{D} = \varepsilon_0\vec{E} + \vec{P} = \varepsilon_0\vec{E} + \varepsilon_0\chi\vec{E} = \varepsilon_0(1+\chi)\vec{E} = \varepsilon_0\varepsilon_r\vec{E} \tag{1.2}$$

where ε_0 is the vacuum permittivity, χ is the electric susceptibility and $(1+\chi) = \varepsilon_r$ is the relative permittivity of the material. For an alternating electric field, $\vec{E} = |E|e^{j\varphi}\hat{E}$ applied to a dielectric material, the change in the polarization does not occur instantly and causes energy dissipation in the process. This can be accounted for by defining permittivity as a complex quantity. Frequency introduces a phase difference between the flux density and electric field, which is quantified as:

$$\varepsilon = \frac{|D|}{|E|}e^{-j\varphi} \tag{1.3}$$

where |D| and |E| are the respective magnitudes of flux density and electric field, and φ is the phase angle. The permittivity can therefore be represented as:

$$\varepsilon(\omega) = \frac{|D|}{|E|}(\cos\varphi - j\sin\varphi) = \varepsilon'(\omega) - j\varepsilon''(\omega) \tag{1.4}$$

Equation (1.4) defines the complex permittivity for dielectric media where $\varepsilon'(\omega)$ represents the real component of the permittivity and $\varepsilon''(\omega)$ is the imaginary part.

The time-variant Maxwell's equation can be stated as:

$$\nabla \times \vec{H} = \vec{J} + j\omega\vec{D} = \vec{J} + j\omega\varepsilon\vec{E} \tag{1.5}$$

where H is the magnetic field and J is the electric current density.

Substituting the expression for complex permittivity from equation (1.4) in equation (1.5), we obtain:

$$\nabla \times \vec{H} = \vec{J} + j\omega(\varepsilon' - j\varepsilon^{"})\vec{E} \tag{1.6}$$

$$\nabla \times \vec{H} = \vec{J} + \left(\omega\varepsilon^{"} + j\omega\varepsilon'\right)\vec{E} = \vec{J} + \sigma(\omega)\vec{E} \tag{1.7}$$

In equation (1.7), the first term denotes the static current density and the second term represents the current density caused by the alternating electric field. Hence, the second term defines the complex conductivity as:

$$\sigma(\omega) = \sigma'(\omega) + j\sigma^{"}(\omega) = \omega\varepsilon^{"}(\omega) + j\omega\varepsilon'(\omega) \tag{1.8}$$

where $\sigma'(\omega)$ represents the real part and $\sigma^{"}(\omega)$ represents the imaginary part of the conductivity.

The expressions in equations (1.4) and (1.8) state that the complex conductivity and permittivity are complex conjugates of each other. The relation of these quantities is often expressed as a single complex function:

$$\varepsilon(\omega) = \varepsilon_0\varepsilon_r(\omega) + j\frac{\sigma(\omega)}{\omega} \tag{1.9}$$

The above equation identifies the overall dielectric behavior of the material is defined by conductivity and permittivity and is a function of frequency.

1.4.3 Dielectric Relaxation theories

For dielectrics, the application of an electric field causes a lag or a delay between the frequency of the applied field and the resulting changes in polarization. Due to this, the permittivity of the material depends on the frequency of the applied electric field as a complex function, and this behavior is described as *dispersion.* As stated earlier, Schwan in his work identified three regions of dispersion – α, β, and γ. For lower frequencies (≤1kHz), the α dispersion is prominent which defines the effects primarily due to ionic diffusion across the cellular membranes, counterion effects and the dielectric losses at lower frequencies. As has been indicated in Figure 1.3, permittivity changes significantly in this region whereas conductivity is relatively constant. The β dispersion constitutes the frequency range from 1 kHz – 100 MHz and accounts for the capacitive response of the cellular membranes. However, the frequency range limits may vary for different tissues. The γ region highlights the dipolar orientation effects in water molecules and is prevalent at microwave frequencies.

The delay induced by the varying polarization and the electric field describes the time constant of the system which is referred as *relaxation time* (τ).

a) Debye Theory of Dielectric Relaxation

The Debye theory, introduced by Debye (1913)[68], for dielectrics, represents the ideal behavior of dipoles where they all experience the same delay/lag. Hence, the system exhibits a single relaxation time or a single time constant. The complex permittivity of such dielectrics is expressed as:

$$\varepsilon(\omega) = \varepsilon_\infty + \frac{\varepsilon_o - \varepsilon_\infty}{1 + j\omega\tau} \tag{1.10}$$

where, ε_∞ is the permittivity at very high frequency, ε_0 is the permittivity at very low frequency or DC, and τ is the relaxation time (time constant) of the system.

This approach is widely used to identify the properties of polar compounds and systems that can be electrically modeled as equivalent RC circuits. The behavior in equation (1.10) is particularly suited to describing the properties of polar solvents and compounds. However, it might not be suitable for an accurate analysis of biomaterials possessing complex properties, especially human tissues.

b) Maxwell-Wagner Effects

The Maxwell-Wagner-Sillars effect [69]–[71] or simply the Maxwell-Wagner effect is a dominant contributor to the dielectric response of material at low frequencies. The relaxation due to Maxwell-Wagner effects arises due to the existence of a single charge layer at the interface of dielectrics. It is one of the major contributors in the β dispersion range where the capacitive effects of cellular membranes lead to interfacial polarization. It characterizes the inhomogeneity of tissues, suspensions, colloids, liquid crystalline polymers and other such materials.

c) Cole Theory

The Debye theory of dielectric relaxation proposed the frequency dependence of dielectricity as a single relaxation system, which is unable to describe the electrical response of complex polymers and biological tissues. Cole and Cole in 1941 ([72], [73]) proposed an empirical relation for systems with multiple, distributed time constants and defined it in the form known as the Cole equation:

$$\varepsilon(\omega) = \varepsilon_\infty + \frac{\varepsilon_o - \varepsilon_\infty}{1 + (j\omega\tau)^{1-\alpha}} \tag{1.11}$$

where, $0 \leq \alpha < 1$ and α is the coefficient of relaxation, indicating how the time constant changes with frequency. For $\alpha = 0$, the expression simplifies to a Debye-type response.

This relation has been found to be appropriate to define the frequency dependent dielectric parameters of biological tissues. The Cole equation can be defined in terms of complex permittivity, complex conductivity, and the overall impedance, the latter being expressed as:

$$Z(\omega) = R_\infty + \frac{R_o - R_\infty}{1 + (j\omega\tau)^{1-\alpha}} \tag{1.12}$$

where $Z(\omega)$ is the overall impedance, R_∞ is the resistance at very high frequency, R_0 is the resistance at very low frequency (DC resistance), and τ is the relaxation time (time constant) of the system. The equation can be geometrically interpreted as a Nyquist plot between the real and imaginary parts of the impedance as a function of frequency and is known as a Cole plot.

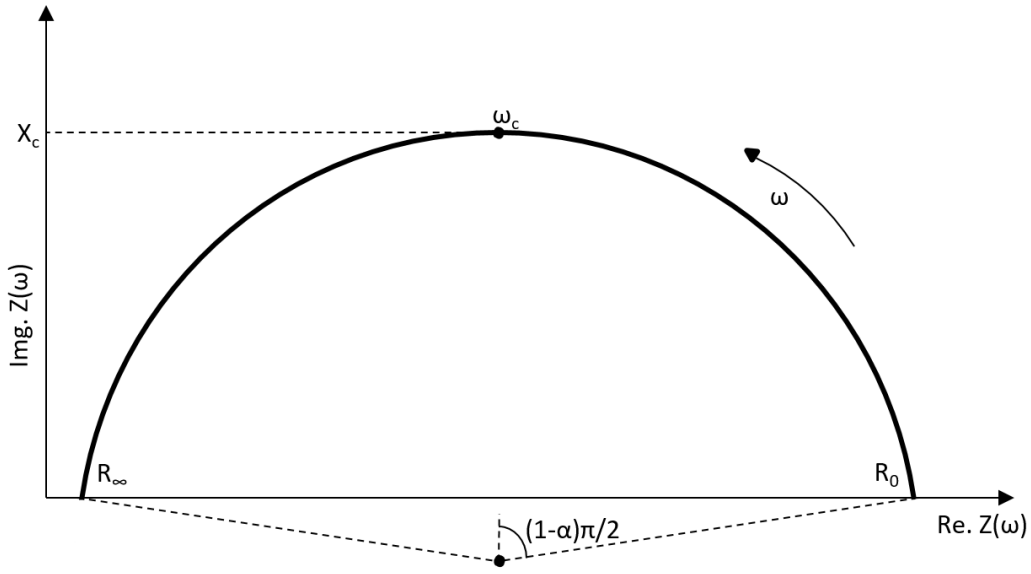

Figure 1.5: Cole plot with different Cole parameters

The Cole plot shows the variation of the imaginary part of $Z(\omega)$ (Img. $Z(\omega)$) with the real part of $Z(\omega)$ (Re. $Z(\omega)$) with increasing frequency as indicated in Figure 1.5. The trend follows the geometry of an arc with its extremes subtending an angle of $(1-\alpha)*\pi/2$ degrees at the center. All the parameters from equation (1.12) can be seen as indicated in the plot of Figure 1.5. As can be deduced, for $\alpha = 0$, the plot follows a semicircle which is a Debye-type response. In addition to the earlier defined parameters, the plot indicates frequency ω_c yielding a maximum reactance X_c. This frequency is termed the characteristic frequency of the

response. The Cole-Cole equation describes a frequency dependent basis to electrically model the dielectric properties of biological tissues.

1.5 Closure

This chapter described applications of bioimpedance measurements (IPG, ICG, and EIT) the biophysics involved (lead field theory and models of complex dielectricity) and the electrical properties of tissues (models of dielectric relaxation phenomena). These understandings underpin the proposed research, which is concerned with investigating impedance variations due to pulsatile blood flow in the human limbs. The investigation plan incorporates a numerical simulation of the forearm system which will be compared to an experimental simulation using tissue-mimicking phantom materials. Results from both of these will also be compared to parametric models of the system based on lead field theory (Figure 1.6). Finally, a pilot in-vivo study will be performed to ascertain whether the numerical, experimental and analytical models resemble reality.

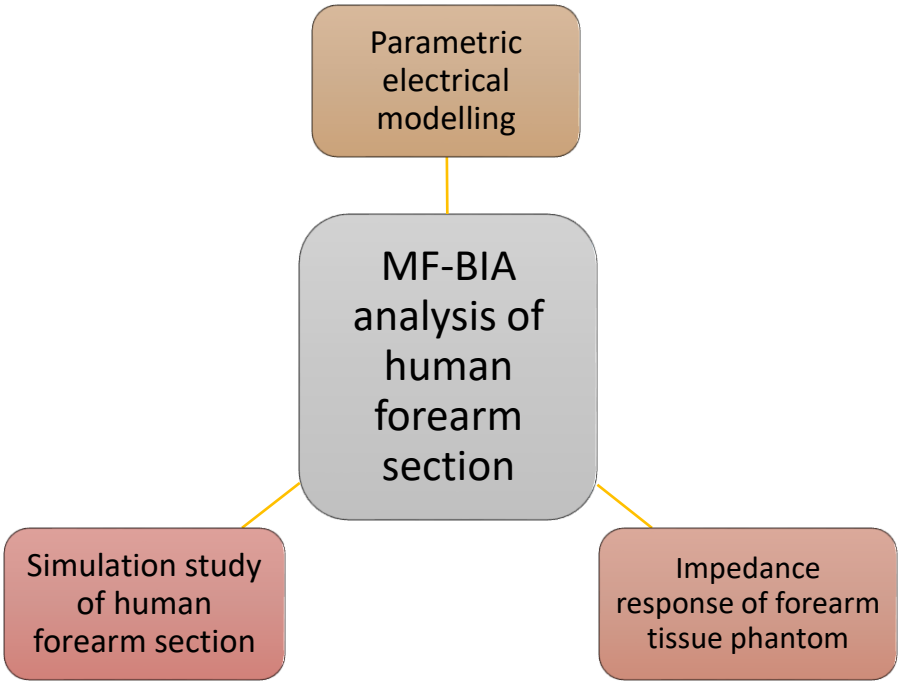

Figure 1.6: Contributions to investigating MF-BIA of human forearm section in this study

To conduct this research plan, it is important to gain further insight into the effect of electrode configurations, measurement circuits, the electrical properties of tissues and

tissue mimicking materials, and appropriate methods of analytical electrical modeling. A survey of literature on these topics is presented in the next chapter.

Chapter 2 LITERATURE REVIEW

2.1 Introduction

This chapter presents a review of literature relevant to this research into the relationship between bioimpedance and changes in arterial diameters in peripheral arteries. The literature review is divided into the following sections:

1. **Instrumentation design**: Includes the various types of circuits and electrode configurations popularly employed for bioimpedance analysis and set-ups for specific BIA applications.
2. **Effect of electrodes used in bioimpedance analysis**: Focusses on the type of measuring electrodes and configurations used for bioimpedance analysis along with different configurations and geometry and their overall effect on the measurements.
3. **Electrical properties of tissues**: Highlights the different studies which quantified the dielectric response of biological tissues.
4. **Tissue-mimicking phantoms:** Discusses research in the areas of construction and electrical properties of fat, muscle and tissue simulants. This section includes the evaluation of several materials and the procedure to identify the physical and electrical characteristics of blood and dielectric characteristics of fat and muscle.
5. **Electrical modeling of bioimpedance measurements**: Focussing on literature discussing the significance of mathematically modeling the dielectric response of the tissues according to Cole theory. Also, highlights some works defining electrical circuit equivalents and analogies to typical tissue response.
6. **Effect of blood flow on bioimpedance measurements**: Outlines the different studies relating to the effect of blood compositional characteristics and flow effects on the overall impedance measurements.

2.2 Instrumentation

2.2.1 Measurement set-up for BIA

The first published results for non-invasive impedance variation monitoring were given by Kubicek et al., 1970 [10], who performed thoracic impedance cardiography using a Minnesota impedance cardiograph (Model 303) [74]. A four-band electrode configuration was used, with the electrodes being conductive strips made of aluminum and taped on (Figure 2.1).

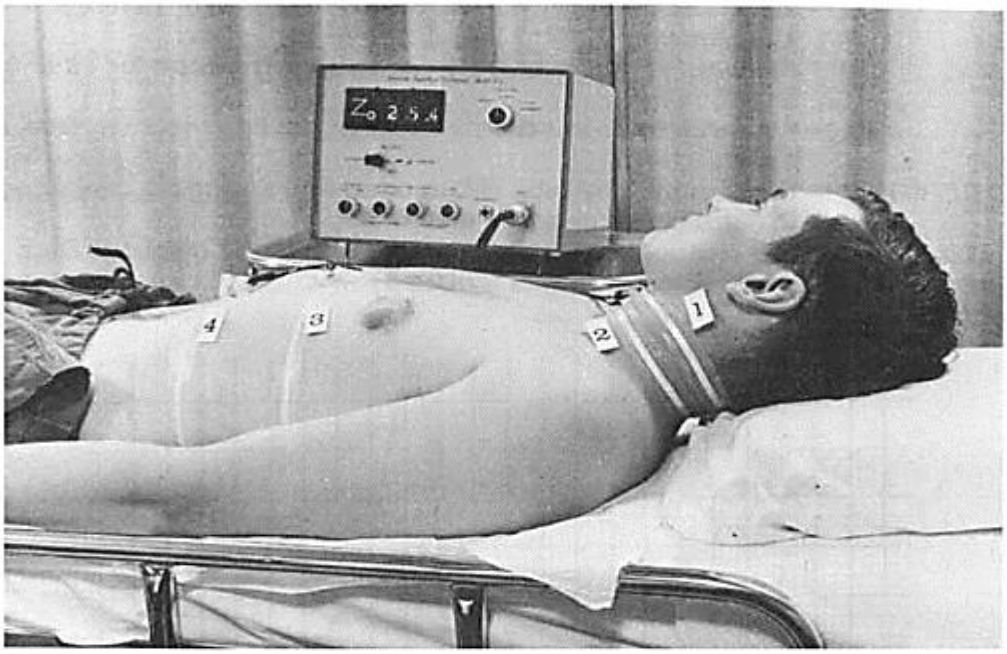

Figure 2.1: A photograph of the tape-on electrodes for impedance cardiography [10]

The instrumentation consisted of a constant current oscillator to transmit a sinusoidal current of 4 mA at 100 kHz. The current was fed in through electrodes 1 and 4, and the voltage was sensed between 2 and 3 which was fed to the detecting circuits with the amplifiers having a high input resistance of 100 kΩs [10].

The signal obtained from the electrodes was corrupted with noise, and so a signal conditioning unit with high input impedance detection amplifiers was used to filter the signal and extract the required components like the impedance signal Z, dZ, dZ/dt and ECG.

Kubicek's work ([10], [74])) was based on the cylindrical thorax modeling to investigate the origination of the bioimpedance signal which was a highly simplified approximation and made the technique unreliable. Also, the model remained unclear regarding the source

of the bioimpedance signal as well as neglecting the contributions of the blood conductivity and the changes in the velocity as pointed out by Mohapatra (1981) [75].

For BIA, the application generally defines the type of measurement setup to be employed. The input stimulation is provided to the electrodes through a current source, and the output signal is picked up by the voltage electrodes to pass through a signal conditioning unit which comprises of instrumentation amplifiers and filters/demodulators to extract the required signal components (as can be seen in Figure 2.2).

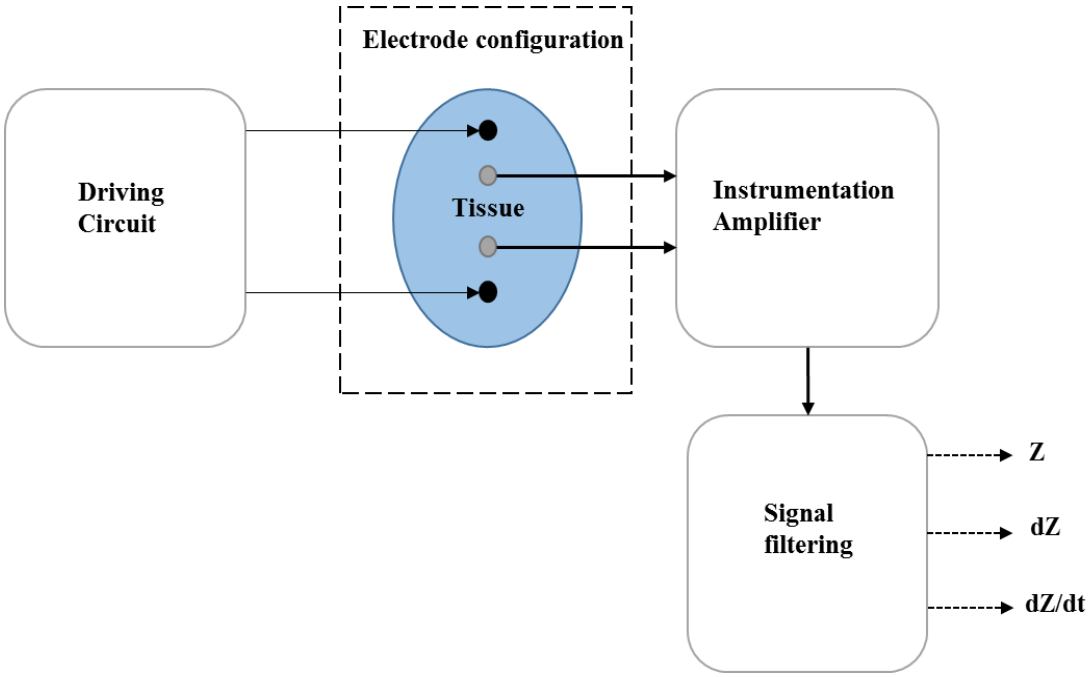

Figure 2.2: Block diagram of a BIA measurement setup

The input is provided by the driving circuits, which normally are voltage controlled current sources (VCCS). The quality of measurement is also decided by the type of electrode configuration which then decides the extent of signal processing.

2.2.2 Bipolar and Tetrapolar electrical circuits

Electrode configurations can be bipolar or tetrapolar. Electrical schematics are shown in Figure 2.3 - A and B, respectively.

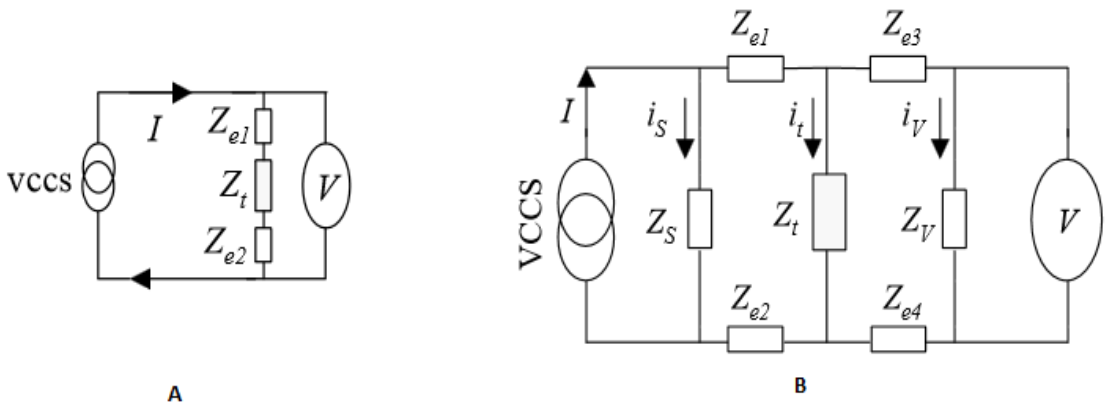

Figure 2.3: The circuit diagrams for A. bipolar and B. tetrapolar electrode configurations [76]

As can be seen in Figure 2.3, a single measurement obtained through the bipolar arrangement is affected by tissue impedance, Z_t, as well as electrode impedances Z_{e1} and Z_{e2}. However, considering the tetrapolar circuit, the output impedance of the current source, Z_s, and the input impedance of the voltage amplifier, Z_v, can be made very high, such that the current through them is negligible so that the sensed voltage corresponds predominantly to the tissue impedance, Z_t.

2.2.3 Operational frequency range and safety considerations

Multifrequency bioimpedance analysis aims at estimating the tissue electrical response over a range of frequencies. There are three main ways to measure tissue impedance over a wide frequency range [76]. Griffiths and Ahmed, 1987 [77] demonstrated one of these by changing the frequency of the drive circuit (current source) and measuring the voltage. Another way is to apply a current with multiple frequency components (Lozano et al., 1990 [78]) whereas the same can be achieved by applying a pulse of broad spectral energy as done by Record et al., 1992 [79] and Waterworth et al., 2000 [80].

Valentinuzzi, 1995 [81], stated the necessity for considering safe limits to the current to be applied since improper measures can cause serious damage to the tissues and the skin. He mentioned the current should be limited to a 1 mA (rms) at 100 kHz. Brown et al. 1999 [82] reports that the threshold current (the current at which sensation starts) increases with frequency. According to the IEC 601 safety regulations, the maximum direct current can be 1 μA (rms) and 100 μA (rms) at 100 kHz.

Brown et al., 1998 [83] used a four-electrode probe for the impedance analysis of the cervical tissue. He applied a current of 10 μA (p-p) between the electrodes. The frequency

range of interest was 4.8 kHz to 614 kHz. A similar electrode probe was used by Gonzalez-Correa et.al.[84] along with a tissue impedance meter within the frequency range of 9.6 kHz to 614.4 kHz to differentiate squamous from columnar epithelium in the esophagus (Figure 2.4).

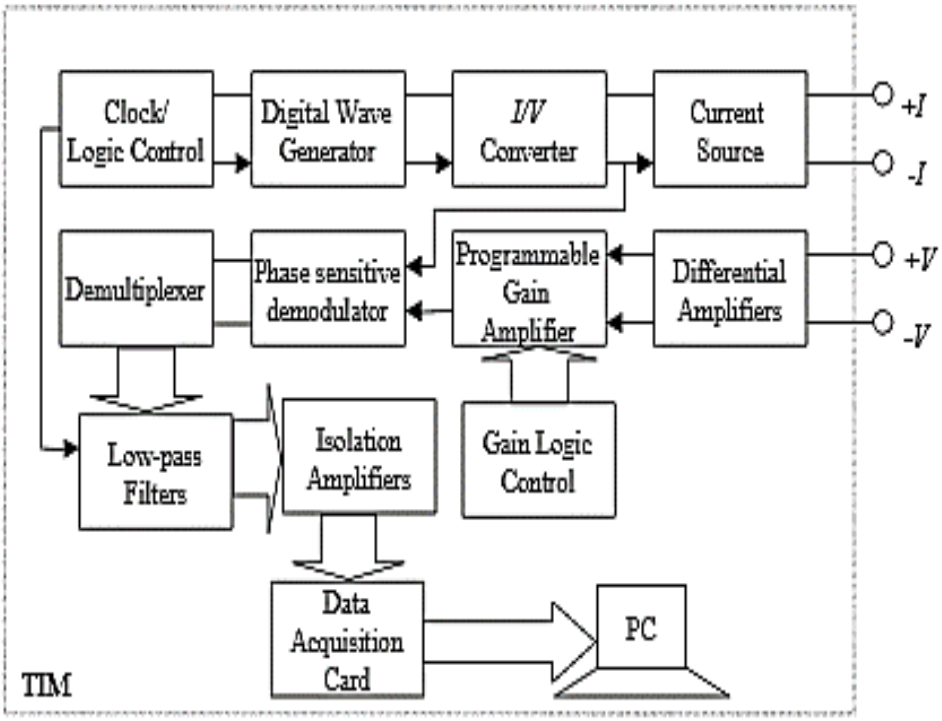

Figure 2.4: The tissue impedance meter as used by González-Correa et al., 1999 [84]

The choice of the system having a single frequency or a multiple frequency operation essentially depends on the bioimpedance application. The multiple frequency operation is required for the application like EIT whereas it is of less importance in impedance cardiography. The cellular electrical properties reveal the different response frequencies for the ECF and the ICF [85], which can be an even wider range considering other impeding layers like fat and bones. A change in the body fluid distribution changes the reactance (X) and the phase such that it shifts the characteristic frequency.

2.2.4 Driving circuits

As mentioned earlier, the driving circuit is essentially a VCCS. The circuit is fed by a voltage source of required input frequency to a VCCS. The performance of the current source is determined by its output impedance, which is ideally required to be infinite.

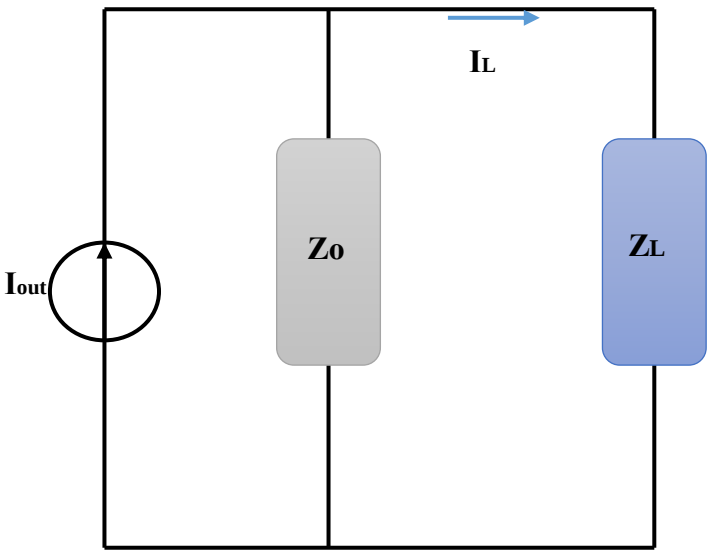

Figure 2.5: Output of a VCCS circuit

From Figure 2.5, the current I_L can be expressed as:

$$I_L = \frac{Z_o}{Z_o + Z_L} I_{out} \tag{2.1}$$

As can be understood from equation (2.1), a higher value of Z_o ensures that the load current I_L will not vary with changes in Z_L.

The importance of the design of the current source is particularly vital in applications like EIT and impedance spectroscopy [86]–[92]. Generally, it is difficult to realize a VCCS with a very high output impedance for frequencies above 1 MHz due to the presence of output and stray capacitances [93]. Smith et al., 1995 [94] proposed that the best way to implement a VCCS is through an isolated negative feedback current source. Some of the designs used to implement VCCS include using an inverting operational amplifier, transformer coupled operational amplifier, current mirror and Howland circuit. For use over a wide frequency range, VCCS for BIA are typically preferred on two designs: through a modified Howland Circuit ([95], [96]) or by using a current mirror architecture ([97], [98]).

1. **Current Mirror:** The current mirror circuit copies the current through the load by controlling the active part of the circuit. It realizes the VCCS without any positive feedback and is essentially an inverting amplifier (Figure 2.6).

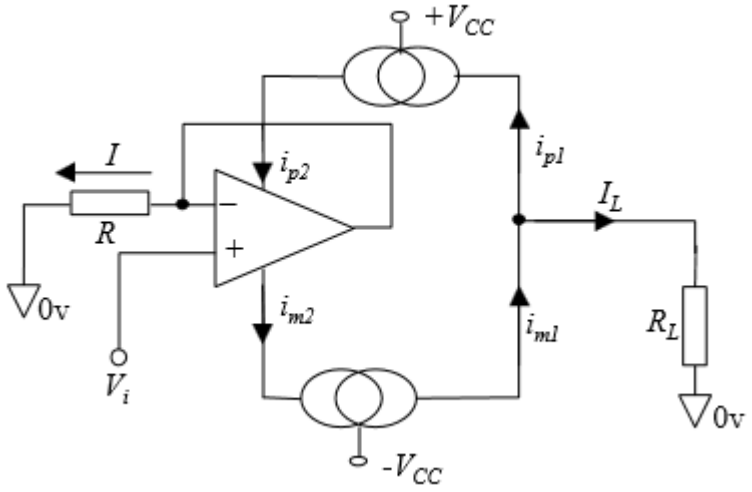

Figure 2.6: A basic current mirror circuit [76]

2. **Howland Circuit:** The circuit consists of a single operational amplifier with both the positive and negative feedback loops (Figure 2.7). This is a preferred choice in EIS and EIT applications as it yields a higher output impedance than the basic current mirror circuit.

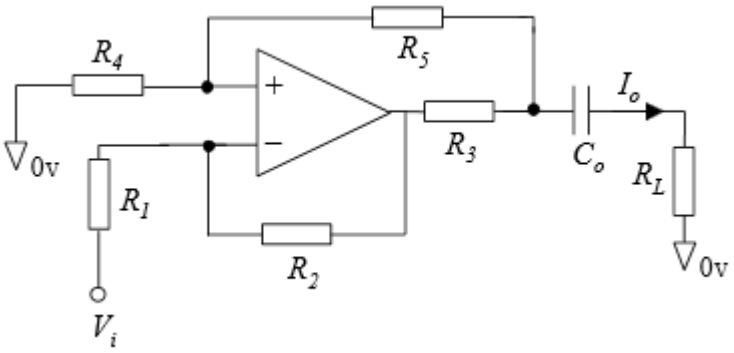

Figure 2.7: An improved Howland current generator circuit used in EIT [76]

2.2.5 Bioimpedance measurement systems

The choice of the circuit elements should be based on the various interacting impedance parameters while attaching the measuring system to the body. In addition to electrode impedance, other stray/parasitic capacitances in a general bioimpedance measurement setup also exist. They may be shown as in Figure 2.8.

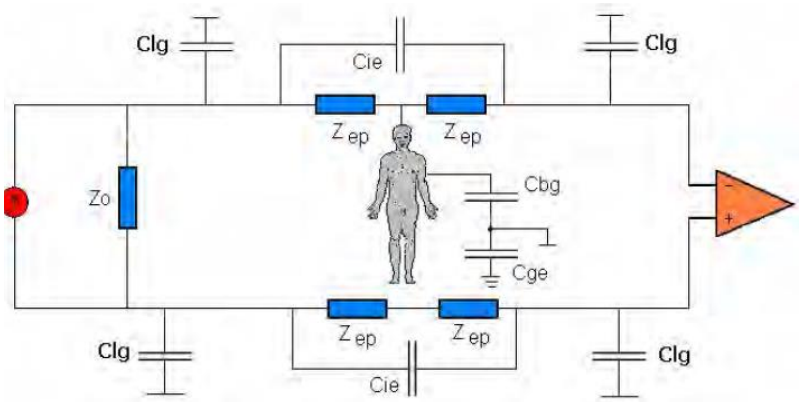

Figure 2.8: Various capacitances and impedances encountered in a BIA setup [99]

C_{ie} is the capacitance between adjacent electrode leads, C_{lg} between the signal leads and ground, C_{ge} between the signal ground and earth and C_{bg} is the residual capacitance between body and ground. The higher the value of Z_{ep}, the greater will be the sensitivity of the system to these parasitic capacitances. The involvement of these extra capacitive elements introduce measurement artifacts and reduce the accuracy of impedance measurement. Wang et al., 2011 [100] explored a regional plethysmographic measurement of the forearm by developing a device delivering a constant single frequency current less than 1 mA at 100 kHz. The measuring device employed a Wein-bridge oscillator as the input to a VCCS delivering a sinusoidal current at 100 kHz. The sensed voltage was fed to a high impedance instrumentation amplifier along with a filtering system comprising a notch filter (to remove 60 Hz noise from the mains), a full wave rectifying demodulator, a fourth order low-pass filter (30 Hz) and a first-order high-pass filter (0.5 Hz) (Figure 2.9).

Shyu et al., 2000 [101] proposed a portable system for impedance cardiography capable of continuous real-time monitoring for longer durations. The upper band limit of the system was based on the assessment made by Hurwitz et al., 1993 [102], and was decided to be around 40 Hz for the dZ component as any lower frequencies attenuated the signal (Figure 2.10).

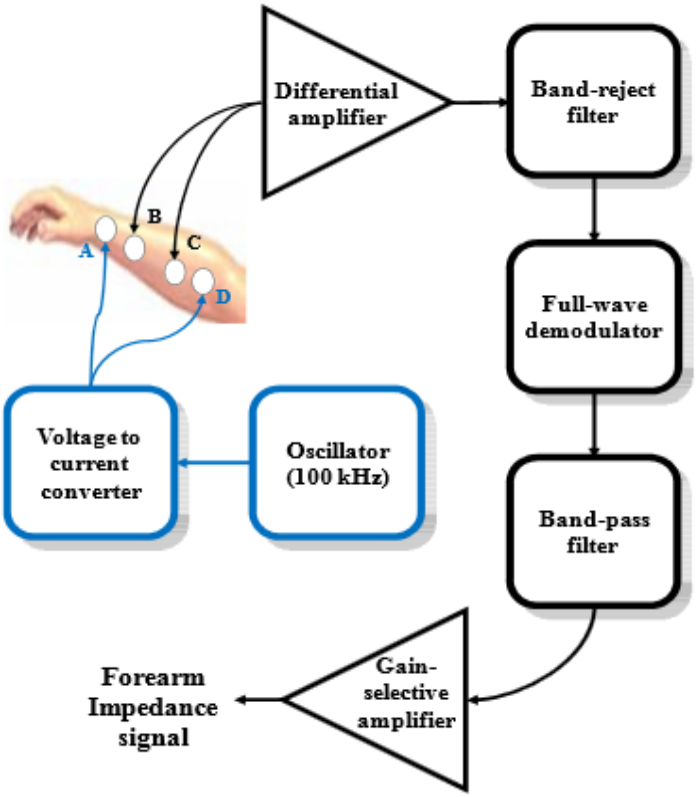

Figure 2.9: Block diagram of the forearm impedance measurement stated by Wang et al., 2011 [100]

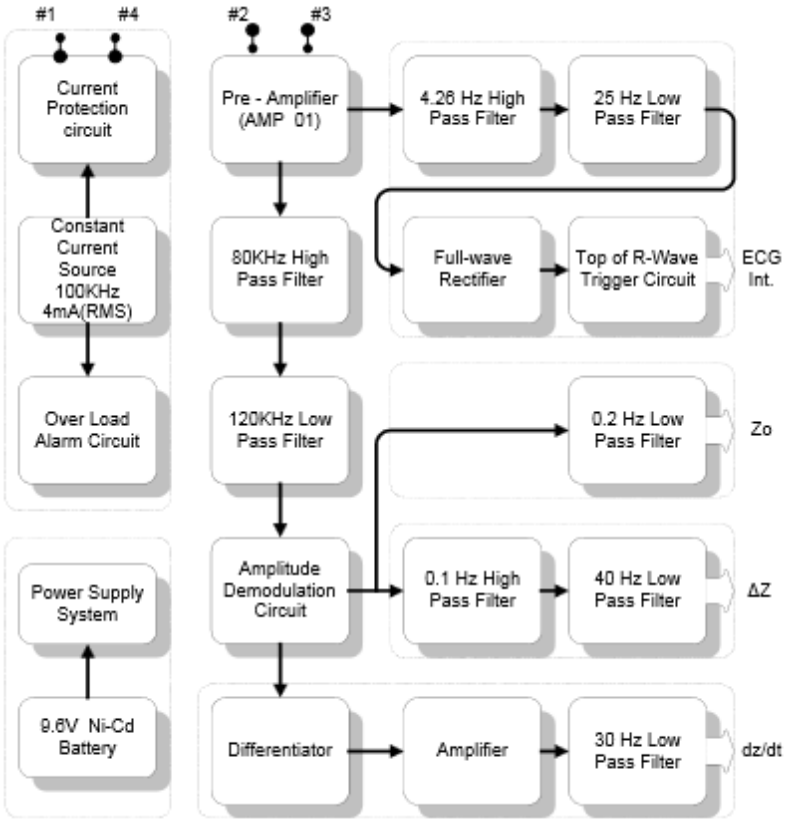

Figure 2.10: The block diagram of the ICG system as proposed by Shyu [101]

Aroom et al., 2009 [103], used a modified Howland circuit as a VCCS (Figure 2.11). The circuit used the signal from a function generator being fed to an instrumentation amplifier which acted as a pre-amplifier to the signal entering the Howland circuit.

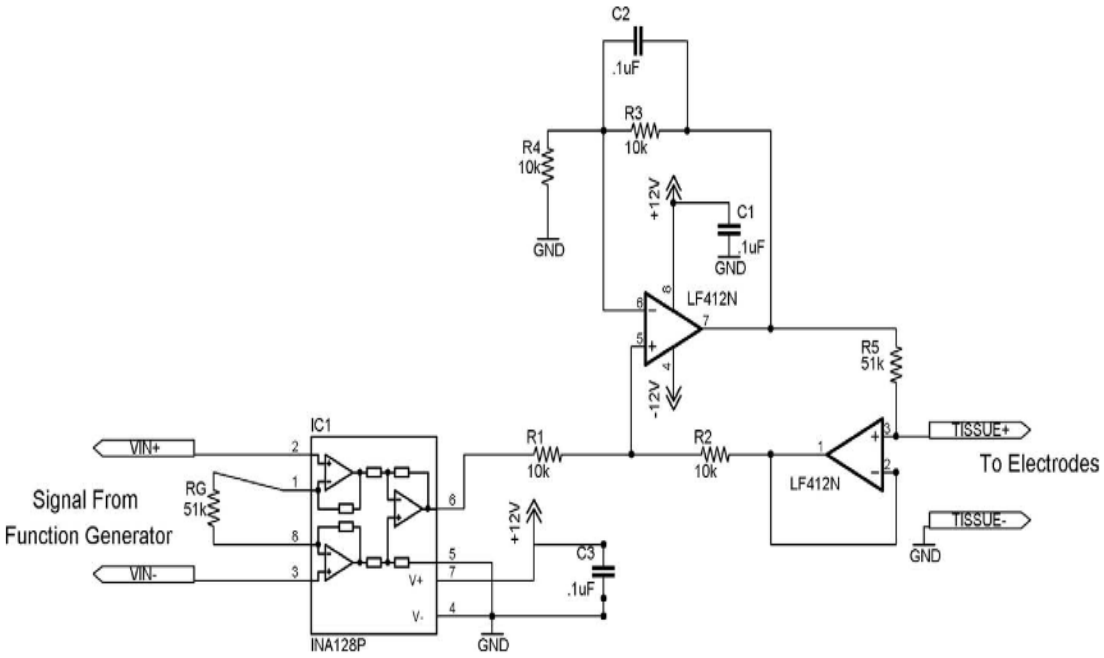

Figure 2.11: A modified Howland circuit proposed by Aroom et al., 2009 [103]

A general choice for the instrument setup requires an appropriate choice for the current source that covers the desired frequency operation. It is difficult to obtain a current source for operation at a frequency in the mega-Hertz range. If this is required, a VCCS using a wide frequency voltage source can be a good choice. Appropriate signal conditioning such as the use of high CMRR instrumentation amplifiers and filtering will be required, depending upon the requirements of the application.

2.3 Effect of Electrodes on Bioimpedance Measurements

2.3.1 General concepts for electrode characterisation

Conventionally, Ag/AgCl electrodes are used in most non-invasive diagnostic measures such as ECG. In bioimpedance measurements, electrodes are used for both current feeding as well as voltage measurement. For the commercially manufactured instrument by Kubicek [74], the input impedance of the amplifiers in the detection system was set at

100kΩ to account for the contact impedance of the electrodes. Also, Kubicek found that the immittivity spectrum is more clear if the signal is measured from a different pair of electrodes than the current feeding pair. Instead, using multi-polar electrode systems with different current carrying and voltage pickup electrodes yields a *transfer* impedance [104]. A very important source of electrode artifact is the electrode polarization. It is a developed barrier potential between the electrode and the conductive medium which is very prominent at frequencies less than 1 kHz. The electrode polarization impedance acts as an error signal when measuring the tissue impedance. As has been deduced from the lead field theory, the transfer impedance depends on the geometry of the electrodes along with the configuration and the alignment pertaining to the region of interest. The fact that the electric field distribution within the tissues depends on the applied field strength and the nature of the electrodes makes the electrode configuration more significant. The placement of the electrodes explains the field distribution depending upon the size, geometry, spacing, and orientation of electrodes.

2.3.2 Types of electrodes

The choice of electrodes depends on the biomedical application and the required sensitivity of measurements. There exists a variety of electrode types for medical diagnostics and the majorly used have been presented in Table 2-1.

There is widespread use of surface electrodes as they readily conform to the body surface geometry. Metal plate electrodes and flexible electrodes are frequently used for ECG measurements and are a favorable choice for BIA. The most commonly used surface electrodes are silver/silver chloride (Ag/AgCl) electrodes that comprise a silver coated disk surrounded by a foam pad along with AgCl as the conductive electrolyte. These are simple, effective and the most suitable for application within this study.

Table 2-1: Types of biopotential electrodes

Types of Electrodes	Characteristics/Use	Figure
Surface Electrodes		
1. Metal Plate Electrodes	• Used in ECGs, EMGs, and EEGs • Comprise of a metal disk surrounded by a disposable foam pad and an electrolyte • Prone to motion artifact	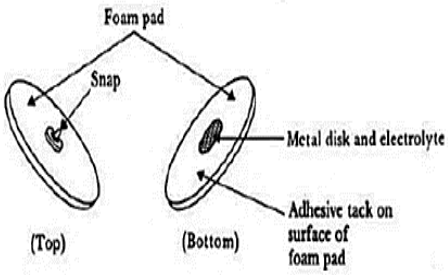 [105]
2. Suction Electrodes	• Without any straps or adhesives • Used in precordial ECG measurements • Short duration	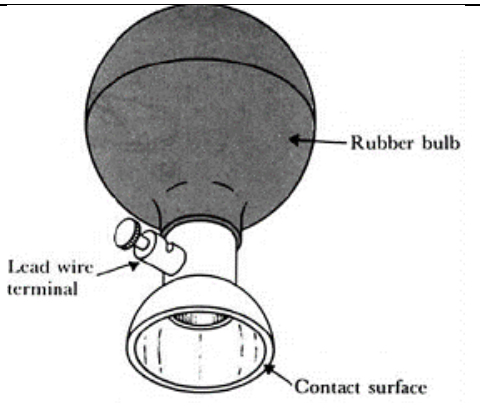 [105]
3. Flexible/Polymer Electrodes	• Conductive polymer composite materials like carbon nanotubes (CNT), poly di-methyl siloxane (PDMS), carbon filled silicon rubber (Mylar) • May or may not require conductive adhesive	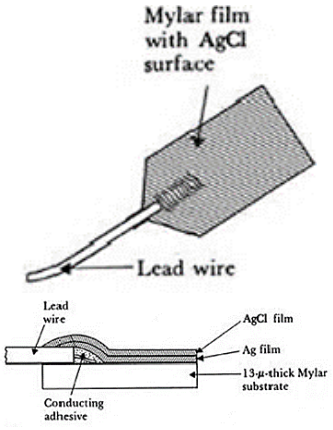 [105]

Table 2.1: Types of biopotential electrodes (continued)

Needle Electrodes	• Used for percutaneous biopotential measurements • Diagnostic muscle activity • Exists as unipolar or bipolar needle electrodes	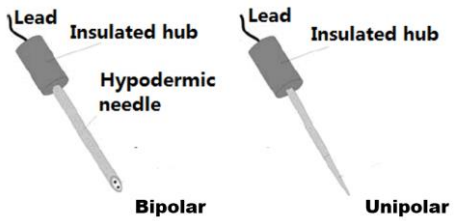 [106]
Microelectrodes	• Used at cellular level measurements • Very small and robust • Highly non-linear response	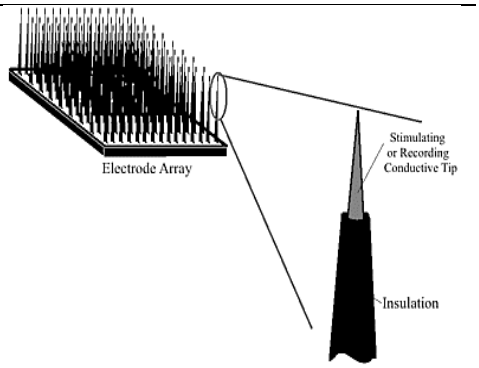 [107]

2.3.3 Electrode configurations

The types of electrodes along with the placement configuration contribute to the overall impedance measurements. From an electrical equivalent perspective, the common electrode configurations used are either bipolar or tetrapolar, which have been discussed before. From the measurement perspective, the following two electrode configurations exist:

1. **Spot Electrodes:**

   These are essentially the surface electrodes which are used very commonly for ECG and BIA measurement. In this configuration, the electrodes are connected in either bipolar or tetrapolar configuration. The placement of electrodes can be easily modified, and the gap between the electrodes can also be adjusted (Figure 2.12).

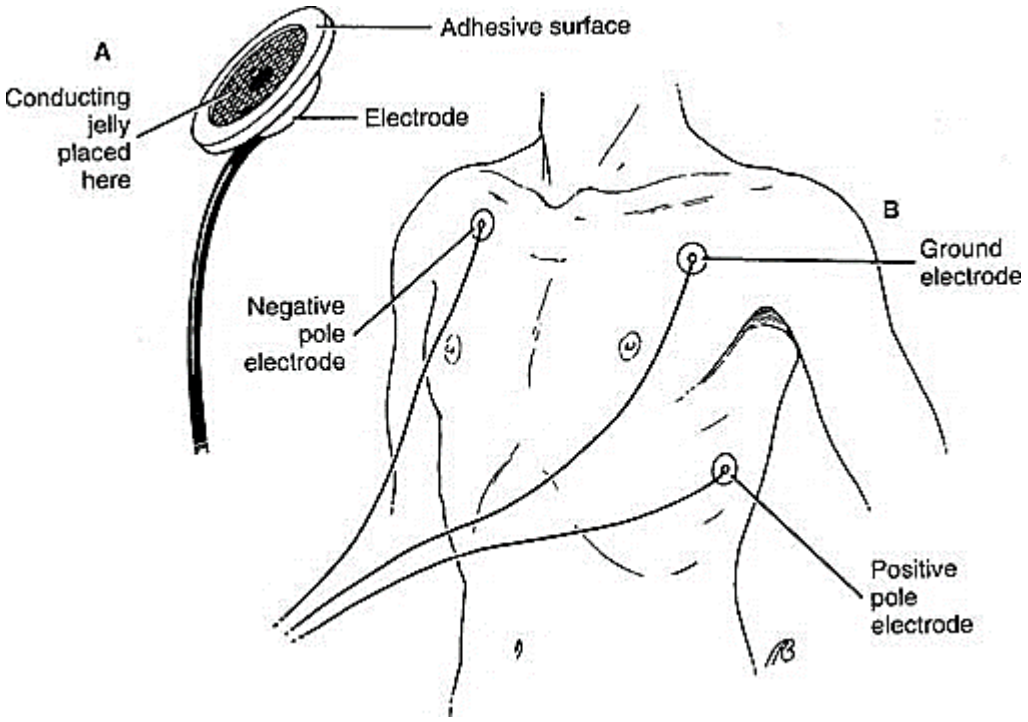

Figure 2.12: Use of spot electrodes for cardiac monitoring [108]

2. Band Electrodes:

These electrodes are employed for ICG measurements, following the proposed electrode configuration by Kubicek in 1968 [74] as can be seen in Figure 2.13. These electrodes offer limited scope for modification of size and placement. They are generally employed to analyze the overall effect of both longitudinal and transverse impedance variations in a tissue segment. Also, they can be employed in conjunction with spot electrodes to monitor multiple modalities such as impedance and ECG.

The Kubicek arrangement of tetrapolar electrodes remains a reference for basic thoracic impedance cardiographic measurements. The use of band electrodes can be replaced by spot electrodes since they provide the same performance with additional comfort [101]. Moreover, an eight electrode system for bioimpedance measurements was proposed by Jaffrin et.al. [109]. In their work, they devised an eight-electrode network to calculate fat tissue mass by placing 4 electrodes on the upper and 4 on the lower limbs as can be seen in Figure 2.14. The sequential measurements between six conduction paths between the voltage pairs 1-2, 1-3, 1-4, 2-3, 2-4, and, 3-4 were used to compute 8 resistances as shown in Figure 2.14.

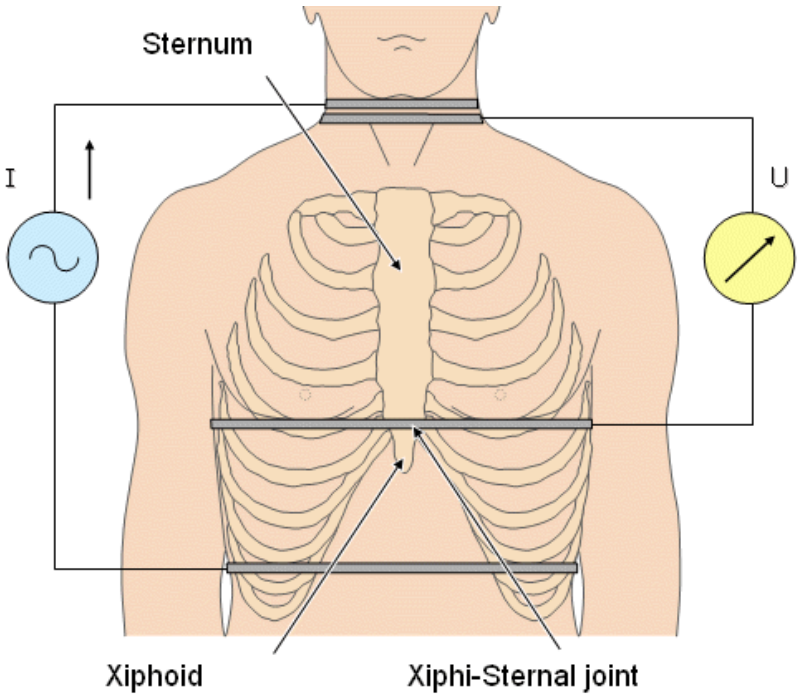

Figure 2.13: Band Electrode configuration for ICG [104]

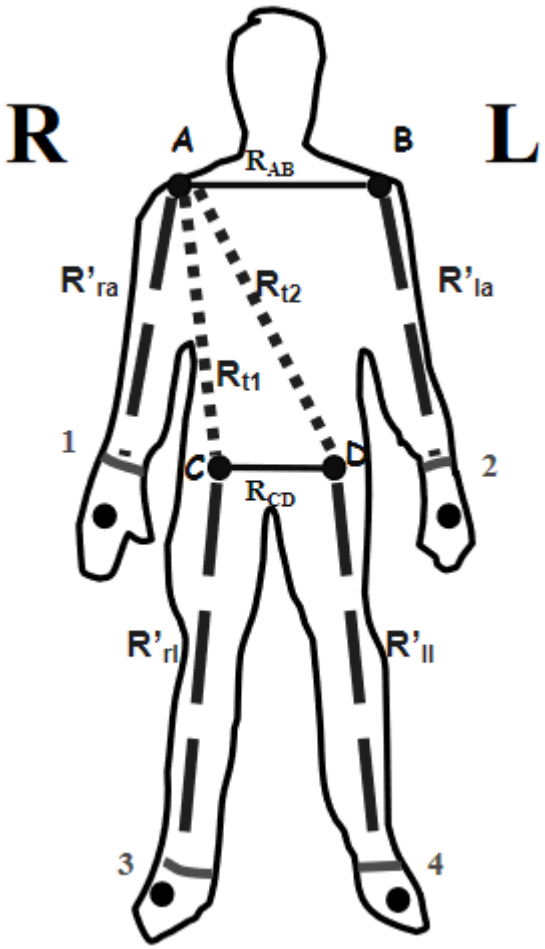

Figure 2.14: 8 electrode system employed by Jaffrin et.al. [109]. Voltage electrodes are numbered 1-4, and current electrodes are A-D

The configuration and the alignment along with the material of the electrodes contribute to the overall measured values. There have been previous significant studies (Nakamura et al., 1992 [110]) regarding the analysis of the impedance changes in muscle tissues to achieve high accuracy for detection of limb motion. Kim et al., 2003 [111] proposed a four channel impedance measurement system to detect limb motion and stated that the optimality in the electrode placements is identified by testing a set of configurations to determine the correlations between the impedance changes and the joint angle as well as the influence from the unwanted signals. Köppä et al., 2012 [112], assessed the electrical model of human skin to analyze the best configuration for electrodes in bioimpedance measurements of skin irritation. The work compared three sequential and three parallel configurations of tetrapolar electrodes to determine the best measurement setup in the skin model. The outcome indicated the best sensitivity distribution was given by the parallel tetrapolar system with minimal spacing.

2.3.4 Skin interaction and textile electrodes

The skin-electrode impedance contributes considerably to the measured impedance changes. Textile fabrication of sensors provides the flexibility to employ capacitive or dry-contact sensing of the voltage, thereby providing more ease of use by avoiding the use of gels. The use of textile electrodes has been reported by several researchers [113], [114] to evaluate the skin-electrode interface modeling and determine the characteristics of skin contact. Not only do the textile electrodes provide different characteristics for skin consideration, but also prove to be non-allergic, comfortable and suitable for ambulatory monitoring. Medrano et al., 2007 [115], measured the skin-electrode impedance using textile electrodes under different temperatures and with different structures. The absence of the electrolytic gel was reflected in a much higher skin impedance on the forearm, and the results confirmed that humidity/moisture of the skin affected the measurements. However, Marquez et al., 2009 [116], compared the employment of textile electrodes in bioimpedance analysis with conventional Ag/AgCl electrodes through the complex spectroscopy tetrapolar wrist to ankle bioimpedance measurements and found no significant difference. Moreover, a similar performance of textile electrodes was found for a wet skin surface.

Medrano et al., 2007 [115] in his work defined a tetrapolar configuration for BIS and modeled the skin-electrode interface with passive elements as well as with a constant phase element (Figure 2.15).

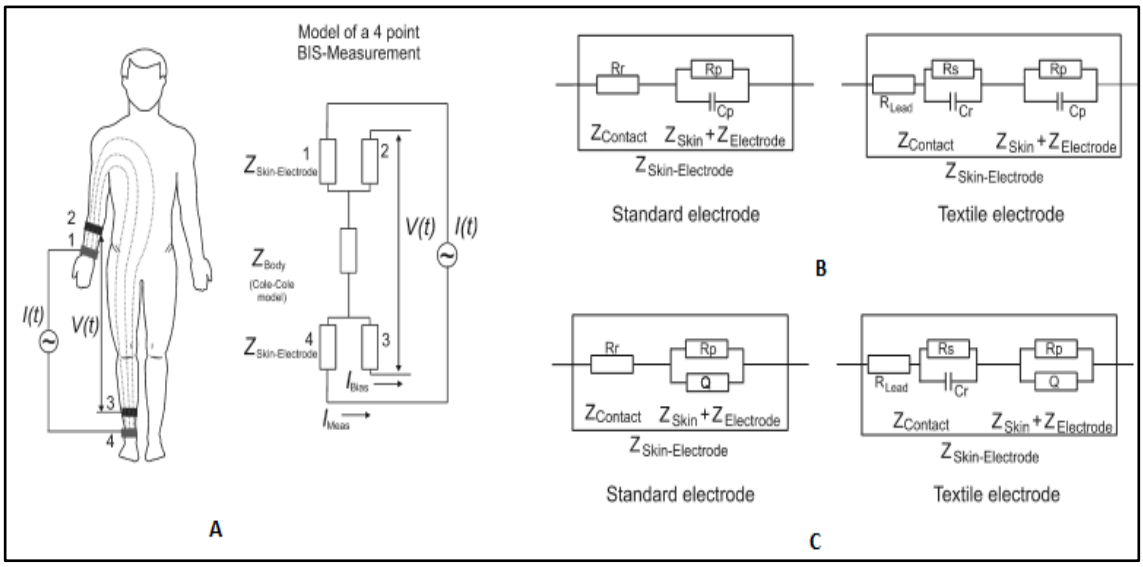

Figure 2.15: A. Tetrapolar BIS configuration with measurement circuit, B. Equivalent circuits for standard and textile electrodes using passive elements, C. Equivalent circuits for standard and textile electrodes using a constant phase element (Q) [115]

The choice of the electrodes and their geometry is essential for accurate measurements; however, it also depends on the requirements of the application. Textile electrodes are suitable for portable monitoring applications, but metal electrodes provide more consistent results in terms of a better signal to noise ratio (SNR). Tetrapolar systems prove to be an optimal configuration for bioimpedance measurements. Spot electrodes offer ease of use anywhere on the human body and in any alignment. Band electrodes offer a suitable choice if the application requires measuring the impedance contributions from both longitudinal and radial directions. Also, skin motion and deformation due to various muscular activities has been known to induce motion artifacts, which may be quite troublesome particularly in ambulatory measuring systems.

2.4 Electrical Properties of Tissues

As has been discussed previously, BIA reflects the electrical response of human tissues. There have been several works that aimed at quantifying the resistivity of different tissue types throughout the human body, which have been summarized in Table 2-2.

In his studies, Pethig [125], stated the conductivity value and the capacitive measure of the cell membranes to be around 10^{-7} S/m and 10^{-2} F/m^2 respectively. This shows the high resistivity of the cell membranes along with the capacitance offered is significant.

As previously mentioned, tissue can be considered as a suspension of cells in a medium with extracellular and intracellular fluid domains. However, the frequency dependence of the fluid resistivity and the membrane capacitance makes it difficult to extrapolate from the dielectric properties of a cell suspension to those of tissue [126]. The behavior of the biological membranes being capacitive as stated earlier by Fricke and later by Cole [72], [127], verifies the impedance of the cells is frequency sensitive. The Cole plot along with the differentiated frequency behavior defined by Schwan led to the conclusion that tissue response cannot be modeled by considering a simple conductive and dielectric passive behavior, but as a *bi-domain* with the impeding elements being frequency dependent. One theoretical basis for electrical analysis is the Cole plot which represents dispersion as pointed out by Schwan and Kubicek's model for ICG. Based on the Cole model, an equivalent circuit distinguishing the extracellular and intracellular responses can be represented as in Figure 2.16.

Notwithstanding all the variability and physiological inhomogeneity of the tissues, they can be electrically modeled using a combination of a conductive element and capacitor in parallel, which is a Debye model. The representation using a resistor and a capacitor can be made adequate at a single frequency but cannot adequately express the immittance of typical tissue over a band of frequencies [104]. At the most, it can be 'fitted' to mimic the response at the extreme frequency values (HF and LF) using the circuit equivalent shown in Figure 2.17.

Table 2-2: Resistivity values for major body tissues

Tissue	Resistivity (Ω-m)	Work/Experimental Reference
Brain • Gray Matter • White Matter • Average	 2.2 6.8 5.8	 Rush and Driscoll (1969) [117] Barber et.al. (1984) [118] Barber et.al. (1984) [118]
Cerebrospinal fluid	0.7	Barber et.al. (1984) [118]
Blood (Ht. 45)	1.6	Geddes and Sadler (1973) [119]
Plasma	0.7	Barber et.al. (1984) [118]
Heart Muscle • Longitudinal • Transverse	 2.5 5.6	 Rush et.al. (1963) [120]
Skeletal Muscle • Longitudinal • Transverse	 1.9 13.2	 Epstein and Foster (1983) [121]
Liver	7	Rush et.al. (1963) [120]
Lungs	11.2	Schwan and Kay (1954) [122]
Fat	25	Geddes and Baker (1967) [123]
Bone • Longitudinal • Circumferential • Radial	 177 15 158	 Saha and Williams (1992) [124]

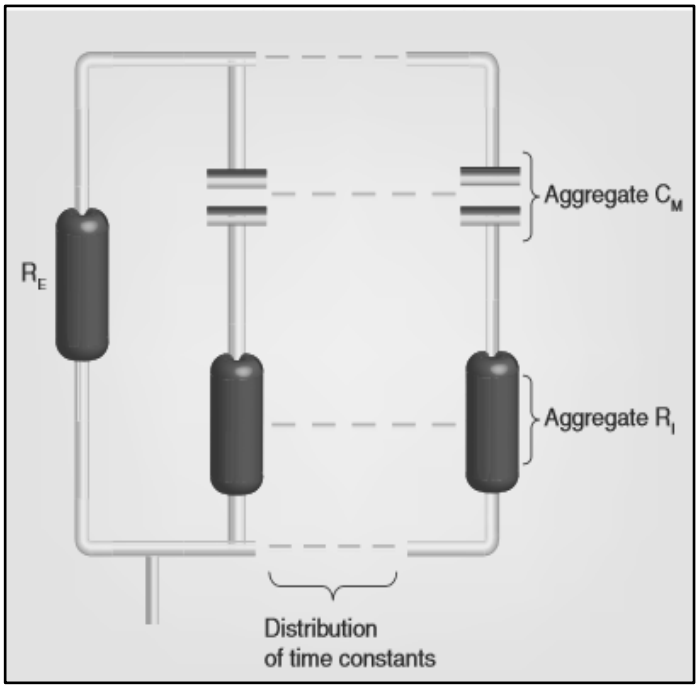

Figure 2.16: Electrical circuit analogous to Cole model [65]

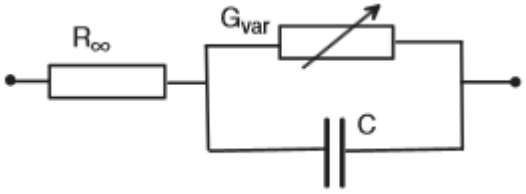

Figure 2.17: Debye model using three frequency-independent components [104]

The requirements of multiple frequency modeling can be met by the introduction of a Constant Phase Element (CPE). It is a form of mathematical realization of a constant phase using a resistor and a capacitor, both of which are frequency dependent such that the phase of the impedance is independent of frequency. This leads to an equivalent circuit (Figure 2.18), the time constant of which is exponentially scaled by a factor, α. The impedance of a CPE can be expressed as [128]:

$$Z_{CPE} = \frac{1}{A\, s^{\alpha}} \tag{2.2}$$

with the dimensions of $\Omega^{-1}\, s^{-\alpha}$ where $s = j\omega$.

This factor α is not correlated to the phase of the impedance [104] but contributes to the overall frequency dependence of the impedance magnitude along with the time constant, being in accordance with Fricke's Law [129].

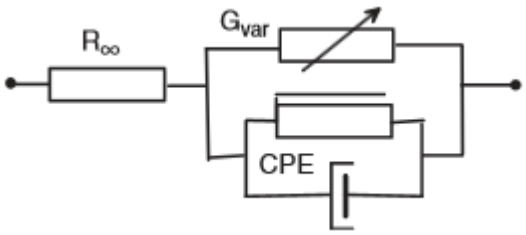

Figure 2.18: An equivalent circuit showing the replacement of capacitor, C, by CPE [104]

Since impedance measurement depends on a variety of factors, it is difficult to reliably define an isolated relation between physiological parameters and model parameters. The modeling is also region specific because the influence of many factors may vary depending upon the area of interest. For example, stroke volume estimation is usually done using the Kubicek model and related equation through ICG. However, for the thorax, the model makes unreliable assumptions such as about the contribution of the lung volume, whereas some of those assumptions may be accepted if the region can be changed to, say, the forelimbs.

Among very few found in literature, an electrical resistivity model was proposed by Zhu and Levin, 2003 [130], defining the relationship between tissues composing a limb (Figure 2.19). R_S, R_F, R_E, R_I, and R_B denote the resistances of the skin, fat, extracellular volume, intracellular volume, and bone, respectively, and represented by the equivalent measured resistance, R_G. C_{IN}, $C_{F,}$ and C_M represent the skin-electrode capacitance, fat capacitance, and capacitance of the cellular membranes, respectively.

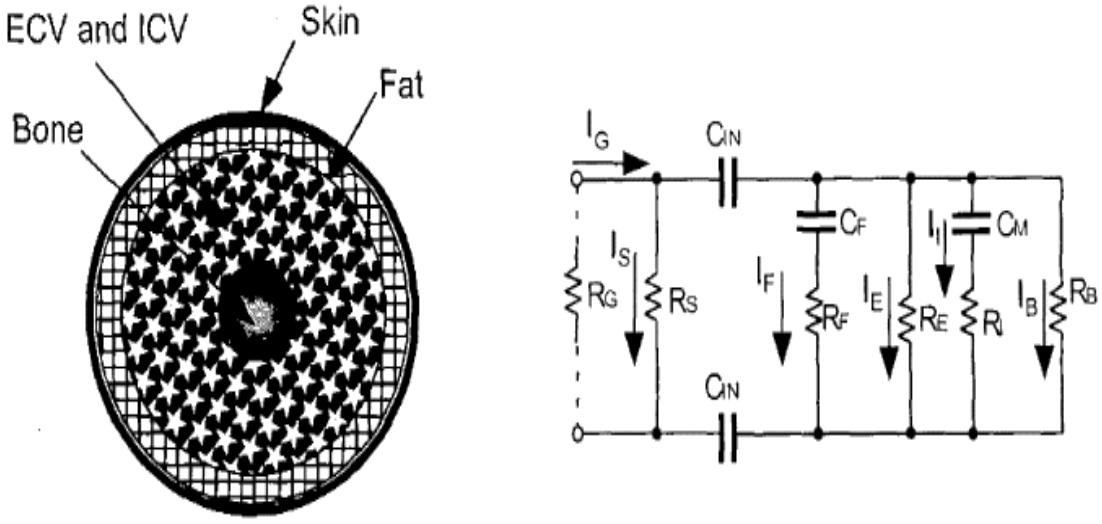

Figure 2.19: A model and the corresponding electrical circuit for a limb segment [130]

2.5 Tissue-Mimicking Phantoms

Biomedical and biophysical investigation is frequently performed using phantoms as alternatives to real tissues. In medical imaging applications, phantoms are employed as imaging samples of known geometric and material structure and are commonly used in the development and categorization of imaging systems. Depending upon the imaging techniques, certain physical properties must be mimicked within a tissue-imitating geometry [131]. As an example, the primary constituent of an ultrasound phantom tends to be water-based (e.g., gelatin, agarose, polyvinyl alcohol, polyacrylamide) which results in a speed of sound similar to tissue [132].

In contrast to real tissue, phantoms can provide repeatable and adaptable tissue-imitating materials with reasonable mechanical, structural and, in this case, dielectric properties keeping in mind the desired goal to accurately mimic human tissues.

Garrett et.al. [133] in their work blended carbon powder and urethane elastic to make a material mimicking human soft tissues. The dielectric properties were measured in the mid-microwave frequency range using a dielectric probe method. Blends of graphite and urethane (0% to half by weight) generally produced low permittivity and conductivity, suitable for impersonating greasy tissues. Blends of carbon black and urethane (0% to 15% by weight) gave an expansive scope of suitable properties. The latter had permittivity and conductivity like higher-water-content tissues. However, the cured specimens were not mechanically suitable for forming into complex shapes. Also, blends of graphite, carbon black, and urethane were developed and tested. These resulted in a range of dielectric properties which could be utilized to mimic a variety of delicate tissues.

One popular tissue mimicking material is a hydrogel which exhibits similar elastic and acoustic properties as that of soft tissues [132]. The two varieties of hydrogels are physical gels and chemical gels, which are obtained by undergoing physical procedures and chemical reactions respectively [134]. Some of the most widely used alternatives to soft tissues are gelatin and agar because they are simpler and safer to use than chemical gel alternatives such as polyacrylamide. However, especially in medical imaging (ultrasonic elastography), physical gels are employed owing to two features: stability and easiness to preserve.

Davidson and Cole (1951), in their work [135], quantified the complex dielectric constants of polar alcohols at frequencies from less than 20 c/s to 5 mc/s over a

temperature range of −40° to −75°C for glycerol, −45° to −90°C for propylene glycol, and −80° to −140°C for n-propanol. The results for n-propanol verified it to be a Debye-type liquid (possessing a single time constant system), however, the properties of the other two exhibited a modified behavior to the standard Debye theory, relating to a more extensive scope of scattering at higher frequencies. In every one of the three fluids, substantial evidence was found for a second scattering area at higher frequencies, which represents a great part of the distinction between the optical dielectric constant and the radio frequency. The relaxation times were quantitatively calculated over wide ranges by an empirical rate mathematical equation of a structure which fitted the measured values.

Another work which replicated the dielectric properties of blood, wet skin, muscle tissues and fat in the frequency range from 0.3 to 20 GHz was proposed by Yilmaz et.al. [136] with the objective of non-invasive and continuous measurement of blood glucose levels. For the whole frequency range, the phantoms demonstrated dielectric properties with certain deviations for relative dielectric constant conductivity. The change in the dielectric properties of the blood-mimicking material was identified by a Cole-Cole analysis. The four-layered tissue mimicking material was used to test the resonator, and the models were verified by performing the measurements repeatedly using these materials with different amounts of glucose.

Marchal et.al. [137] developed phantoms which were a blend of gelatin, water and sodium chloride for imitating human soft tissues and organs. These could be formed into various shapes depending on the tissue to be modeled. The changes in relative permittivity were tested at 10, 27 and 50 MHz from temperatures between 15° and 50°C. At 27 MHz, the mixture with 20% gelatin was proposed suitable to be used as a muscle equivalent phantom with electrical conductivity ranging from 0.27 to 0.48 S/m and relative permittivity from 90 to 93. They could be easily obtained, were of low cost and their preservation was not difficult.

2.5.1 Blood Mimicking Phantoms

Blood is not used readily as a standard fluid in experimental studies because of its short shelf life and easy contamination which significantly affect its properties, hence the necessity for blood-mimicking fluids.

Blood-mimicking fluids (BMFs) are used as blood alternatives in Doppler ultrasonography. Liu et.al. [138] produced a BMF comprising a mixture of degassed and de-ionized water and low-density polyethylene microspheres, gellan gum, nylon particles, and glycerol for the acoustic and thermal characterizations of high intensity focused ultrasound ablation devices. Another work [139] proposed a BMF to be used as Doppler flow test object, which was a combination of ultrafine polyamide particles with a fluid base of (% weight): pure glycerol(10.25%); ICI synperonic N surfactant(0.92%); pure water (85.41%) and Sigma D4876 dextran of average molecular weight 185000D (3.42%). This blood-mimicking fluid highlighted details of the required physical properties like density, viscosity and particle size, and acoustic properties such as velocity, backscatter, and attenuation.

Yousif et.al.[140] produced a blood-mimicking fluid (BMF) to match typical silicone elastomers with refractive indices ranging from 1.40-1.43 and with dynamic viscosity as that of human blood (4.4 ± 0.5 cP) for particle image velocimetry. It was a three-component BMF consisting of water (47.38%), glycerol (36.94%), and sodium iodide (NaI) (15.68%). Different compositions of each component were taken, and the refractive index measurements were determined through an Abbe refractometer by adding sodium iodide salt in regular increments to achieve the expected refractive index matching the silicon phantom. The initial glycerol-to-water ratio was 44:56 by weight for refractive index measurement but was decreased to 40:60 for obtaining the required value of dynamic viscosity.

In this research, it is the electrical properties of blood which are of particular interest. Blood contributes to the overall admittance of an anatomical region due to its high conductivity. There have been several studies of the dielectric parameters of blood which have been compiled by Gabriel [141]–[144] in terms of conductivity and relative permittivity (Figure 2.20).

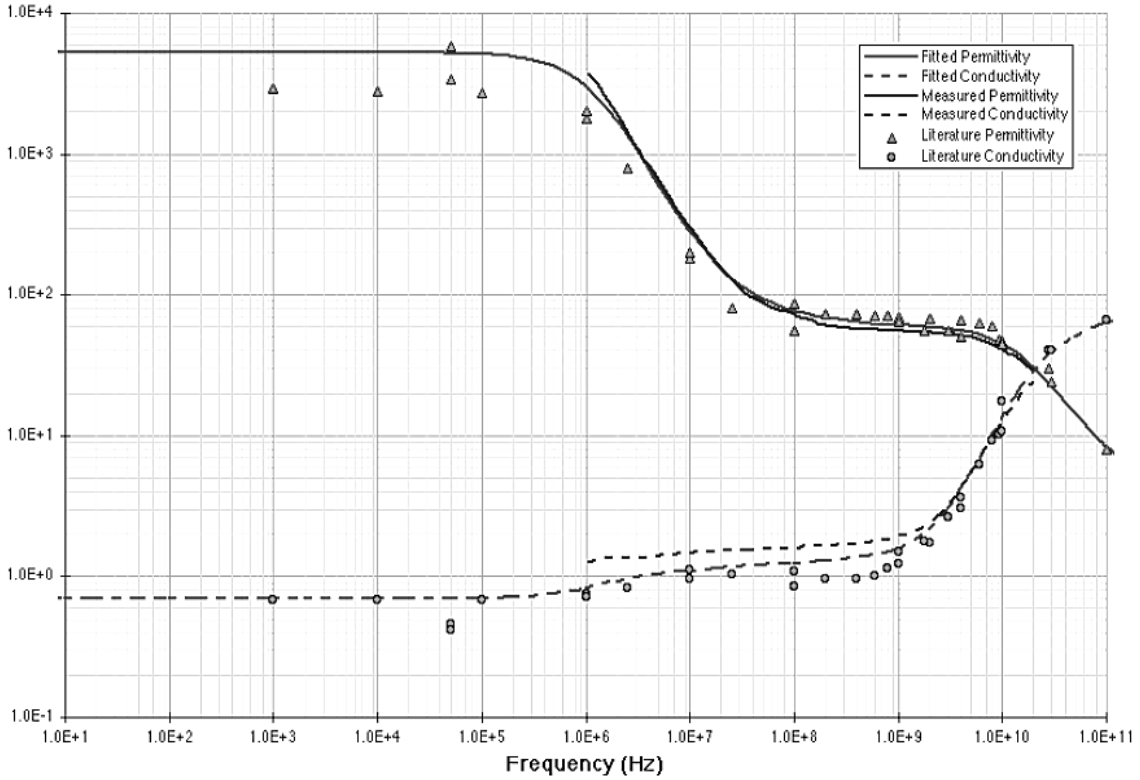

Figure 2.20: Electrical Conductivity and Rel. Permittivity for Blood as compiled by Gabriel [141]–[144]

2.5.1.1 Dielectric Response of Propylene Glycol, Ethanol, and Glycerol

The dielectric response of tissues is due to the complex dielectric relaxation dispersion over its response range of frequencies. The dielectric relaxation dispersion of blood can be suitably approximated by some of the Debye-type dielectric relaxation liquids such as mono and poly hydroxyl alcohols. Three alcohols in particular – propylene glycol, ethanol, and glycerol exhibit a Debye response along with physical properties such as density and dynamic viscosities that make them candidates for blood mimicking substances in this work.

One study [145] carried out dielectric relaxation measurements on propylene glycol-water mixtures over varied concentration ranges at 25°C in the frequency range of 10 MHz to 4 GHz using time domain reflectometry. For this frequency response, the dielectric loss peak was noted at only one point for all the mixtures. The dielectric study of the propylene glycol-water system provided insight into the type of molecular interactions among the combining molecules. As propylene glycol is soluble in water, clusters form due to inter- and intramolecular hydrogen bonds and hence, the shift in the shapes of relaxation curves was investigated. The Debye model for single relaxation time was used to describe the

relaxation of this mixture. The Havriliak-Negami equation was used to fit the frequency dependent complex permittivity data as seen in Figure 2.21.

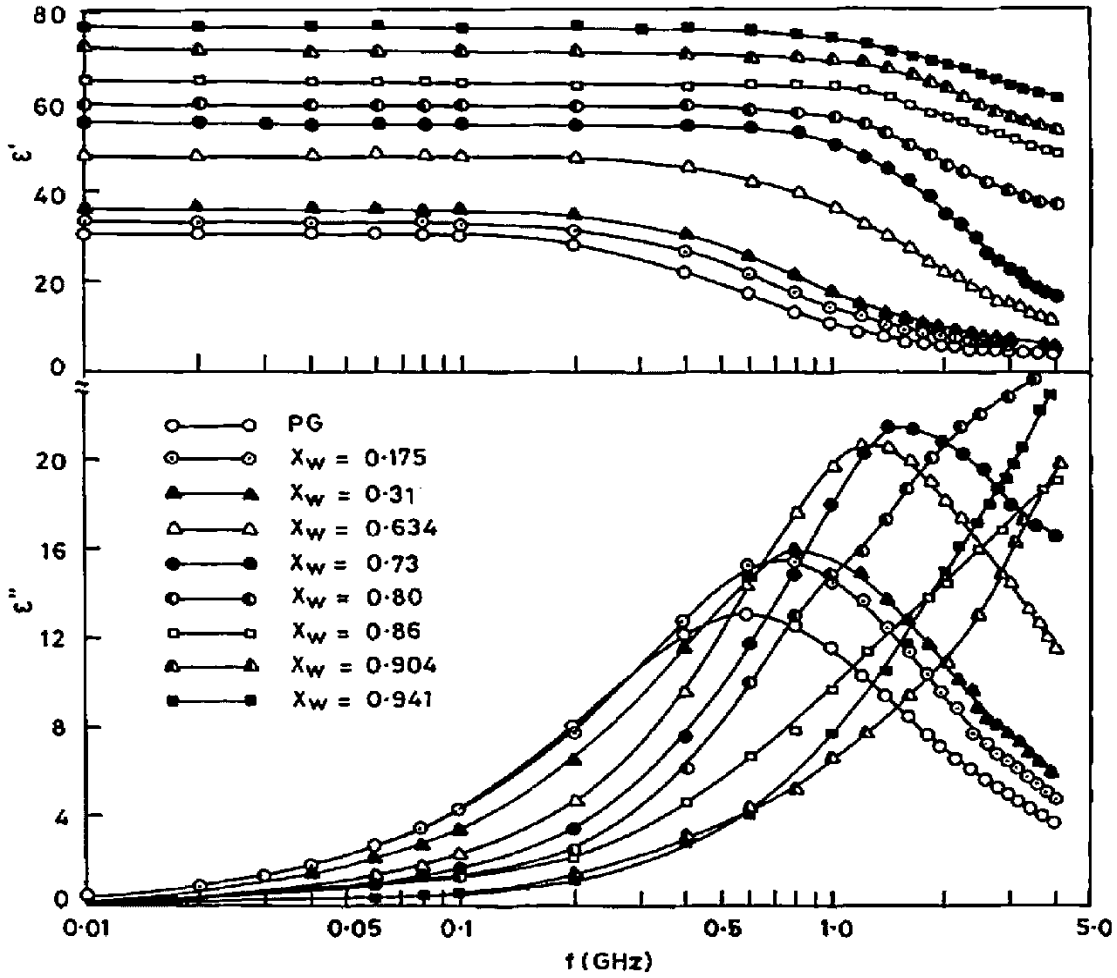

Figure 2.21: The frequency dependence of complex permittivity for propylene glycol-water mixture at various concentrations [145]

Another work [146] discussed the complex permittivity of ethanol-water mixtures which was measured in the frequency range of 1 MHz to 24 GHz. Three methods were applied to measure complex permittivity as a function of frequency in the range from 1 MHz to 24 GHz: a) quasi-static input impedance measurements for frequencies up to 3 GHz, b) automated transfer function measurements for frequency range from 5.3 GHz to 18 GHz, and, c) non-automated propagating wave transmission measurements between 20 and 24 GHz. For frequencies < 10 GHz, the real part of the permittivity spectra followed the Debye-type relaxation function. Water was shown to have similar permittivity data when compared with ethanol, but with different dispersion regions at higher frequencies. The dielectric spectra of ethanol-water mixtures were represented by the Davidson-Cole relaxation spectral function.

In a study by Sengwa [147], the dielectric complex permittivity of propylene glycol, poly(propylene glycol) and their blends with concentration of 25, 50 and 75 vol% of propylene glycol were measured in the frequency range from 10 MHz to 4 GHz at 25°C utilizing time domain reflectometry (TDR). A single frequency dependent dielectric loss peak was obtained during the study for these alcohols and their mixtures. The relaxation for these mixtures was portrayed by a single relaxation time utilizing Debye model. The observed relaxation time for the molecules of propylene glycol indicated the development of clusters of molecules. It was found that the relaxation time for propylene glycol-polypropylene glycol blends was smaller than for propylene glycol-polypropylene glycol molecules, and it was proportional with the concentration of the propylene glycol in the blends. The relaxation time observed was taken as proof of the exchange of solvent–solvent to solvent–polymer association.

In another work [148], the complex (dielectric) permittivity of glycerol-water blends was measured as a function of frequency around 1MHz and 40GHz at six temperatures between 10 and 50°C and at different mole fractions (χ) of glycerol ($0< \chi \leqslant 0.9$). The spectra of the glycerol/water blends were represented by a Davidson-Cole relaxation function that uncovered an asymmetrical relaxation time conveyance.

2.5.2 Muscle and Fat mimicking Phantoms

One of the major challenges in estimating the dielectric properties of tissues is their complexity and heterogeneity. The variation in the electrical response of tissues is non-uniform and varies significantly for each individual and physiological condition. Fat and muscle can be perceived as semi-solids or gelatinous materials exhibiting different degrees of anisotropy in their physical properties. Usually, it is difficult to simulate properties of actual muscle and fat, due to the perfused blood and distributed domains of their existence in the human body. However, a homogeneous replication of their electrical conductivity and permittivity can provide an approximate simulation of their response and contribution to the overall impedance of a part of the anatomy.

As previously mentioned, although there have been several studies of tissue dielectric properties, one of the biggest challenges is to obtain living samples. Obtaining fat and muscle tissues is not difficult, but the normal shelf life and availability does not easily allow determining the ‘living’ properties. The tissue layers (especially fat, muscle and blood) exist perfused together which makes mimicking the actual electrical response

difficult through separately obtained tissues. Another factor is the frequency of interest. The frequency response of tissues is different for each tissue type and the overall response of the tissues varies with the chosen frequency range of interest. Hence the development of a phantom becomes application specific.

Gabriel [141]–[144] in his work compiled and parametrically modeled the bulk values of fat and muscle conductivities and relative permittivities from several works (Figure 2.22, Figure 2.23, and Figure 2.24, respectively). The compilation provides approximate values of the conductivity and relative permittivity for developing the corresponding phantoms. The fitting was performed by employing a four-Cole dispersion mechanism.

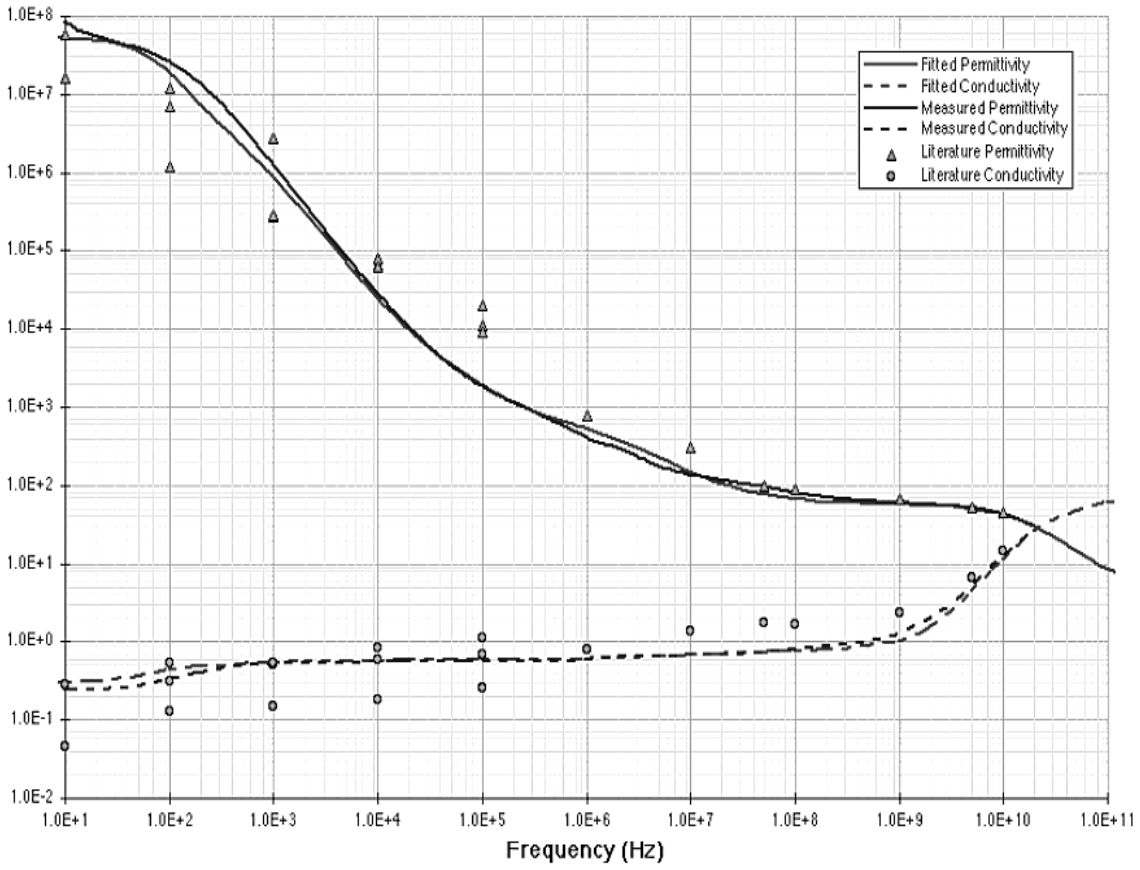

Figure 2.22: Electrical Conductivity and Rel. Permittivity for muscle – parallel as compiled by Gabriel [141]–[144]

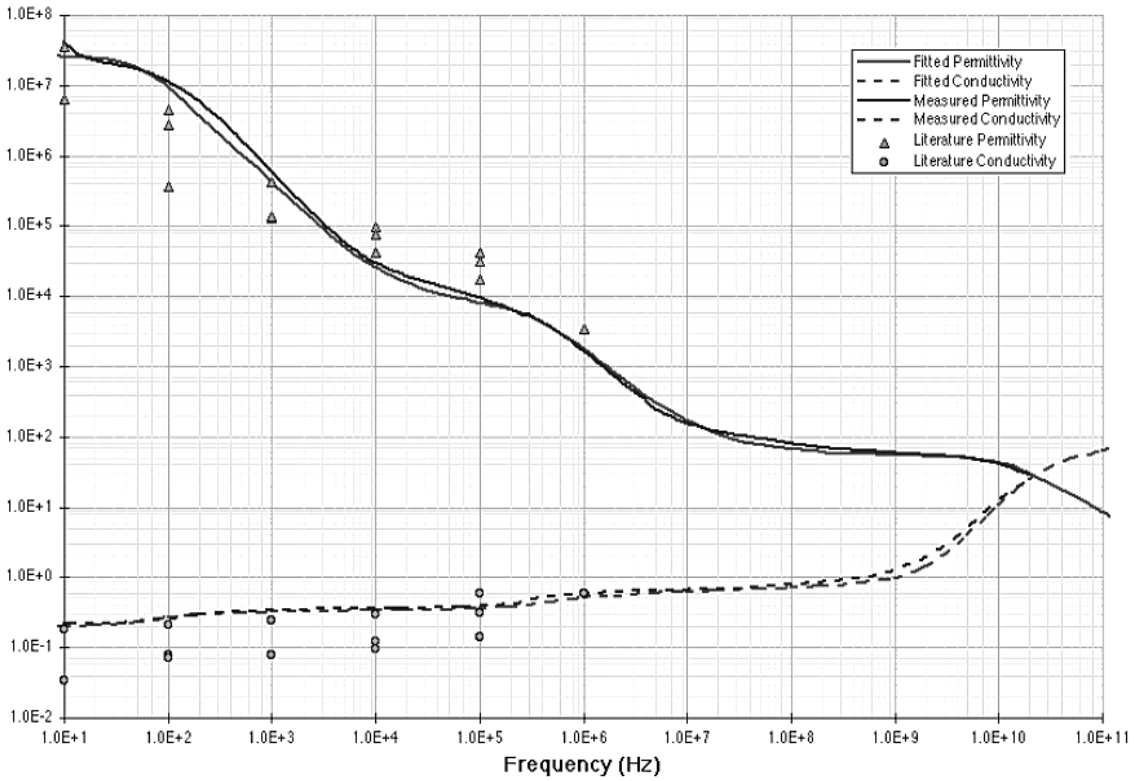

Figure 2.23: Electrical Conductivity and Rel. Permittivity for muscle – transverse as compiled by Gabriel [141]–[144]

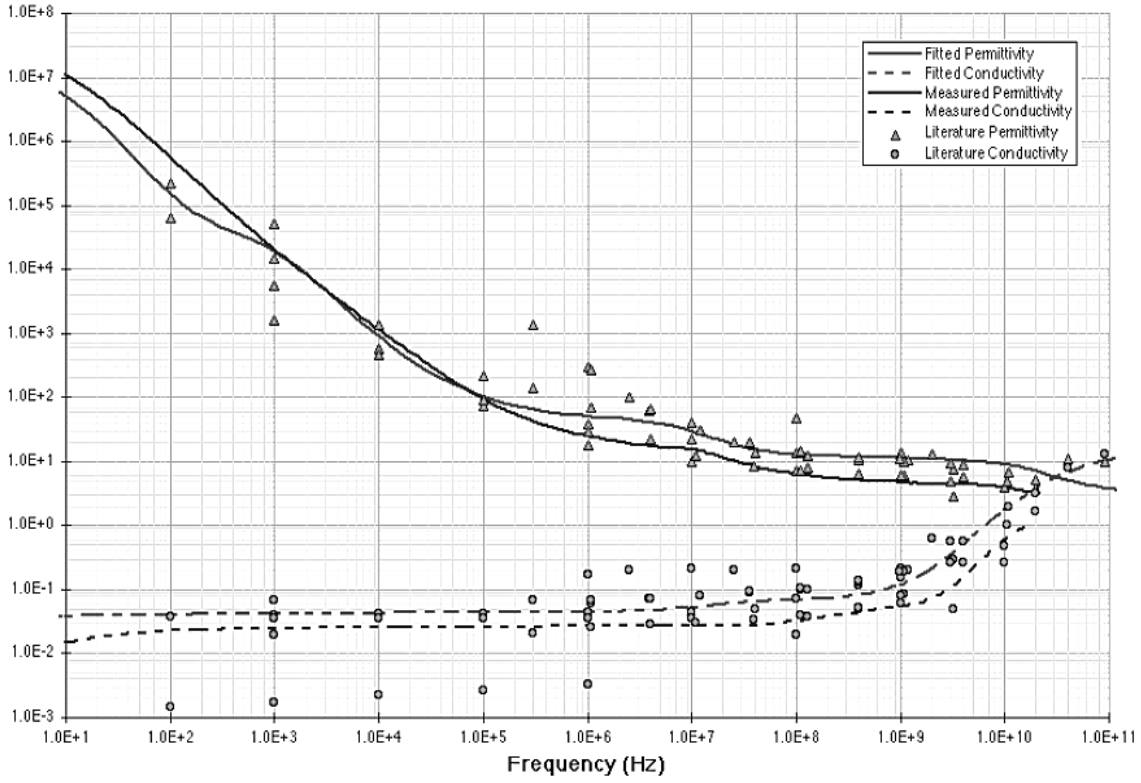

Figure 2.24: Electrical Conductivity and Rel. Permittivity for fat as compiled by Gabriel [141]–[144]

Guy, 1971, [149] developed a gel phantom to mimic different muscle tissues. He proposed a wet phantom made of saline solution, polyethylene powder and a gelling agent – TX-150. The concentration of the salinity of water was used to regulate the conductivity and polyethylene was used to alter the permittivity. A similar process was adopted by Ito et.al. [150] in their work to mimic the overall biological tissue response using a high-water content phantom at microwave frequencies. The phantom comprised of agar, saline water, TX-151 and polyethylene powder to produce the desired values of dielectric parameters. Muscle equivalent phantoms were proposed by Marchal et.al. [137] by using gelatine-water phantoms to mimic and control the electrical parameters of the phantom relating to muscle. The work examined the influence of changing saline concentration on the overall conductivity and permittivity and proposed a phantom with 20% gelatine offering a conductivity within 0.27 – 0.48 S/m and relative permittivity of 90 - 93 at 27 MHz.

An important observation from the properties of fat and muscle helps determine the probable materials to constitute the corresponding phantom. The overall conductivity of muscle is higher than fat along with a higher relative permittivity. The higher permittivity of muscle owes to higher water content and blood perfusion. Due to the comparatively lower permittivity of fat, the phantom materials for fat may include materials like polyenes and oil based emulsions to lower the permittivity of the resulting phantom. Lazebnik et.al. (2005) [151] characterized oil-gelatine dispersions to mimic the dielectric properties of human soft tissues at microwave frequencies. The proposed phantom assumed slightly in-homogenous properties of the tissues without changing the overall geometry. Fomundam and Lin (2016) [152] in their work developed a compound phantom to mimic the dielectric properties of the human surface within 30 MHz – 200 MHz. The phantom consisted of skin, fat and muscle layers, the constituents of which are listed in Table 2-3.

Table 2-3: Phantom material composition as proposed by Fomundam and Lin (2016) [152]

Tissues	**Constituents**
Skin	88.7% Water + 7% Sucrose + 0.3% NaCl + 4% TX-151
Muscle	81.6% Water + 11% Sucrose + 0.4% NaCl + 7% TX-151
Fat	13% Water + 54% Oil + 7% NaOH + 26% Flour

For skin and muscle tissues, water served as the base material with NaCl to increase the ionic conductivity, TX-151 as a gelling agent and sucrose to adjust the permittivity. Fat was simulated using a water-oil dispersion using coconut oil with a high-fat content. Also, NaOH and flour were used to control the conductivity and permittivity. Dec et.al. [153] proposed phantom materials to simulate electrical properties of the human torso (within 75%) within 300 kHz – 40 MHz. The work presented agar and gelatine based formulations which were simulated in the proposed frequency range and tested for longevity and durability (Table 2-4 and Table 2-5).

Table 2-4: Agar based formulation as tested by Dec et.al. [153]

Material	**Quantity (% by weight)**
De-ionized water	82.1
TX-151	1.5
Sucrose	13.3
Agar	2.5
NaCl	0.2
Suttocide (a moldicide to extend shelf life)	0.3
Germall Plus (a moldicide to extend shelf life)	0.2

Table 2-5: Gelatine-based formulation as proposed by Dec et.al. [153]

Material	**Quantity (% by weight)**
De-ionized water	97.4
NaCl	0.2
Gelatine powder	2.4

The agar-based phantom was found to be good in mimicking the dielectricity of soft tissues. The gelatine based formulation also produced the desired conductivity of 0.46 S/m (approximately) but was discarded due to its poor shelf life. However, gelatine was a popular choice in several other studies ([154], [155]) to fabricate low-cost phantoms for impedance spectroscopy for mimicking the electrical response of soft tissues. Robinson

et.al. [156] in their work proposed two materials to mimic muscle and fat equivalent tissues. The high permittivity material (muscle equivalent) constituted water – 40%, NaCl – 2%, ethanediol – 48% and gelatine – 10%. The low permittivity material (fat equivalent) comprised of ethanediol – 55%, polyethylene – 40%, gelatine – 5% and a drop of detergent.

The above-mentioned investigations highlight the use of different materials for mimicking human soft tissues. After analyzing the electrical properties of both muscle and fat and considering the choice of materials by several reported studies, it appears that wet phantoms have a potential to mimic muscle equivalent tissues and solid phantoms (with comparatively lower water content) would be more suitable for a fat simulant. However, the choice of materials depends on the requirements of conductivity and permittivity in the operating range of frequencies. Gelatine/water or gelatine/alcohol phantoms (with high water content) appear to be important constituents when simulating muscle response within the frequency range for this work. Agar/water or agar/alcohol phantoms can be used to simulate fat, although modifications must be made to achieve the desired conductivity and permittivity.

2.6 Effect of Blood flow and compositional properties

The determination of stroke volume from impedance cardiography described by Kubicek [74], was based on a number of assumptions, one of which was assuming constant blood conductivity and velocity. Additionally, approximating the blood volume change as the volume change in a cylindrical cross-section is a major simplification. As is evident from the work of Mohapatra in 1981 and 1988 [75], [157], there is a considerable contribution from the changing blood velocity which is mainly reflected in the systolic behavior of dZ, and the effect of changing blood volume is primarily reflected during the diastolic region of the dZ curve.

The impedance monitoring of blood is affected by various factors as illustrated in Figure 2.25. The overall impedance of the blood is due to the blood composition as well as the blood flow which includes the related changes in the volume and velocity resulting in impedance variations.

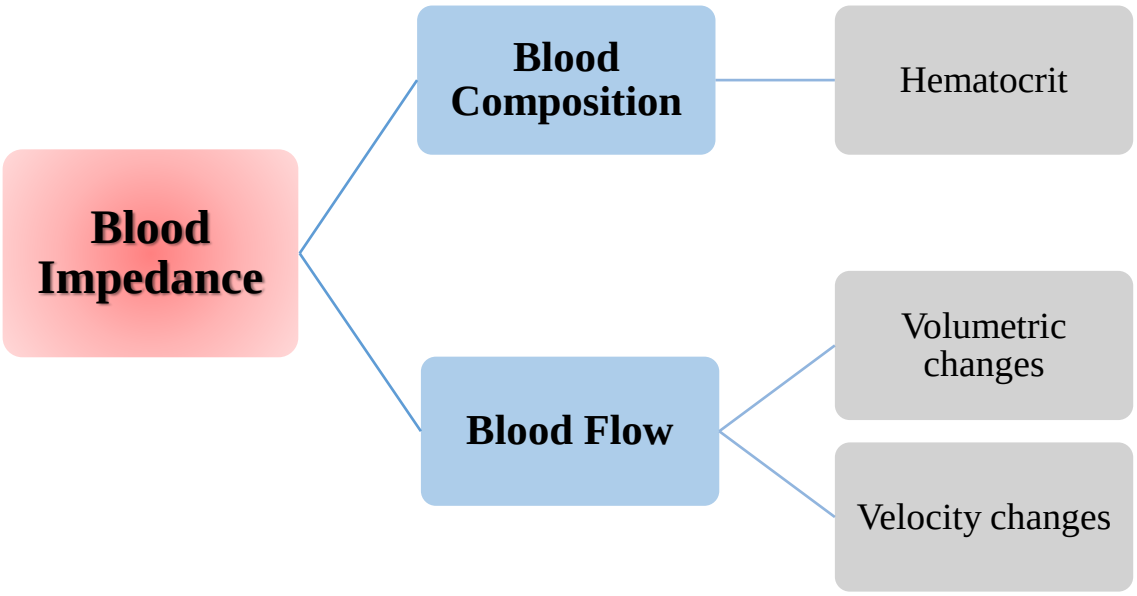

Figure 2.25: Factors contributing to the impedance of blood

2.6.1 Blood resistivity dependence on haematocrit

The use of bioimpedance techniques to determine physiological parameters has been accompanied by the development of biophysical models of the impedance of various tissue types. Every tissue is perfused to some extent with blood and therefore the effect of the compositional characteristics and the dynamics of blood cannot be neglected. Blood is a fluidic tissue which is composed of blood cells (red blood cells and white blood cells) and plasma. The resistivity of blood has been found to depend on the haematocrit value [158]–[160]. In 1975 Mohapatra and Hill [161] verified the dependence of blood resistivity on haematocrit concentration and temperature. They devised a mathematical model relating the specific resistance of the blood with the temperature and the haematocrit, with the temperature rise or haematocrit decrease resulting in the decrease of resistivity. Fricke, 1924 [162], through his theoretical studies of spheroid suspensions, represented the relationship between haematocrit and blood resistivity in the form of Maxwell-Fricke equation. Also, Geddes and Sadler, 1973 [119], depicted the relationship between haematocrit to blood resistivity in the form of an exponential relationship. A comparison of these models is given in Figure 2.26.

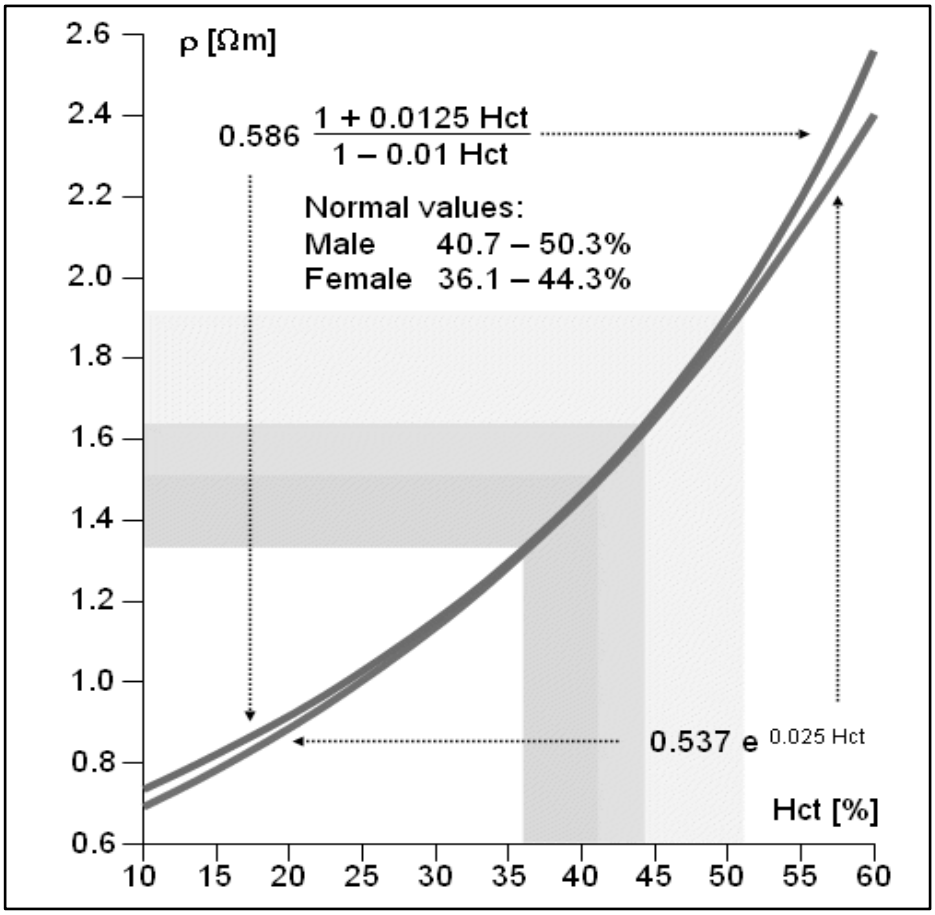

Figure 2.26: Resistivity increase with haematocrit modelled by two equations [66].

2.6.2 Blood flow induced impedance changes

Changes in blood conductivity also occur due to its flow. The change in blood impedance during pulsatile flow has much significance in impedance cardiography and plethysmography. The erythrocyte concentration provides a major contribution to the blood conductivity changes as shown by the work of Hause et al., 1989 [163].

According to Sigman et al., 1937 [164], the electrical conductivity of blood is changed when it is set in motion. His experiments on beef blood concluded that when blood is set in motion from rest, initially, there is an increased electrical resistance which changes to a decreasing trend at faster flows which can be seen in Figure 2.27. It was explained that the initial increase was due to unknown effects between the relative motion of the blood and the electrode (called the electrode effect) and the gradual decrease at faster flows (called the flow effect) depends on changing blood composition associated with its velocity.

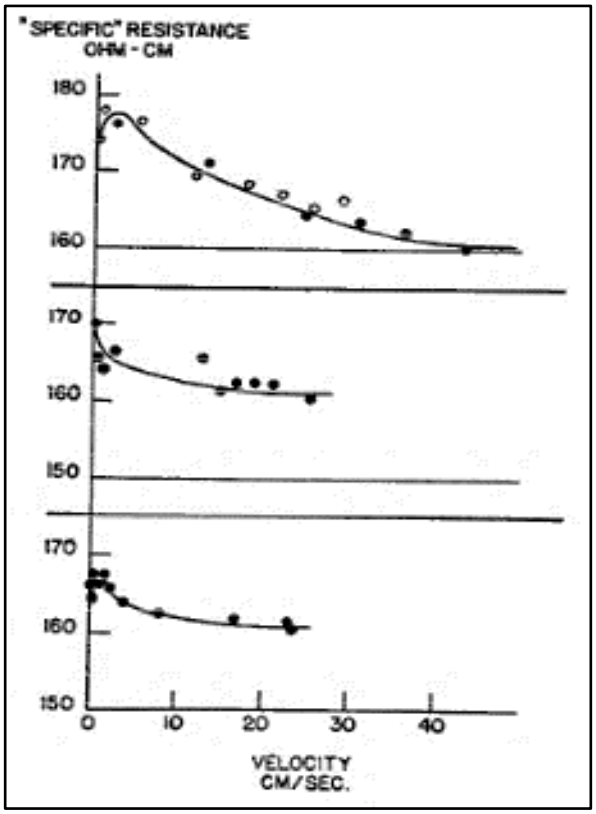

Figure 2.27: Specific resistance variation with velocity for three samples of beef blood [164]

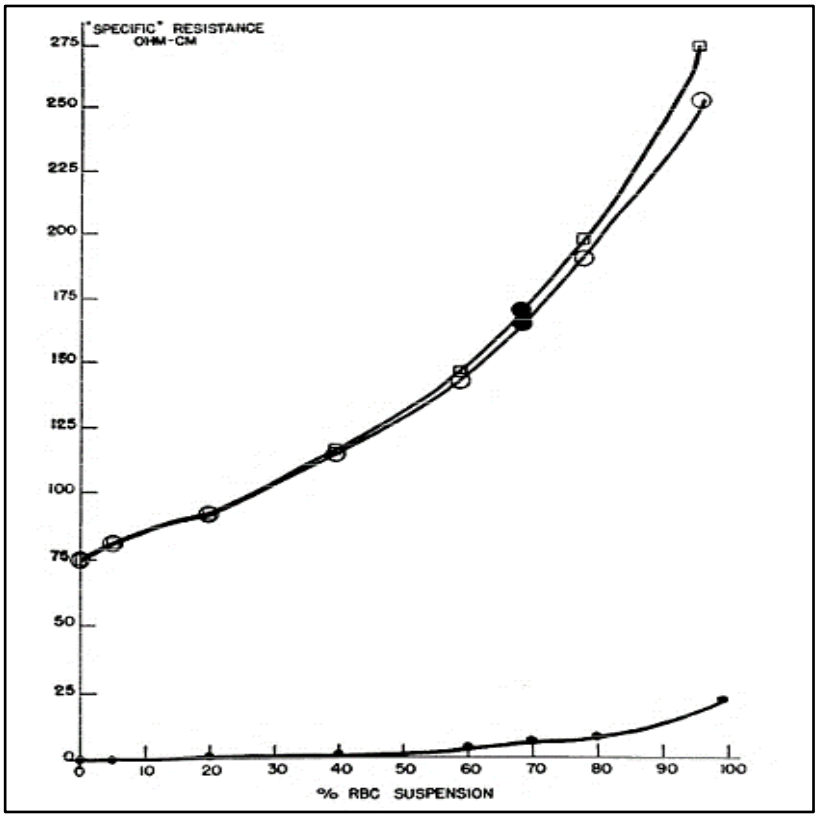

Figure 2.28: Comparison of the varying specific resistance with haematocrit at rest (upper curve) and at a linear velocity of 15cm/sec (middle curve). The lower curve states the difference between the two curves [164]

About the compositional changes of the blood during motion, Sigman stated that the changes in electrical resistance were mainly due to the motion of the erythrocyte fractions, rather than the serum. Also, the flow effect was found to increase by increasing the erythrocyte concentration in the sample as seen in Figure 2.28.

An initial hypothesis was that the variation in resistance with flow was based on the orientation of the erythrocytes or red blood cells (RBC) with respect to the line of flow. However, experiments revealed a decrease in resistance in both the longitudinal and transverse axes of the same order of magnitude. An observed smaller decrease in the transverse direction was accounted by the velocity of blood being smaller along the surface of the tube than in the center; hence eliminating any role of erythrocytes orientation in the flow effect. The work deduced that this flow effect was unique to blood only and is due to the formation of groups of red blood cells during flow. The RBCs clump together when blood is stationary and get separated during the flow, which accounts for resistance changes.

2.6.3 Spatial representation of Blood conductivity changes

Impedance variation caused by the orientation of erythrocytes has been mentioned in previous works [165]–[170], which contradicts Sigman's deduction. Also, Sigman stated the resistance of the erythrocytes to be 3 to 5 times that of serum at 1 kHz which was in accordance with the views of Brooks, 1925 [171]. This was not in complete agreement with the work of Stewart, 1929 [172], and Wtorek and Polinski, 2005 [173], who stated the erythrocytes to be non-conducting resulting in the impedance variations in the blood occurring due to plasma and haematocrit. This creates an interesting argument which can be resolved through experimental studies and better approximations of all the contributing parameters in blood conductivity. Currently it is unclear whether changes in the conductivity are due to the change in the shape of erythrocytes and/or their extent of clumping and de-clumping depending on the blood flow. Considering all the above postulates, Wtorek and Polinski in their work state that the conductivity of blood can be defined as a scalar at rest and by a tensor in motion to account for the medium anisotropy. The entire resistance change of a sample of blood is then dependent on the conductivity change weighted by the scalar product of the two electric fields – the applied electric field and the potential gradient caused due to the conductivity changes. The change in the

resistance due to conductivity changes in the transverse direction was found to be negligible compared to that of the longitudinal direction [173]. The ratio of the transverse resistance change to the longitudinal resistance change ranged between 11 to 63 for the haematocrit values from 0.4-0.5. The changes in the axial conductivity were almost constant throughout the vessel, whereas the transverse component varied periodically with the location in the vessel. This partially accorded with the deductions made by Visser et al., 1976 [174] that the resistance in the longitudinal direction decreases with an increasing rate of flow (as was also deduced by Sigman [85]) and that in the radial direction increases.

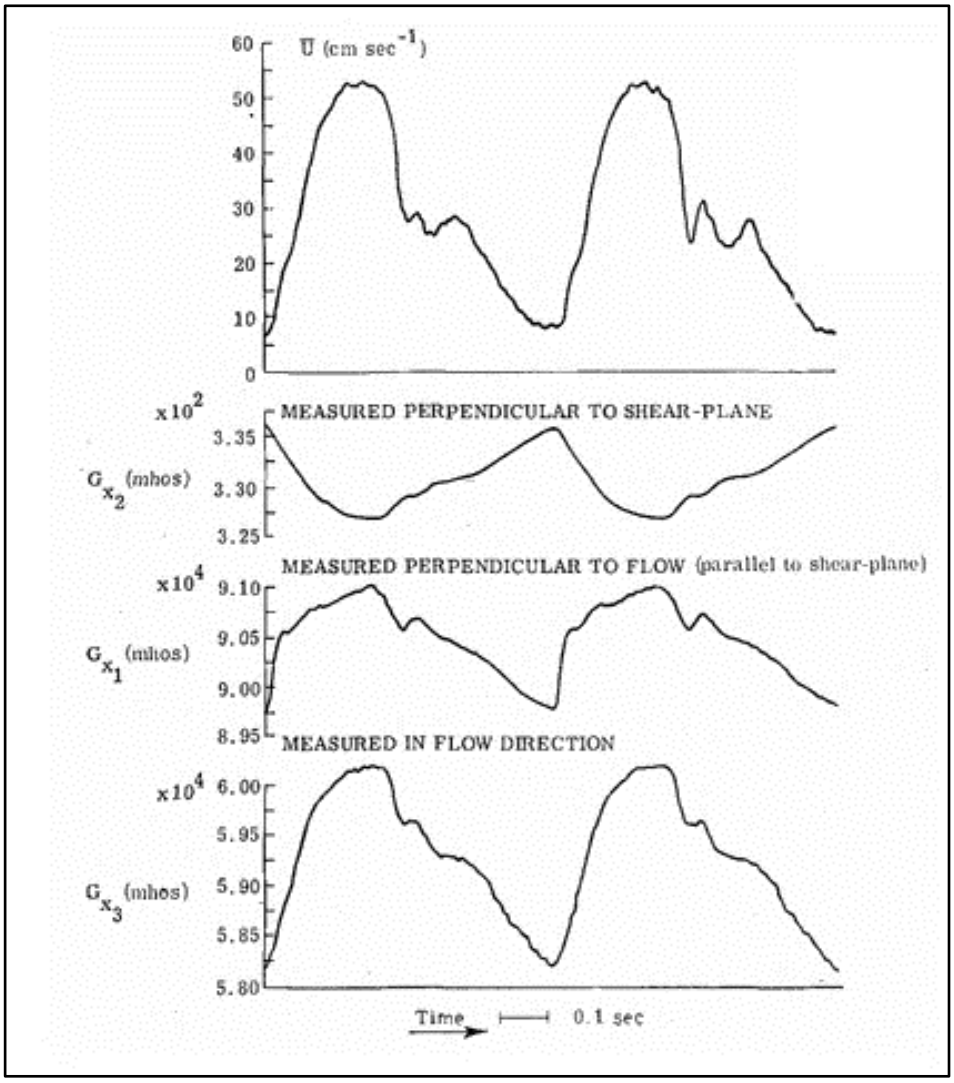

Figure 2.29: Change in conductance in three orthogonal planes with the change in mean velocity [175]

2.6.4 Significance of shear rate, volume changes and microcirculation in determining overall blood conductivity change

An electrical impedance signal obtained from a limb section has contributions from both the blood volume and the resistivity changes. Dellimore and Gosling, 1975 [175] (Figure 2.29), showed that the conductivity in erythrocyte suspensions depends on the volume concentration, shear and the time rate of change of shear. Also, it was stated by Visser, 1989 [176] that the changing resistivity of the blood is a function of its shear profile, for which he defined the variation depending on an amount of reduced average velocity under axisymmetric conditions. He also stated that the resistivity changed in synchrony with the flow in the case of accelerating motion, but not in the case of deceleration. In numbers, the axial conductivity increases by about 4% as the shear rate decreases from 300 to 0 s^{-1} [166]. A combined inference can be drawn that the blood resistivity contribution to the impedance signal ranges within 10-20% (Peura et al., 1978 [177], Shankar et al., 1985 [178]), pointing to the significance of the combined effects of volume changes and inertial effects (Figure 2.30 and Figure 2.31). Prior to these works, there were many under and over-estimations regarding the contributions from resistivity and volume changes. These were addressed by Shankar et al. (1985) by modeling the flow circulation system with physiological transmural pressure in the artery. They measured impedance changes on the compliant artery and on the rigid plastic tube to account for the total impedance signal and that due to only resistivity changes respectively. The signals were recorded for blood flow with low and high transmural pressures along with measurement of a 0.9% saline solution (instead of blood) with high transmural pressure. A strong contribution to impedance (21.5%) was found due to resistivity changes but was out of phase from a more significant volume change contribution (78.5%). Also computed were estimates of other contributions under normal resting conditions which were significant (up to 18.6%) for microcirculation.

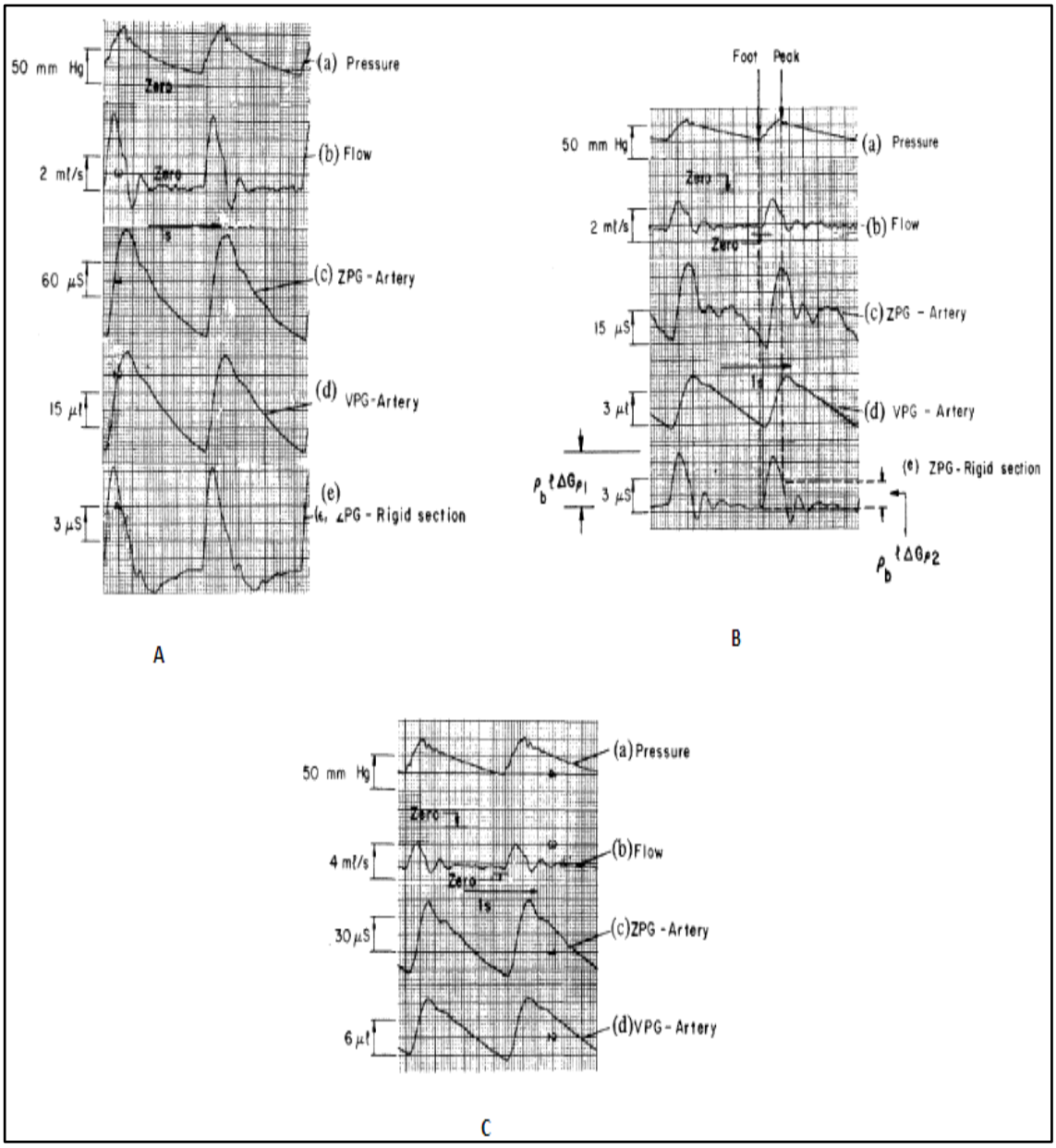

Figure 2.30: Experimental recordings for a bovine artery with A. Blood at low transmural pressure, B. Blood at high transmural pressure and C. Saline solution at high transmural pressure; with a set of readings from (a) arterial pressure. (b) flow, (c) impedance plethysmograph (ZPG) signal from the artery, (d) signal from the strain gauge plethysmograph (VPG), and (e) ZPG from the rigid section [178]

	Large Artery		Microcirculation	
Case	Volume Change (%)	Blood Resistivity Change (%)	Volume Change (%)	Blood Resistivity Change (%)
Normal	77.5	3.9	5.2	13.4
Reactive Hyperemia	82.3	3.3	13.2	1.2
Atherosclerosis	67.3	10.2	8.8	13.7
Peak Compliance	97.7	2.3	0	0

Figure 2.31: Relative Contributions to the impedance signal for a limb section [178]

2.6.5 Consideration of Blood Acceleration

A study by Gaw et al., 2008 [179] explored the relationship between the impedance variations and its relationship to the velocity and acceleration of the blood during its pulse in the cardiac cycle. The analysis was done in a rigid tube circulatory system and the corresponding relationships were studied. The velocity change affects the impedance non-linearly at low velocities and deceleration, and almost linearly during acceleration (Figure 2.32 and Figure 2.33). The effect of the velocity change is less at higher velocities until it reaches a saturation defined by the alignment and clumping/de-clumping of all the RBCs [166], [176], [180]–[184].

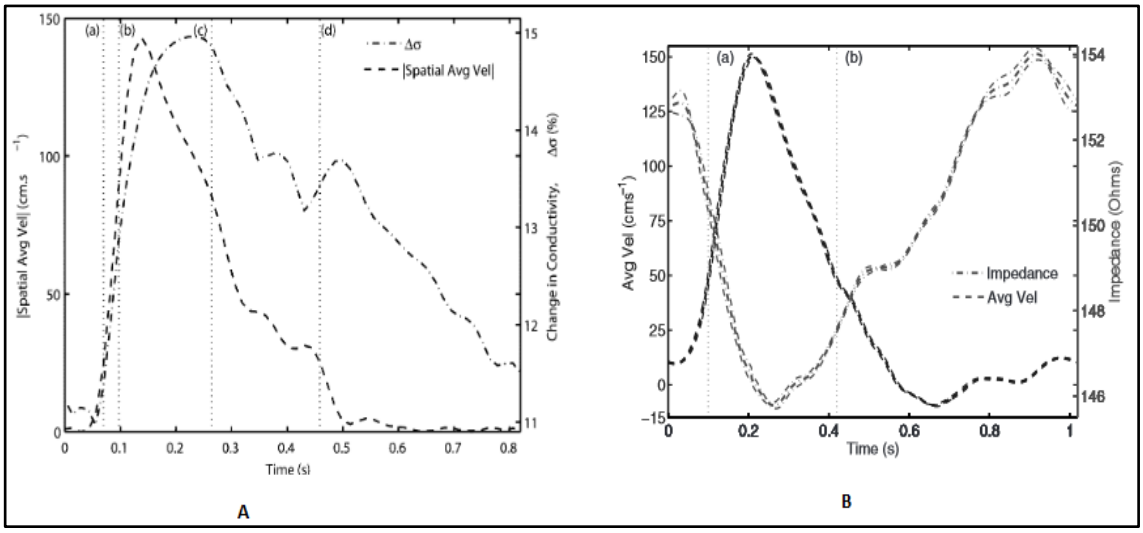

Figure 2.32: Ensemble averaged velocity versus A. conductivity and B. impedance of blood over one pulse (Hct=45%) [179]

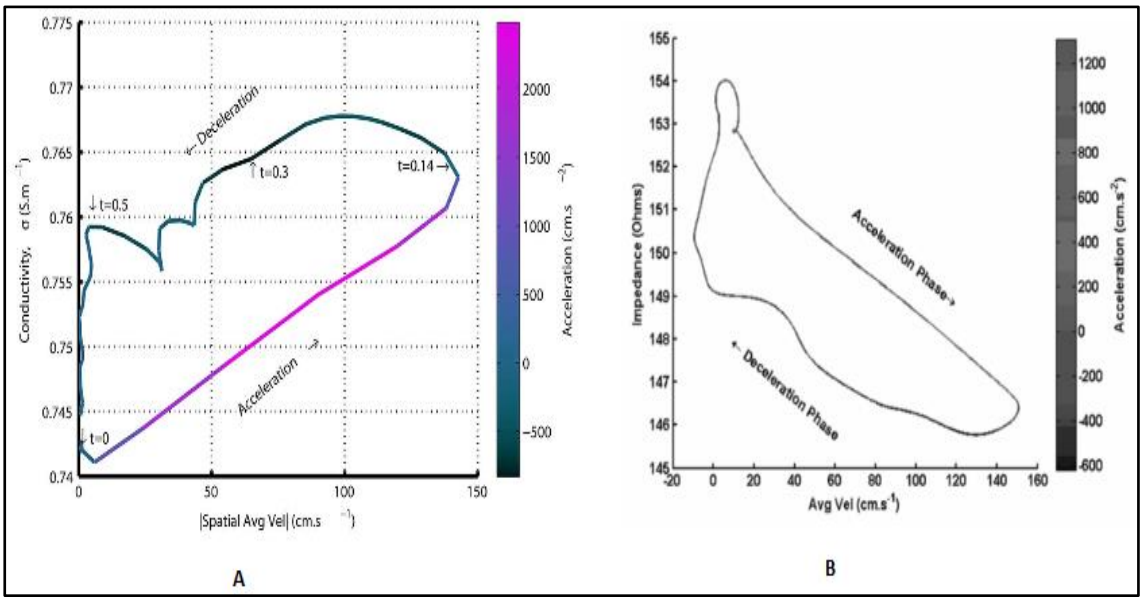

Figure 2.33: A. Conductivity and B. Impedance versus spatial velocity with acceleration and deceleration phases [179]

2.6.6 Modeling of the 'Sleeve effect' and non-Newtonian properties of blood

The electro-mechanical properties of blood were examined by Jager et al., 1965 [185], when they tried to model an electrical analog of the oscillatory flow impedance of blood. The work was limited to regions of left ventricle, aortic valves and the adjoining peripherals. The assumption of laminar flow in all arteries was taken. Their work aimed at investigating the 'sleeve effect' (interaction between the inertial and viscous

phenomenon) and non-Newtonian fluid behavior [186]. The sleeve effect was considered using the relationship derived by Womersley [187] for laminar oscillatory flow in an elastic tube, resulting in a change in the longitudinal impedance and not the transverse impedance (Figure 2.34).

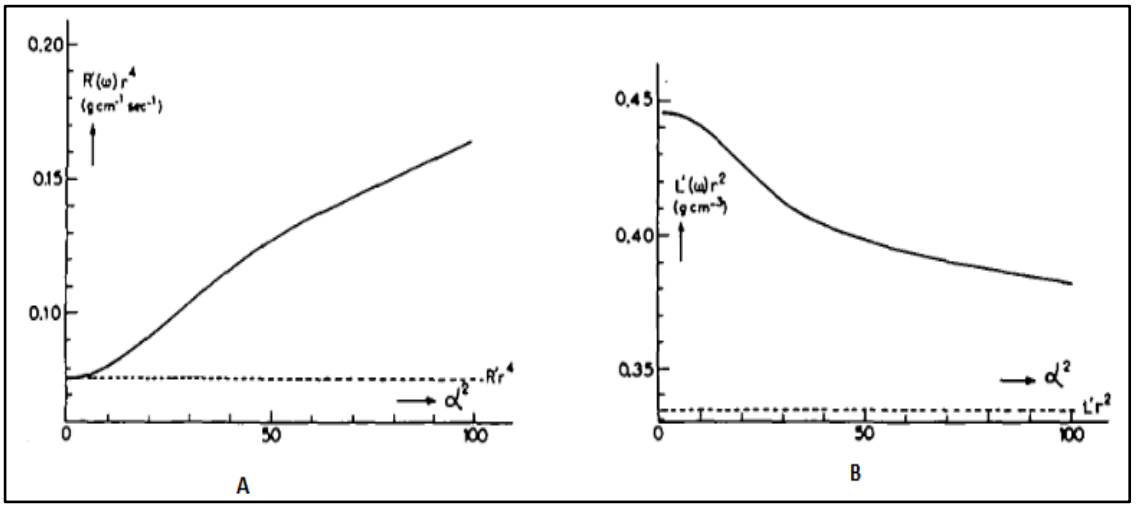

Figure 2.34: A. Real part and B. Imaginary part of longitudinal impedance; with (solid line) and without (dotted line) sleeve effect [185]

The electrical analog obtained by Jager et al., 1965 [185] is shown in Figure 2.35 . The model shows the tissue behavior as a parallel lumped parameter network of R-L circuits. The model shows that the overall behavior of the tissue domains can be approximated through parallel networks of passive elements to define the overall dielectric behavior.

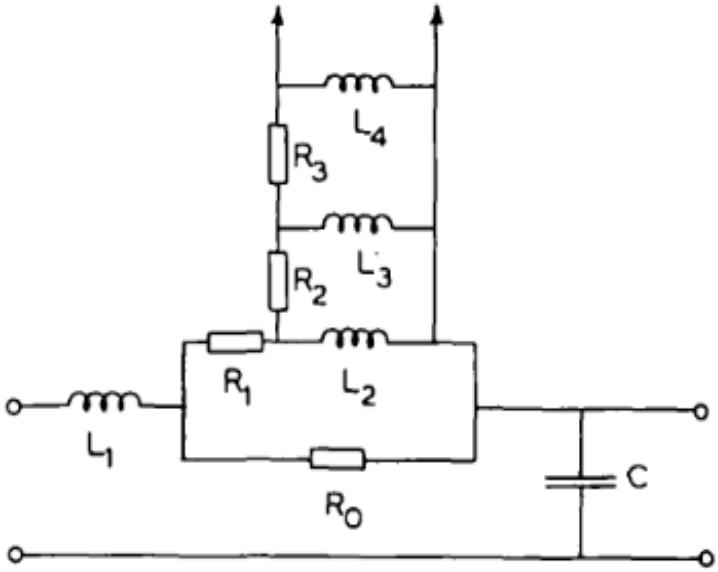

Figure 2.35: Electrical analog for oscillatory blood flow impedance with all suitable corrections (R_o is the correction for anomalous viscosity, C is the capacitance and R_i, L_i are the longitudinal impedance parameters where the extent of i defines the accuracy of the system [185]

The anomalous effect of viscosity on oscillatory flow was also considered. It is known that the viscosity of blood depends on the rate of flow and the tube dimensions as it decreases with the increasing rate of flow, where the flow itself varies with the diameter. This, again, may be due to the clustering of RBCs or their orientation [188]–[191]. Taylor [191] provided appropriate modifications to introduce the viscosity effects in the electrical analogy, again for which, only the longitudinal impedance was affected by a factor accounting for both the sleeve effect and the slip at the arterial wall.

2.7 Research Gaps

The literature review has highlighted the many facets affecting the application of BIA in measurement systems. It is apparent that there is still much to be learned in many of these areas. In particular:

- The driving circuits required for MF-BIA have been found to perform within a limited frequency range. There is a need to address the current source requirements at frequencies higher than 1 MHz to adequately investigate the β dispersion tissue response.
- There have been very few works directed towards modeling the dielectric properties of human limb sections. More specifically, existing electrical equivalent models are based on isotropic behavior of tissue properties and are hence defined using passive electrical elements.
- The choice of the tissue mimicking materials is predominantly limited to simulating the high frequency (above 1 GHz) behavior of the human tissues and extrapolating the obtained measurements to lower frequencies through parametric model fitting. Not enough literature addresses the polarization impedance of suspension mixtures at frequencies less than 100 kHz.
- There is no clear evidence to support the cause of impedance variations due to blood flow. The blood composition contributes passively to the overall impedance but there is not enough literature supporting the clustering of erythrocytes as the reason for changing blood resistivity as stated by Sigman [164] – which has been counteracted by Wtorek and Polinsky [173].
- Inadequate modeling of the effect of mechanical effects such as blood velocity and shear rate on the electrical response of blood has been found. This is important

to correctly quantify the overall contribution of hemodynamics to the impedance measurements.

- No work presents a simulation perspective to modeling the dielectric properties and response of human forearm section. Moreover, there are limited works presenting the evaluation of tissue dielectricity, within β dispersion frequency range, through phantom development.
- There is not enough literature documenting the contribution of different tissues to the overall impedance measurements in human limbs. This is important as it helps understand and quantify the electrical interaction of different tissue dielectric domains.
- No literature supporting the use of MF-BIA for hemodynamic monitoring and relating the volumetric changes in the radial artery to be reflected through impedance response at multiple frequencies. MF-BIA offers a wide range of possibilities in terms of characterizing individual tissue response and hence can be used to isolate the blood flow induced impedance changes from the overall tissue response.

The work presented in this thesis does not attempt to address all of the above points. Its specific research objectives are presented next.

2.8 Research Objectives

The main objective of this research is to **understand the relationship between arterial diameter changes due to blood flow and multi-frequency bioimpedance response**. Existing literature uses SF-BIA to estimate the blood flow waveform but is based on an approximated derivative of empirical stroke volume relations. This research will contribute a more in-depth analysis employing multi-frequency bioimpedance measurements (MF-BIA) to estimate the effects of arterial diameter changes with blood flow. The following objectives support the main goal of this study:

- **Investigate the dielectric response of fat, muscle and blood tissue domain in the human forearm at frequencies within β dispersion region through a simulation study of a forearm model at different arterial diameters.** This will help to understand the distribution of an externally applied electric field within

the forearm section at several instances of radial artery diameter. Such a study has not previously been performed.

- **Identify potential materials to mimic the dielectric properties of fat, muscle and blood, constructing a forearm phantom from which impedance spectra can be measured and compared with the simulation response.** This part of the research will identify new materials which simulate dielectric responses at lower frequencies than generally reported in the literature. The constructed forearm phantom will provide a unique platform of validation for the simulation study.
- **Electrically modeling the simulation response of the tissues in terms of Debye and Cole parameters.** This will aim to fit the obtained response from the simulation study to Debye and Cole electrical equivalent circuits including the modeling of the arterial diameter as a parameter contributing to the impedance changes. This approach differs significantly from the usual semi-empirical relationships reported between blood flow and impedance. It will contribute new models that can form the basis for clinical estimation of artery diameters from impedance measurements.

To address the above-mentioned research objectives, the rest of the thesis has been structured according to the following format:

1. Chapter 3: Presents a simulation analysis of a human forearm model with three tissue layers – fat, muscle and blood – simulating the measurement of multi-frequency impedance response and investigating the contribution of individual tissue layers.
2. Chapter 4: Discusses the development of a tissue mimicking phantom for a human forearm section to approximate the dielectric properties of fat, muscle and blood. The chapter includes the identification of each tissue simulant and how they are used together to measure the overall multi-frequency impedance response, which is compared to the simulated response.
3. Chapter 5: Presents new electrical models for the human forearm BIA response in terms of Debye and Cole dielectric relaxations, along with the modeling of arterial diameter contribution to the impedance spectra. The models are compared to the simulation and phantom behavior.
4. Chapter 6: Relates the results of a pilot study of BIA measurements in the human forearm to the simulation, phantom and modeling components of this research.

5. Chapter 7: Presents conclusions of this research and possible future directions for research in this area.

2.9 Closure

This chapter presented a literature survey of different factors that affect and contribute to the multi-frequency bioimpedance measurements. The literature survey was divided into five parts addressing instrumentation for the BIA measurement, effects of electrode types on BIA measurements, the electrical properties of tissues, potential tissue phantom materials and the contribution of blood composition and flow to the BIA measurements. The literature survey was followed by the identification of research gaps and the research question for this project. The research objectives were highlighted and the consequent structure of this thesis was outlined.

Chapter 3 SIMULATION ANALYSIS OF HUMAN FOREARM MODEL

3.1 Introduction

This chapter focusses on the initial objective of understanding the effect and distribution of an electrical field within the tissue structures of the human forearm subject to bioimpedance measurement. This has been investigated through computer simulation including of different tissue layers and particularly the blood-filled artery. This section focusses on investigating the type of dielectric response of the overall forearm section model. Moreover, the contributions of the various tissue layers are analysed to understand their respective dielectric behavior. The major objective is to investigate the effect of different arterial diameters on the overall impedance measurements, thereby mimicking the effect of blood flow induced volumetric changes in the artery.

The first section of this chapter introduces the ANSYS ® HFSS platform which was used to model and simulate the impedance response between 1 kHz – 2 MHz. The following section discusses the construction of the human forearm section geometry with the three tissue domains – fat, muscle and artery (blood). This is followed by an explanation of the simulation setup and the results for simulated impedance responses for three diameters of the artery.

3.2 ANSYS® HFSS

The construction of the model as well as the analysis was carried out using the ANSYS® Electromagnetics 2015 (ANSYS, Inc., USA), and particularly the electromagnetics suite (Electronics Suite, including Electronics Desktop and Maxwell, for more recent release of ANSYS®). In particular, the High Frequency Structure Simulator (HFSS) was used due to the signal frequencies being simulated.

ANSYS ® HFSS has been built to provide an extensive analysis of 3-D electromagnetic fields within a structure at high range of frequencies. It uses advanced solvers based on solving complex, time-varying Maxwell's equations, finite element modelling and integration for analyzing electronic devices or sensors [192].

The different steps employed in simulating a structure in ANSYS Electronics Desktop/HFSS can be summarized as follows:

- Construction of the structure geometry
- Choosing the Solution type: Modal, Terminal or Transient
- Assigning the boundaries and excitations
- Defining the material properties for each component or layer
- Defining the mesh operation settings for finite element modelling
- Adding the solution setup – defining the solution frequency and/or number of adaptive iterations
- Validating the design and all the included definitions
- Analyzing the design

The post-analysis operations include visualizing the simulated electric field (E), magnetic field (H), current density (J) and others. Additionally, the results or any quantity can be processed using an in-built calculator that provides ability to perform general calculations to complex surface or volume integrations within and around the geometry. This was used to derive quantities which were not directly produced as results.

3.2.1 ANSYS® HFSS Solver

HFSS solver is based on the assumptions and solutions of Maxwell's equations that describe all electromagnetic phenomenon. These equations relate the electric field $\vec{E}$ with magnetic field $\vec{H}$ through the material properties defied by electrical permittivity ε, electrical conductivity σ and magnetic permeability μ. In ANSYS® HFSS, the parametric models are considered in the differential form of Maxwell's equations:

$$\nabla \times \vec{E} = -j\omega\mu\vec{H} \tag{3.1}$$

$$\nabla \times \vec{H} = (\sigma + j\omega\varepsilon)\vec{E} \tag{3.2}$$

$$\nabla . \varepsilon\vec{E} = \rho \tag{3.3}$$

$$\nabla . \mu\vec{H} = 0 \tag{3.4}$$

where $\omega = 2\pi f$ (f is the frequency in Hz) and ρ is the current density. As is evident from the above equations, the electric and the magnetic field components are coupled and give rise to different effects like radiation and phase delays, which are important in high frequency applications. The basic solution of these Maxwell's equations by the HFSS solver is based on the assumption that the wavelength at the maximum solution frequency

is significantly higher than the size of the geometrical model (approximately ten times) [192]. Also, the total current injected into the source terminal equals the net current leaving the sink terminal, i.e., negligible displacement current for calculating the inductances, and inductive voltage drops (produced by the time varying magnetic fields) are neglected while calculating capacitances. In addition, the solver offers capabilities to define the material properties as frequency dependent. However, the frequency dependent material properties are considered to be isotropic at each solution frequency to yield a linear solution.

The solution for most quantities requires specification of an excitation on the model. The most basic way to simulate bioimpedance measurement is to apply a known excitation current into the tissue domain. This was specified as 1 mA considering the tissue properties and practical bioimpedance measurement implementations. Due to the tissue domains being considered as lossy dielectrics, the solution described the electric field as a complex quantity, which was used to calculate the potential difference across the electrodes by considering a line integral between the two electrodes. The calculated real and imaginary parts of the voltage were used to identify the resistance and reactance of the model at a particular frequency.

3.3 Human Forearm Model

A 3D finite element model of a simplified human forearm was constructed using ANSYS® HFSS to allow the simulation of the electrical response in the desired frequency range. Our investigation is limited to the β dispersion region as it is in this frequency range (1 kHz to 100 MHz) that tissues reflect maximum passive cell membrane capacitance and intracellular organelle capacitance effects. [193]. Hence the β dispersion behavior provides important information related to the dielectric response of the tissues, which is realized through bioimpedance measurements.

The forearm was modelled as a structure consisting of three tissue domains **– fat, muscle and artery** (Figure 3.1). The fat layer served as the outermost layer and was concentric to the muscle domain. The radial artery was included as an important site for impedance contributions due to pulsatile blood flow. The other blood vessels in the forearm were not included in this study. Even though bone is a major part of the forearm, the overall contribution of bone to the electrical impedance changes was expected to be negligible

over the β dispersion frequency range. Hence, the initial simulation setup was considered without including bone in the geometry.
The high impedance of the skin layer was expected to be an insulator in the path of a very low amplitude current to be used for excitation. This effect, is however, mitigated by using gel electrodes but would be prevalent for the simulation setup which has been discussed later. Hence, the model was initiated with only three dielectric domains of fat, muscle and artery.

The fat and muscle regions were considered as layered and concentric along the same axis, whereas the arterial geometry overlapped the domains of both the muscle and fat regions. This design, in which the dielectric domains in the model are not all concentrically layered, represented a degree of distribution of the different tissue domains in the model. The longitudinal dimension of the section of the arm was 70 mm, with the fat layer having a thickness of between 3 to 6 mm and muscle with a thickness of 10 to 15 mm from the axis. The artery was modelled to mimic the anatomical radial artery properties using three different diameters – 2.3 mm, 2.35 mm, and 2.4 mm as reported by previous work [194], [195]. The artery (blood) geometry was defined as a tubular structure of uniform diameter of 2.3 mm extending through the 70 mm forearm section. The arterial wall was not considered due to it having similar dielectric properties in β dispersion frequency range as those of muscle tissue.

3.4 Simulation Setup

The simulation of the bioimpedance measurement setup comprised of the forearm section attached to two pairs of coaxial conductors, each serving as an electrode site for the application of current and voltage measurement respectively (Figure 3.1 and Figure 3.2). The amount of current injected was limited to 1mA for simulation purposes which reflects the safety limits as specified by the IEC 601 standards [196]. The aim of the simulation was to provide a frequency sweep of the dielectric response of different layers and, more specifically, the distribution of current in each dielectric domain. The arm structure was enveloped with a radiation boundary and a vacuum region to mimic the prevention of any electromagnetic interference from an outside source. The boundary conditions between domains is defined by their material properties [192]. The trade-off between the

computing complexity and model efficacy was optimized by selecting the mesh element sizes of 10 and 5 mm for outside layers and artery respectively.

The electrode material was chosen to be copper due to its relatively high bulk conductivity (58000000 S/m) and a relative permittivity of 1.0. The electrodes were modelled to be 2 mm in diameter. The outer set of electrodes (for current input) were spaced 24 mm apart and the inner pair of electrodes (for voltage measurement) were spaced 11 mm apart.

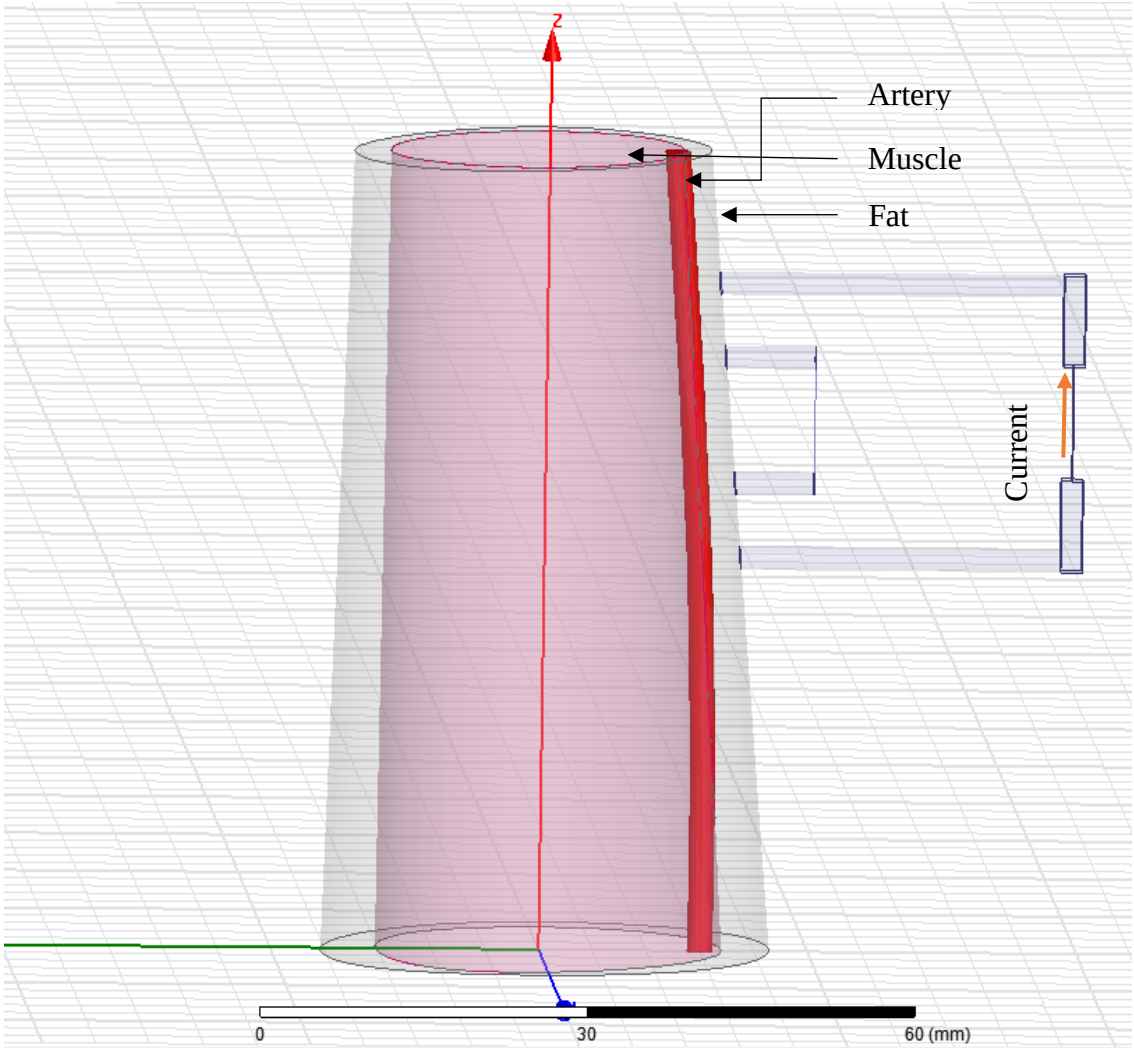

Figure 3.1: Longitudinal view of the constructed model in Ansys® HFSS

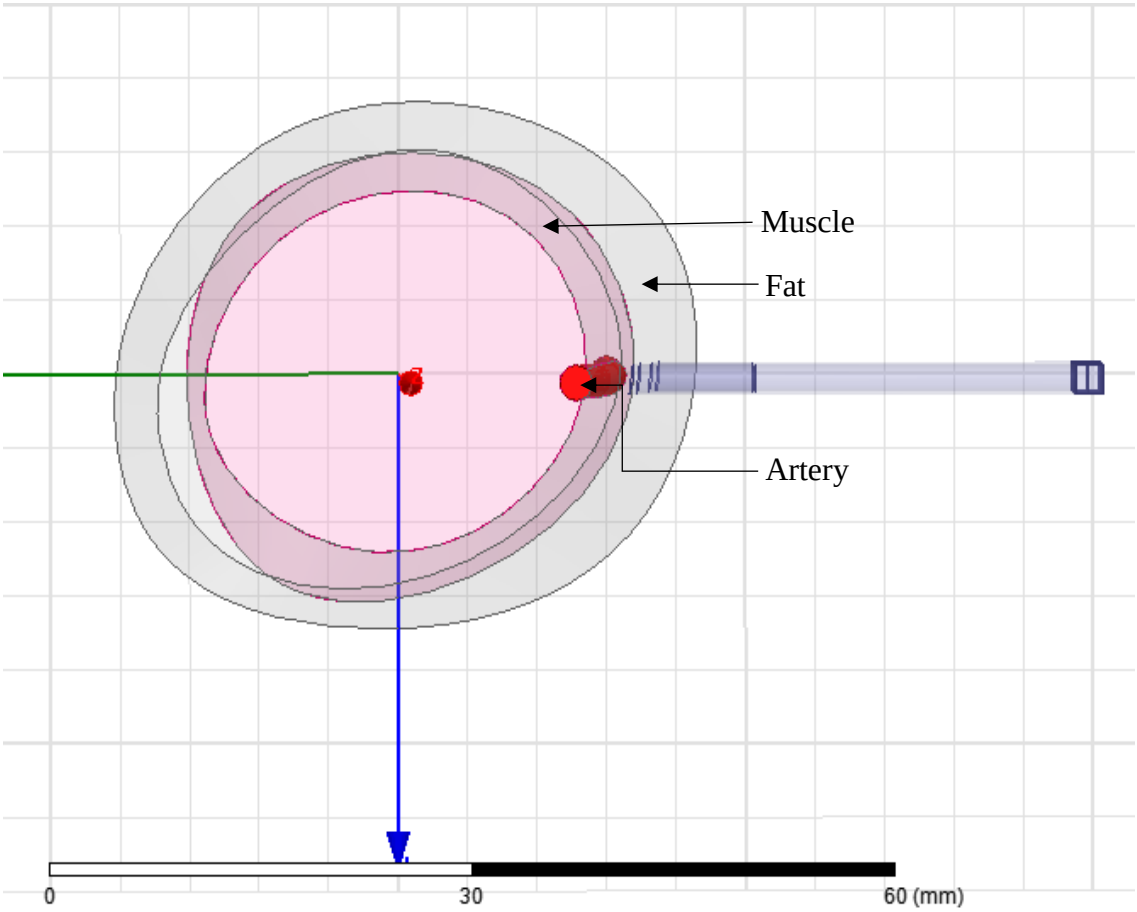

Figure 3.2: Top view of the model

3.4.1 Finite Element Modelling of fat, muscle and artery domains

The forearm tissue model required a finite element (FE) meshing method to determine the interaction between the different tissue domains and resulting effects. ANSYS® Workbench has various methods that can be employed for meshing and design analysis. The methods include Automatic, Tetrahedrons, Hex-Dominant, Sweep and Multi-Zone [197]. A tetrahedral meshing relies on tetrahedrons as elements which allows the meshing to be easily combined with proximity and curvature sizing tools to refine the mesh at critical sites. However, the node counts are typically higher than any other type of meshing method. It works on two types of algorithms – Patch Conforming and Patch Independent. In the first, a surface mesh generated from a Delaunay mesher creates a volume mesh based on TGRID Tetra algorithm. In the second algorithm, a volume mesh is projected to the surfaces and is based on ICEM CFD Tetra algorithm [197]. Parameters common to the two methods include minimum and maximum sizes, curvature and

proximity functions, smoothing and mesh metrics. Mesh quality can be improved through features like sizing, inflation, refinement etc.

Here, the tetrahedral meshing with a patch independent algorithm was employed to mesh the volume first and then project to the faces. The quality of the mesh produced was checked by analyzing the skewness of the mesh, which quantitatively measures of the distortion of an element's shape relative to its ideal shape. As a reference, the quality of the mesh produced can be classified according to different ranges of skewness [197]:

- 0 – 0.25: Excellent
- 0.25 – 0.5: Very Good
- 0.5 – 0.8: Good
- 0.8 – 0.98: Acceptable
- 0.98 – 1: Bad

The model was meshed using the Mesh component system through ANSYS® Workbench using an electromagnetics preference, high relevance center, high smoothing and fine span angle center. Various element size limits for refinement and approximate number of elements per part were tried which balanced a fine quality mesh against complexity and time of analysis. Results presented here are for a minimum size limit set as 0.001 mm and the approximate number of elements per part being 100,000.

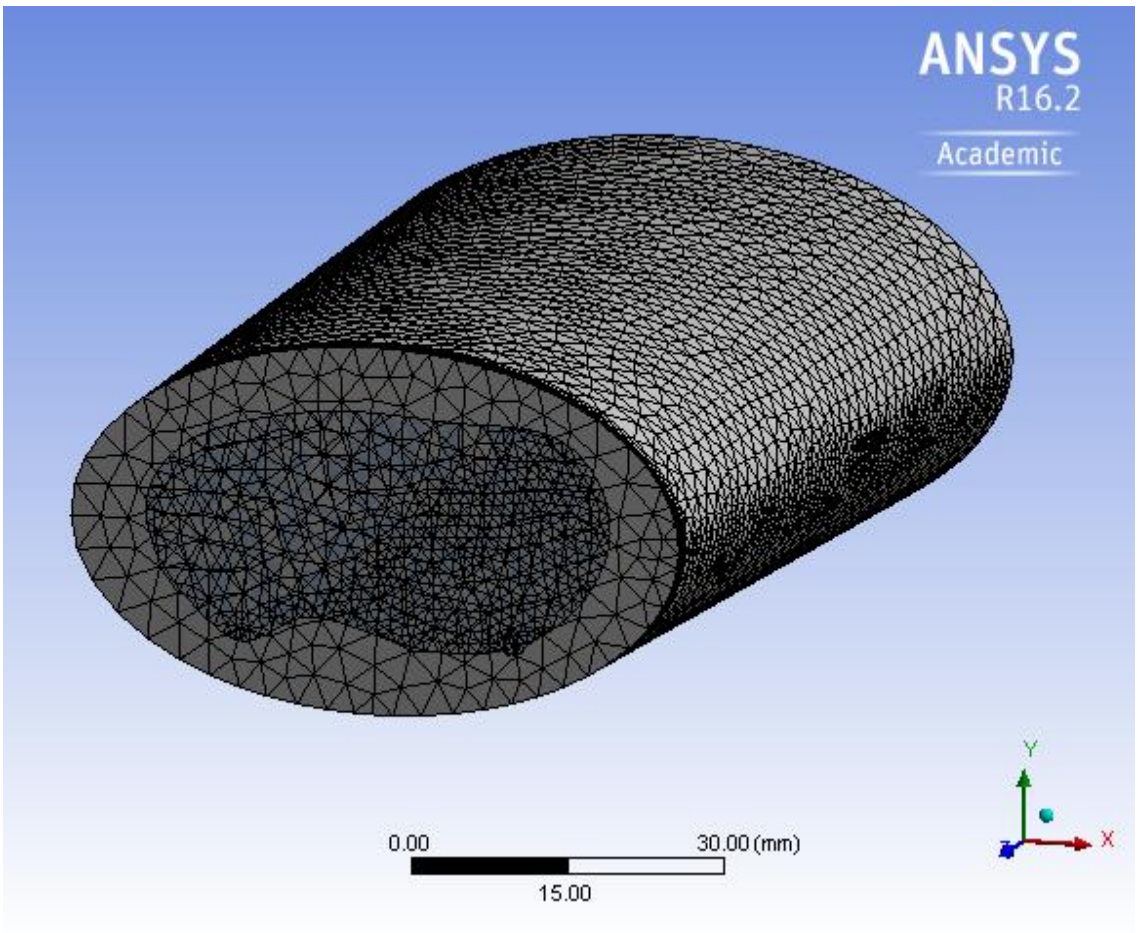

Figure 3.3: Meshing in the forearm model geometry

For the mesh in Figure 3.3, the total number of nodes amounted to 879,760 with the number of elements being 626,652. The number of contact elements were 30,803. The overall skewness distribution of the mesh is as shown in Figure 3.4.

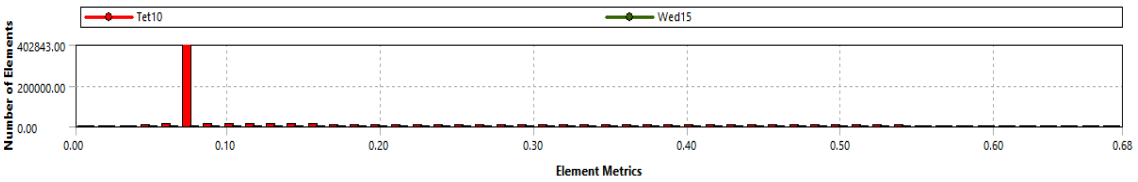

Figure 3.4: Skewness metric for the mesh generated for forearm model

Figure 3.4 shows a large percentage of elements concentrated below a value of 0.1, which indicates an excellent quality of mesh. The overall skewness ranged within a minimum value of 0.00127 and a maximum of 0.68368. Further analysis of individual tissue domains was carried out using the Finite Element Modeler component of ANSYS® Workbench. The summary of nodes and elements for individual tissue domains is given in Table 3-1. The mesh distribution for individual tissue domains has been shown in Figure 3.5, Figure 3.7 and Figure 3.9.

Table 3-1: Summary of elements for individual tissue domains

Tissue	No. of Nodes	No. of Elements
Fat	148,243	103,939
Muscle	581,467	421,302
Artery	150,050	101,411

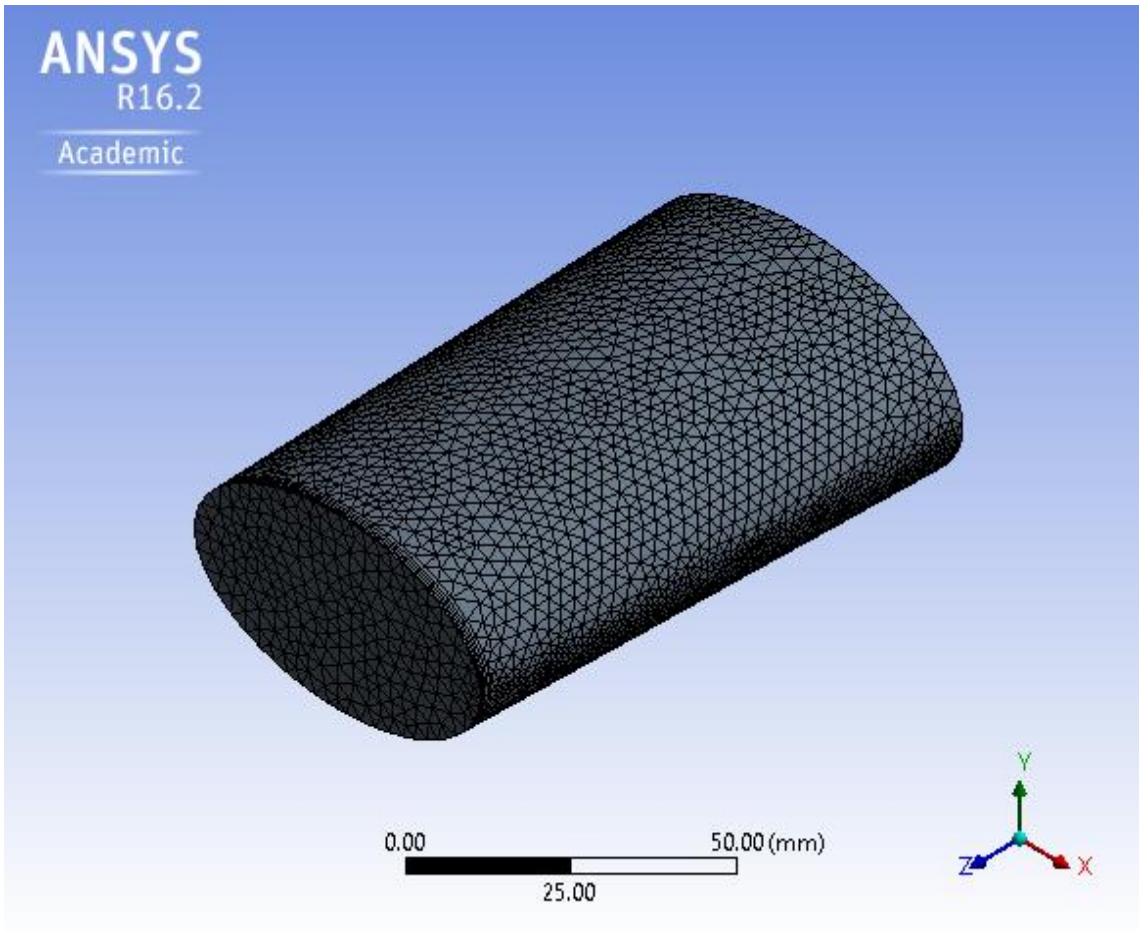

Figure 3.5: Mesh distribution in the Fat domain

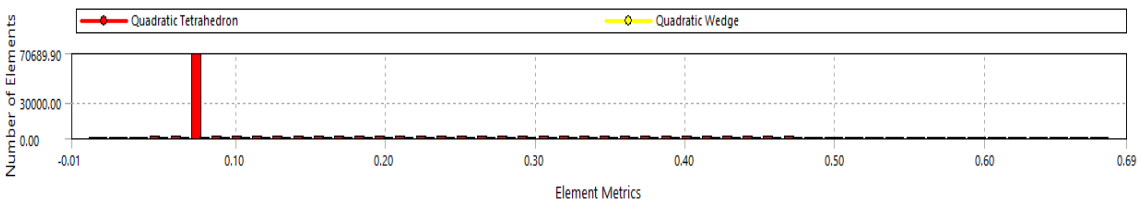

Figure 3.6: Skewness distribution for meshing in Fat domain

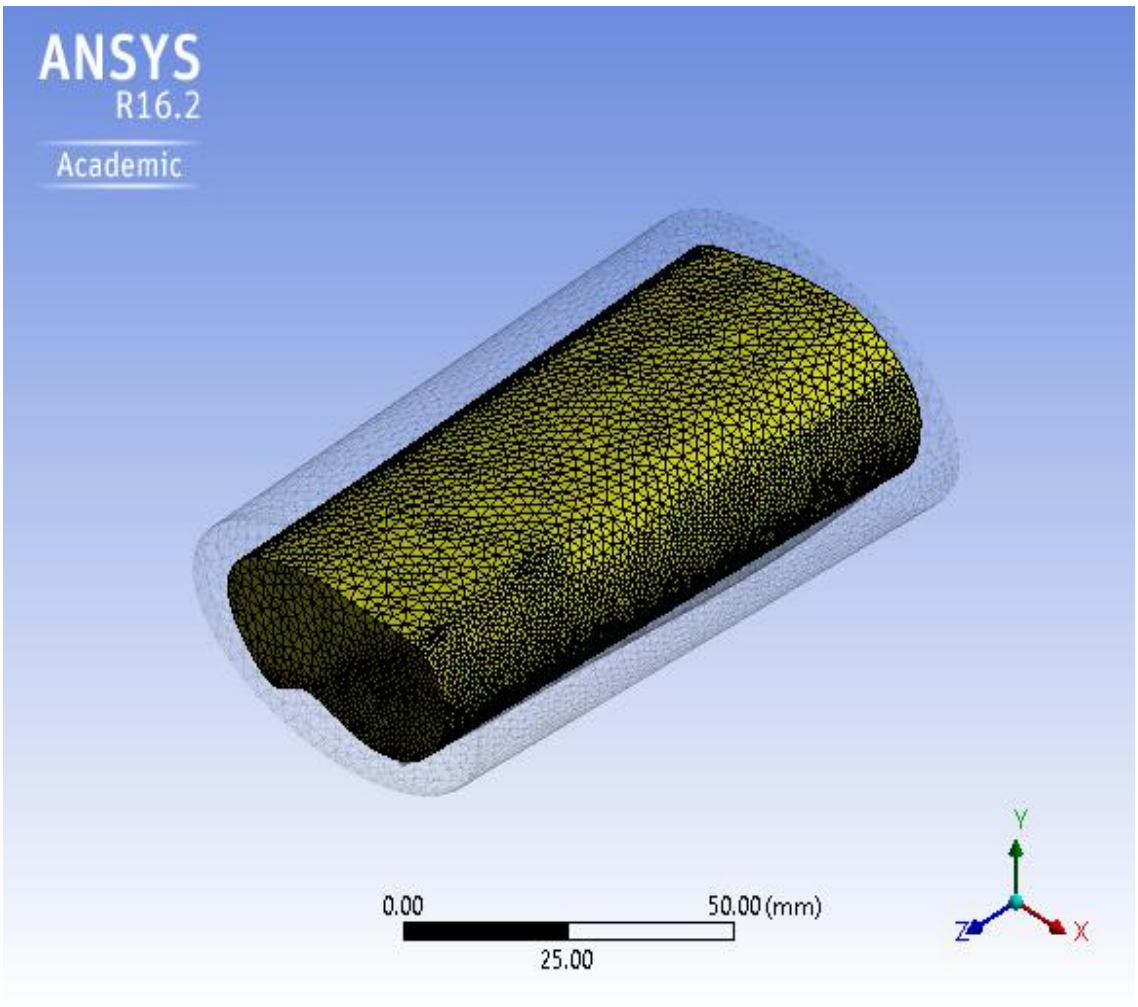

Figure 3.7: Mesh distribution in the Muscle domain

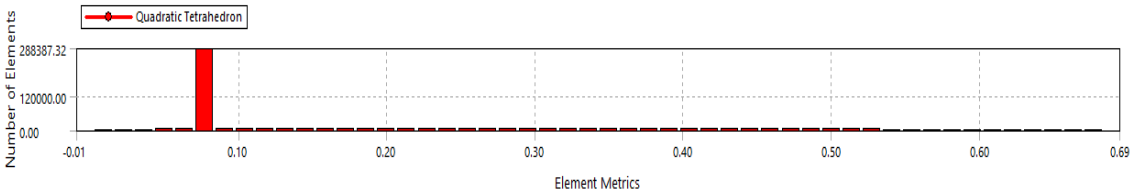

Figure 3.8: Skewness distribution for meshing in the Muscle domain

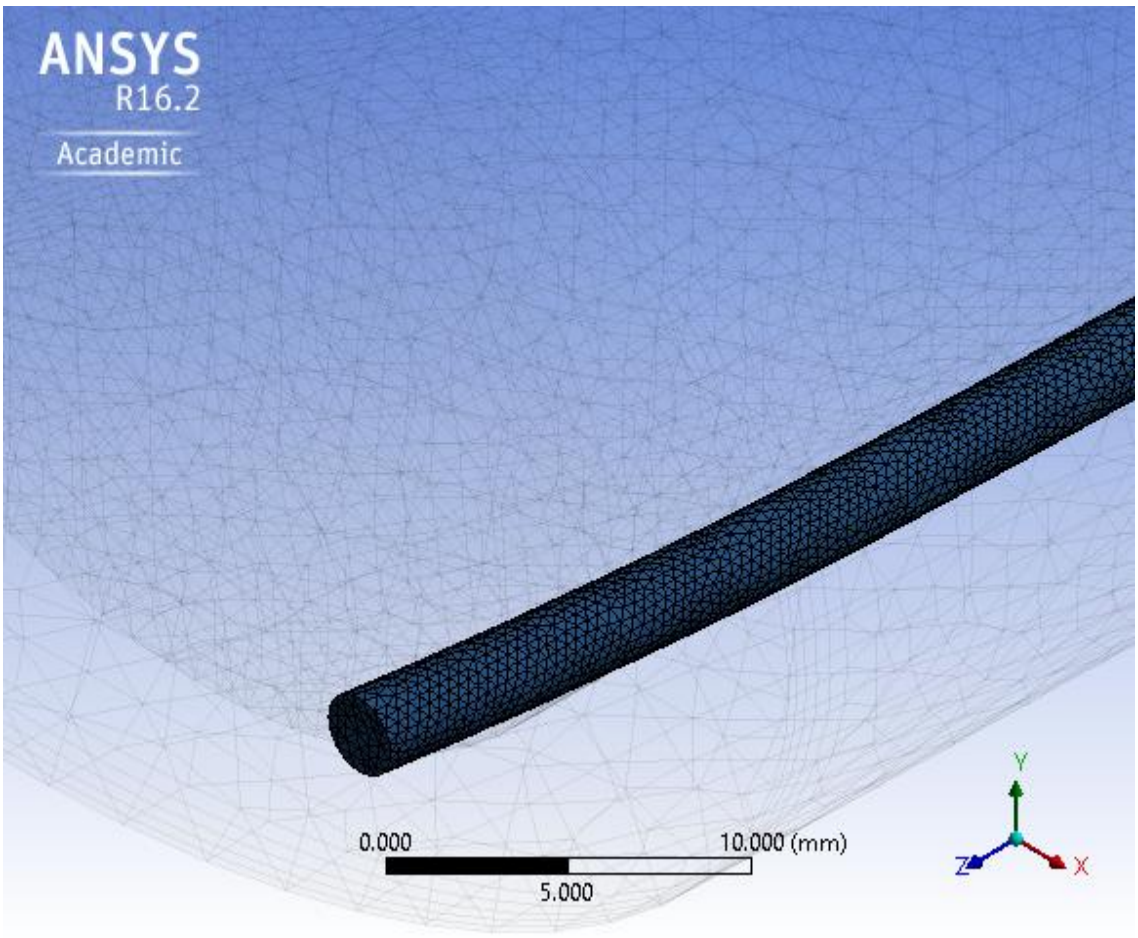

Figure 3.9: Mesh distribution for the Artery domain

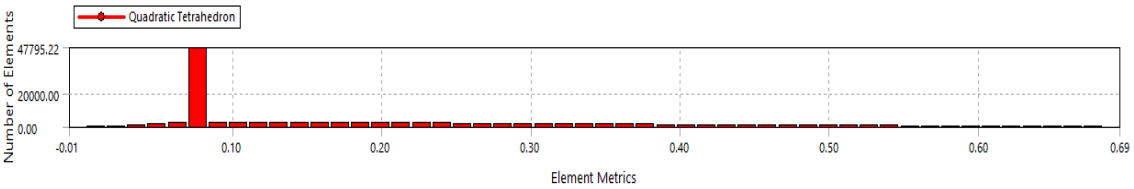

Figure 3.10: Skewness distribution for meshing in Artery domain

As is evident from Figure 3.6, Figure 3.8 and Figure 3.10, the skewness distribution is excellent for individual tissue domains as was for the overall geometry. This mesh configuration was hence used for further electrical analysis.

3.4.2 Material properties for the tissue domains

The materials for each of the tissue domain were specified as frequency dependent in the desired frequency range. The frequency dependent dielectricity of the materials was defined in terms of bulk conductivity and relative permittivity. The database developed

by Gabriel [141]–[144] for parametrically defining the dielectric properties of several human tissues was used as a reference (Figure 3.11).

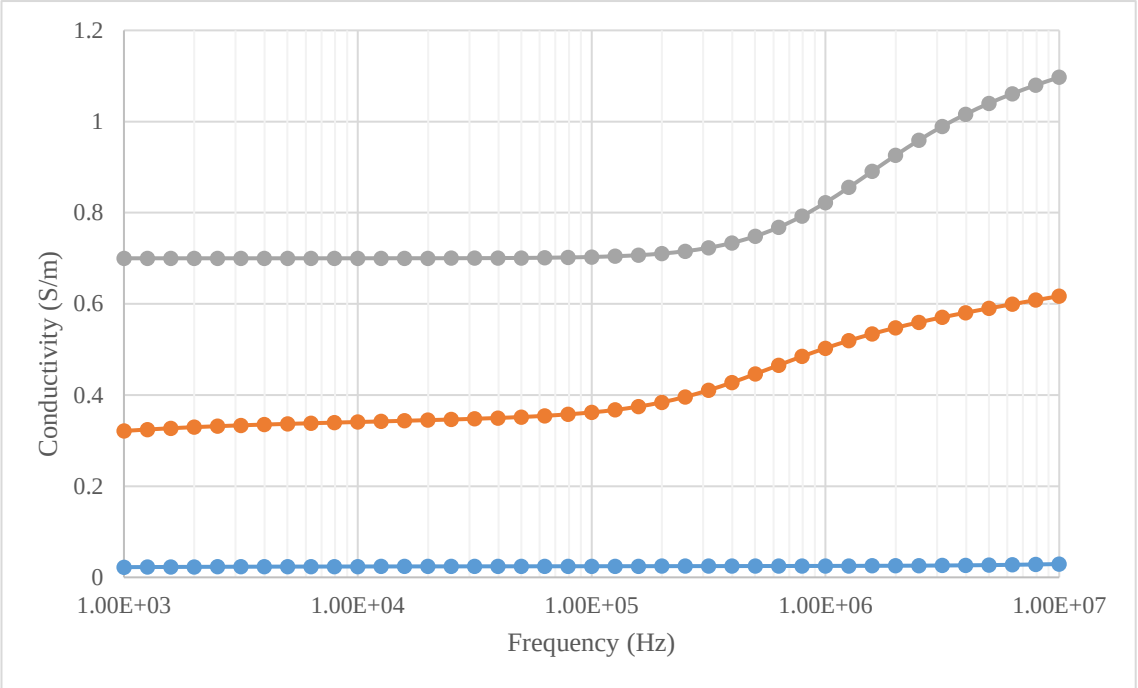

(A)

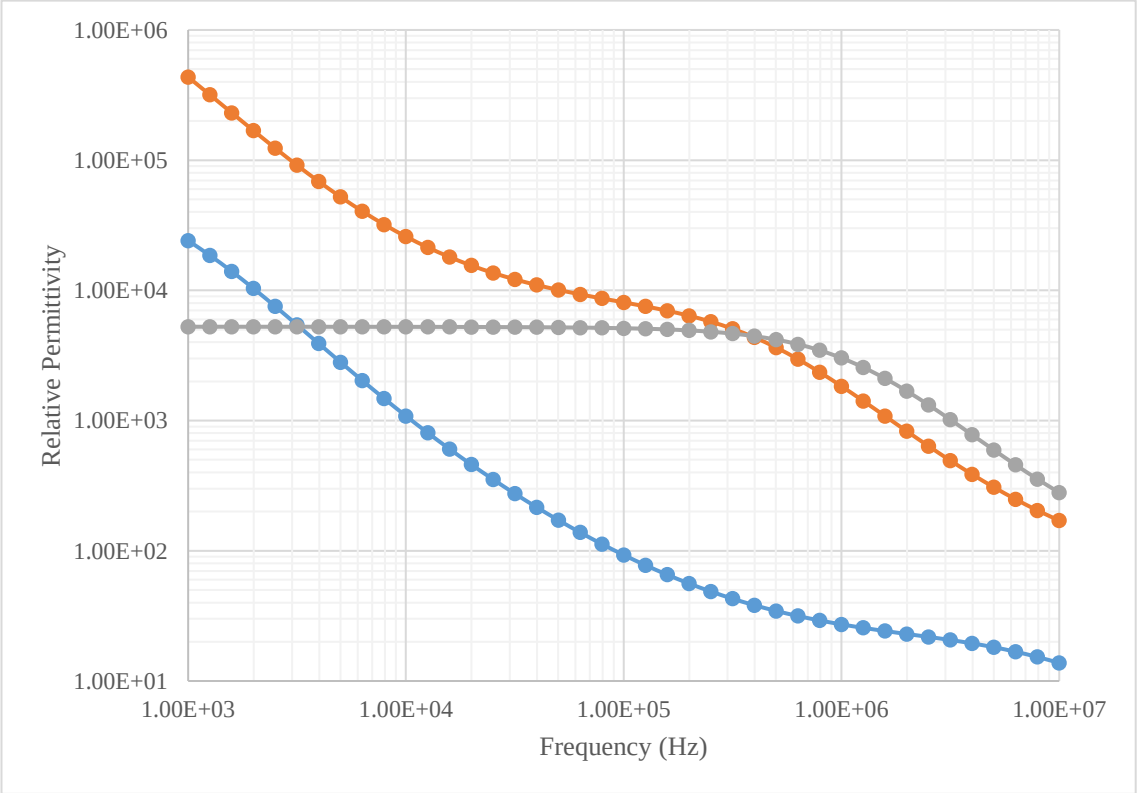

(B)

Figure 3.11: (A) Conductivity and (B) Relative Permittivity values for fat, muscle and bat used in the simulation as compiled by Gabriel [141]: fat, muscle, and blood

3.5 Simulation Results – Initial Geometry

The simulation was performed with the constructed dielectric model of forearm for specific frequencies within 1 kHz and 2 MHz. The frequency steps chosen were 1 kHz, 5 kHz, 10 kHz, 50 kHz, 100 kHz, 150 kHz, 200 kHz, 250 kHz, 400 kHz, 500 kHz, 600 kHz, 700 kHz, 800 kHz, 900 kHz, 1MHz, 1.25 MHz, 1.5 MHz, and 2 MHz. IEC 60601 technical standards [196] describe safety of medical equipment and prescribe allowable current ranges. The preferred range is between 100 μA to 1 mA for the frequency range of interest [198] and hence 1 mA was chosen for simulation purposes. Figure 3.12, Figure 3.13, Figure 3.14 and Figure 3.15 show the distribution of electric field at the frequencies 1 kHz and 2 MHz.

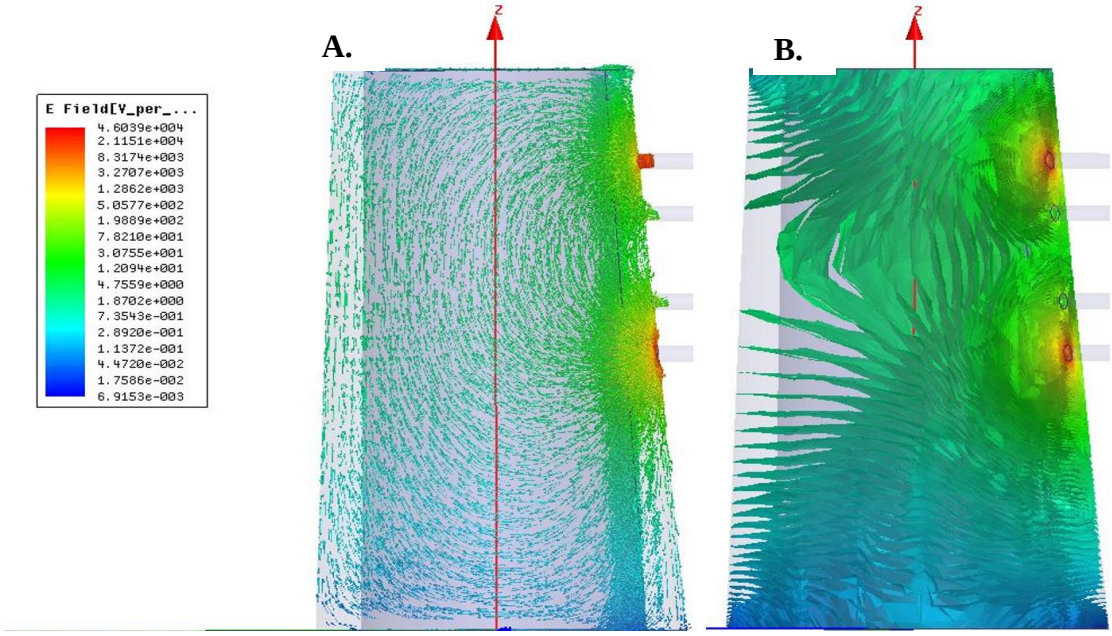

Figure 3.12: A. Vector and B. magnitude plots for Electric Field distribution (in Volts per meter) at 1kHz (arterial diameter = 2.4mm) – Longitudinal view

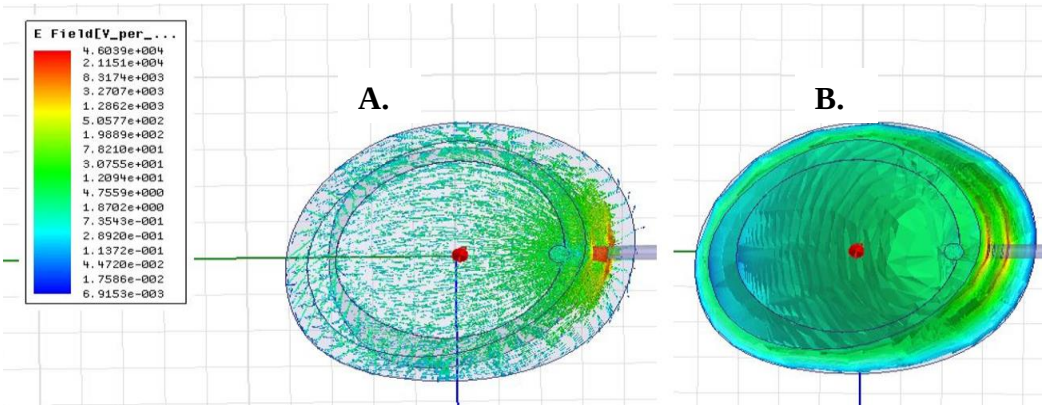

Figure 3.13: A. Vector and B. magnitude plots for Electric Field distribution (in Volts per meter) at 1kHz (arterial diameter = 2.4mm) – Top view

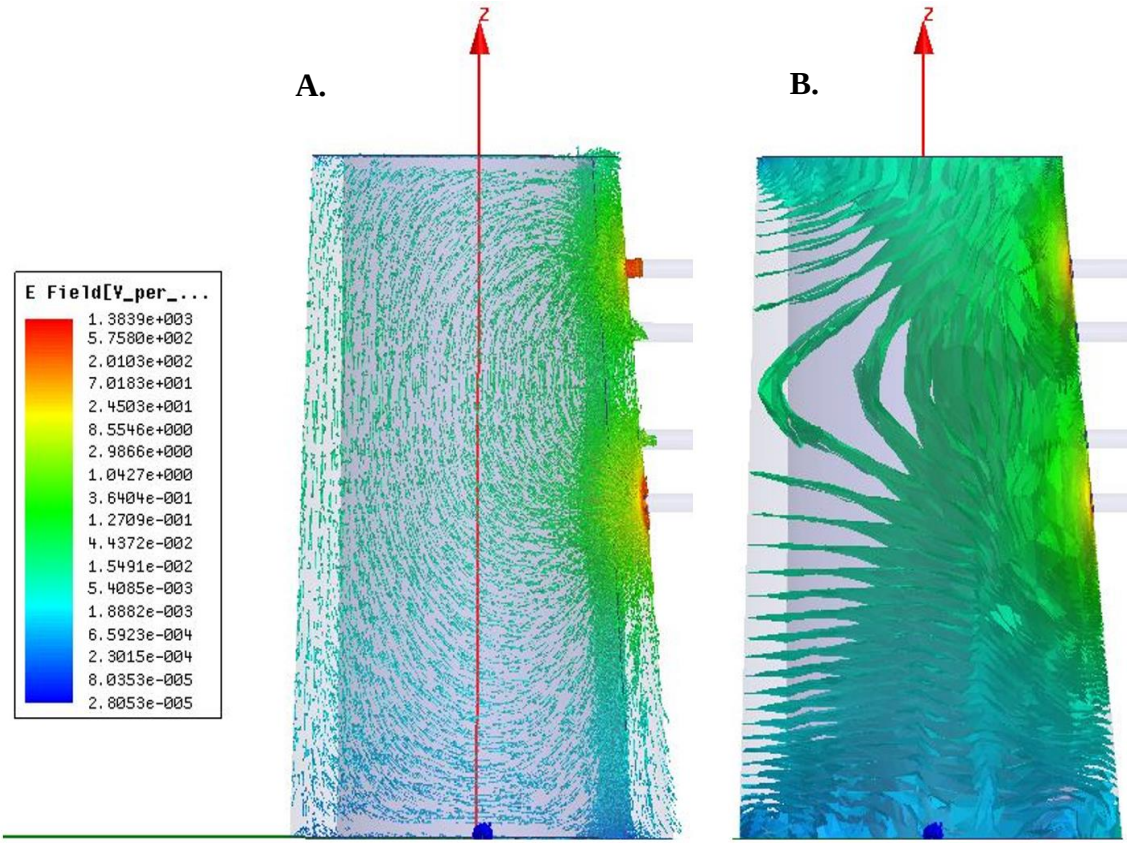

Figure 3.14: A. Vector and B. magnitude plots for Electric Field distribution (in Volts per meter) at 2MHz (arterial diameter = 2.4mm) – Longitudinal view

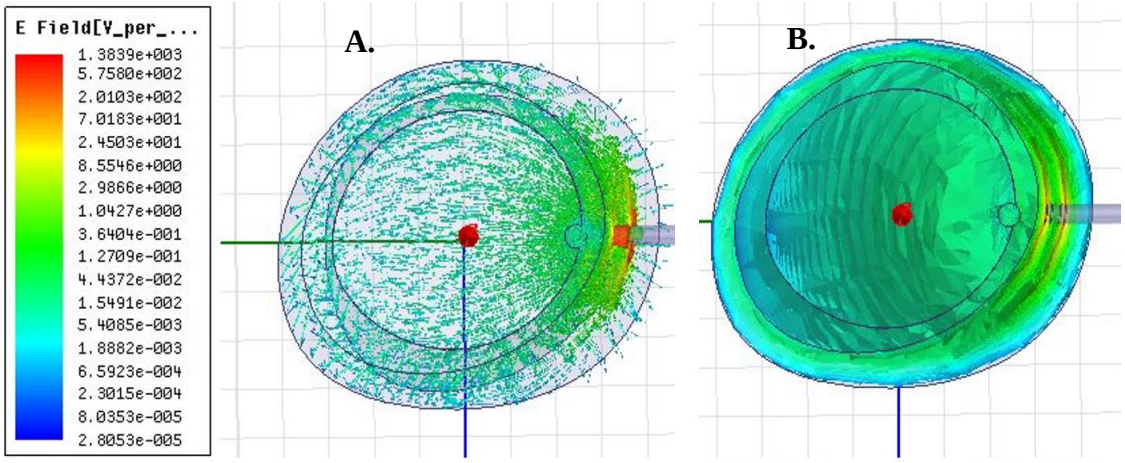

Figure 3.15: A. Vector and B. magnitude plots for Electric Field distribution (in Volts per meter) at 2MHz (arterial diameter = 2.4mm) – Top view

The distribution of the electric field determines the flow of current throughout the volume of the forearm model. The generation of an electric field gradient within the volume of the model allows the current to flow along the conduction paths. Simulated impedance was measured by calculating the ratio of the inner electrode pair potential difference to

the current applied on the outer pair of electrodes. The potential difference was measured by computing the line integral of the electric field between the inner electrodes.

The frequency sweep was performed for three different instances of arterial diameter – 2.3 mm, 2.35 mm and 2.4 mm to mimic blood flow induced volumetric changes. The impedance for each frequency was calculated and plotted as a Nyquist plot between the real part of impedance and the imaginary part of impedance (Figure 3.16, Figure 3.17 and Figure 3.18).

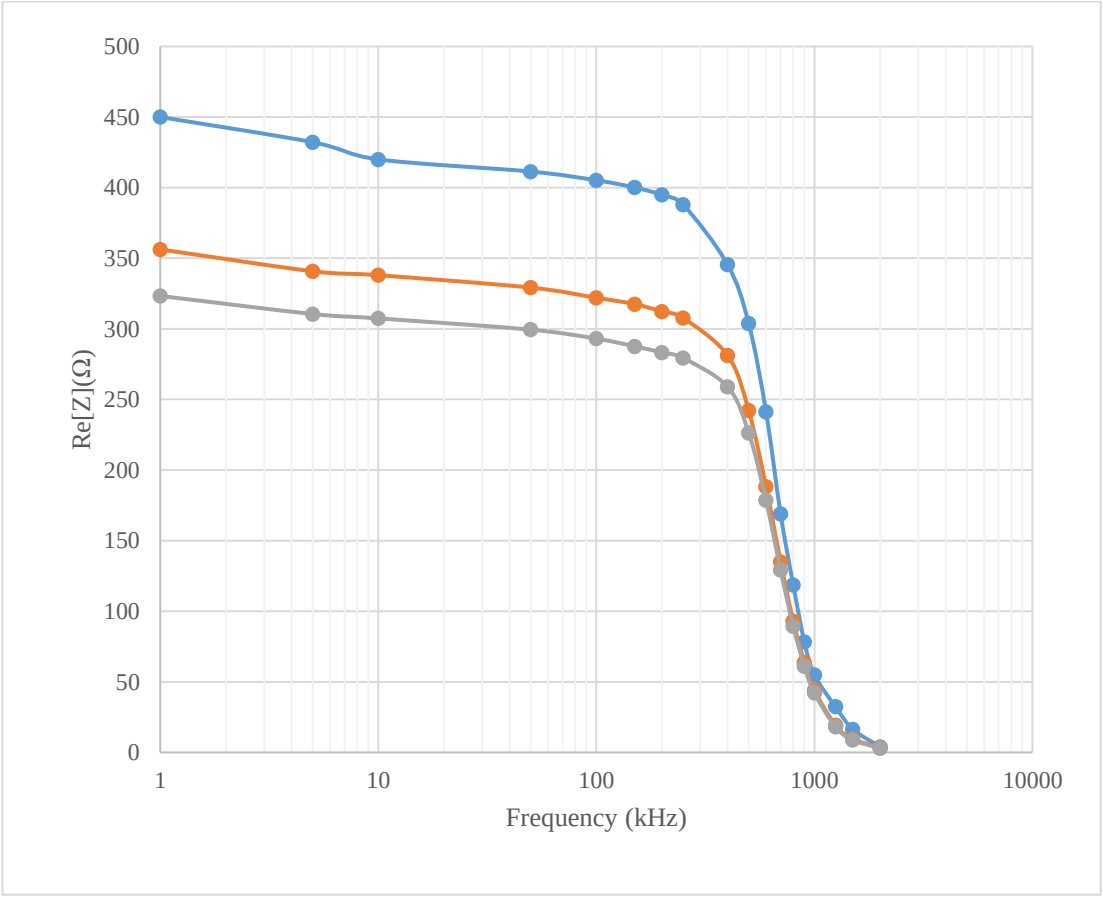

Figure 3.16: Variation of Re (Z), resistance, for the three arterial diameters with frequency – without bone: 2.3 mm, 2.35 mm, and 2.4 mm

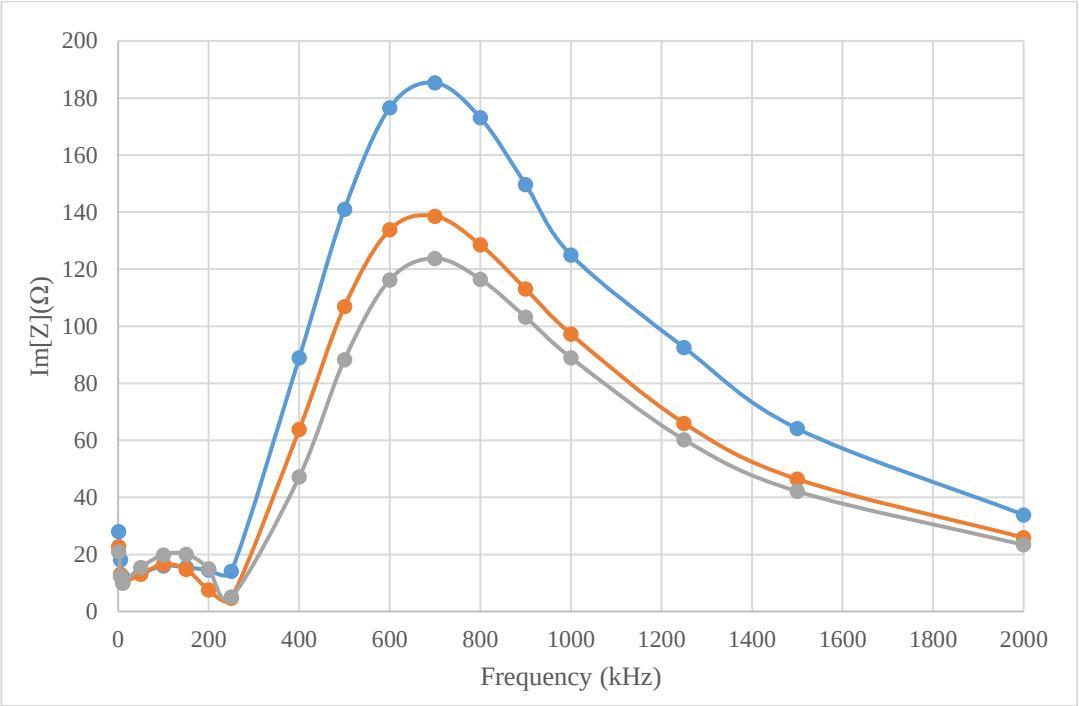

Figure 3.17: Variation of Img (Z), reactance, for the three arterial diameters with frequency – without bone: 2.3 mm, 2.35 mm, and 2.4 mm

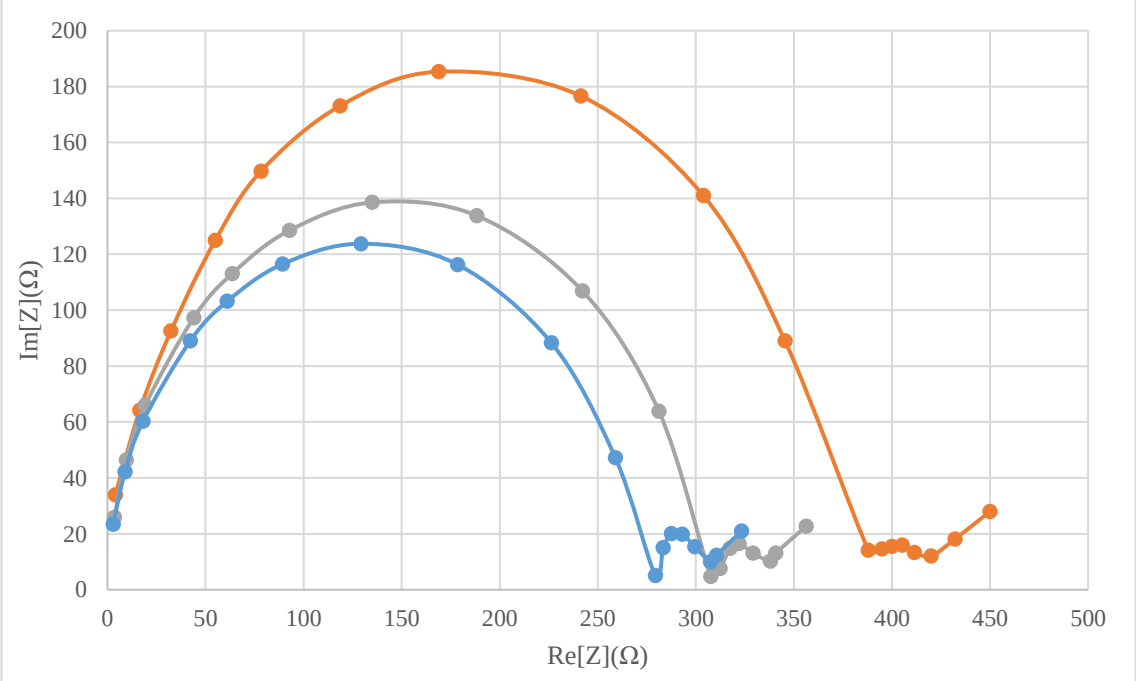

Figure 3.18: Nyquist plot (Cole plot) of Re(Z) vs Img.(Z) for three arterial diameters: 2.3 mm, 2.35 mm, and 2.4 mm

3.6 Simulation Results – Effect of Bone tissue

The latter part of the simulation focused at analyzing the contribution of the individual tissue domains in the model geometry to overall results. The major exclusion in the

previous simulation case was bone. Figure 3.19, Figure 3.20 and Figure 3.21 compare the overall response with and without bone geometries observed for arterial diameter 2.3 mm.

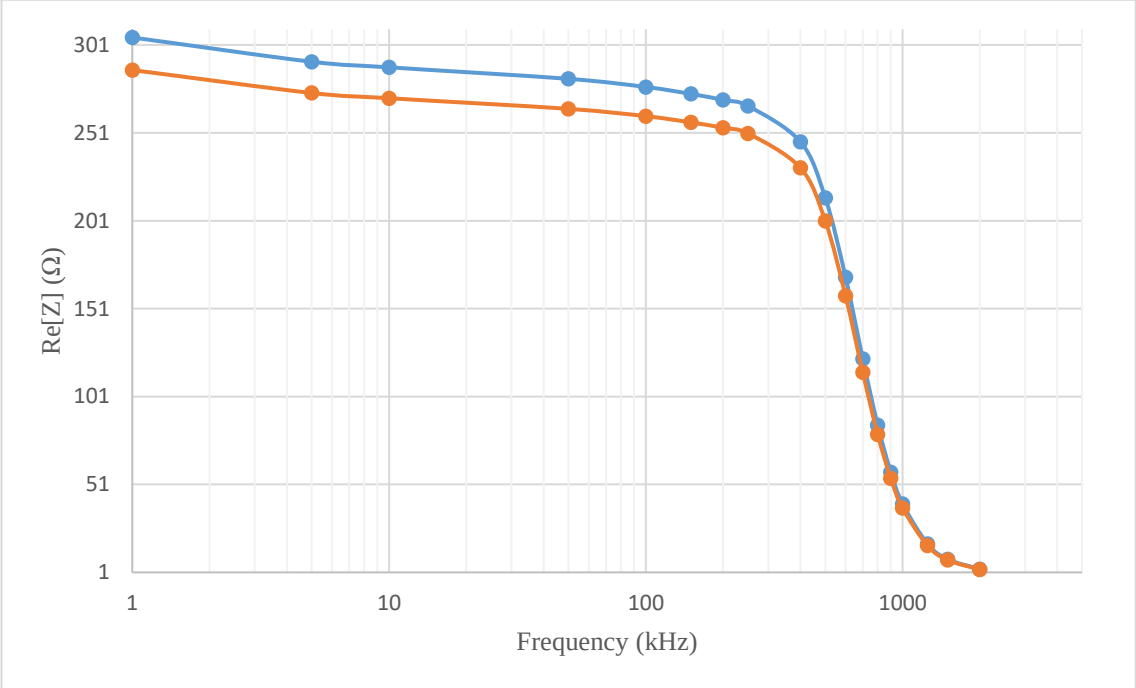

Figure 3.19: Comparison of the variation in Re (Z), for arterial diameter of 2.3 mm, with frequency between with and without including bone in the simulation geometry: —●— *with bone, and* —●— *without bone*

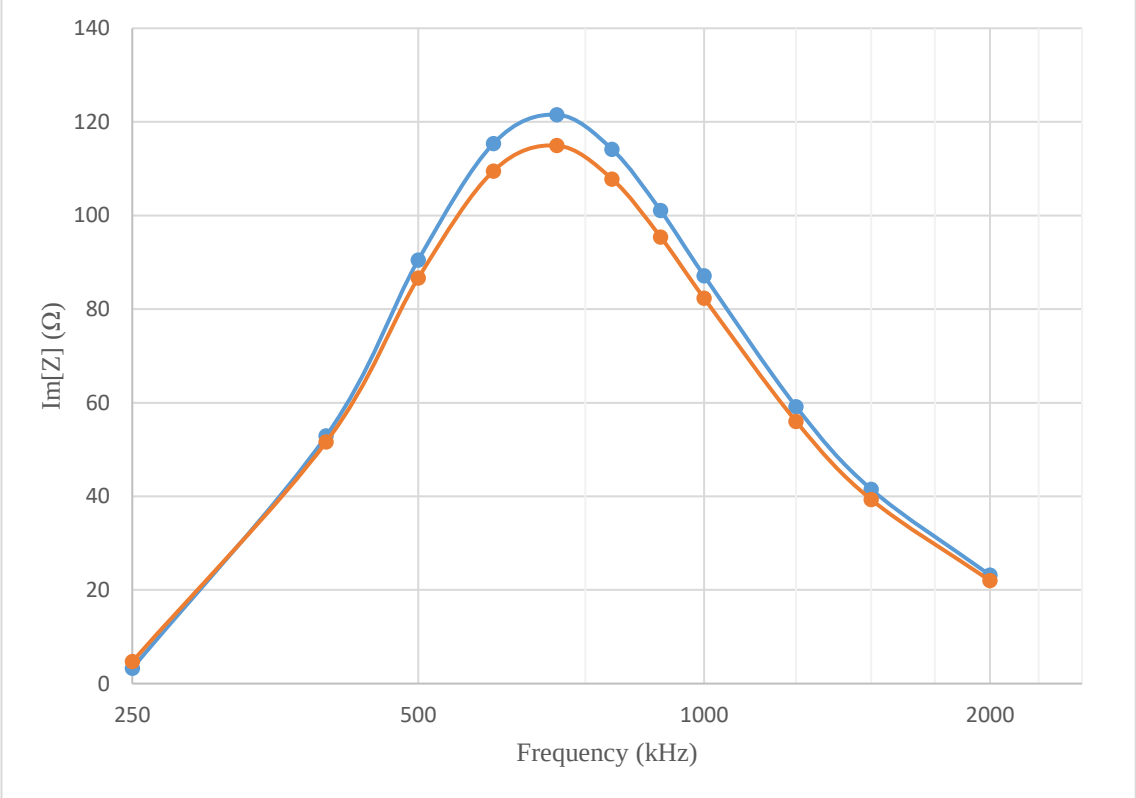

Figure 3.20: Comparison of the variation in Im (Z), for arterial diameter of 2.3 mm, with frequency between with and without including bone in the simulation geometry: with bone, and without bone

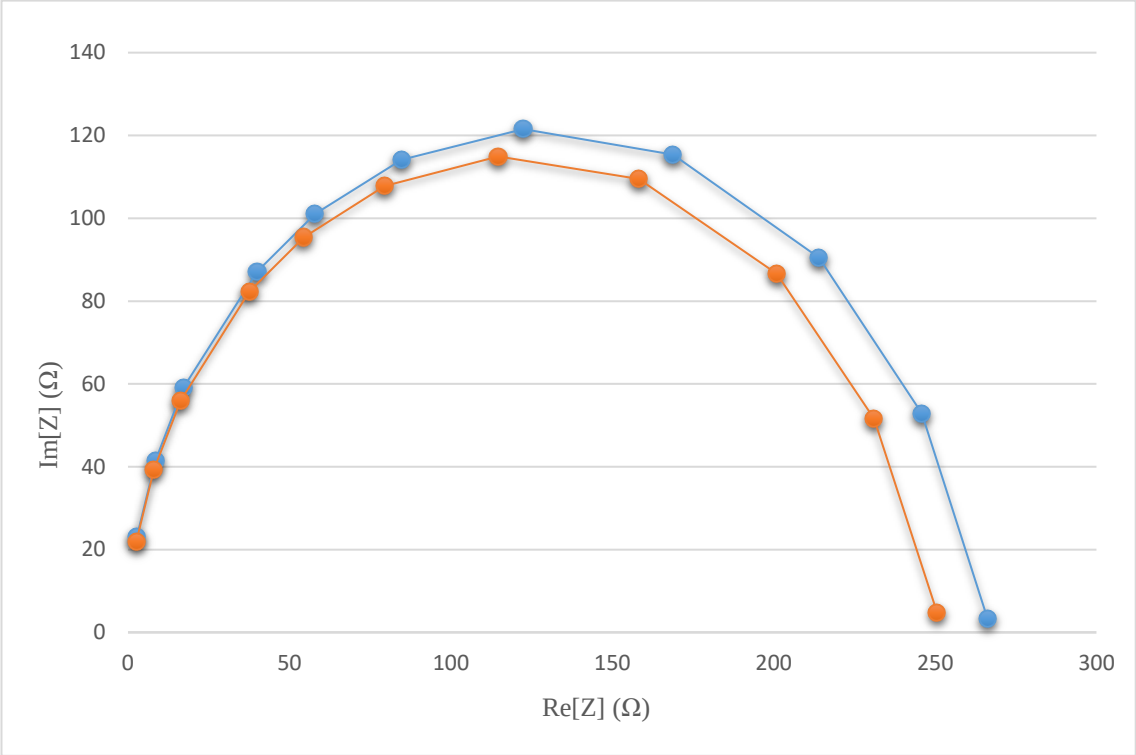

Figure 3.21: Comparison of the Im (Z) vs Re (Z) plots for arterial diameter of 2.3 mm between with and without including bone in the simulation geometry: with bone, and without bone

3.7 Discussion

This section aimed at investigating three main objectives through the simulation study:

- Investigating the type of dielectric response of the forearm section with three tissue layers – fat, muscle and the artery,
- Determining the contribution of different tissues to the overall impedance measurements, and,
- Investigating the effect of arterial diameter changes on the impedance measurements

The electrical behavior of biological tissues has previously been shown to be well-represented using the Cole model. The Cole equation describes the frequency dependence

of tissue conductivity and permittivity. The results obtained through the simulations of the present study identify the type of tissue dielectric response to agree with the Cole model in the way resistance and reactance values vary with frequency. The semi-circular shape of the major portion of the plots in Figure 3.18 agrees with a Cole model. However, the simulation diverges from this model for lower frequencies

The maximum resistance and reactance values were observed as 445Ω and 178.5Ω, 356Ω and 138Ω, and 368Ω and 144.3Ω for diameters 2.3mm, 2.35mm, and 2.4mm respectively for the initial simulation. The expected values at the extremities of the Cole plot (R_0 and R_∞) can be found by extrapolating the Cole trend and observing the values at the resistance axis. The above values of the impedance were found within agreeable limits of previous results such as [199] (which found average value of forearm resistance of 346 Ω) and [32] (which found mean±standard deviation values of resistance of 319±21.9 Ω and reactance of 30±2.3 Ω for arm at 50 kHz).

The values obtained at lower frequencies do not follow the Cole trend and reflect the minimum values of reactance for each plot. The simulation results at lower frequencies (1- 200 kHz) were found to be mainly resistive and exhibited a different trend than the rest of the plot. The high resistance values and corresponding changes with diameters at lower frequencies are a result of significant change in the conductivity due to change in the arterial diameter. Due to the large conductivity of blood, the major change in the impedance occurs as a resistive change due to change in arterial dimension. Hence at lower frequencies, the response is dominantly resistive.

The value of maximum reactance for each Cole plot is defined by a characteristic frequency (F_c) which was found to be slightly different for the three diameters of the artery. This reflects that the increase in the artery diameter changes the overall response of the system and slightly shifts the dispersion mechanism defining the total dielectric response.

Although bone as a biological tissue does possess frequency dependent dielectricity, it possesses a constant conductivity over the frequency range of interest. The low variability of conductance makes it a redundant when observing impedance changes with a pulsating artery. However, as can be seen when comparing the plots in Figure 3.19, Figure 3.20 and Figure 3.21, it offers a monotonic decrease in overall resistance value while not changing the dielectric behavior of the impedance spectrum.

Although the above simulation model lacks blood flow, consideration of different arterial diameters accounts for the volumetric changes in the artery with flow. The simulation assumes constant diameter artery in the region of interest. This is reasonable considering the wavelength of the pulse wave in the artery is consistent with the long wavelength approximation [201]. The Moens-Korteweg Equation [202] gives the pulse wave velocity, (c):

$$c = \sqrt{\frac{Eh}{2r\rho}} \tag{3.5}$$

where, E is the arterial elastic modulus, h is the arterial wall thickness, r is the radius and ρ is the blood density. Considering c = f λ, the wavelength (λ) can be calculated where the fundamental frequency (f) corresponds to the heart rate, for which a typical values is 72 bpm, or 1.2 Hz [203]. Considering the range of pulse wave velocity (c) between 8 to 10m/s (based on results of several studies [204]–[206]) and the maximum fundamental frequency (corresponding therefore to the minimum wavelength) of the blood pressure pulse as 25 Hz [207], [208], λ evaluates to 32 to 40 cm which is significantly longer than the dimension of the model. For comparison, the inter-electrode spacing was 1.1 cm . Hence, each wavelength of blood can be assumed 'longer' than the proposed arterial dimensions.

The obtained results with different diameters give an indication of the influence of arterial hemodynamics on impedance measured from the forearm. The different impedance spectra for three arterial instances prove that the overall electrical response has contributions from both the compositional properties of the tissues and the blood flow. The latter, particularly, is supported by several studies ([20], [163], [164], [166], [170], [175], [179], [209]) analyzing the blood flow effects and contributions to the bioimpedance readings.

The following points outline some of the limitations of this simulation study:

- Bone is not included in this study which is expected to offer higher resistance and capacitance being predominantly piezoelectric, although dynamic mechanical deformation was not simulated [210]. However, bone was not expected and later found to contribute to any change in the dielectric behaviour of the overall model. Figure 3.19, Figure 3.20 and Figure 3.21 show a comparison of the Re [Z], Im [Z] and the Cole response, respectively, for the geometry with and without the inclusion of the bone tissue. The results show a similar trend in the frequency

spectra for all the three diameters, where the impedance is found to decrease with increasing arterial cross-section. However, the overall magnitude of the impedance spectra for all three diameters is smaller than the original results where bone was not included in the geometry. This is shown more clearly in Figure 3.22. The electrical contribution of bone also depends on its compositional fraction of the total geometry. Due to the bone having a significant volume, it only changes the overall magnitude of the impedance but not its behaviour.

- This simulation analysis neglects any dynamic effects, for example, that may cause non-uniform diameter changes along the length of the artery.

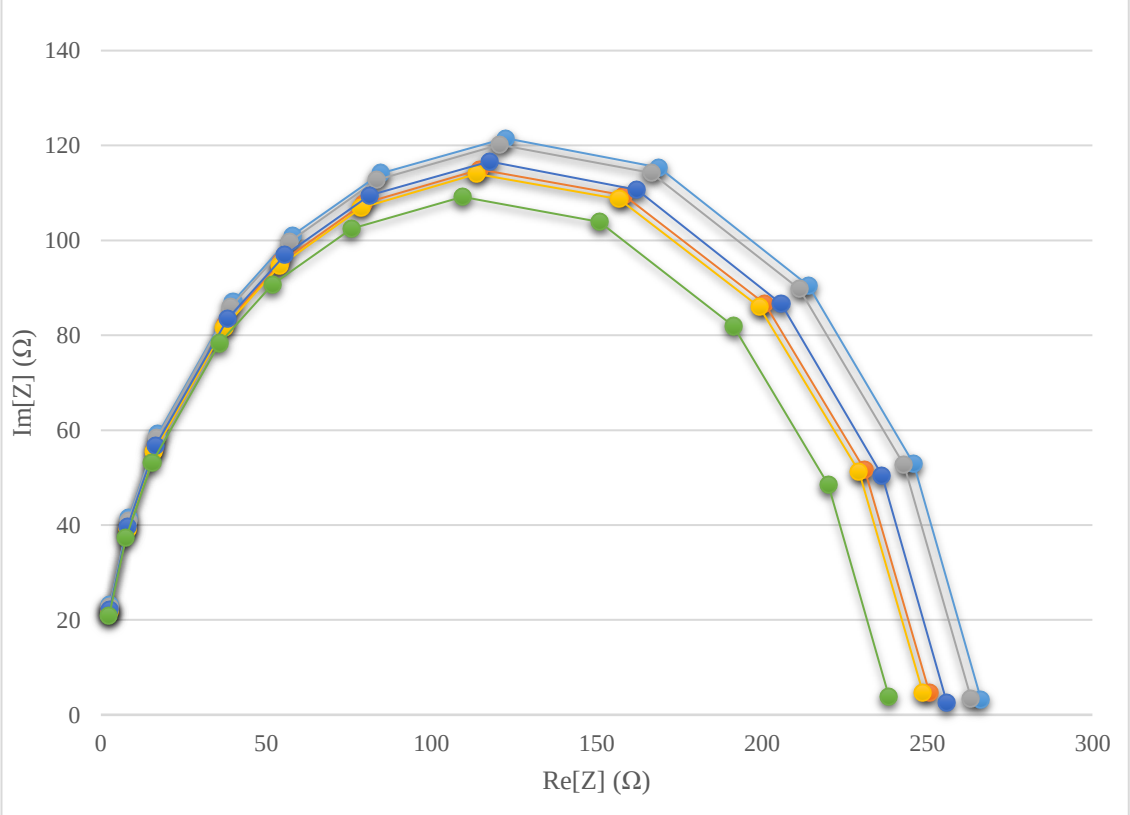

Figure 3.22: Comparison of the Cole plots for all three diameters with and without bone geometries: 2.3 mm – with bone, 2.3 mm – without bone, 2.35 mm – with bone, 2.35 mm – without bone, 2.4 mm – with bone, and 2.4 mm – without bone

There are several other factors such as age, gender, electrode geometry and physiological condition of the subject that would affect the impedance measurements. However, none of these change the timescale of a single pulse, which is the focus of this simulation.

3.8 Closure

This chapter provides an insight into the simulation perspective of the complex dielectricity of human tissues. The chapter described the construction of a human forearm geometry and simulating it for electrical response using ANSYS® HFSS / Electronic Desktop. The description of various model parameters and setup formulation for analysis in the HFSS were discussed. The meshing of the forearm model, along with individual tissue layers were mentioned. The simulation setup was formulated by defining the dielectric material properties from Gabriel's database [141]. The description of the modelling procedure was followed by the simulation results and characterisation based on Nyquist (Cole-Cole) plots of the impedance. Moreover, the effects on the overall impedance variations due to bone tissue were also simulated and observed.

From this simulation analysis, it was found that:

- The overall forearm tissue behaviour exhibited a Cole-type dielectric response
- The overall impedance measurements were found to change with changing arterial diameters, reflecting the significance of blood flow induced impedance changes.
- The total contributions to the impedance comprised of – the contribution as a result of the dielectric properties of fat, muscle and artery (blood) and the contribution due to blood flow which was reflected through different impedance spectra at different arterial diameters.

The understanding of the variations in impedance observed at three instances of radial artery diameter provide evidence that multi-frequency impedance response has potential to be used to measure forearm arterial diameter changes. The next chapter describes support for the simulation modelling through experimental investigation into the dielectric response and consequent characterisation of the behavior of a forearm phantom.

Chapter 4 EXPERIMENTAL INVESTIGATION USING A HUMAN FOREARM PHANTOM

4.1 Introduction

Phantoms, or physical simulants of biological specimens are useful for research and development due to the unavailability of real tissues. One such example is human blood, which is a precious resource in healthcare and is not normally available for research purposes, unless it is no longer fit for human use. Moreover, working with biological tissues can be costly and complicated. Tissues cannot be stored for long periods as their properties and structure tends to change with time, although the practice of cryopreservation and hypothermic storage for cell and tissue preservation has somewhat alleviated this problem. In the case of blood, it can be preserved, if it has not been segregated in its components, for a few weeks at low temperatures using strong anticoagulants like Ethylene di-amine tetra-acetic acid (EDTA) and Citrate phosphate dextrose adenine solution (CPDA-1).

These complications in the use of fresh tissues has led to the development of alternatives or tissue-mimicking materials which exhibit some of the properties of real tissue. These tissue-mimicking materials are used to create bio-phantoms which serve as alternatives and are better for reproducible or long-term experimental analysis.

This chapter highlights the considerations for developing tissue mimicking materials specifically to exhibit the dielectric properties of fat, muscle and blood. The experimental procedures employed to develop, test and select phantom materials has been discussed. This includes constructing the electrodes and their configurations to measure the conductivities and permittivities of both liquid mixtures (for blood) and gelatinous/semi-solid materials (for fat and muscle), most appropriately. Moreover, the effect of electrode geometry and configuration on the overall impedance measurements has been observed and discussed.

The range of conductivity and relative permittivity values for fat, muscle and blood domains, as highlighted through parametric modelling of tissue properties by Gabriel [144], have been compiled in Table 4-1.

Table 4-1: Conductivity and Relative Permittivity of tissues as modelled by Gabriel [144]

Tissue	Frequency Range	Bulk Conductivity	Relative Permittivity
Fat	1 kHz – 10 MHz	0.02 – 0.03 S/m	24104 – 13
Muscle	1 kHz – 10 MHz	0.32 – 0.61 S/m	434930 - 170
Blood	1 kHz – 10 MHz	0.7 – 1.1 S/m	5260 - 250

Although this research is mainly concerned with the dielectric properties of phantom materials, in the case of blood, consideration was also given to finding potential liquid materials that also possessed similar physical properties such as density and dynamic viscosity.

This chapter aims at identifying potential tissue simulants for fat, muscle and blood to mimic the dielectric properties. Furthermore, the tissue simulants would be used to construct a forearm phantom and tested for the overall impedance response for three different arterial diameters.

4.2 Measurement Setup and Methodology

A rheometer was used to measure mechanical properties of the mixtures and this is described in section 4.2.1. Three systems were configured to measure impedance. In the first (described in section 4.2.2), measurement was performed in a test setup using a glass manifold. These measurements were sensitive to the configuration of electrodes but provided some insight into the effect of electrode spacing. In the second (described in section 4.2.3), a coaxial measurement configuration was used to help with precise determination of dielectric behaviour. This coaxial system was used extensively to characterise the candidate materials. The third impedance measurement system (described in section 4.2.4) was a commercially available device employed to provide a higher rate of measurement of the impedance spectrum, albeit for a reduced set of excitation frequencies.

4.2.1 Density and viscosity measurement

The densities and dynamic viscosities of the liquids were also measured. The density measurements were carried out by weighing a 50cc sample of each liquid at room temperature (Schimadzu AUW 120 Balances, Schimadzu Scientific Instruments, USA).

Viscosity was estimated using a Brookfield RST Rheometer (Brookfield AMETEK, USA) with a dynamic viscosity range of $0.1x10^{-3}$ to $5.4x10^{6}$ Pa-s. The device is a rotational, controlled-stress rheometer (Figure 4.1). The instrument's measuring drive uses high-precision optical encoders to estimate the position of spindle geometry. It functions according to two basic measurement methods. One is rotational measurement under controlled shear rate (CSR) and the other is rotational measurement under controlled shear stress (CSS). The device can also provide temperature controlled measurements, working within a maximum temperature of +180°C and a minimum of -20°C. The device was self-calibrated before each measurement.

In the rheometer, samples are positioned in the measuring gap between the stationary measuring cup and the rotating spindle (or bob). The measurements were carried out at a shear rate of 1000 s^{-1} at 20°C using both the measuring systems, CCT-25 and CCT-40. The results are presented as an arithmetic mean of multiple sample measurements over the specified duration.

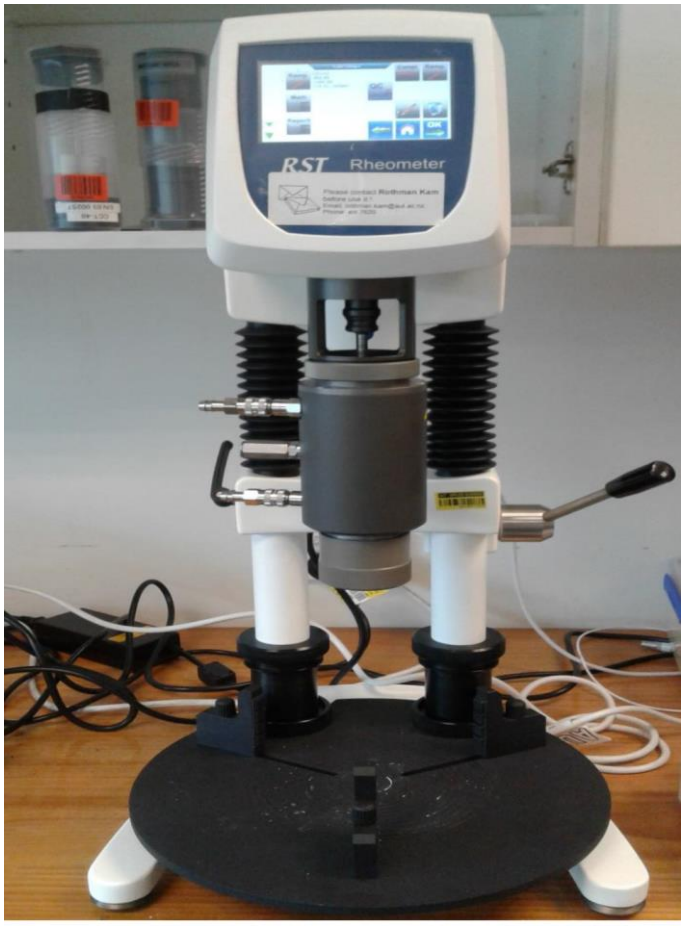

Figure 4.1: BrookField® RST Rheometer used for measuring the viscosities

4.2.2 Manifold measurement system

The impedance measurements were carried out using a Keysight E4980A Precision LCR meter (20 Hz to 2 MHz) (Keysight Technologies®, USA) (Figure 4.2). It was used along with a pair of clip leads (16089E Kelvin Clip leads (Keysight Technologies®, USA)). The frequency sweep was set at 50 logarithmically spaced steps between 1 kHz to 2 MHz.

Figure 4.2: E4980A Precision LCR meter with the Kelvin clip leads

The measurement set up consisted of a transparent glass manifold with four mouths which could be closed using a stopper through which the electrodes were inserted. The horizontal ends provided for a valve connection for controlled entry and ejection of the liquids. The measuring electrodes were copper rods of 3 mm in diameter. Four such electrodes were marked A, B, C and D. Six different combinations of electrode pairs were chosen namely, AB, BC, CD, AC, BD and AD. Consecutive electrodes in this set-up, A and B, were placed 7 cm apart, and the spacing between A and C, and, A and D, were 14 cm and 21 cm respectively. (All spacing are measured from centre of each mouth/electrode) (Figure 4.3 and Figure 4.4)

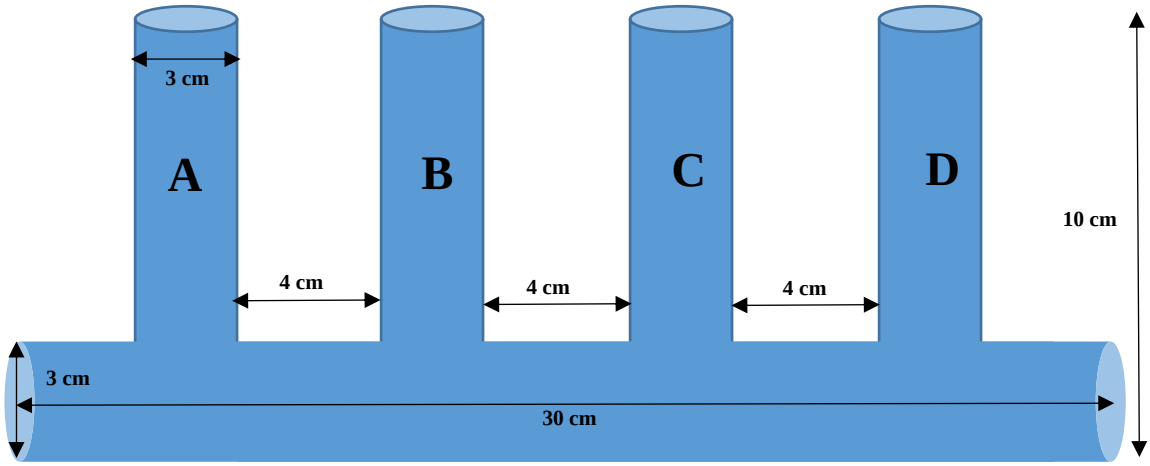

Figure 4.3: Schematic of the manifold setup for impedance measurements for the liquids (with dimensions)

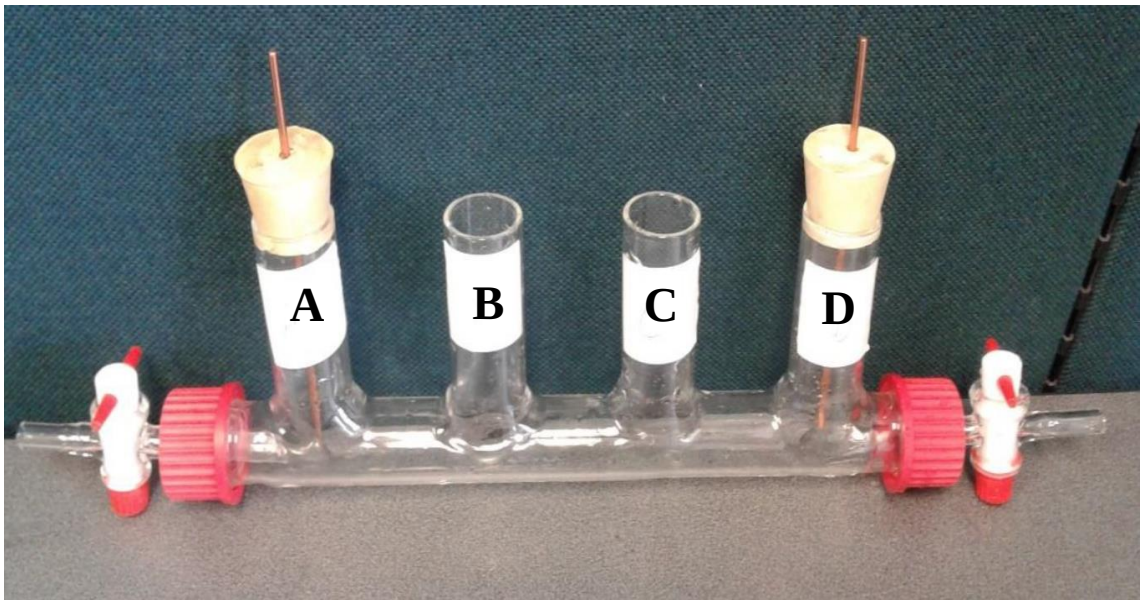

Figure 4.4: Four mouth glass manifold setup with the rubber stoppers and copper electrodes across sites A and D

4.2.3 Coaxial Measurement System

The measurement of the dielectric properties of any material involves measuring the electrical conductivity and permittivity. Although the measurement of complex permittivity alone provides for the calculation of complex conductivity, the conductivity can also be measured through its relation to an extensive property, such as, resistance through:

$$R = \rho \frac{l}{A} = \left(\frac{1}{k}\right)\left(\frac{l}{A}\right)$$

where, R is the resistance, ρ is the resistivity, l is the length of the conduction path, A is the effective area of cross-section of the conduction path and k is the conductivity. A wide range of methods and techniques allow for the measurement of conductivity such as two-electrode method, four-electrode method, two-toroid technique etc., which offer lower accuracy due to varying conduction pathways (non-uniform cell constant) and fringe effects. The implication of using a cylindrical pair of concentric electrodes is that it provides a uniform cell constant through limiting the conduction pathway radially between the two electrodes, and can be used in a way that negates any fringe effects.

4.2.3.1 Coaxial Cylindrical sensor design

A coaxial cylinder consists of cylindrical electrodes where an inner cylindrical rod is positioned concentric to the outer cylindrical tube. The two electrodes are positioned coaxially and are separated by a dielectric material which is not intended to come in contact with the liquid under test. The electrodes are immersed into an appropriate vessel with the liquid at certain depth(s) and electrical parameters are measured. A schematic of a coaxial cylinder electrode is as shown in Figure 4.5.

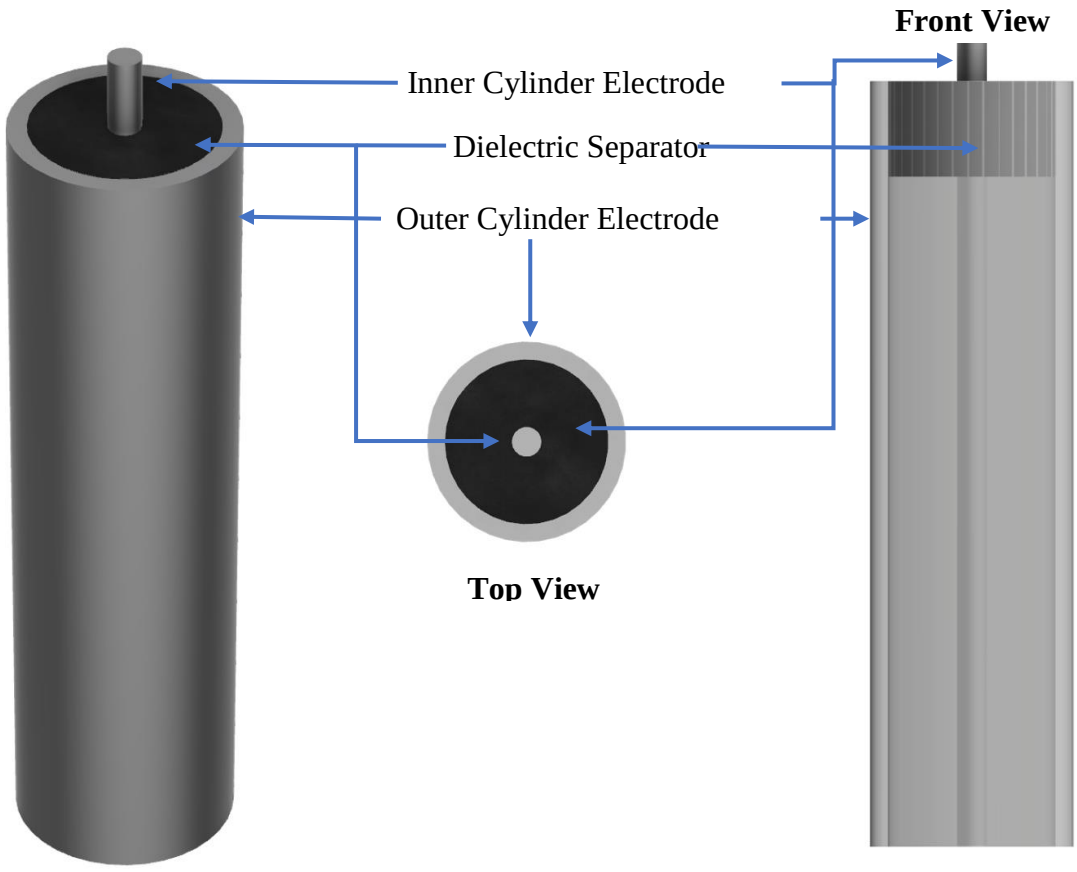

Figure 4.5: Coaxial Cylinder sensor schematic for dielectric measurements

For this work, a coaxial sensor was constructed using 316 stainless steel for the outer cylinder tube and the cylinder rod. The cylinder rod was 4 mm in diameter and the cylindrical tube was 3/8" (9.525 mm) in diameter with a thickness of 18SWG (1.219 mm). Stainless steel was chosen due to its excellent performance as an electrode with minimal chemical reaction or corrosion.

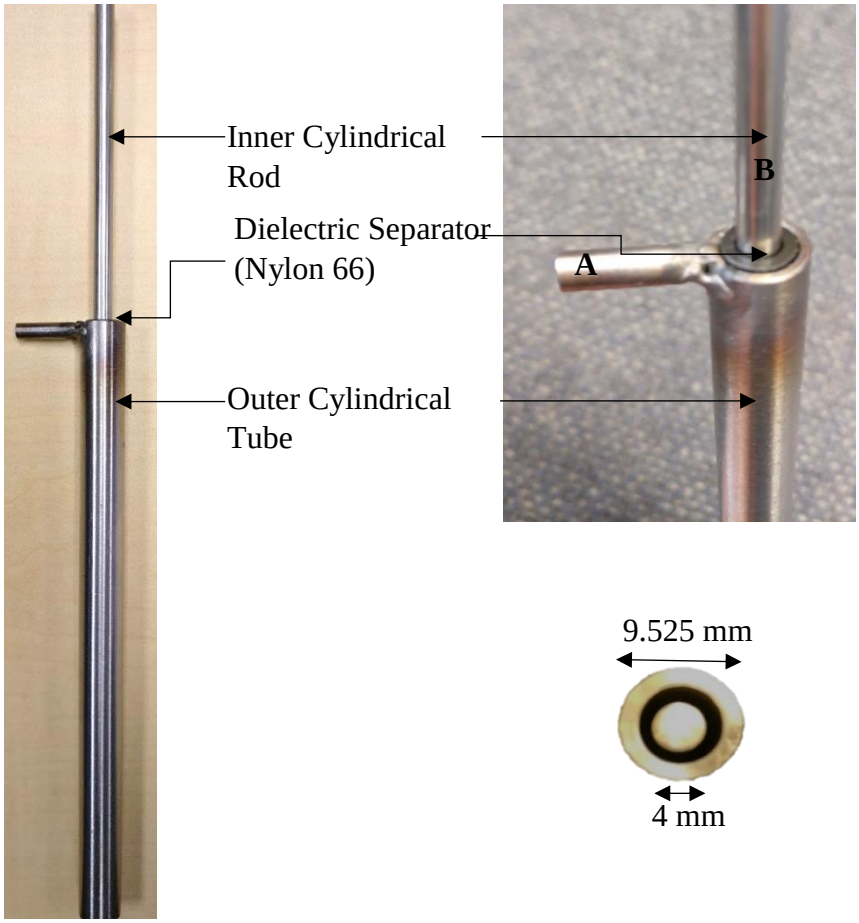

Figure 4.6: Coaxial Cylinder sensor developed for dielectric measurements

Figure 4.6 shows the constructed coaxial sensor with the dimensions of the inner and outer electrode. As can be seen, a dielectric material has been positioned on the top part of the cylindrical section that measures 25 mm in length. A hole was made just below the dielectric separator to allow for air to exit when the probe is submerged. The material chosen for the separator was Nylon 66 with a known dielectric relative permittivity of 3.2 [106]. Additionally, the sections A and B from the figure were used to act as measuring sites for the LCR meter clip leads. The section A was welded to the outer cylinder using the same stainless-steel rod material as the inner electrode, and section B is the extended part of the inner electrode.

4.2.3.2 Dielectric measurements using Coaxial Cylindrical sensor

A. Conductivity Measurement

Measurement of conductivity is carried out through the measurements of complex impedance, Z*. The measured, multi-frequency impedance includes contributions from the effect of electrodes and connecting leads. Therefore:

$$Z^*_{meas} = Z^*_{liq} + Z^*_{electrodes} + Z^*_{leads}$$

where Z^*_{meas} is the measured impedance, Z^*_{liq} is the impedance of the liquid under test, $Z^*_{electrodes}$ is the impedance contribution of the electrodes and Z^*_{leads} is the impedance contribution from the leads. Hence, the measured impedance is not equal to the impedance of the liquid under test. In order to compensate for this, the impedance of the electrodes is measured when shorted and without any media. This measurement represents the combined contribution from the electrodes and the leads, i.e. $Z^*_{electrodes} + Z^*_{leads}$ and is subtracted from the overall measured impedance to provide the impedance of the media, i.e. the liquid.

Since conductivity is measured through resistance, we consider the real part of the calculated impedance of the liquid for analysis. The real part of the calculated impedance represents the overall resistance of the liquid that includes the resistance due to radial conduction pathways (R_{radial}) and the resistance due to fringe effects (R_{fringe}) which occurs due to the leakage of stray electric field around the interface between the electrodes and the liquid. These are parallel resistances so the following relation holds:

$$\frac{1}{Z^{real}_{liq}} = \frac{1}{R_{radial}} + \frac{1}{R_{fringe}} \tag{4.1}$$

The radial conduction pathways are purely dependent on the electrical properties of the liquid media under test whereas the fringe effect constitutes the pathways which are not radial and hence affected by the test geometry [211] (Figure 4.7). The fringe portion is effectively constant for the coaxial cylinder geometry at different depths of submersion and hence is easier to manipulate.

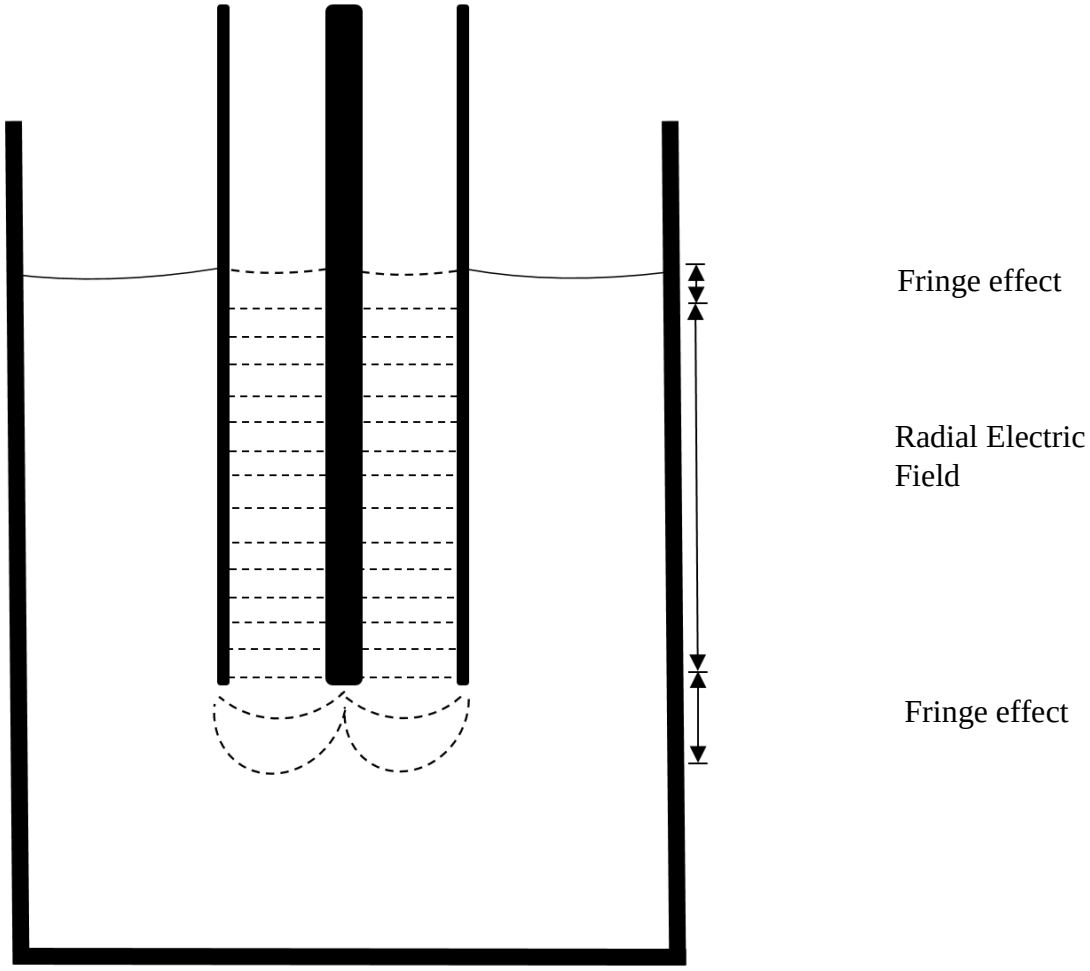

Figure 4.7: Conduction pathways for a coaxial cylinder immersed in a liquid [211]

The conductivity for the coaxial cylinder configuration is related to resistance by:

$$\frac{1}{R_{radial}} = k\left(\frac{2\pi l}{\ln\left(\frac{b}{a}\right)}\right)$$

where k is the conductivity, l is the effective length of the electrode immersed in the liquid, b is the inner diameter of the outer electrode and a is the diameter of the inner electrode [212], [213]. The effect of R_{fringe} is separated from R_{radial} by repeating the measurements at several immersion depths. Taking the differentiation of the equation (4.1) with respect to immersion depth l, we get:

$$\frac{d(1/Z_{liq}^{real})}{dl} = \frac{d(1/R_{radial})}{dl} \tag{4.2}$$

The fringe term, being constant for a particular geometry of the coaxial cylinder electrodes, does not appear in equation (4.2). Hence conductivity (k) can be calculated as:

$$k = \left(\frac{\ln\left(\frac{b}{a}\right)}{2\pi}\right)\left(\frac{d(1/Z_{liq}^{real})}{dl}\right) \quad (4.3)$$

From equation (4.3), the calculation of the conductivity only depends upon the relative position of the electrodes. This is the main advantage of this technique where the geometry contribution is a constant $\left(\frac{\ln\left(\frac{b}{a}\right)}{2\pi}\right)$ which can be calculated and hence removes the need for calibration. The only measurement required is that of impedance with different immersion depths. However, the procedure does require some precautions. There might be some sources of error due to unsymmetrical geometry (the inner electrode not being parallel to the outer tube), and the approach of the electrodes too close to the bottom of the liquid container. If the setup is immersed too deep into the container such that it is within a distance of 2 (b-a) from the bottom, it changes the conductance due to the variation in the lower fringe fields [211]. Consideration was given to these errors while carrying out the measurements for this work.

B. Measurement of Relative Permittivity

The calculation of the permittivity as an extensive property is done my measuring the capacitance of the medium under test, in this case liquid. Here, we consider the imaginary part of the measured impedance or measure capacitance directly through a set of measurement modes offered by the Keysight E4980A LCR Meter. The imaginary part of the measured impedance consists of contributions from the medium under test, the electrodes and the leads.

$$Z_{meas}^{imag} = Z_{liq}^{imag} + Z_{electrodes}^{imag} + Z_{leads}^{imag}$$

The capacitance for a coaxial cylinder is given by the following expression:

$$C = \frac{2\pi\varepsilon_0\varepsilon_r * l}{\ln(\frac{b}{a})} \quad (4.4)$$

where C is the capacitance, ε_0 is the absolute permittivity of vacuum (8.854 x 10^{-12} F/m), l is the length of the cylindrical capacitive column, b is the inner diameter of the outer cylindrical tube electrode and a is the diameter of the inner cylindrical rod electrode. The estimation of the relative permittivity of the liquid can be done by calculating the capacitance of the liquid from the value of overall measured capacitance, C, from equation (4.4). The combined capacitance of the leads and the electrodes can be separated from the liquid by taking separate measurements of capacitance without any media.

From equation (4.4), it is evident that capacitance for a cylindrical geometry is a linear function of capacitive length, l. Now, the relative permittivity of the liquid under investigation can be calculated as:

$$\varepsilon_l = \frac{C_{liquid}^{l}}{C_{air}^{l}} \tag{4.5}$$

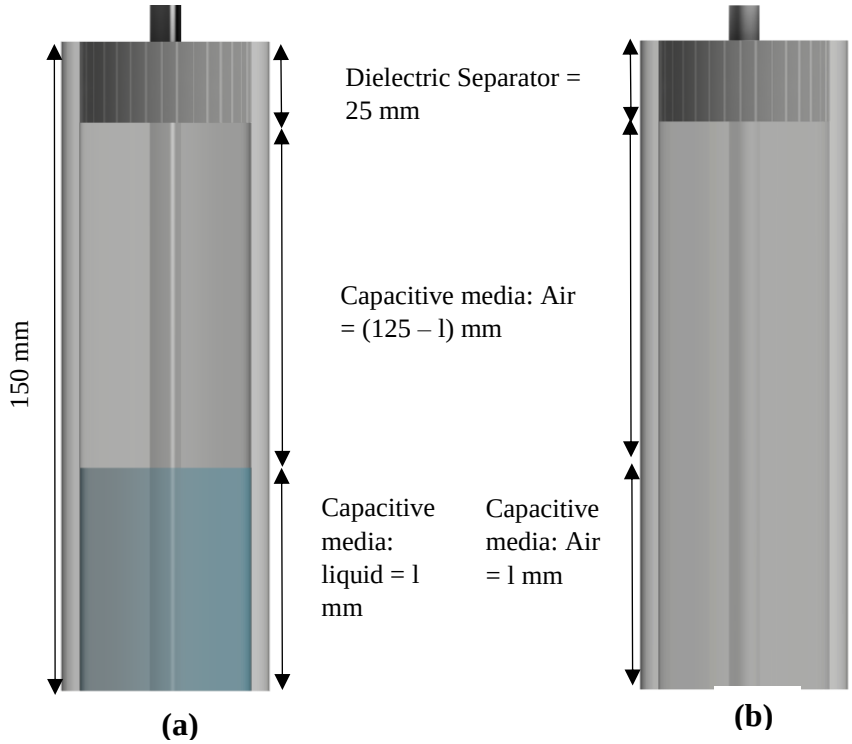

Figure 4.8: Comparison between two schematics to calculate capacitance from (a). Electrodes with liquid and (b). Electrodes without liquid

where ε_l is the relative permittivity of the liquid, C_{liquid}^{l} is the capacitance of liquid with a column length of l and C_{air}^{l} is the capacitance of air within the same column length, l (Equation (4.5)).

Figure 4.8 shows the two cases considering the electrodes with and without liquid to measure the capacitance. Assuming a linear proportionality of cylindrical capacitance with length, the capacitance for setup (a) can be expressed as:

$$C_a = C_N + C_{air}^{125-l} + C_{liquid}^{l} \tag{4.6}$$

where C_a is the total capacitance for setup (a), C_N is the capacitance of the Nylon dielectric separator of constant length 25 mm, C_{air}^{125-l} is the capacitance contribution from the 125-

l mm section of air and C_{liquid}^{l} is the capacitance of the liquid with a section length of l mm. Substituting the expressions for capacitance for a cylindrical configuration, we get:

$$C_a = \frac{2\pi\varepsilon_0\varepsilon_N * 0.025}{\ln(\frac{b}{a})} + \frac{2\pi\varepsilon_0 * (125 - l) * 10^{-3}}{\ln(\frac{b}{a})} + \frac{2\pi\varepsilon_0\varepsilon_l * l * 10^{-3}}{\ln(\frac{b}{a})} \tag{4.7}$$

where ε_N is the relative permittivity of dielectric separator (Nylon) and ε_l is the relative permittivity of the liquid under test. Simplifying the equation further, we get:

$$C_a = \frac{2\pi\varepsilon_0 * 10^{-3}}{\ln(\frac{b}{a})}\{25 * \varepsilon_N + (125 - l) + l * \varepsilon_l\} \tag{4.8}$$

For setup (b), the capacitance can be expressed as:

$$C_b = C_N + C_{air}^{125-l} + C_{air}^{l} \tag{4.9}$$

where C_{air}^{125} is the capacitance of 125 mm of air as the media. This can be further expressed as:

$$C_b = \frac{2\pi\varepsilon_0 * 10^{-3}}{\ln(\frac{b}{a})}\{25 * \varepsilon_N + 125\} \tag{4.10}$$

From equation (4.6), we can obtain:

$$C_{liquid}^{l} = C_a - (C_N + C_{air}^{125-l}) \tag{4.11}$$

$$C_{liquid}^{l} = C_a - \{\frac{2\pi\varepsilon_0\varepsilon_N * 0.025}{\ln\left(\frac{b}{a}\right)} + \frac{2\pi\varepsilon_0 * (125 - l) * 10^{-3}}{\ln\left(\frac{b}{a}\right)}\} \tag{4.12}$$

From equation (4.9), we obtain:

$$C_{air}^{l} = C_b - (C_N + C_{air}^{125-l}) \tag{4.13}$$

$$C_{air}^{l} = C_b - \{\frac{2\pi\varepsilon_0\varepsilon_N * 0.025}{\ln\left(\frac{b}{a}\right)} + \frac{2\pi\varepsilon_0 * (125 - l) * 10^{-3}}{\ln\left(\frac{b}{a}\right)}\} \tag{4.14}$$

Different media sections in a cylindrical capacitance configuration exist as parallel combinations of each other. Hence the equivalent capacitance is the sum of capacitance

of individual media such that the capacitance of the air section is given by $C_{air} = C_b - C_N$. Also, capacitance in the cylindrical configuration is a linear function of length, l and hence can be considered as capacitance per unit length. Hence the capacitance for a section of length l with air can be defined as mentioned in equation (4.15).

$$C_{air}^{l} = (C_b - C_N) * \frac{l}{125} \tag{4.15}$$

Substituting the values of C_{liquid}^{l} from equation (4.12) and C_{air}^{l} from equation (4.14) to equation (4.15), we get:

$$\varepsilon_l = \frac{C_a - \left\{ \frac{2\pi\varepsilon_0\varepsilon_N * 0.025}{\ln\left(\frac{b}{a}\right)} + \frac{2\pi\varepsilon_0 * (125 - l) * 10^{-3}}{\ln\left(\frac{b}{a}\right)} \right\}}{\left\{ C_b - \frac{2\pi\varepsilon_0\varepsilon_N * 0.025}{\ln\left(\frac{b}{a}\right)} \right\} * \frac{l}{125}} \tag{4.16}$$

The above equation calculates the relative permittivity of the liquid under test employing two measurements of capacitance - with and without liquid (C_a and C_b, respectively) for this setup.

C. Eliminating Electrode Polarization effects

Measurements performed using the coaxial probe method are highly prone to electrode polarization, especially in the case of capacitance readings. This is due to an existential barrier charge deposition at the electrode-liquid interface that increases the overall capacitance at lower frequencies. The conventional methods for negating the effects of polarization involve the use of four-probe methods or high frequency analysis followed by extrapolation to lower frequencies of interest. However, this study was influenced by both these limitations due to a coaxial cylindrical electrode configuration and a low frequency range of interest (β-dispersion). Schwan in his study [214] of electrode polarization impedance in biological tissues postulated the dependence of the polarization capacitance, C_p for small currents as:

$$C_p = A\omega^{-n}$$

where A is a constant, ω is the frequency and n is the power coefficient. The work suggested the values of n generally lie between 1.5 and 2. The work also mentioned

certain techniques to reduce polarization, most of which were not applicable to the proposed electrode configuration for this study. More generally, the power law relationship for the polarization effects can be extended to the whole frequency range of interest by considering a relaxation system to define the polarisation effects. For the total measured impedance, the following relation then holds:

$$Z_{meas} = Z_{electrodes} + Z_{polarisation} + Z_{liquid}$$

The contribution of the electrodes can be accounted by performing open and short-circuited measurements as described previously. The polarisation contribution can be defined as a fractional capacitive element with a total impedance defined as:

$$Z_p = \frac{R_p}{1 + (j\ \omega\ C_p)^{\alpha}}$$

where R_p denotes the polarisation resistance, $(j\ \omega\ C_p)^{\alpha}$ denotes the fractional capacitive contribution of polarisation capacitance C_p with the relaxation coefficient α.

4.2.3.3 Measurement setup and calibration

Figure 4.9 (a) and (b) shows the configurations used for measurement. The electrodes were marked with levels of depth (or the height of liquid rise within the sensor). The setup was connected to the LCR meter as shown in Figure 4.10.

Initially, a standard saline solution with documented dielectric properties was tested to determine the efficacy and calibration of the setup. 1mM NaCl solution was developed using sodium chloride, reagent grade (Scharlau Chemei S.A., Barcelona, Spain) dissolved in 250 ml distilled water. Impedance measurements were taken at three different immersion depths.

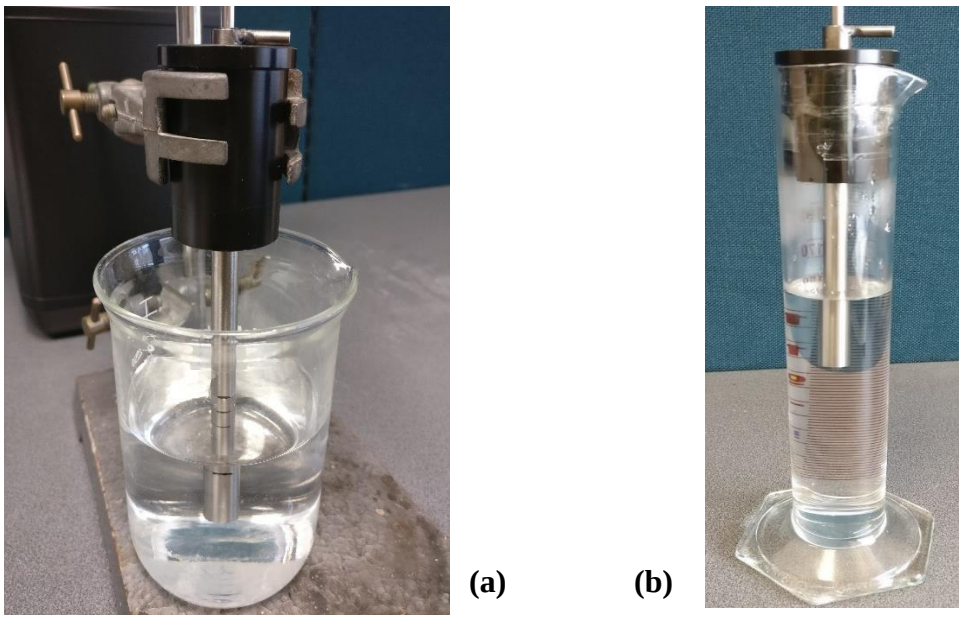

Figure 4.9: Measurement setups for dielectric measurements using – (a). Glass beaker, and, (b). Measuring Cylinder

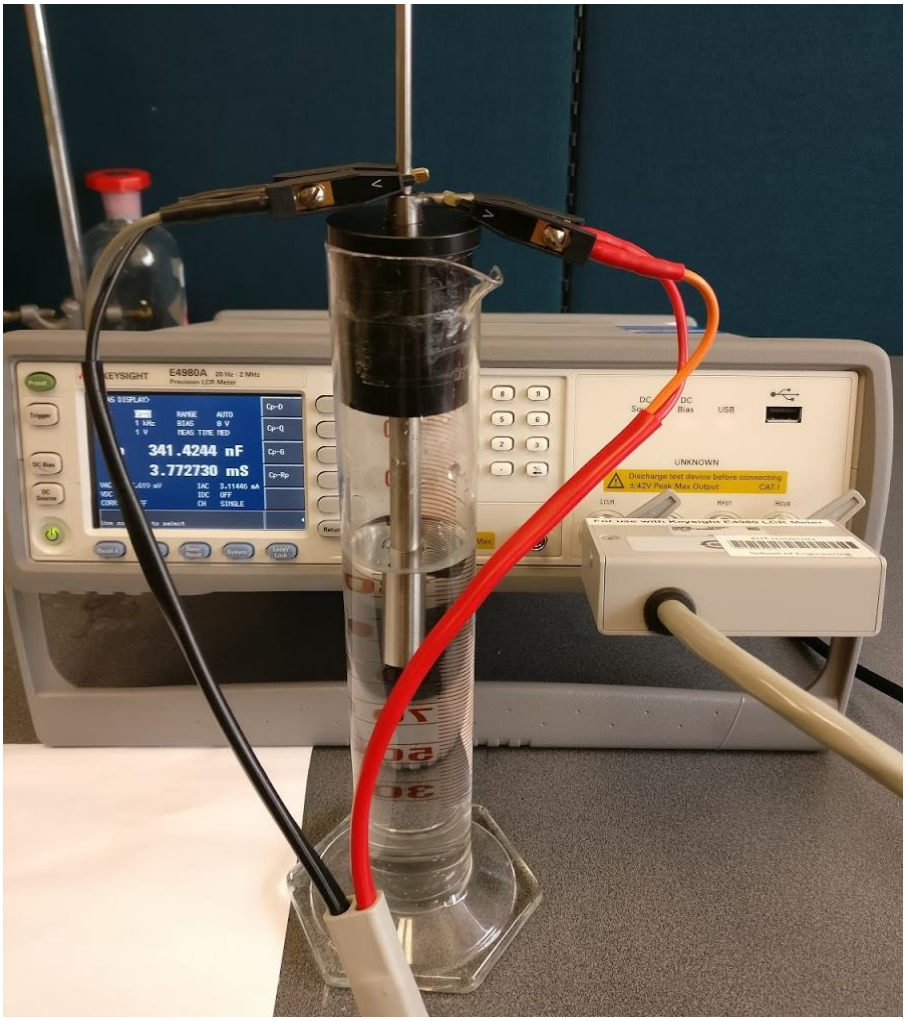

Figure 4.10: Measurement setup connected to the LCR meter through clip leads

The measurements were processed using Wolfram Mathematica® Student Edition (v 10.0) [215].

The measurements were made in terms of impedance magnitude (Z) and phase (θ). This ensured a general impedance response of the overall system without assuming any equivalent electrical model, although the electrical response for ionic solutions can be accurately described using a parallel RC circuit. The real and the imaginary parts of the impedance were fitted to an assumed model defining the combined behaviour of the solution bulk impedance and polarisation impedance, as follows:

$$Z^{l}{}_{meas} = \frac{R_b}{1 + j\,\omega\,R_b C_b} + \frac{R_p - R_b}{1 + (j\,\omega\,\tau_p)^{\alpha}} \tag{4.17}$$

where $Z^{l}{}_{meas}$ is the measured impedance of the solution, $\frac{R_b}{1+j\,\omega\,R_b C_b}$ being the bulk impedance of the solution with R_b and C_b as resistance and capacitance respectively, and, $\frac{R_p - R_b}{1+(j\,\omega\,\tau_p)^{\alpha}}$ was assumed to describe the polarisation effect with a relaxation time τ_p and dispersion coefficient α.

The measured impedance was fitted to the equivalent model in equation (4.17) through minimizing the sum of squared errors (SSE) between the real and imaginary parts given by the equation:

$$SSE = \sum_{i=1}^{N}\left(R^{i}_{fit} - R^{i}_{data}\right)^2 + \sum_{i=1}^{N}\left(X^{i}_{fit} - X^{i}_{data}\right)^2$$

The difference of the measured impedance and fit obtained for the polarisation impedance was considered as the actual response of the liquid, which was solved to obtain conductance (G) and capacitance (C) at the measurement frequencies.

4.2.3.4 Calibration Results

The measured impedance values for 1mM NaCl solution at three immersion depths (20 mm, 30 mm and 40 mm) are presented in Figure 4.11 (A), (B) and (C) respectively.

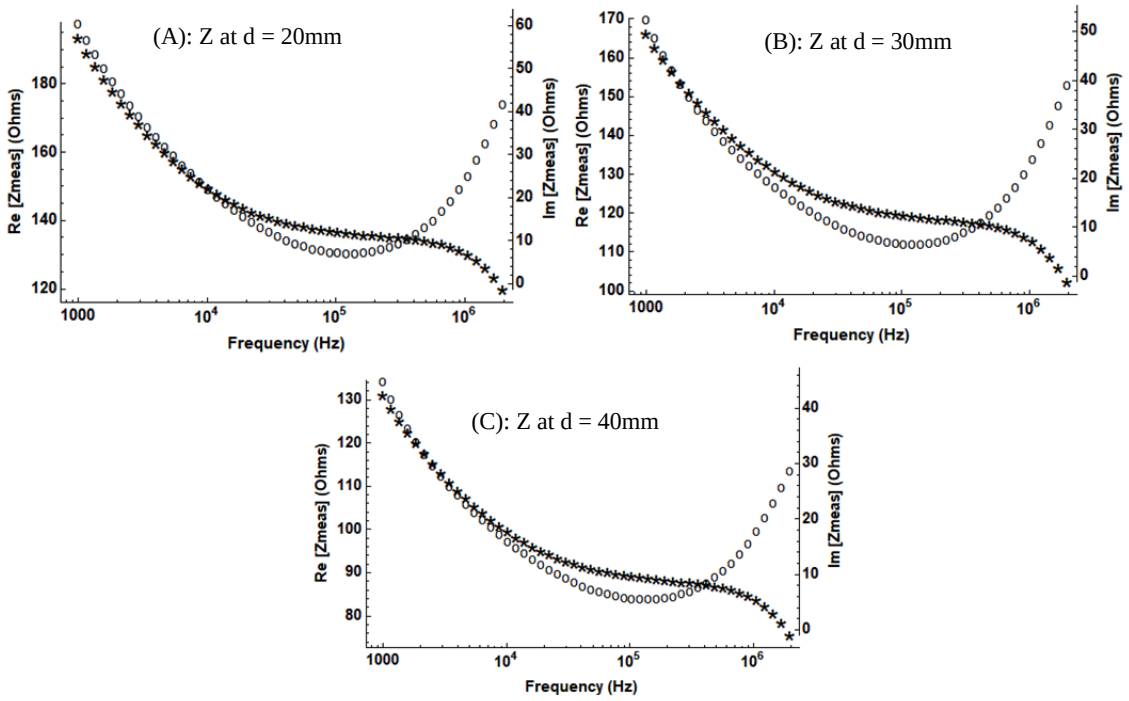

*Figure 4.11: Measured Impedance plots for 1mM NaCL with immersion depths of (A): 20, (B): 30 and (C): 40mm - * Re[Z], and o Im[Z]*

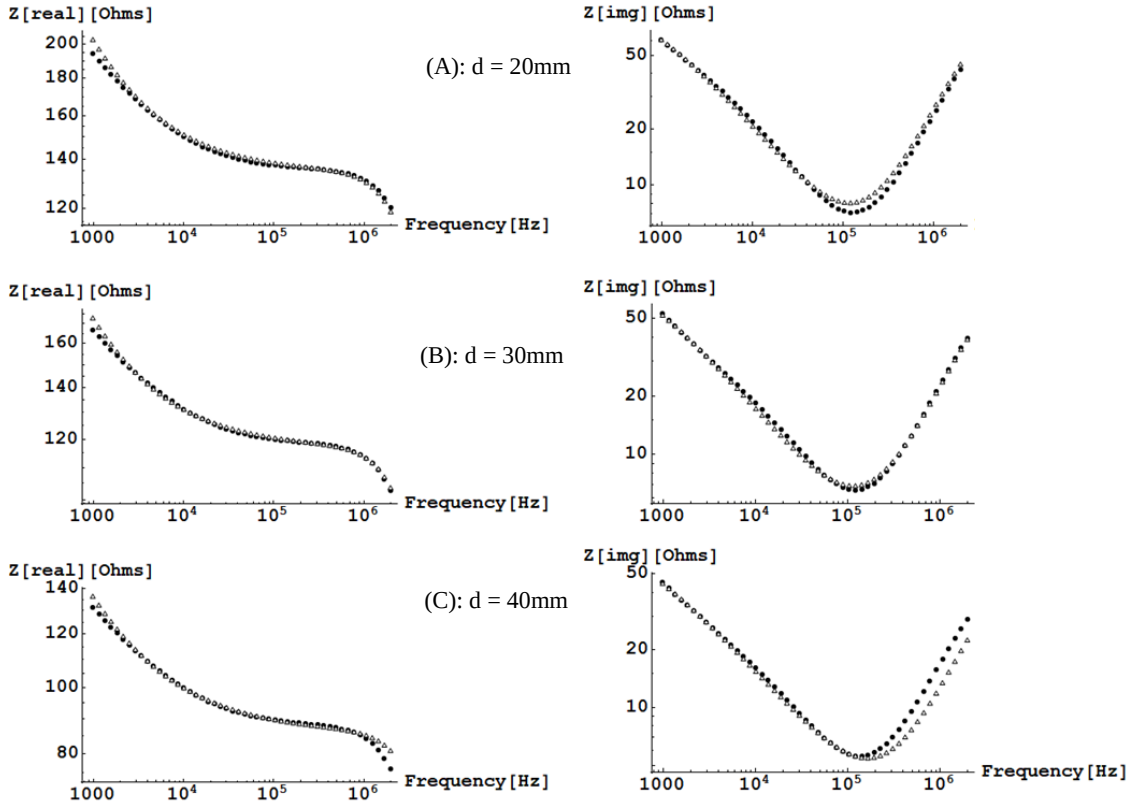

Figure 4.12: Comparison of measured and fit data for 1mM NaCL for calibration: • measured data, and ◿ fit data

The comparison of the measured data with the fit can be seen in Figure 4.12, with the values of the fit parameters obtained being tabulated in Table 4-2.

Table 4-2: Fit Parameters for 1mM NaCl calibration measurements

Fit Parameters → **Immersion ↓ Depth**	**R_b (Ω)**	**C_b (nF)**	**R_p (Ω)**	**τ (s)**	**α**
20mm	133.76	22	461.89	0.00094	0.602
30mm	116.4	25	468.73	0.00171	0.579
40mm	85.42	24.93	427.08	0.0023	0.5498

The impedance of the liquid was obtained by subtracting the polarisation contribution (obtained through the fitted model) from the measured impedance. This was used to calculate the conductance and capacitance of the solution at all the three depths by considering a parallel RC electrical response of ionic electrolytes. The variation of conductance for the different immersion depths was reconstructed as an interpolation function which was used to analyse the approximate conductance variation with immersion depth (Figure 4.13).

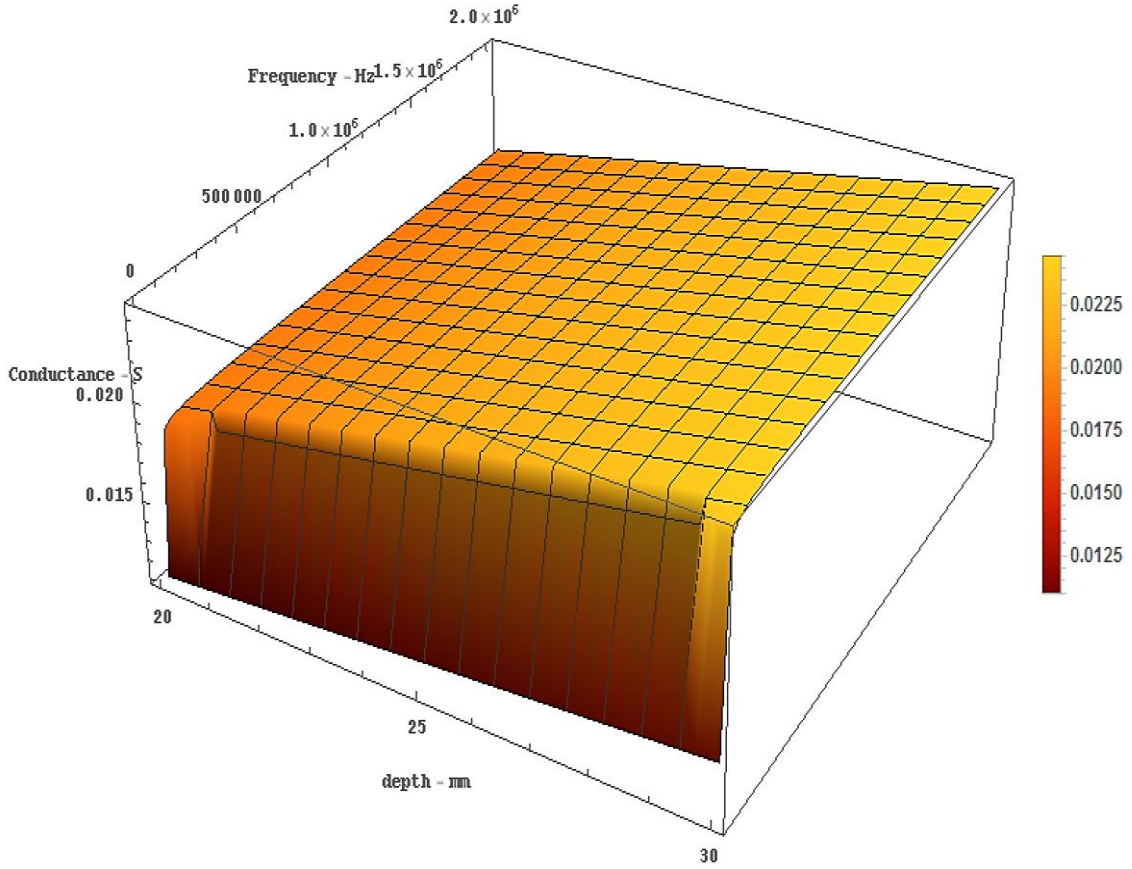

Figure 4.13: Interpolated surface plot showing variation of conductance for 1mM NaCL with immersion depths and frequency

The interpolation function was used to calculate the conductivity as the derivative of the interpolant at specific immersion depths as seen in Figure 4.14.

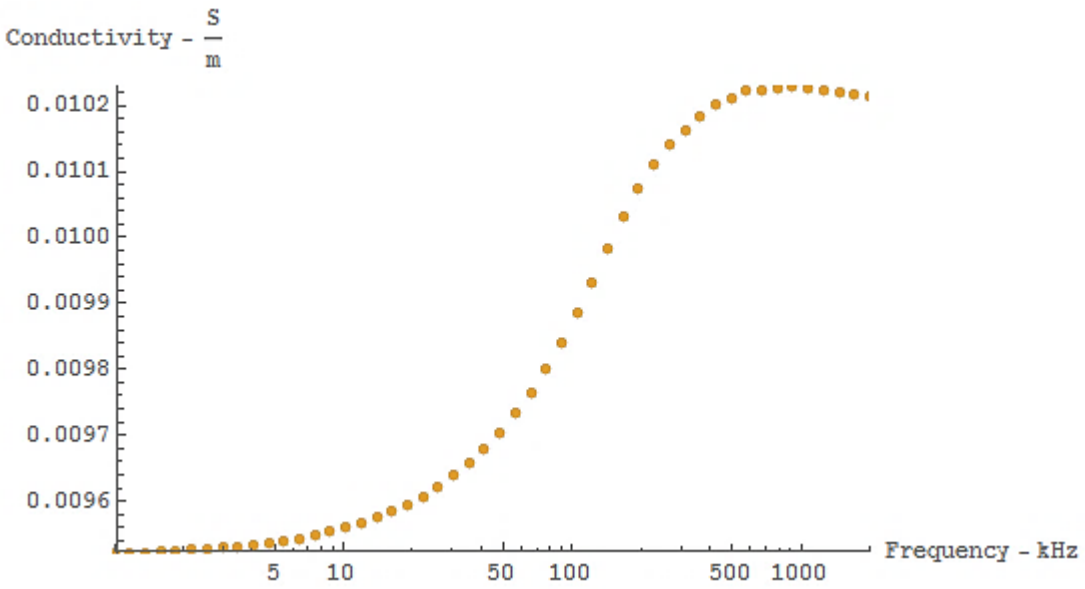

Figure 4.14: Log-Log plot showing the variation of conductivity of 1mM NaCl within 1 kHz – 2 MHz

The permittivity was calculated at different depths using the methodology as discussed in the previous section. The obtained permittivity for different depths, after accounting for polarisation can be seen in Figure 4.15.

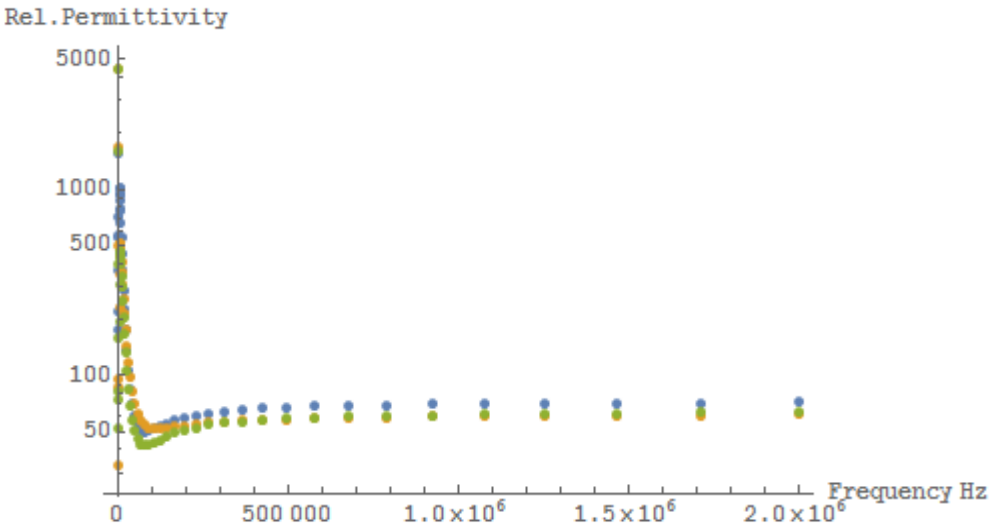

Figure 4.15: Relative Permittivity of 1mM NaCl as calculated: • 20 mm, • 30 mm, and • 40 mm

The obtained conductivity and permittivity for the solution was found to be in good agreement with many previous works (σ_∞ = 0.012 S/m, ε_∞ = 78.8 [200], [201]). As expected, the non-linear behaviour of capacitance at lower frequencies did affect the permittivity values which was mainly observed due to slight difference in the obtained fit and the impedance data.

4.2.4 Quadra Measurement Setup: Impedance Spectroscopy device

The Quadra® impedance spectroscopy device provides a platform for fast and real time impedance measurements for dielectric subjects. It is a patented product from Eliko Technologies (OÜ Eliko Tehnoloogia Arenduskeskus, Tallinn, Estonia) for portable impedance spectroscopy solutions (Figure 4.16). The device provides a capability of measuring simultaneous impedance spectra at 15 different frequencies with a sampling rate of 1000. The detailed specifications of this device have been mentioned in Appendix IV. The device features the use of application specific front ends required according to the type of measurement object and electrode excitation.

Figure 4.16: Quadra® Impedance Spectroscopy module from Eliko Technologies

The device enabled the spectral measurements to be performed offering a highest frequency limit of 349 kHz with the setting of 15 frequencies between 0.5 Hz – 349 kHz through frequency divider configuration. Different types of front ends that could be employed with this device include:

- Single shunt front end: This front end uses a potential divider configuration where a voltage excitation is applied to a fixed shunt resistor in series with the test impedance. It offers the selection of differential and unipolar excitation along with two or four-wire mode of measurement.

- Transimpedance front end: This front end provides a voltage excitation with the conversion of the measured current from the object to a voltage using a transimpedance amplifier. It offers a fixed current to voltage ratio and provides good compensation against current leakage.

- Current source front end: It features a current to voltage ratio of 1V = 1 mA to excite the test subject. However, it suffers from leakage at higher frequencies (> 10 kHz) and hence compromises the accuracy.

- Breakout front end: It offers a modular connection schematic to impedance measurements where the settings of excitation and sensing must be defined manually. It provides easy access to the pins of Quadra® impedance spectroscopy module.

For this study, a set of 15 frequencies between 1 kHz and 349 kHz was chosen to obtain measurements and model fitting and extrapolation was used to obtain the complete response between 1 kHz – 2 MHz.

A single shunt front end circuit was employed in a four-wire differential mode of measurement for this study. The schematic of the single shunt front end is shown in Figure 4.17.

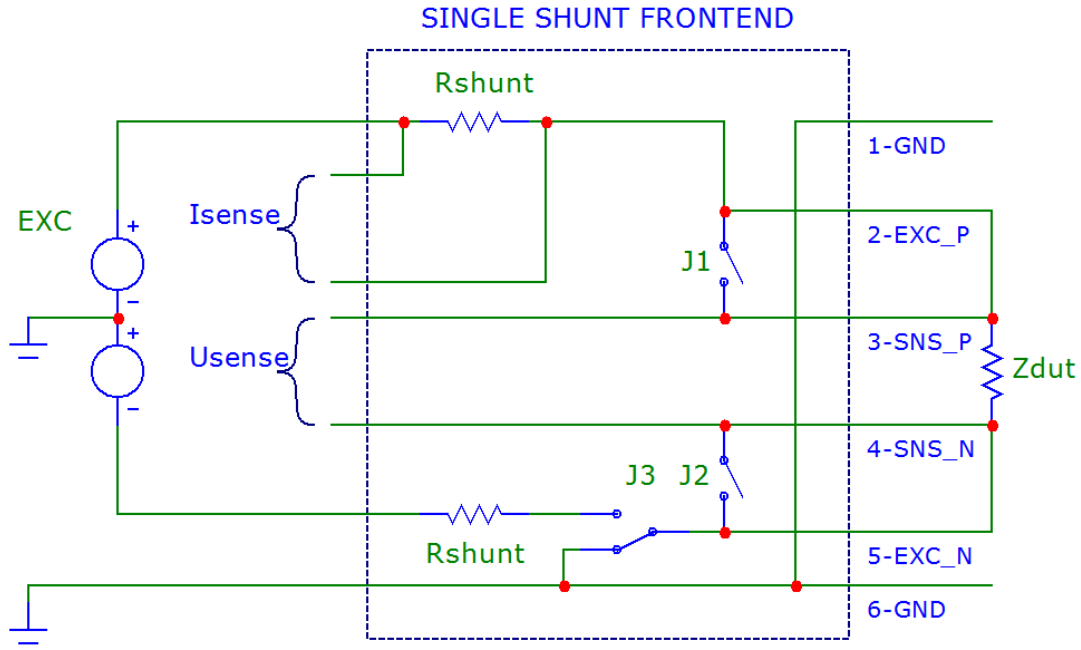

Figure 4.17: Schematic of the Single Shunt Front end used for this study [218]

J1, J2 and J3 denote the jumpers to select between differential or unipolar excitation and two or four-wire measurement. The pins 1 – 6 denote the input ports of the front end across which the electrodes are connected at pins 2, 3, 4 and 5 from the setup as shown in Figure 4.17. The inner pair (3-4) was configured for voltage sensing and the outer pair (2-5) was configured for excitation. The arrangement of the front end with the impedance module can be seen in Figure 4.18.

Figure 4.18: Single shunt front end connected to Quadra® impedance spectroscopy module in a four-wire, differential mode of measurement

The electrodes used for measurements were Kendall™ ECG electrodes (Covidien™, MA, USA). They were placed to achieve the inter-electrode gap of 10 mm used in the simulation study (Figure 4.19).

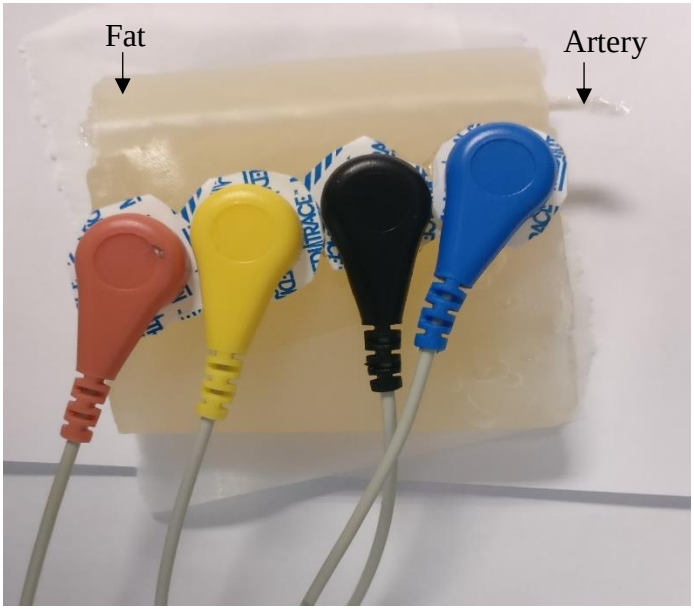

Figure 4.19: Measurement setup for the forearm phantom

4.3 Blood Phantom

Propylene glycol, ethanol and glycerol are known to exhibit single dielectric relaxation dispersion and hence are Debye-type liquids. As blood is also known to exhibit Debye behavior, these three liquids were candidates for components of a blood tissue simulant. Propylene glycol ($C_3H_8O_2$), also known as propane-1,2-diol, is a colourless, hygroscopic and clear liquid which is non-corrosive and has very low toxicity. Ethanol (CH_3CH_2OH), also known as ethyl alcohol, is a colourless, volatile and flammable liquid and has a slight chemical odour. Glycerol, commonly also known as glycerine, is a clear, hygroscopic and odourless liquid which is made from plant oils. It finds its use in several medical applications because of its safety together with its functional properties. All three chemicals are miscible with water. The properties have been tabulated in Table 4-3.

Table 4-3: Physical Properties of the three liquids.

	Molar Mass (g/mol)	**Viscosity (Pa.s)**	**Density (g/cc)**
Propylene Glycol	76.10	0.042	1.036
Ethanol	46.07	0.0012	0.789
Glycerol	92.09	1.412	1.261

The experiments for developing a suitable blood phantom were performed in two parts. The first part dealt with quantifying the impedance response and dielectric dispersion behavior of the chosen liquids using the manifold measurement system (as described in section 4.2.2). Viscosity and density were also measured, as described in section 4.2.1.

The second part of the investigation dealt with finding appropriate mixtures to mimic the dielectricity of blood. The conductivity and relative permittivity of the most probable liquid mixture from first set of experiments was tested and modified by changing the concentrations to approximate the electrical properties of blood as closely as possible.

4.3.1 Manifold results

The first stage of the experimental investigation aimed at measuring the impedance of the three liquids under test using the two-electrode manifold measurement setup.

The measured variation of impedance with frequency is represented as Cole plots for each of propylene glycol, ethanol and glycerol within 1 kHz to 2 MHz (see Figure 4.20, Figure 4.21 and Figure 4.22, respectively).

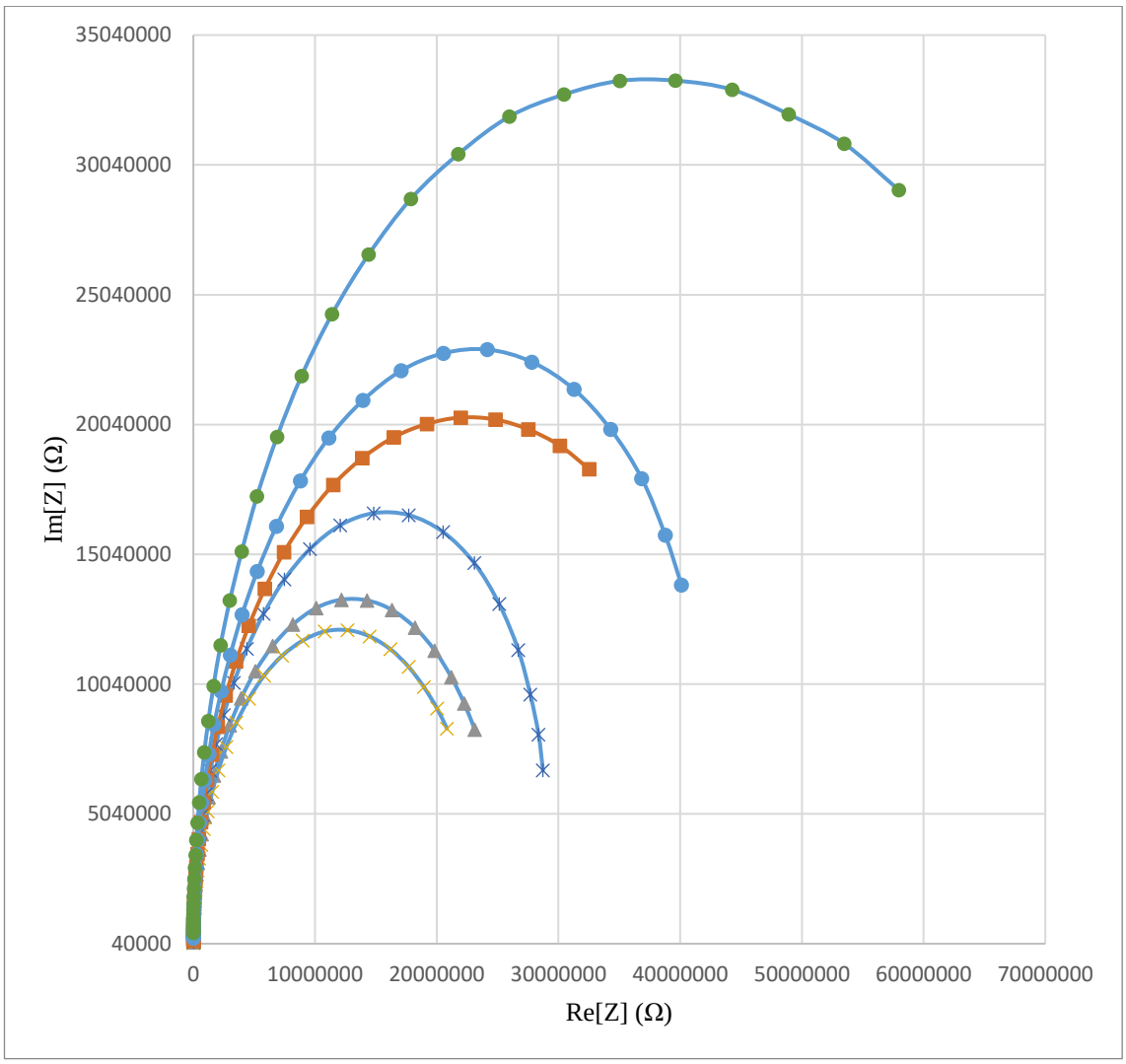

Figure 4.20: Cole plot for propylene glycol (PG) between different pairs of electrodes: A-B, B-C, C-D, A-C, B-D, and A-D

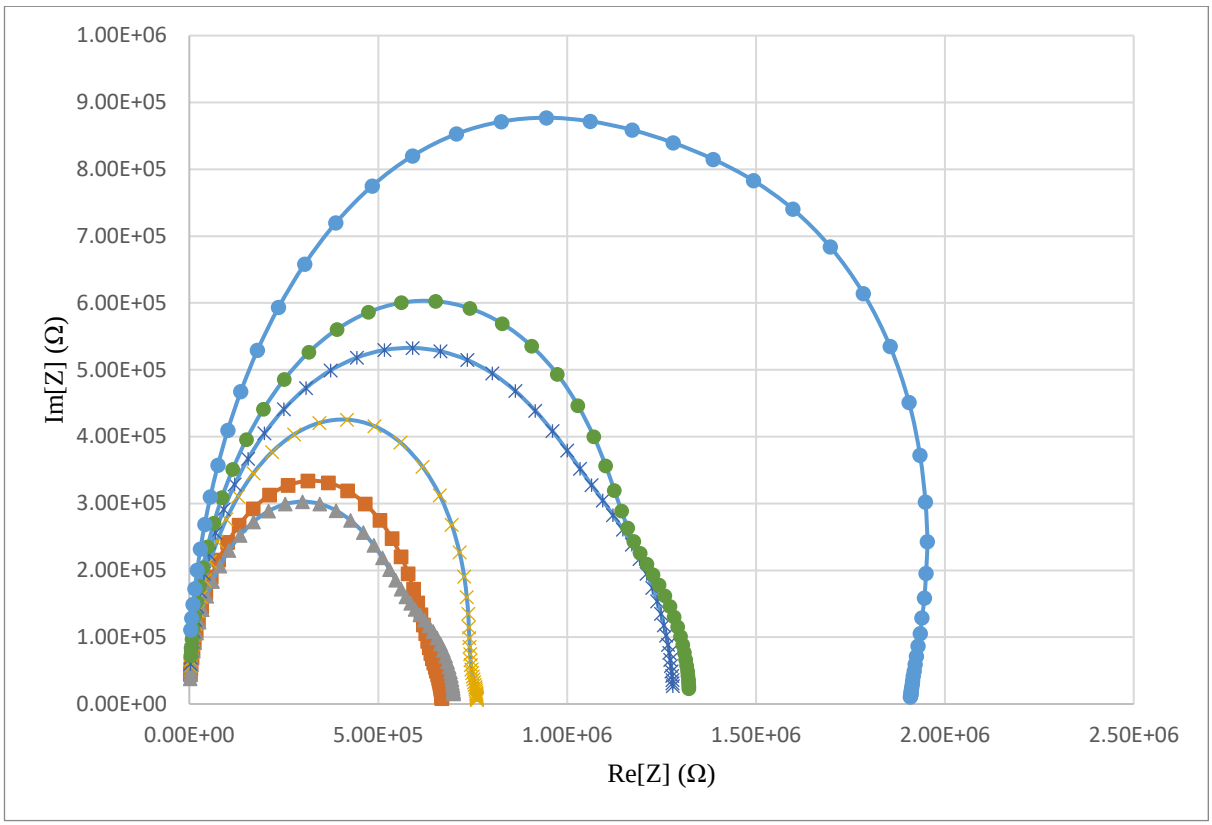

Figure 4.21: Cole plot for ethanol (ETH) between different pairs of electrodes: A-B, B-C, C-D, A-C, B-D, and A-D

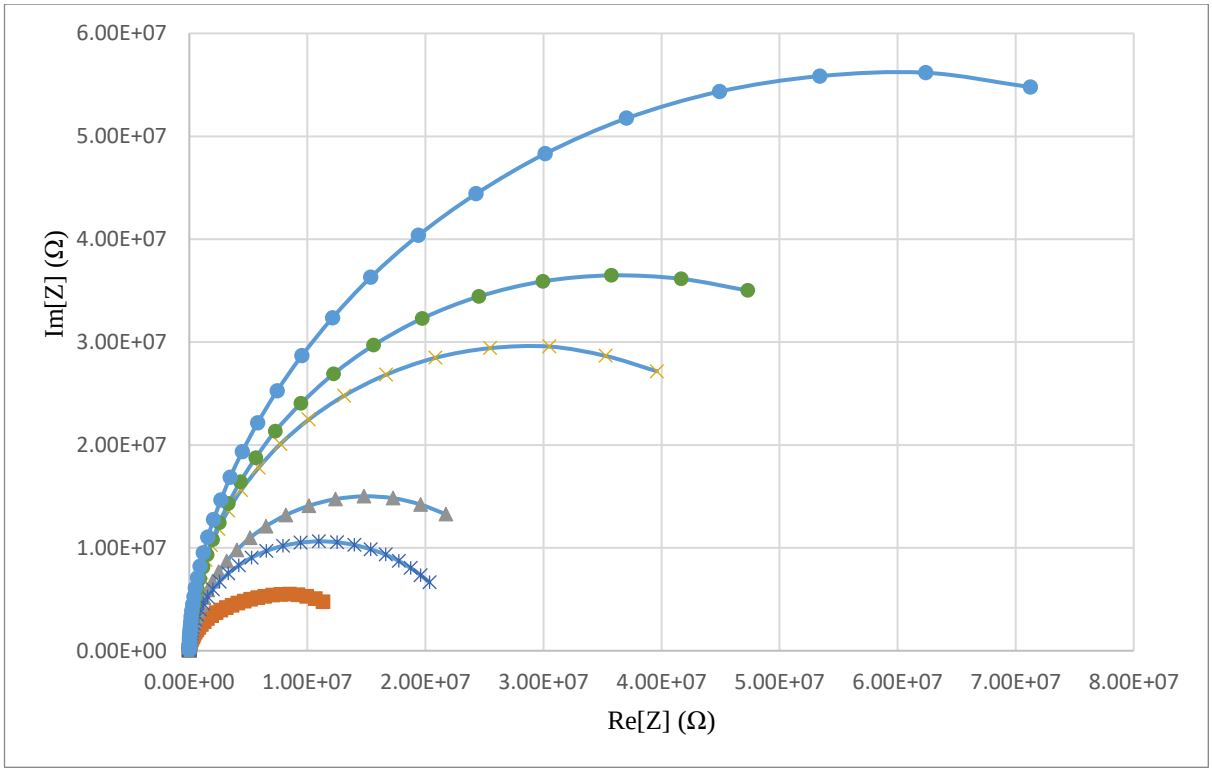

Figure 4.22: Cole plot for glycerol (GLY) between different pairs of electrodes: A-B, B-C, C-D, A-C, B-D, and A-D

4.3.2 Density and Viscosity results

The measurement of viscosities was done for propylene glycol and glycerol. Viscosity was measured for propylene glycol and glycerol samples using the Brookfield Rheometer at room temperature. The results are shown in Figure 4.23 and Figure 4.24, respectively. Ethanol was tested but was not measured correctly due to the limited capabilities of the rheometer setup for liquids with lower viscosities (such as water and ethanol).

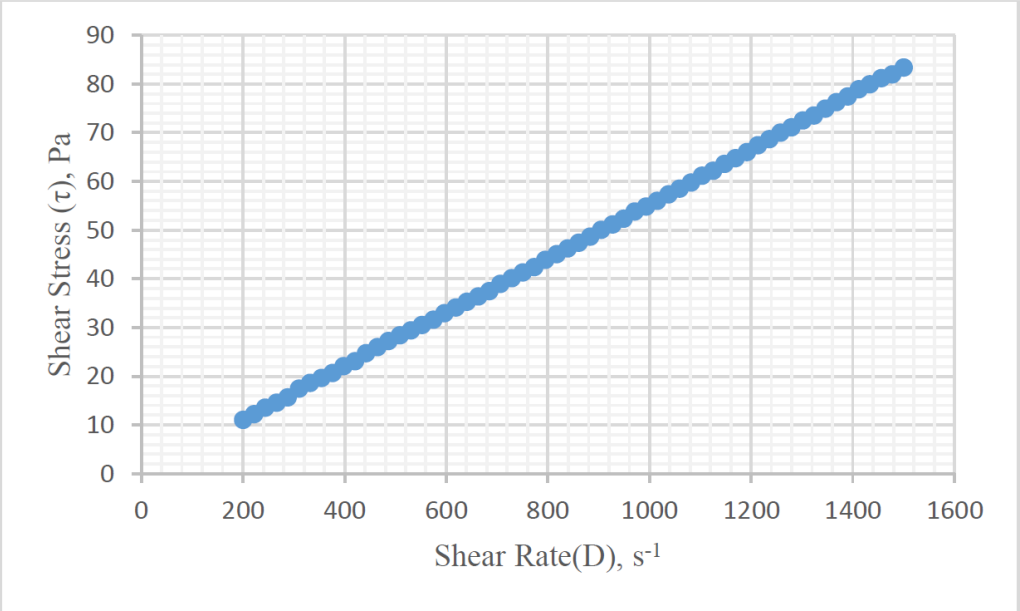

Figure 4.23: Shear Stress – Strain curve for propylene glycol

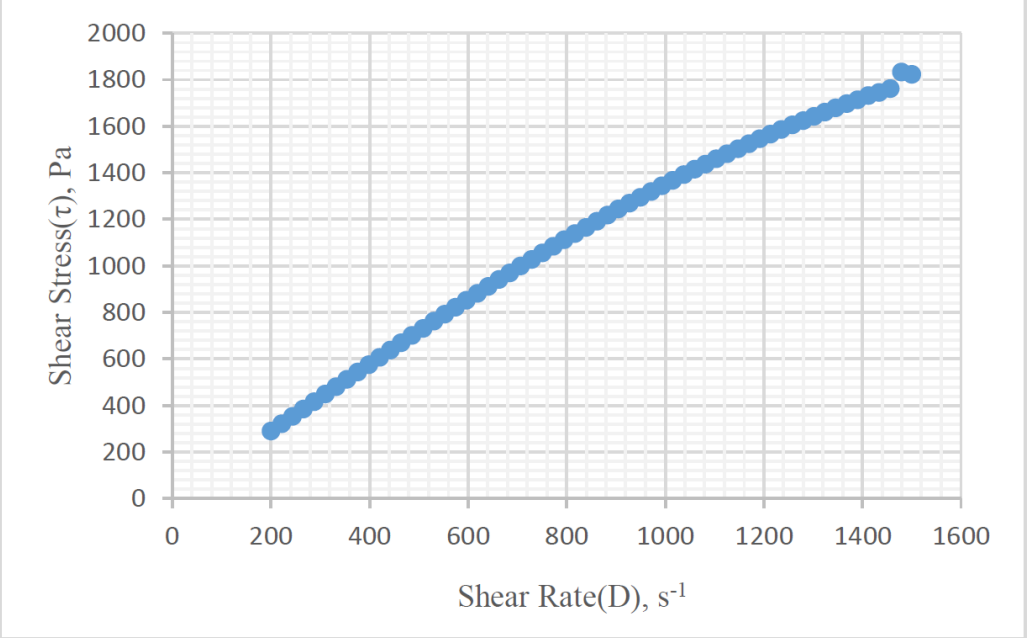

Figure 4.24: Shear Stress – Strain curve for glycerol

A comparison between the measured values of viscosities and standard values for propylene glycol and glycerine are mentioned in Table 4-4.

Table 4-4: Viscosities of glycerol and propylene glycol

Liquids	**Experimental value (Pa s)**	**Standard value (Pa s)**
Glycerol	1.366	0.950
Propylene Glycol	0.055	0.042

For the density measurement, 50 cc of each sample was weighed in an electronic balance to measure the mass in grams. As the sample was taken in a measuring flask, the weight of the flask was zeroed prior to taking the measurement. Three consecutives measurements were done, from which the average value of density was estimated (Table 4-5).

Table 4-5: Densities of Ethanol, Glycerol, and Propylene Glycol

Liquids	**Experimental value (g/cc)**	**Standard value (g/cc)**
Ethanol	0.783	0.789
Glycerol	1.1772	1.261
Propylene Glycol	0.956	1.036

Based on the above obtained results for dynamic viscosities and densities of each of the fluids, the next step targeted the development of mixtures to mimic the physical properties of blood. For a mixture, the overall dynamic viscosity, μ, was calculated theoretically using the formula employed in the work of Kendall [219], stated as:

$$\sqrt[3]{\mu} = \chi_a . \sqrt[3]{\mu_a} + \chi_b . \sqrt[3]{\mu_b} \tag{4.18}$$

where χ_a is the mole fraction of the component a, χ_b is the mole fraction of the component b, μ_a is the dynamic viscosity of the component a, and μ_b is the dynamic viscosity of the component b. Based on this mixture formula, two mixtures which approximated to the criterion of overall density as 1.06 g/cc (density of blood [220]) and dynamic viscosity as 3-4 mPa.s (viscosity of blood [221]) were of propylene glycol/ethanol (0.68 and 0.32 mole fractions, respectively) and propylene glycol/distilled water (0.26 and 0.74 mole fractions, respectively). Viscosities (Figure 4.25 and Figure 4.26, Table 4-6) and densities for both the mixtures were measured.

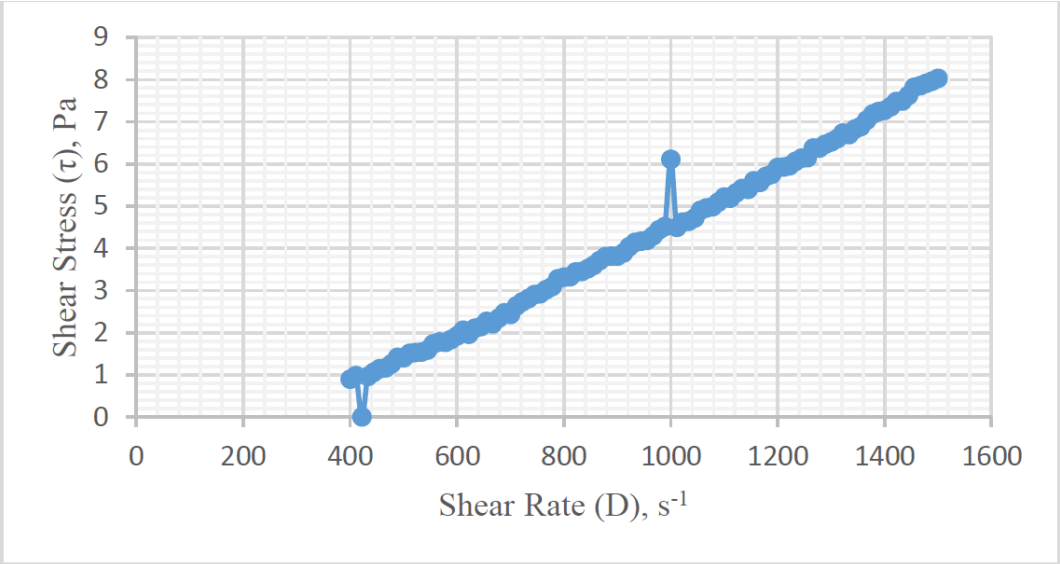

Figure 4.25: Shear Stress – Strain curve for propylene glycol/ethanol mixture

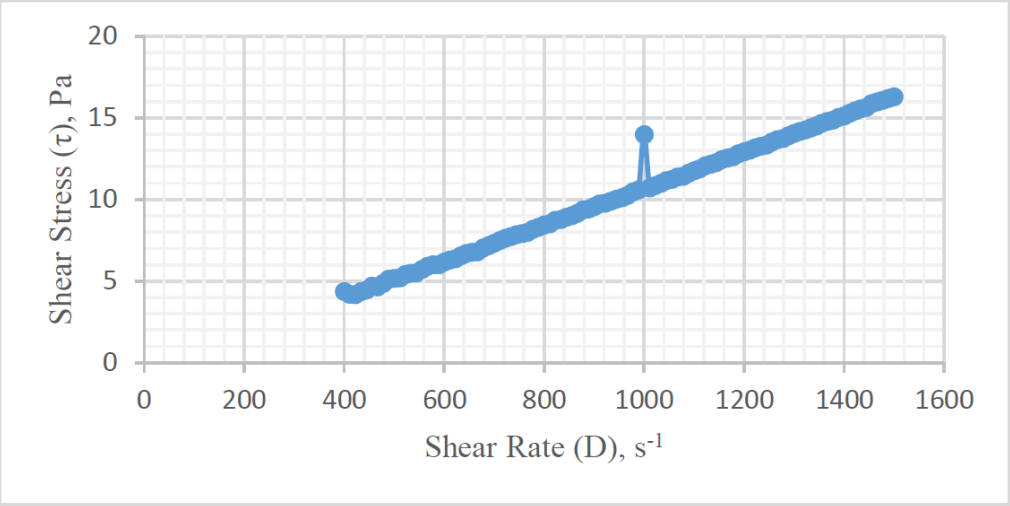

Figure 4.26: Shear Stress – Strain curve for propylene glycol/distilled water mixture

Table 4-6: Calculated and measured viscosities of the mixtures

Mixtures	**Calculated viscosity (mPa.s)**	**Measured viscosity (mPa.s)**
Propylene Glycol/Ethanol	3.02	4.18
Propylene Glycol/Distilled Water	5.159	5.43

The results of the density measurements were 0.88 g/cc for the propylene glycol/ethanol mixture and 1.02 g/cc for the propylene glycol/distilled water mixture.

4.3.3 Coaxial Probe results

With the density and the viscosity values for both mixtures measured, they were tested for their dielectric response using the setup defined in section 4.2.3. The results are shown in Figure 4.27 and Figure 4.28 for propylene glycol/ethanol and propylene glycol/distilled water mixtures, respectively.

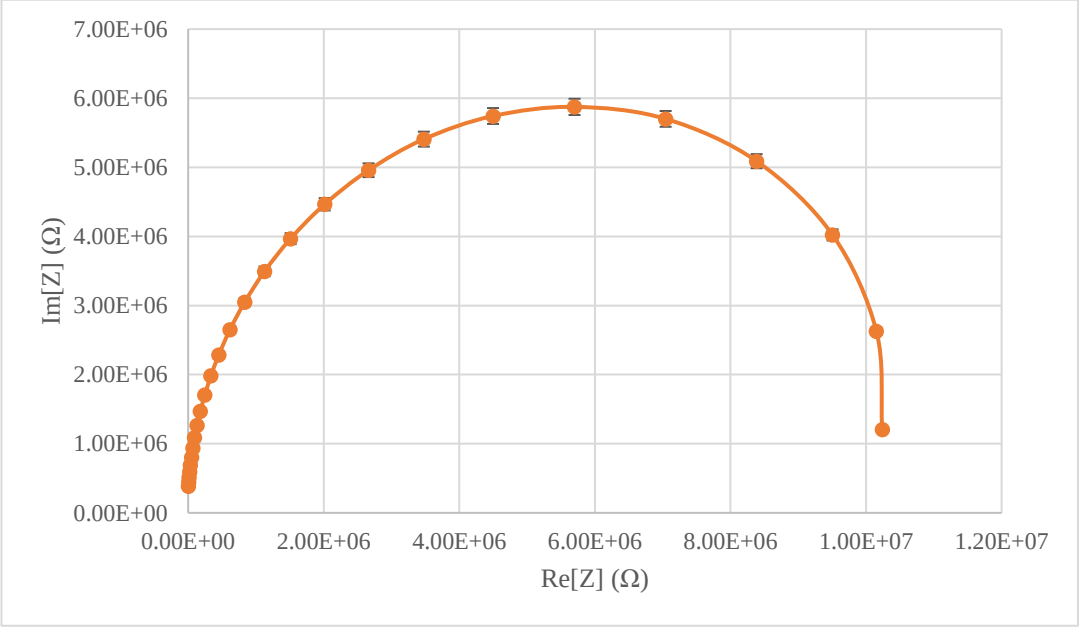

Figure 4.27: Cole plot for propylene glycol/ethanol mixture within 1kHz – 2MHz. The error bars show the range of deviation from the average of two measurements.

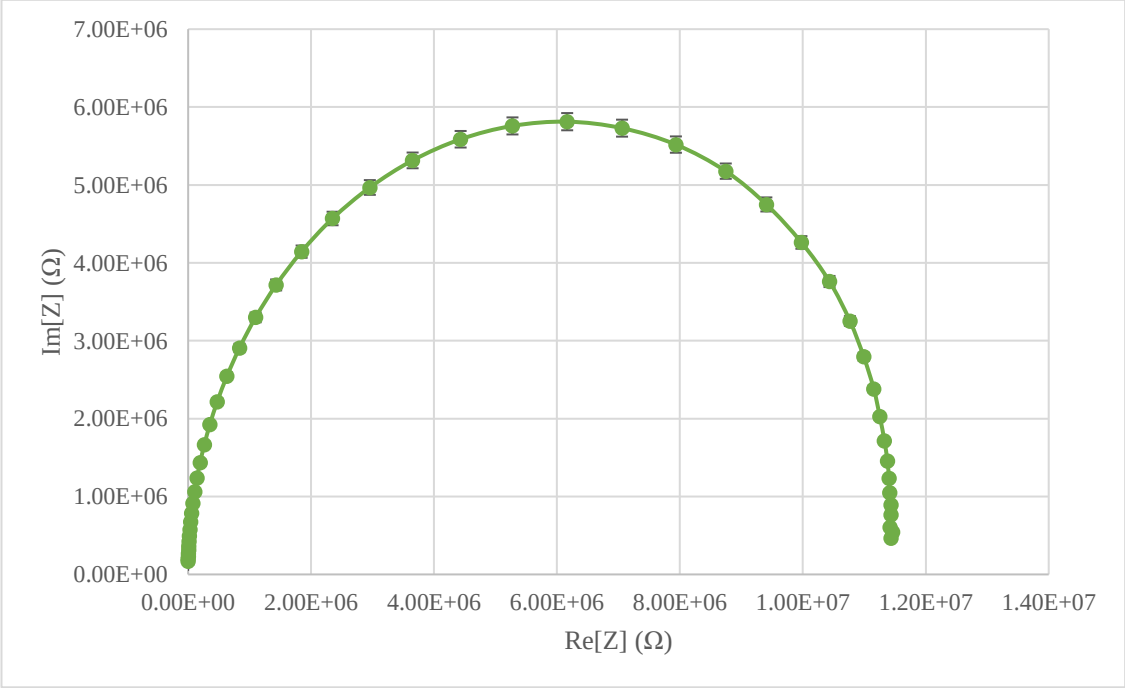

Figure 4.28: Cole plot for propylene glycol/distilled water mixture within 1kHz – 2MHz. The error bars show the range of deviation from the average of two measurements.

The measure of impedance response for the mixture reflected very high magnitudes of resistance and reactance, thereby arising a need to modify the composition of the mixture.

After calibrating the coaxial electrode setup, mixtures with different concentrations and ratios of propylene glycol in water were tested to try to better mimic the dielectric properties of blood.

An increase in conductivity was brought about by using a NaCl solution instead of distilled water. The concentration of NaCl was also investigated. After several trial and error measurements, a mixture with 80% propylene glycol and 20% 4 M NaCl solution was found to exhibit dielectric properties close to those of blood (Figure 4.29, Figure 4.30 and Figure 4.31).

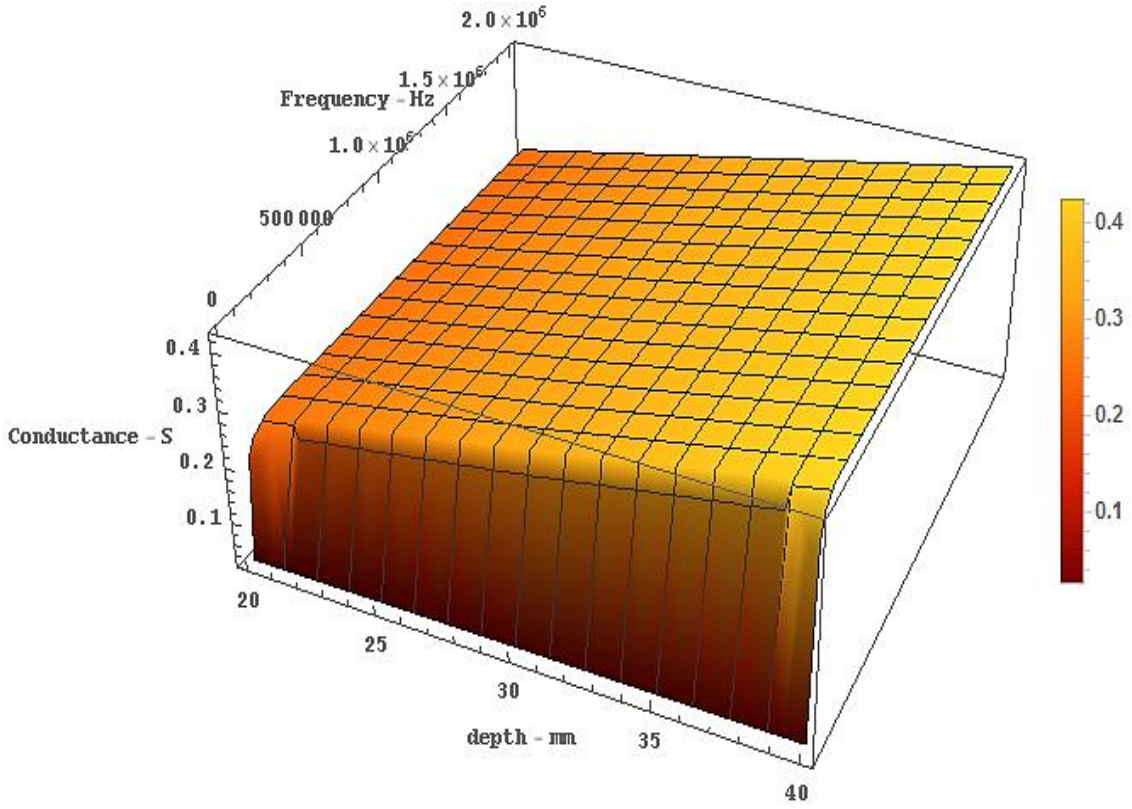

Figure 4.29: Interpolated conductance plot for the identified mixture at different depths

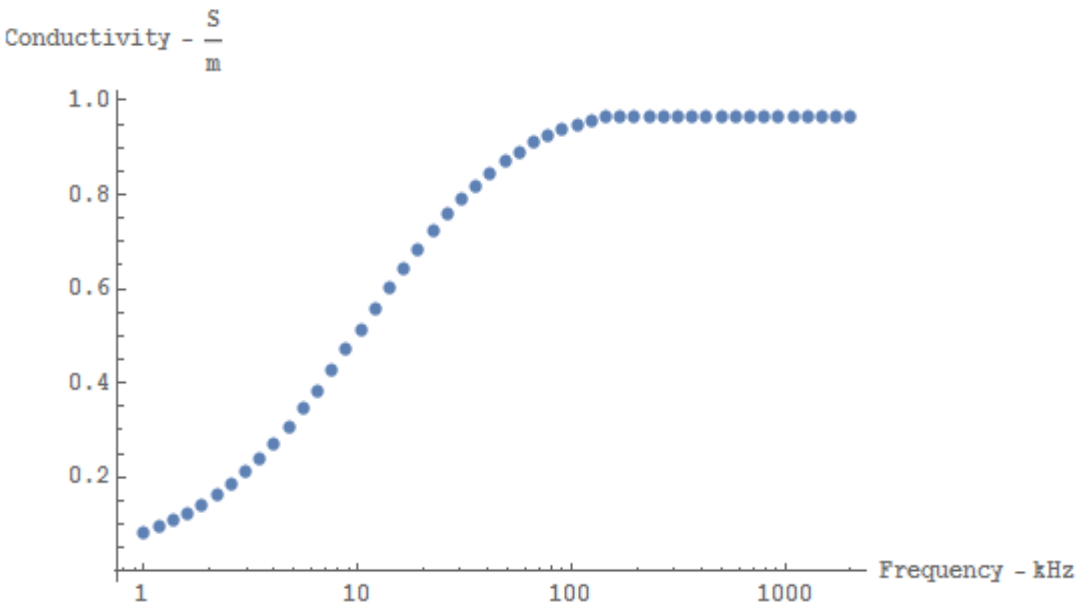

Figure 4.30: Log plot for conductivity of the identified solution

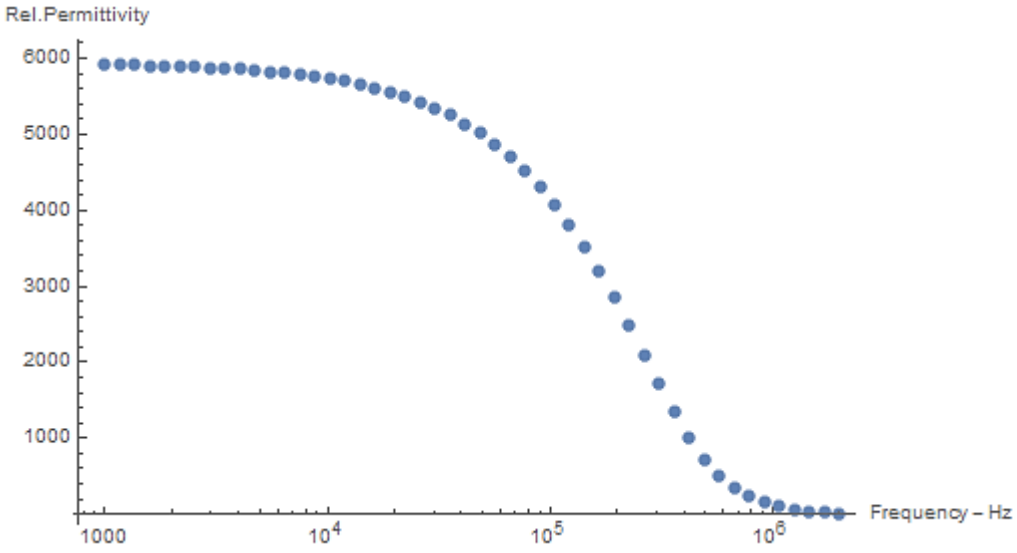

Figure 4.31: Relative Permittivity for the identified solution

The calculated values of conductivity and permittivity deviate slightly from those compiled by Gabriel [144], but more importantly approximate a similar dielectric behaviour. A comparison of these values can be observed in Figure 4.32 and Figure 4.33, respectively. The value of conductivity of the solution was found to vary from 0.1 – 1.1 S/m whereas that of relative permittivity varied between 5918-13 within the frequency range of 1 kHz – 2 MHz. This approximates the values compiled by Gabriel for conductivity (0.7 S/m – 1.1 S/m) and relative permittivity (5259 – 280) within the same frequency range.

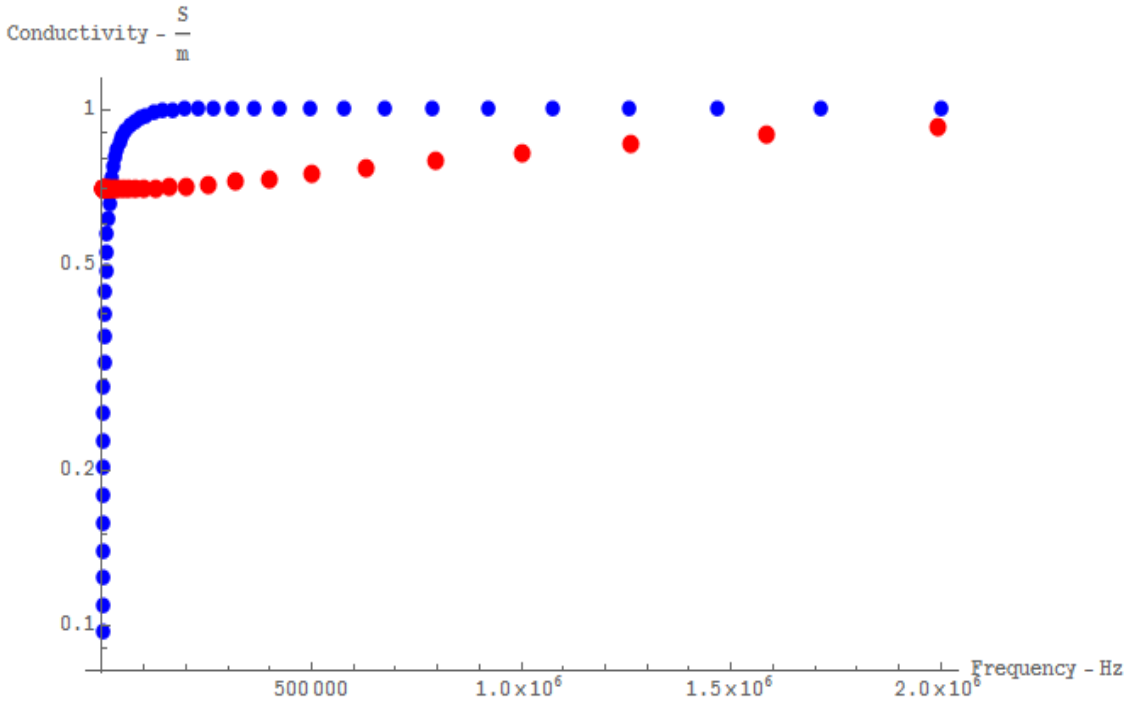

Figure 4.32: Comparison of the calculated conductivity of blood simulant with the conductivity of blood as modelled by Gabriel [144]*: ● Conductivity – solution, and ● Conductivity – blood (according to Gabriel)*

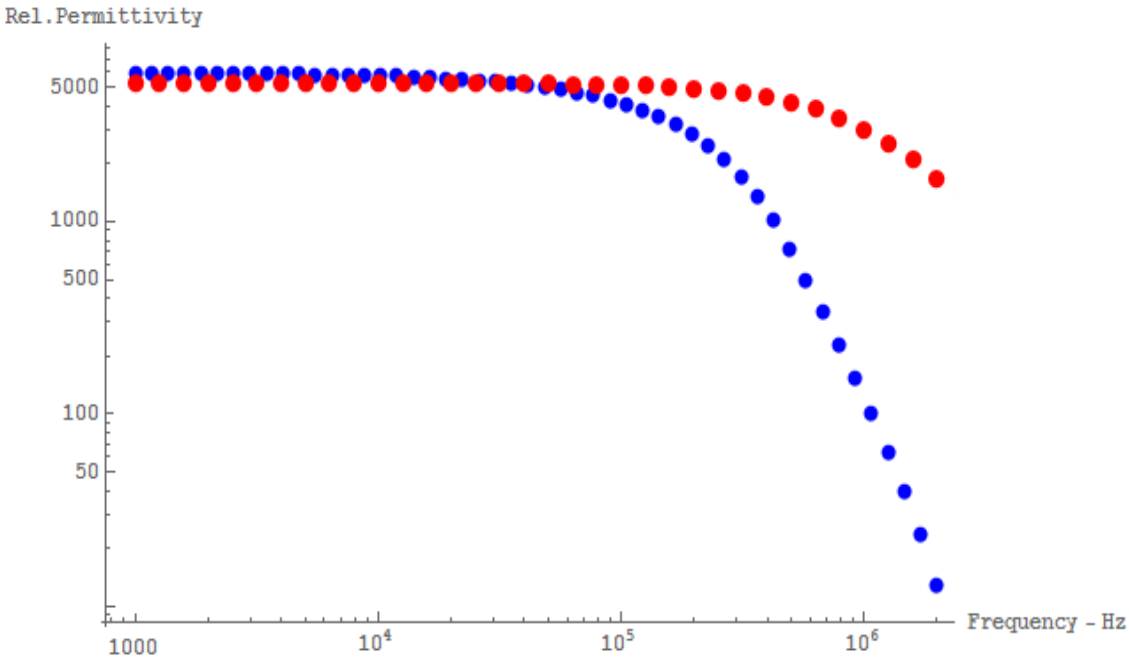

Figure 4.33: Comparison of the calculated relative permittivity of blood simulant with the permittivity of blood as modelled by Gabriel [144]*: ● Rel. Permittivity – solution, and ● Rel. Permittivity – blood (according to Gabriel)*

4.4 Fat Phantom

As was highlighted in the literature review, the electrical properties of muscle can be simulated by developing a wet phantom whereas a similar phantom with less water content can replicate fat. The choice of the materials for developing the phantoms was agar, gelatine, distilled water and NaCl with appropriate measures and modifications to obtain the desired range of corresponding conductivities and permittivities.

The principle for measuring the dielectric parameters for gelatinous suspensions was same as that of liquid mixtures. The coaxial sensor was used to measure the impedance variations at different depths for suspensions. However, the impedance measurements were made after the gelatinous suspension could set at room temperature.

4.4.1 Experimental procedure

The materials shortlisted to be used for developing a fat mimicking phantom were – agar (gelling agent), distilled water (base material) and NaCl (for ionic conductivity). The initial phantom preparation was performed in the following steps:

1. Making a saline solution (NaCl in distilled water) of known concentration. The initial concentration was chosen to be 0.001% NaCl (by weight).
2. Heating the solution to around 50°C using a magnetic stirrer hot plate (Chiltern Scientific, USA) and adding 2% (initially) Agar AR powder (J.T.Baker Chemicals, USA)
3. Boiling the solution to around 100°C using a clean glass lid to condense the evaporated water and cooling to about 50°C using a vacuum desiccator to preserve from moisture adsorption.
4. Mixing the constituents thoroughly and allowing the suspension to settle overnight for measurements at room temperature.

For the measurement of impedance using the coaxial electrode, the solution was taken after step 3 (as above) and the electrode was dipped in the hot mixture to a known immersion depth. Then the setup was allowed to stay and settle for at least 6 hours during the day or overnight for the measurements to be performed for the settled wet phantom at room temperature. The measurements were made using the LCR meter through the clip leads as for the liquid mixtures for blood phantom development.

Several trial and error measurements were performed by changing the concentration of agar within 2% - 15%. The saline solution was also altered to increase the conductivity with 0.001% - 0.1% NaCl (by weight). After several trials, a composition of 0.05% NaCl solution with 5% agar was found to approximate the conductivity and permittivity values of fat within the frequency range for this study.

4.4.2 Coaxial Probe results

The measurements for impedance were performed at three different depths of 25, 31 and 35 mm.

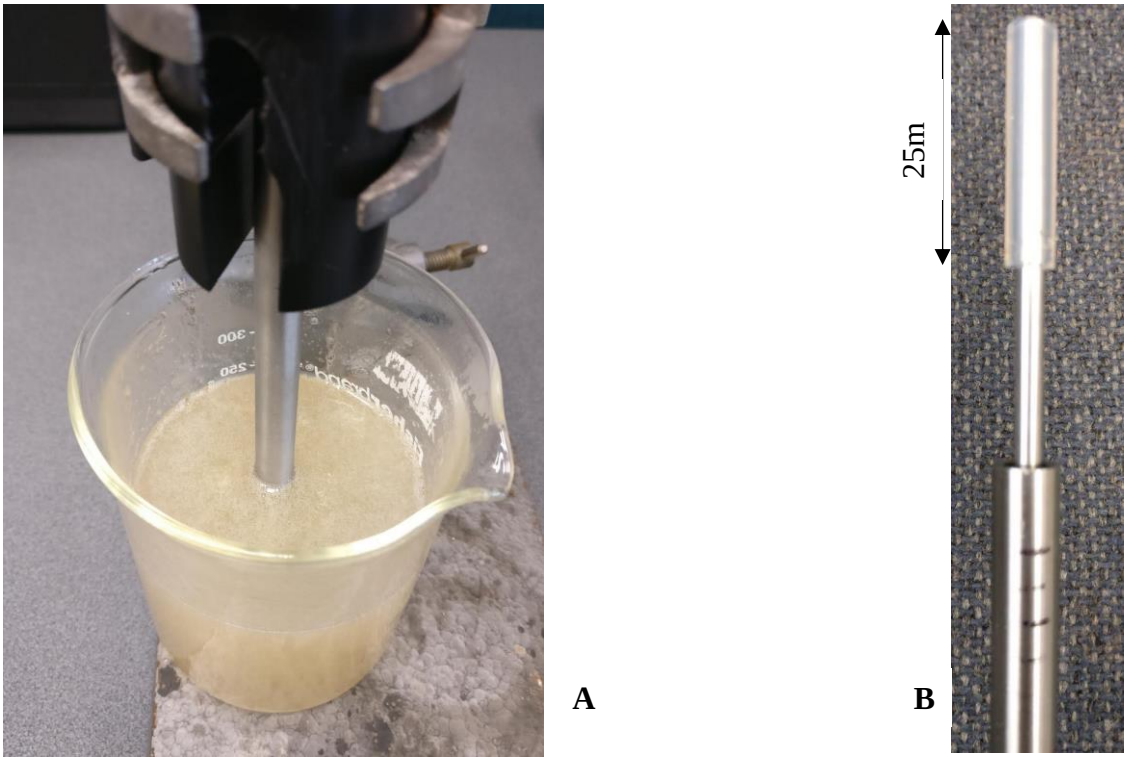

Figure 4.34: Setup for testing the fat phantom: (A): Before the suspension has settled, and (B): The settled section of phantom for a specific immersion depth (25mm)

The conductance was calculated and interpolated to calculate the continuous derivative with respect to the depth (Figure 4.35 and Figure 4.36).

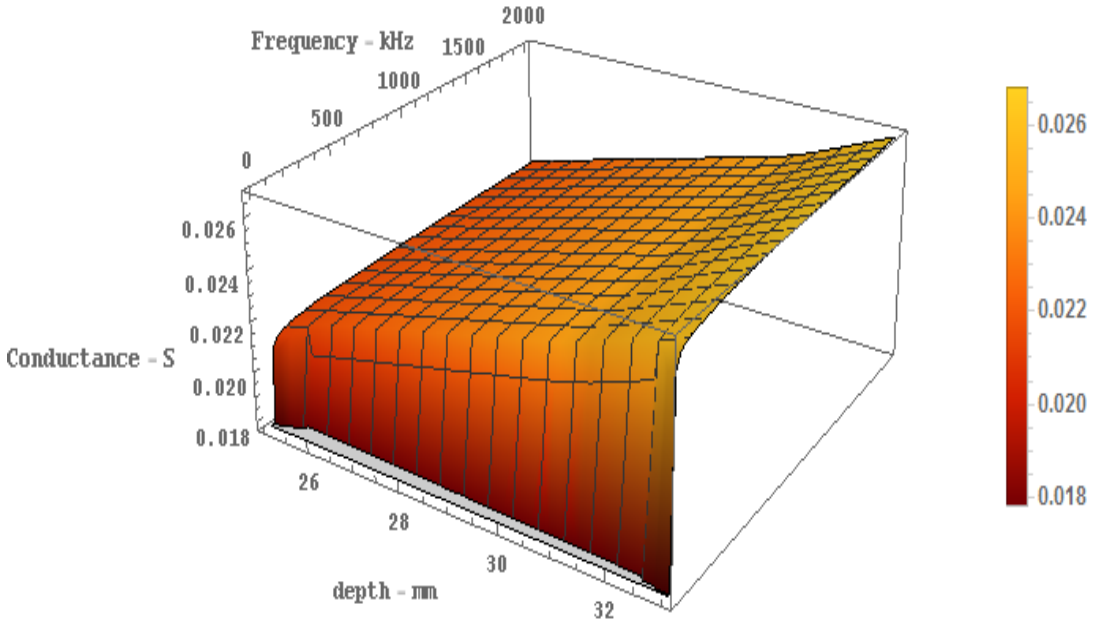

Figure 4.35: Interpolated conductance plot for the identified fat simulant

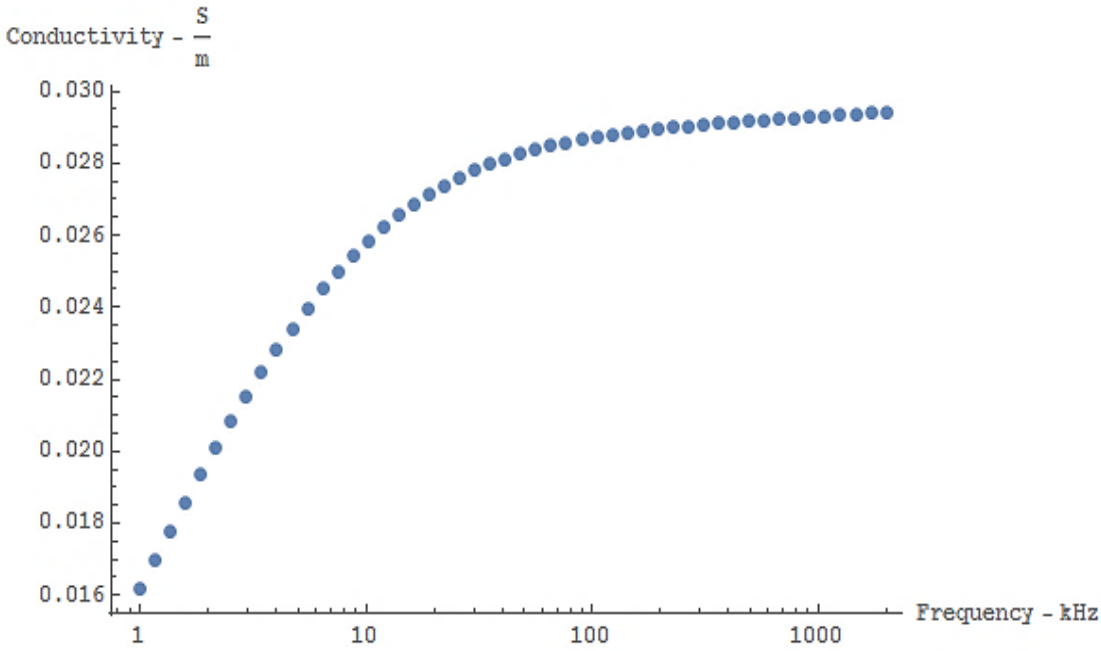

Figure 4.36: Log plot for conductivity of the fat simulant

The obtained permittivity values can be seen in Figure 4.37.

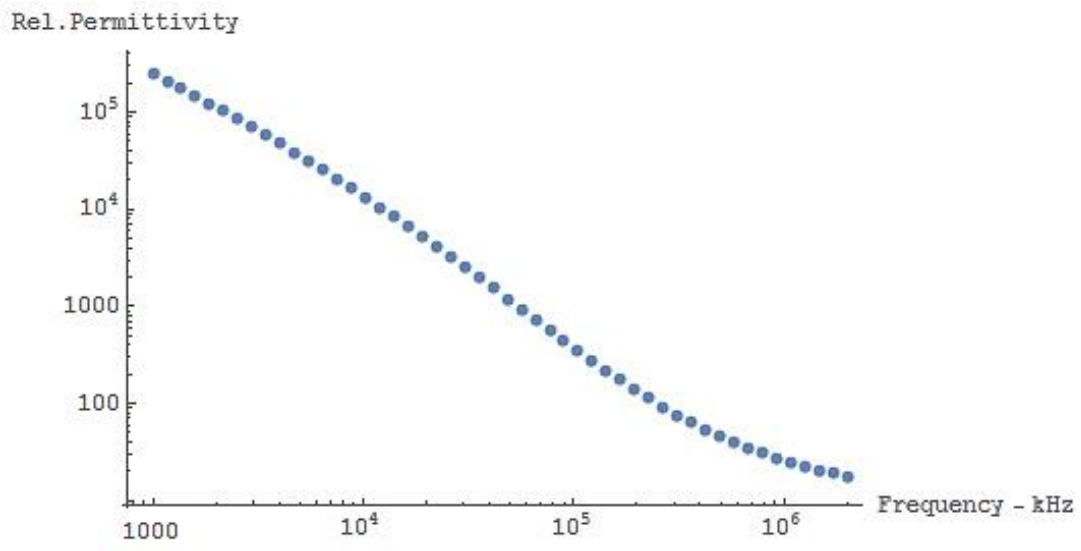

Figure 4.37: Log plot for the relative permittivity as calculated for the simulant

The calculated values were found to approximate the conductivity and permittivity of fat with good agreement with Gabriel's database. As is evident from Figure 4.38 and Figure 4.39, the similarity between the calculated values of conductivity and permittivity is high. Although there are noticeable deviations at the lower frequencies, they do not reflect a very significant effect on the overall dielectricity of the phantom.

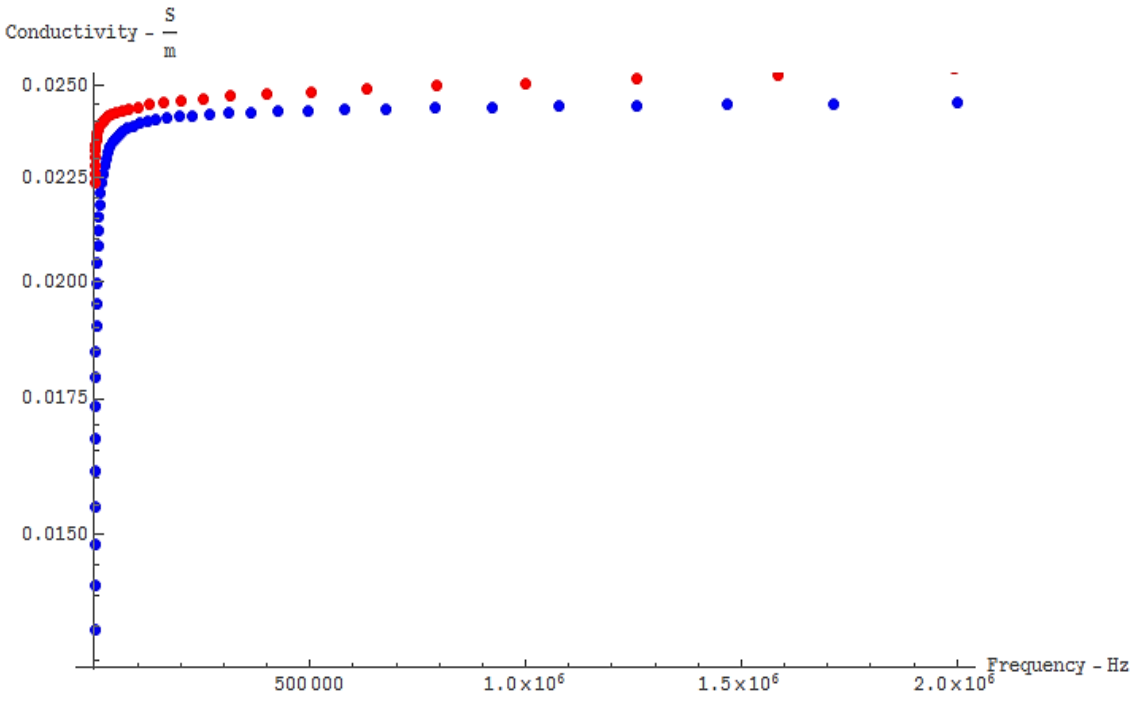

Figure 4.38: Comparison of the conductivity of the fat simulant with Gabriel's compilation of fat conductivity [144]*:* ● *Conductivity – fat simulant, and* ● *Conductivity – fat (according to Gabriel)*

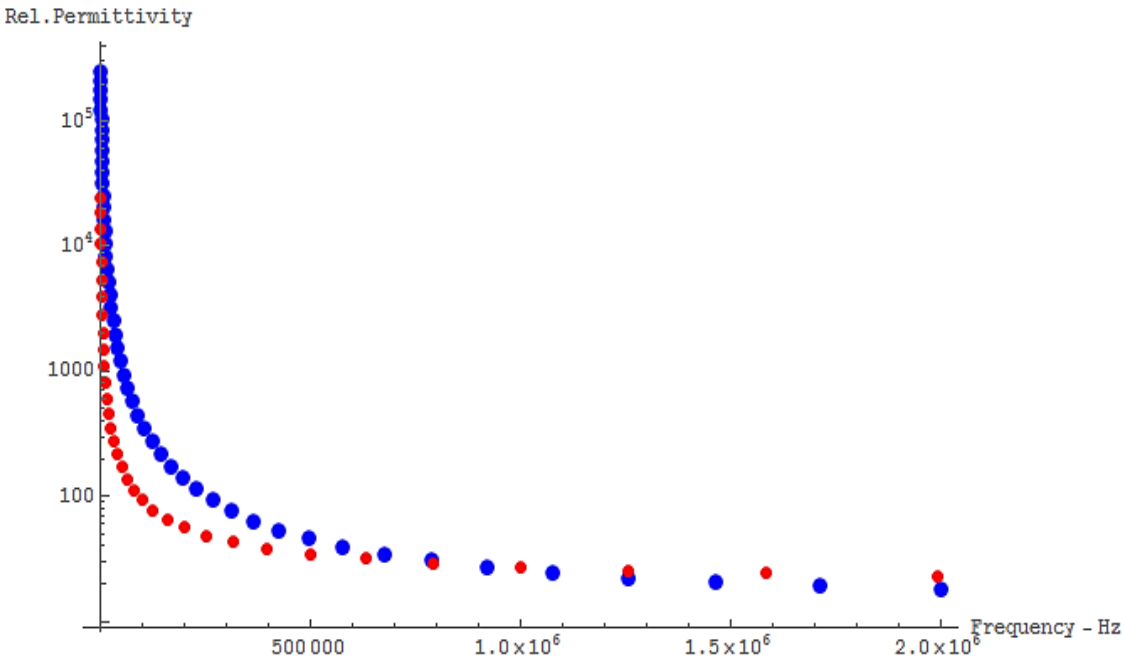

Figure 4.39: Comparison of the relative permittivity of the fat simulant with Gabriel's compilation [144]*:* ● *Rel. Permittivity – fat simulant, and* ● *Rel. Permittivity – fat (according to Gabriel)*

The deviations observed for the relative permittivity of the phantom are not negligible, however the overall trend of the permittivity spectra follows that modelled by Gabriel.

4.5 Muscle Phantom

4.5.1 Experimental procedure

As was highlighted in the literature review, the muscle simulant would essentially be a wet phantom possessing a higher conductivity than fat and a higher relative permittivity. Initially, several measurement procedures were performed using only gelatine-water phantoms, with their conductivities being altered using NaCl. The procedure for constructing the phantom was the same as that of fat. However, it was not feasible to use only gelatine as it was not able to settle when using small concentrations as required for a muscle equivalent phantom. Hence, agar was added as a gelling agent along with gelatine in variable concentrations. An initial series of experiments were performed with the concentrations of agar varying from 1–5%, gelatine from 1-5% in 1-5% saline solution. Later, propylene glycol was added to lower the permittivity and offer a Debye-type response. After several trials, the composition in Table 4-7 was found to approximate the muscle behaviour.

Table 4-7: Composition of the Muscle Equivalent Phantom

Materials	Quantity (% by weight)	Purpose
Distilled water	75.4	Base material for a wet phantom
NaCl	0.03	Increasing the ionic conductivity
Agar	3.77	Gelling agent
Gelatine	1.88	Gelling agent
Propylene Glycol	18.72	adjusting the permittivity and offering a Debye response

4.5.2 Coaxial Probe results

The impedance measurements were performed at three depths of 28, 31 and 35 mm. The conductance was calculated and interpolated as a surface (Figure 4.40) showing a linear variation in the impedance spectra of conductance with depth. The conductivity variation with frequency for the phantom was obtained as can be seen in Figure 4.41.

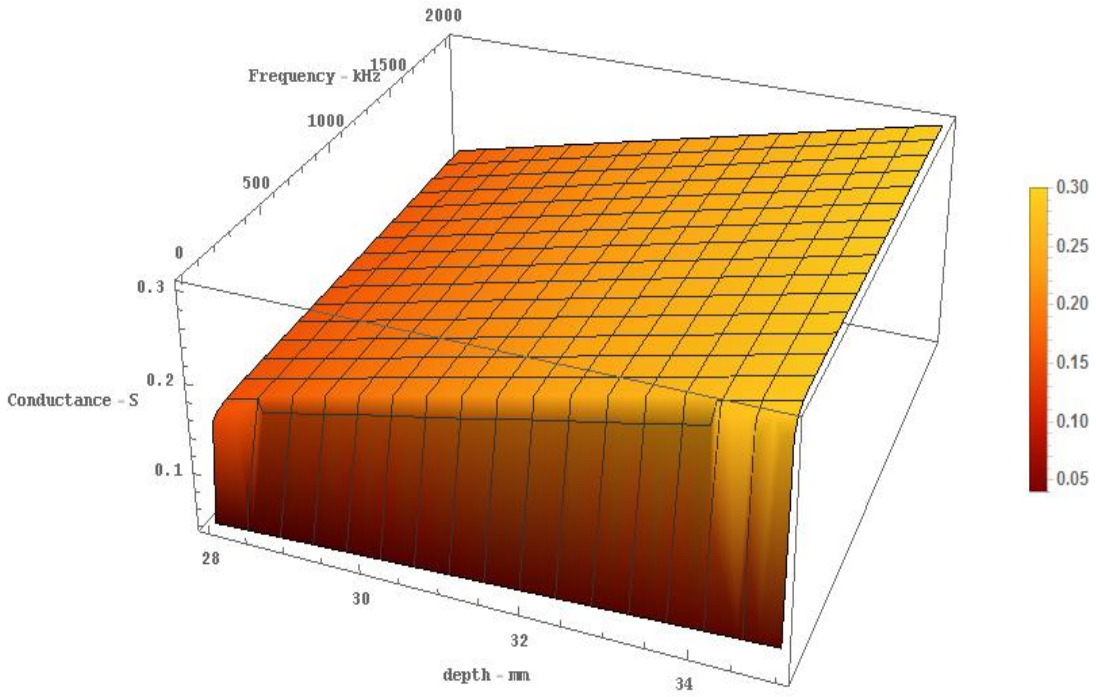

Figure 4.40: Interpolated conductance surface plot for the muscle equivalent phantom

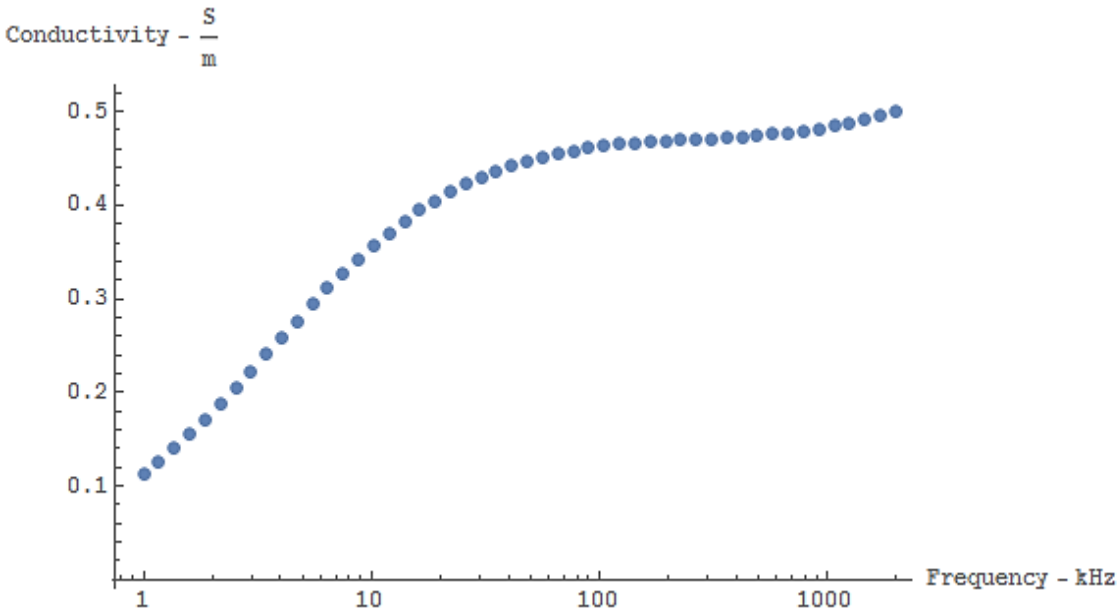

Figure 4.41: Log plot for the conductivity of the muscle equivalent phantom

The permittivity for the phantom was calculated and is shown in Figure 4.42.

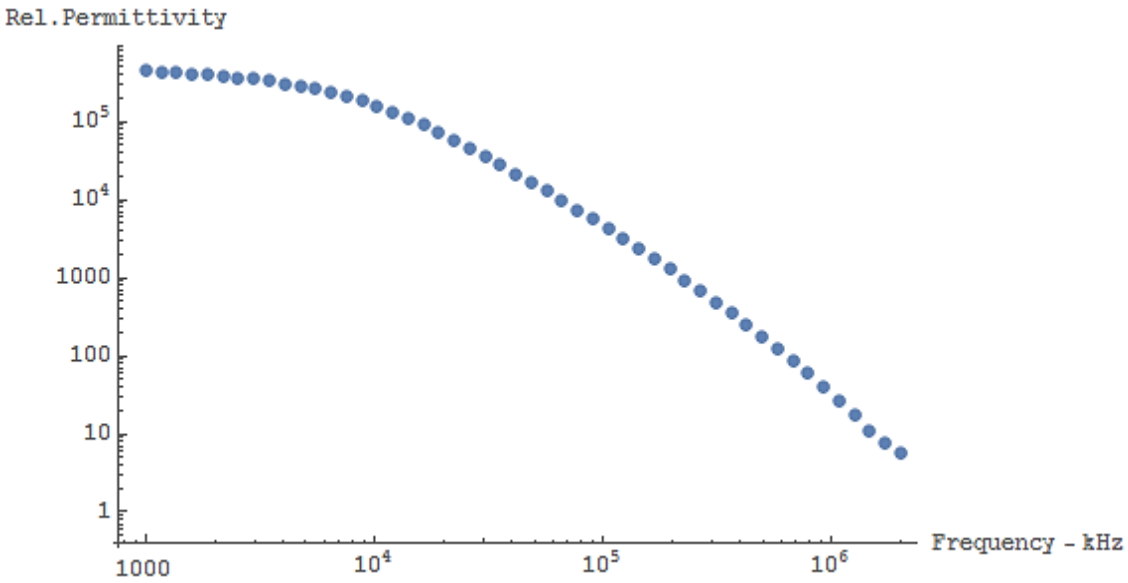

Figure 4.42: Log plot showing the relative permittivity spectrum for the muscle phantom

These obtained values were compared against Gabriel's compiled properties for muscle. Both the conductivity and the permittivity variation is observed to lie within acceptable agreement for this study. The deviation in the trend observed in Figure 4.43 and Figure 4.44 for conductivity and permittivity respectively is attributed to the different coefficient of dispersion defining the overall dielectric behaviour of muscle response. The overall range of values lie within the same range as that specified in Gabriel's compilation of dielectric properties. However, the difference in the trends is due to the different

dispersion characteristics where the literature data was parametrically modelled by Gabriel using a 4 dispersion Cole model [144].

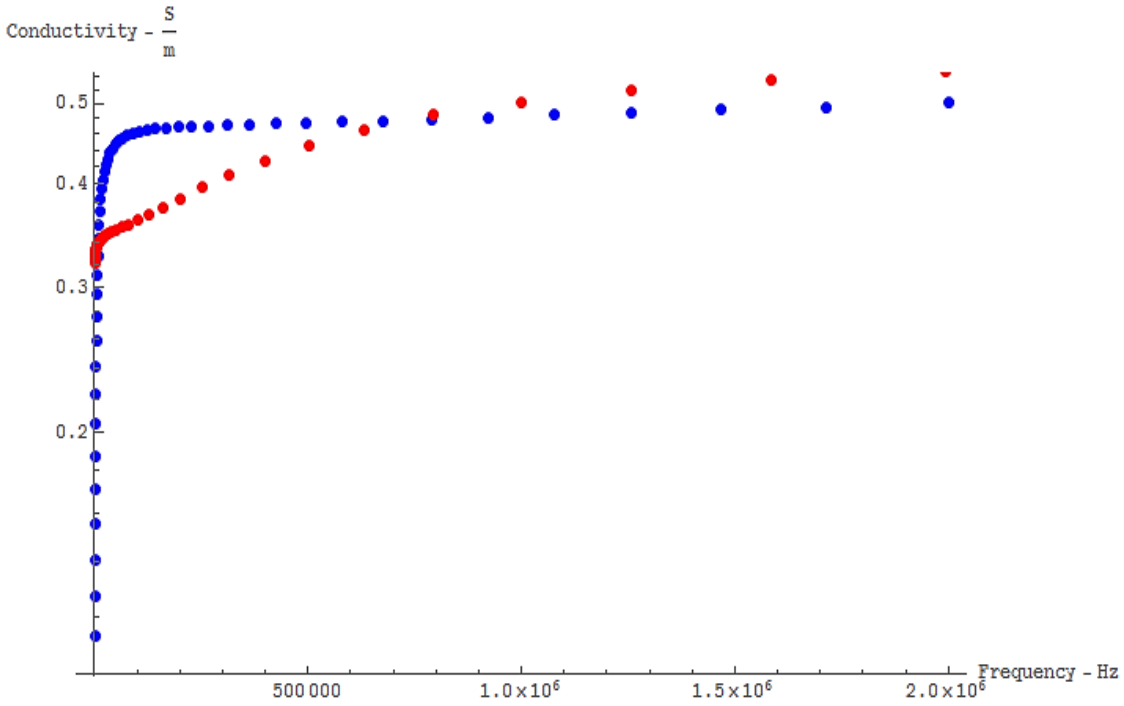

Figure 4.43: Comparison of the conductivity of the muscle phantom with Gabriel's compilation of muscle conductivity [144]*: ● Conductivity – muscle simulant, and ● Conductivity – muscle (according to Gabriel)*

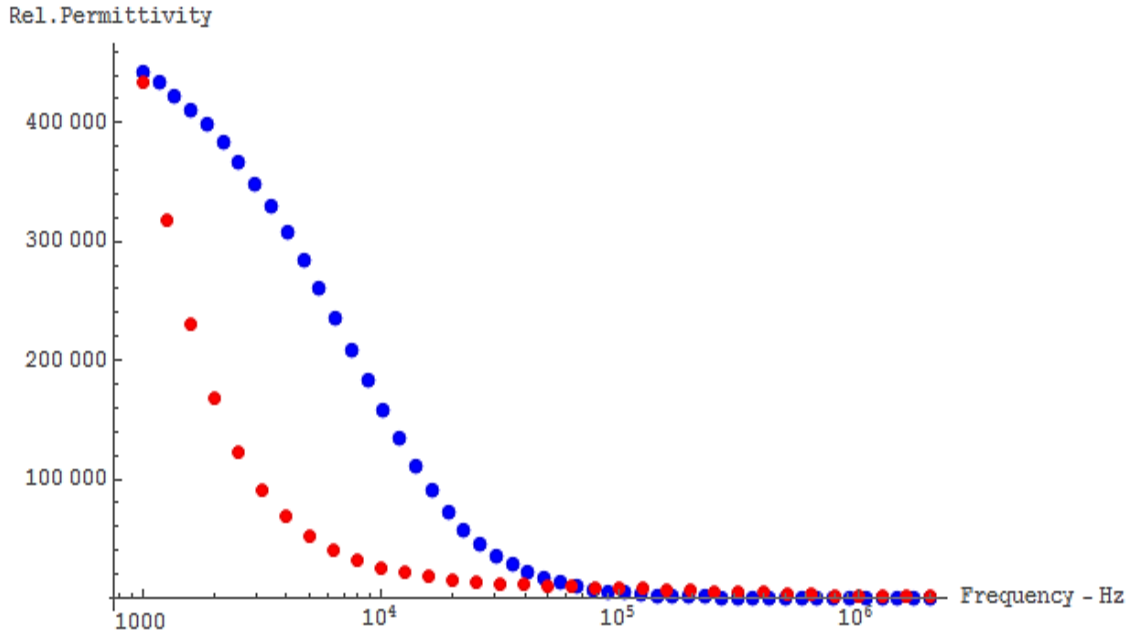

Figure 4.44: Comparison of the relative permittivity of the muscle phantom with Gabriel's compilation of muscle permittivity [144]*: ● Rel. Permittivity – muscle simulant, and ● Rel. Permittivity – muscle (according to Gabriel)*

4.6 Human Forearm Phantom

This section describes the development of a human forearm section phantom using the materials identified in the previous sections as simulants for each type of tissue. As was the case in the simulation study (Chapter 3), only three tissue domains were considered and constructed: fat, muscle and artery. The phantom was designed to mimic the approximate anatomy and similar dielectric properties to the human forearm. Simulation of the mechanical properties of the tissue layers was beyond the scope of this study. The phantom development and subsequent measurements were carried out it the following steps:

1. Choosing the approximate dimensions of each tissue layer based on literature data and simulation study.
2. Designing and fabricating suitable moulds for producing the phantom in the desired shape and size.
3. Measuring the impedance of individual tissue layers produced using a test mould to verify the dielectric response.
4. Constructing the final phantom as a forearm section constituting all the three layers.
5. Measuring impedance from the phantom
6. Comparing these results with simulation

4.6.1 Mould fabrication

Based on the dimensions of each tissue layer used in the simulation, a forearm phantom was developed using the materials described in the previous sections.

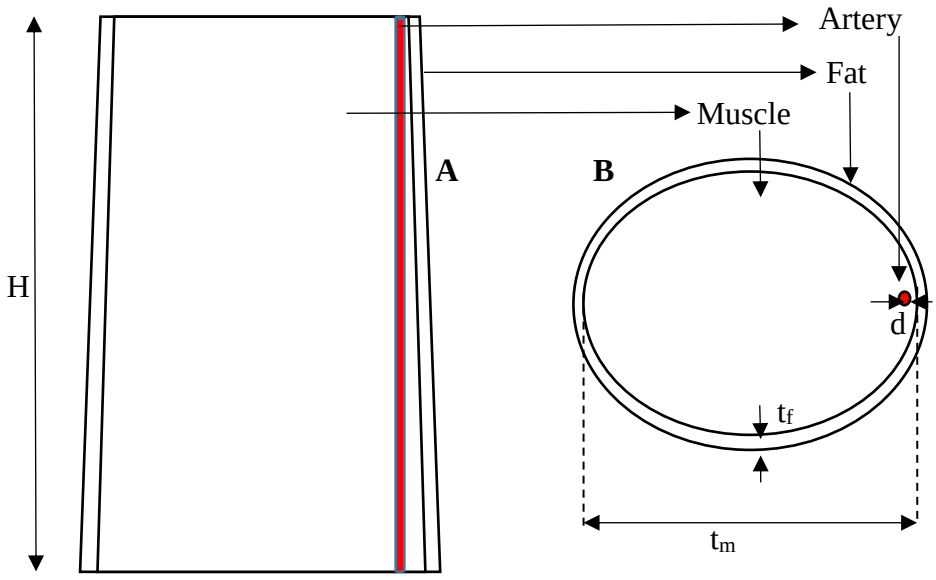

Figure 4.45: (A): Longitudinal and (B): top view schematics for the dimensions of the forearm phantom

Figure 4.45 shows the dimensions of the forearm phantom. The values of the dimensions are shown in Table 4-8.

Table 4-8: Phantom dimensions for each tissue layer for Box and Forearm phantom development

Tissues	**Forearm Phantom**	
	H	$t_f/t_m/d$
Fat	70mm	3 – 4mm
Muscle	70mm	20 - 25mm
Artery	70mm	2.3, 2.35 and 2.4mm

These dimensions were decided based on the values of thickness of fat, muscle and radial artery diameter in the human forearm reviewed in section 3.3. 3D CAD geometry was created using Autodesk Fusion 360 (Autodesk®, USA). Mould sets were designed to enable casting of each of the tissue layers, along with three different diameters of the radial artery. The moulds for each part were 3D printed using nylon-66. The mould for constructing the forearm phantom consisted of three parts: the outer shell, the inner shell and a solid cylindrical tube. The outer shell was closed at one end to hold the gel material and allow it to set. The outer shell along with the inner shell were used to mould the fat

tissue, the inner shell and the cylindrical tube were used to mould the muscle tissue and the hollow section left after removing the solid tube was used as the arterial domain (Figure 4.46).

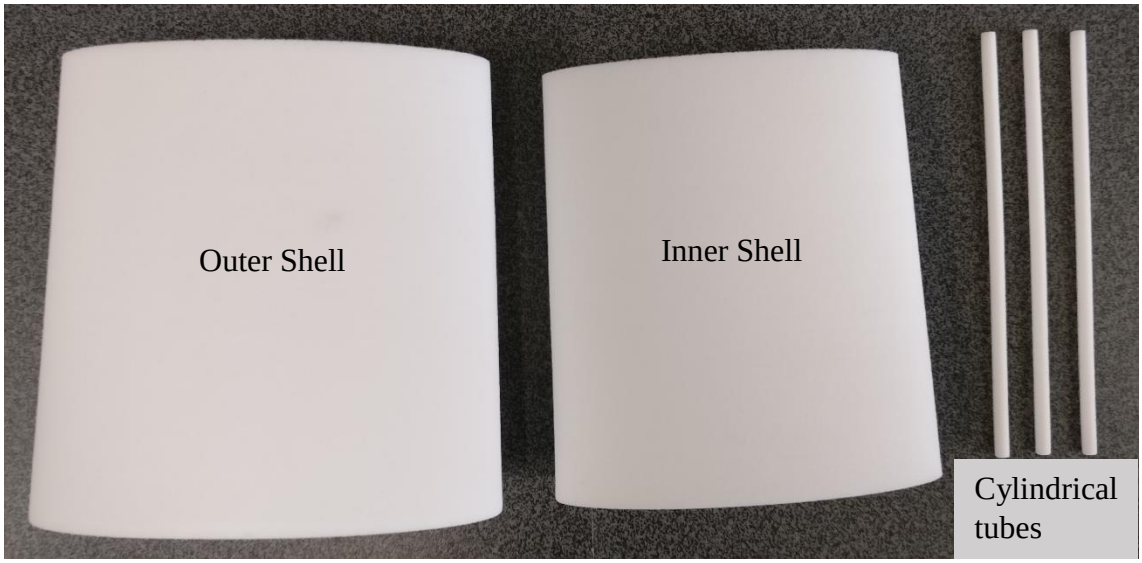

Figure 4.46: Parts of the mould for constructing the forearm phantom

All the parts of the mould were used in conjunction as shown in Figure 4.47. Region 'A' was used to fabricate the fat tissue of thickness varying between 2.5 – 3.5 mm and region 'B' was used to mould the muscle simulant with a thickness variation of 15 – 25 mm. After the cylindrical tube (for artery) was taken out once the muscle and fat tissue layers were set, it left behind region 'C' into which was poured the blood simulant. The dimensions of each of the parts took into consideration the tolerance for each tissue layer. The three cylindrical tubes that were used to preserve the space for the phantom arterial had diameters of 2.3 mm, 2.35 mm and 2.4 mm. As such, three setups were arranged to construct three phantoms for three arterial diameters.

Before using the mould, the outer shell was covered with baking paper on the inside surface to prevent sticking of the phantom to the inside wall of the mould. The outer surface of the inner shell was covered with plastic food wrap to easily take the inner mould out after the fat tissue phantom set. Blood simulant was introduced carefully through a sterilised syringe to prevent overflow.

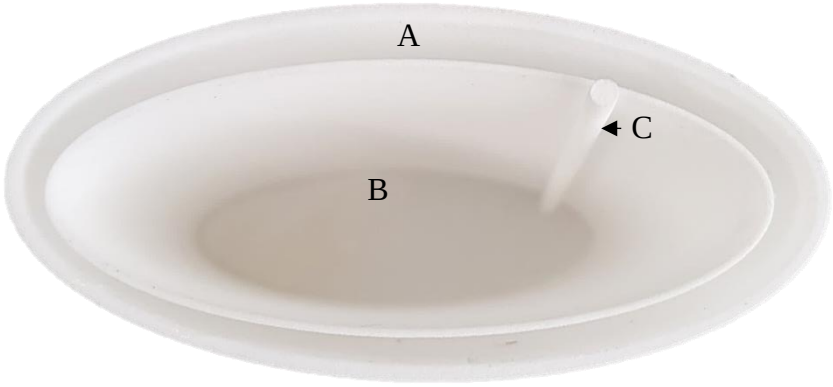

Figure 4.47: Mould setup for constructing the forearm phantom showing regions A, B and C

The mid-process state of the phantom construction is shown in Figure 4.48. The fat and the muscle layers can be seen almost settled with the cylindrical section in place which would make the region available for the blood simulant after being taken out. The baking paper can be seen in place to prevent the phantom from adhering to the inside wall of the mould.

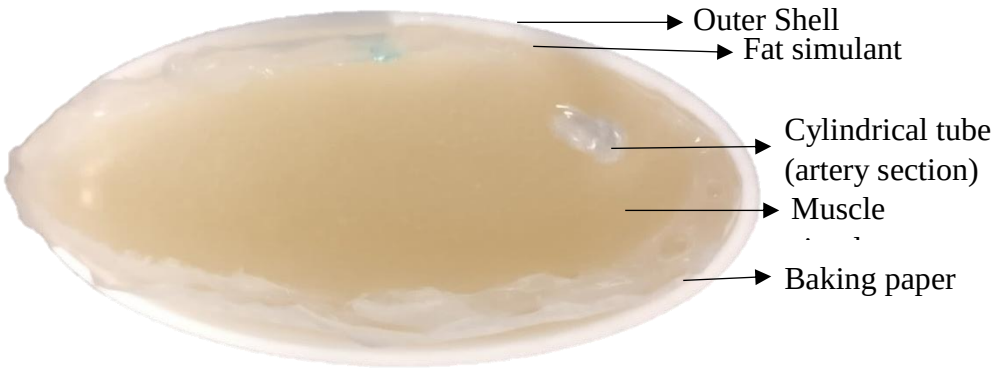

Figure 4.48: Fat and Muscle tissue simulants settled inside the mould

The final constructed phantom can be seen in Figure 4.49.

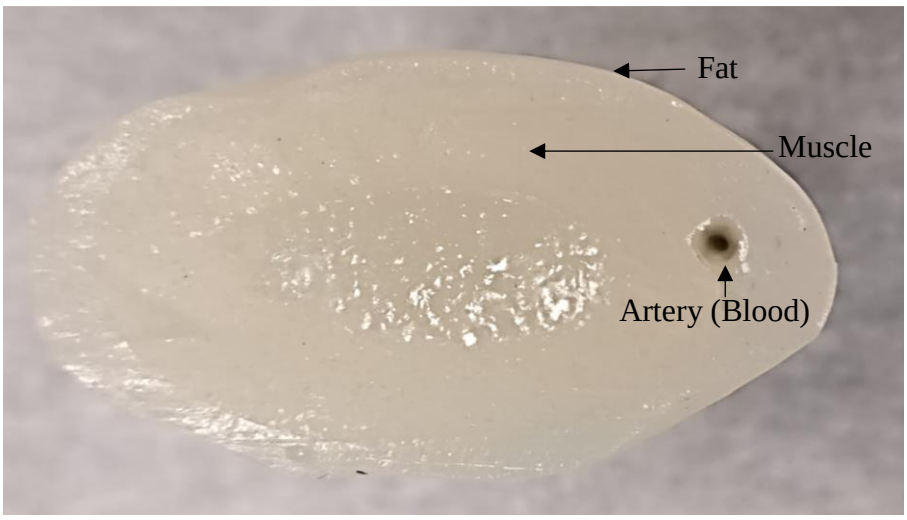

Figure 4.49: Human forearm section phantom – top view

4.6.2 Results

Measurements on the forearm phantom using the Quadra measurement system were taken to mimic the simulation model. As was mentioned before, the forearm phantom was designed to simulate the behaviour at three arterial diameters. Figure 4.50, Figure 4.51 and Figure 4.52 show the relative plots for the real part of measured impedance with frequency, imaginary part of the measured impedance with frequency and the Cole- Cole behaviour, respectively, for the forearm phantom at all three diameters. The obtained Cole parameters for all three diameters after model fitting are provided in Table 4-9.

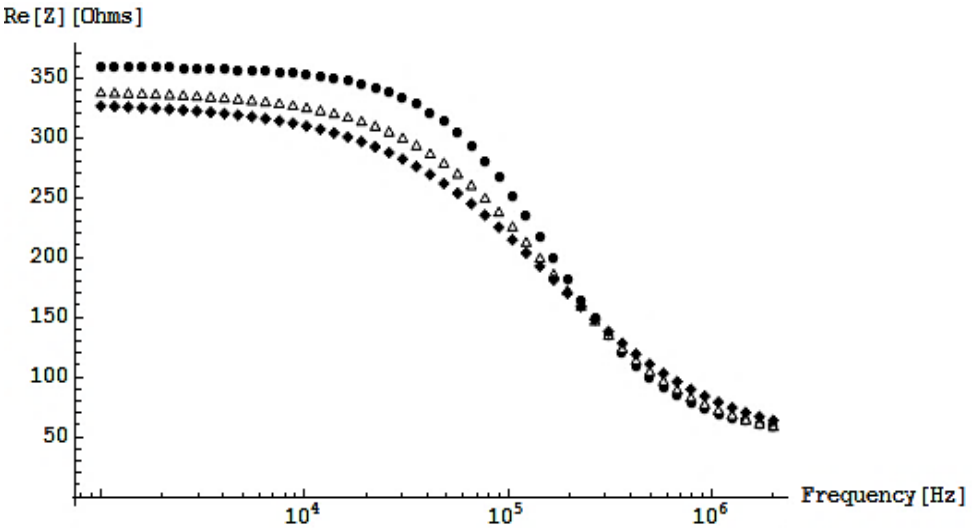

Figure 4.50: Re[Z] vs Frequency plot for the forearm phantom at the three diameters: • 2.3 mm, ▵ 2.35 mm, and ♦ 2.4 mm

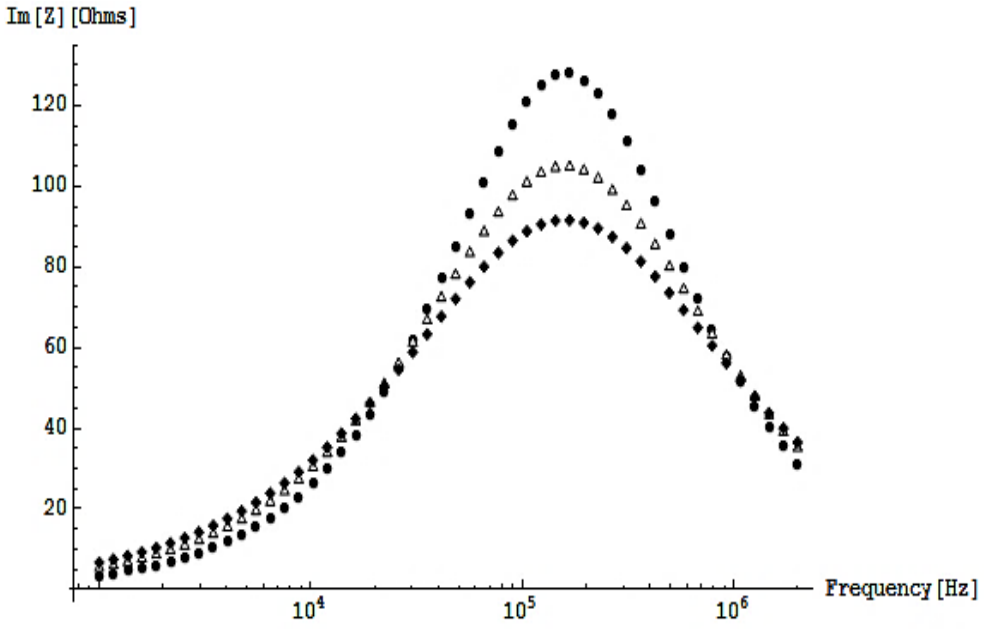

Figure 4.51: Im[Z] vs Frequency plot for the forearm phantom at the three diameters: • 2.3 mm, ▵ 2.35 mm, and ♦ 2.4 mm

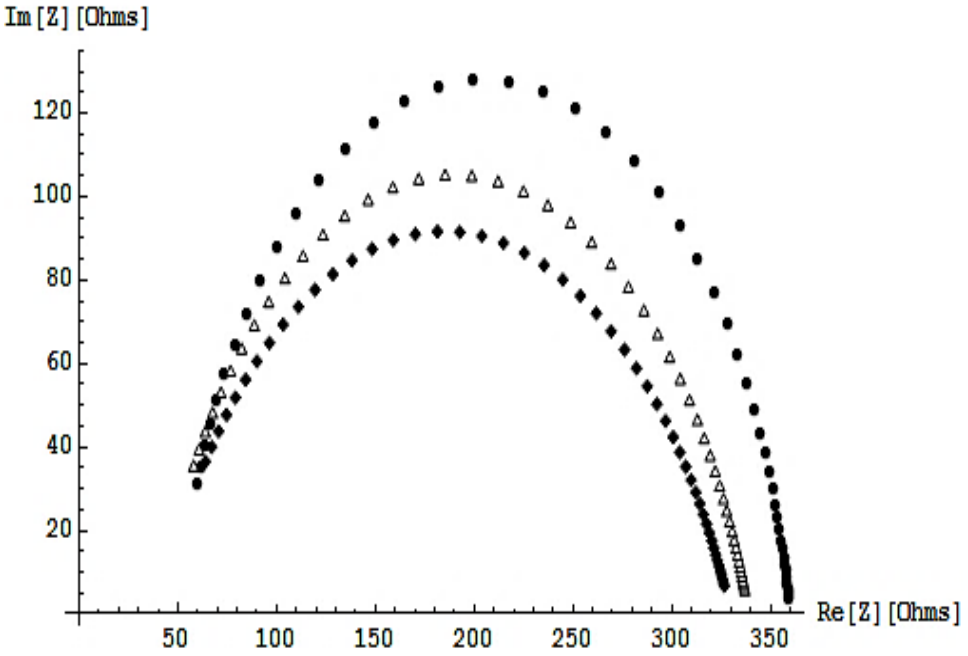

Figure 4.52: Cole plot for the forearm phantom at all three diameters: • 2.3 mm, ▵ 2.35 mm, and ♦ 2.4 mm

Table 4-9: Cole Parameters for the forearm phantom for all three diameters

Diameter (mm)	R_0 (Ω)	R_∞ (Ω)	τ (sec)	α
2.3	361.15	50.1	1.12×10^{-6}	0.87
2.35	339.113	39.98	1.21×10^{-6}	0.78
2.4	332.4	41.32	1.1×10^{-6}	0.72

4.7 Discussion

4.7.1 Blood Phantom

The choice of a suitable liquid or liquid mixture to mimic the properties of blood is not straight forward. In particular, it is difficult to mimic the non-Newtonian properties and sleeve effect of blood flow, which also affects the clustering and de-clustering of erythrocytes which in turn changes the electrical response of blood. In this study, these effects were ignored and the electrical behaviour was approximated as a liquid mixture with single or double relaxation time Debye response with homogeneity in its structural properties.

The dielectric properties of polar liquids such as alcohols, water-alcohol mixtures and alcohol-alcohol mixtures are well established in several works [222]–[229]. The electrical properties of water and lower alcohols are complicated due to their molecular network and strong hydrogen bonds. However, the dielectric relaxation process in these polar compounds is mainly approximated as a single Debye type relaxation behaviour [230]–[233]. Ethanol, propylene glycol and glycerol were chosen due to their appropriateness for simulating both the electrical and physical properties of blood. Moreover, being chemically inert to each other allowed for developing mixtures to more closely mimic the mechanical response of blood in terms of viscosity and density, while preserving an overall dielectric response showing a single relaxation Debye type behaviour.

The first stage of experiments for identifying a potential blood mimicking liquid used a two-electrode configuration connected to a two-point, four-probe measurement lead setup of an LCR meter. Although the two-electrode configuration is not the best-established method for bioimpedance measurements, it was suitable for these experiments where the objective was not only to quantify the dielectricity of chosen alcohols, but also to analyse the effects of electrode placements and separation on the overall measurements. Copper electrodes were chosen due to being easily available and providing high conductivity.

However, they had to be replaced after some iterations, repeatedly, due to electrode polarisation effects resulting in corrosion. Figure 4.20, Figure 4.21 and Figure 4.22 show the Cole plots for propylene glycol, ethanol and glycerol, respectively. From the data, it is very clear that the separation of the electrode pair affects the overall impedance measurements.

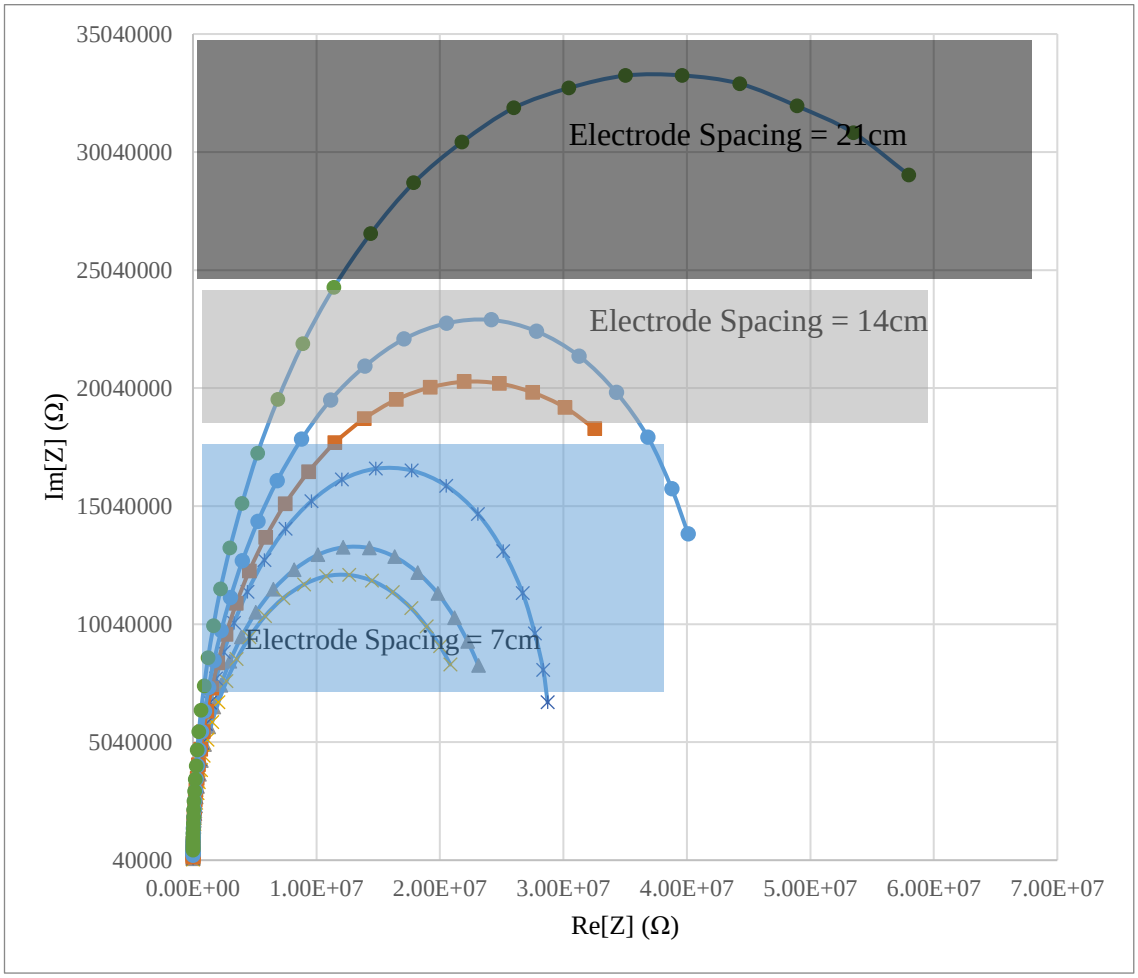

Figure 4.53: Cole plot for propylene glycol (PG) between different pairs of electrodes showing different regions with electrode separations: A-B, B-C, C-D, A-C, B-D, and A-D

Figure 4.53 shows the Cole plot for impedance at various electrode separations for propylene glycol along with the regions marking the range of impedance values for each electrode spacing. The impedance values for the electrode spacing of 7 cm were found to be much lower than those at a spacing of 14 cm which were lower than that at 21cm. Hence, the impedance was found to be increasing with increasing distance between the electrodes, as is expected. However, there is a small amount of deviation between the different configurations of electrode pairs at the same spacing. As an example, the impedance values for electrode pairs A-B, B-C and C-D were found to be lying within the same range, although the impedance increasing trend was C-D > A-B > B-C.

Resistance is well known to be dependent on the length of the material under test and hence justifies an increase in the resistive part with an increase in the electrode spacing. The imaginary part of impedance also is seen to increase. The same trend was observed in the case of ethanol and glycerol as shown in Figure 4.54 and Figure 4.55, respectively.

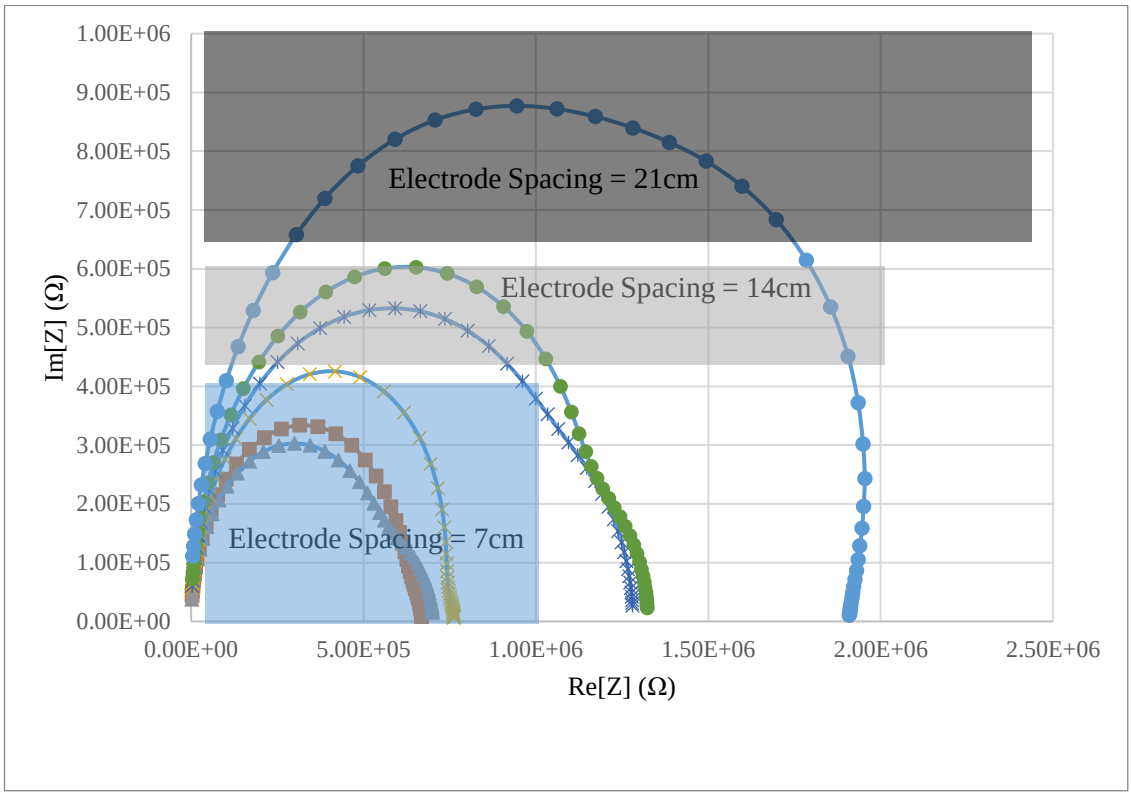

Figure 4.54: Cole plot for ethanol (ETH) between different pairs of electrodes showing different regions with electrode separations: A-B, B-C, C-D, A-C, B-D, *and* A-D

The shape of the Cole plots for all the three liquids show a proportional increase in the resistive part of the measured impedance spectra. For all the three cases, the resistance was found to increase approximately linearly with electrode spacing for each frequency. This also verifies an approximate constant conductivity at each frequency for each of the three liquids.

The other requirement for the blood mimicking fluid was similarity of dynamic viscosity and density. The three chosen liquids were tested for density and viscosity measurements. The density measurements were quite conventional, the mass of 50cc of each of the samples being measured on an electronic weighing balance of a resolution of 0.01g. The viscosity measurements were performed using two different systems offering different rotational speed range due to the very low viscosity of a liquid like ethanol and a comparatively higher viscosity of glycerol. No evidence of any chemical reaction was observed between these alcohols with each other and with distilled water.

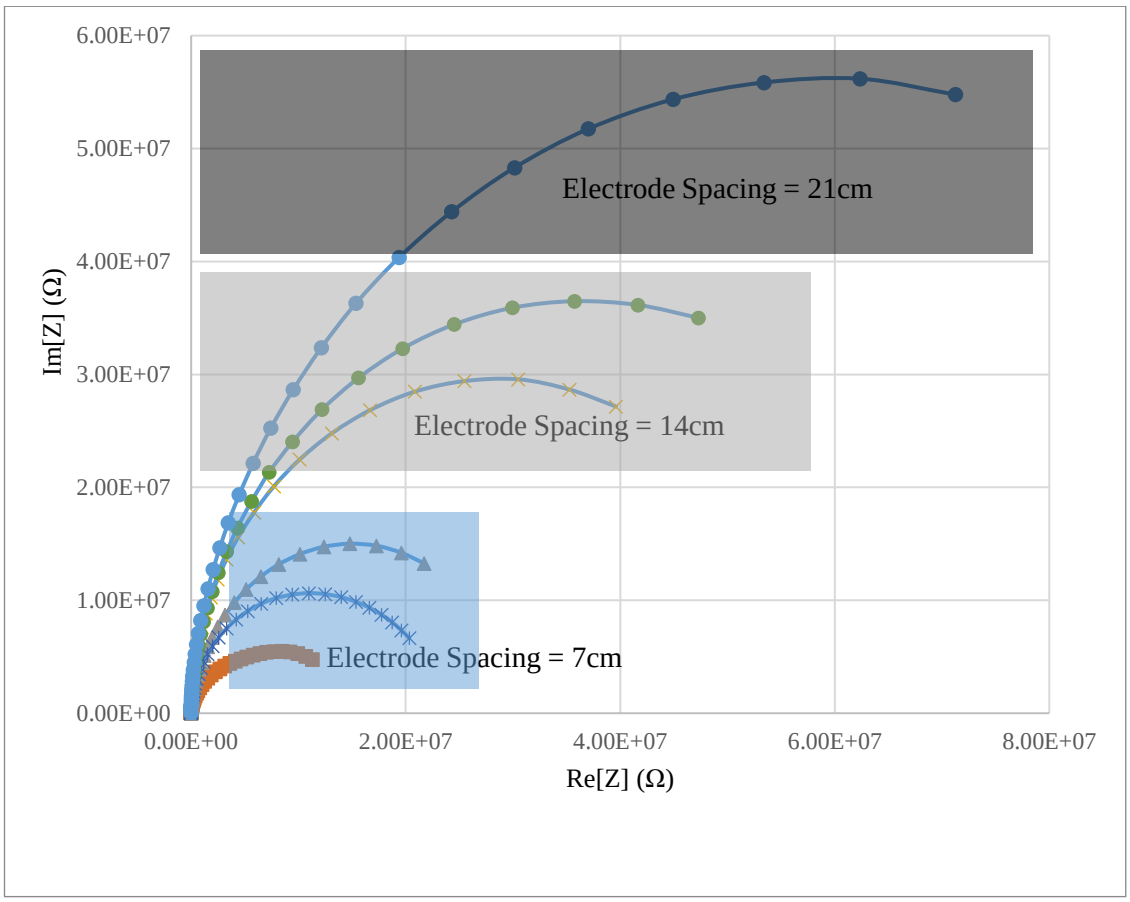

Figure 4.55: Cole plot for glycerol (GLY) between different pairs of electrodes showing different regions with electrode separations: A-B, B-C, C-D, A-C, B-D, and A-D

The chosen concentration of propylene glycol/ distilled water mixture was further modified to meet the required conductivity and permittivity range for blood. From the results obtained after several trials, a mixture of 80% propylene glycol with 20% 4M NaCl solution was found to be a satisfactory blood simulant when considering impedance, and secondarily viscosity and density.

4.7.2 Fat and Muscle Phantoms

As has been observed from the results, the agar-NaCl water phantom approximates fat and a mixture of agar-gelatine-NaCl water with propylene glycol was found to mimic the properties of muscle within acceptable limits of deviation, which were mainly due to shifted dispersion frequencies of response. The role of agar and gelatine was found to be important – not only to act as gelling agents – but also to provide a degree of mechanical strength to the phantom. This work considered the dielectric properties of both fat and

muscle to be isotropic and uniform, although this is not the case in biological tissue. Hence the scope of this work only extended to mimicking the bulk conductivity and relative permittivity of fat and muscle compared to properties compiled by Gabriel [141].

The choice of constituents like agar and gelatine provided low cost, non-hazardous alternatives to chemicals which may otherwise could have been used to simulate more accurate dielectric response of these tissues. Furthermore, these constituents possessed electrical behaviour which was not very sensitive towards environmental conditions or temperature. As a pre-investigative measure, the properties of the developed mixtures for both fat and muscle were measured both before and after the mixture was allowed to cool and settle at room temperature. A 1.5 – 2 % change in the dielectric parameters was observed in the order of the limits of deviations for repeated experiments. Care was taken to cool off the mixture while allowing it to settle in the cylindrical sensor while placed in a vacuum desiccator to avoid any moisture ingress.

One of the major challenges was regulating the concentration of NaCl in the mixture to obtain the desired level of conductivity. Increasing the concentration of NaCl also changed the relaxation spectrum and the modelling of polarisation along with Cole parameters was affected. This was particularly significant in the case of the muscle phantom because of higher required conductivity than fat. It was found that preservation of the dielectric relaxation could be achieved to some extent by adding propylene glycol.

The results obtained for conductivity and relative permittivity for both fat and muscle simulants slightly deviated from Gabriel's compiled properties, especially at very low frequencies within the frequency range of this work, i.e. towards 1 kHz rather than 2 MHz. The significance of this difference should be considered in light of the fact that the compilation of the dielectric properties of biological tissues by Gabriel was a parametric study to fit the observed or measured values from several works to a multi-relaxation Cole model [144]. Since most of the used data were measured at giga-hertz frequencies, it is reasonable to assume the extrapolation at lower frequencies to be not as precise. In particular, there is potential for electrode polarisation effects to compromise the measurement results, not only in quantity but also in behaviour of the impedance spectra. This would lead to imprecise values at extrapolated frequencies. However, the electrode polarisation model proposed for the cylindrical sensor in this study appears to accurately account for the polarisation contribution, which was proved through the calibration results for 1mM NaCl solution in section 4.2.3.4.

4.7.3 Human Forearm Phantom

The dimensions of the forearm phantom were chosen to be analogous to the simulation model with the fat layer thickness of 5 mm and a muscle layer of 20 mm so that the electric field distribution within both the domains would be similar to the simulation study.

The impedance measurements were performed using the Quadra® Impedance Spectroscopy device. This device offers the measurements up to a maximum frequency of 349 kHz which were used to fit the data to a Cole model. This procedure was adopted over the previous method of using the LCR meter, because, for the purpose of this stage in the project, extensive measurements were required, rather than determination of dielectricity of the materials. Quadra also allows a higher rate of acquisition of the bioimpedance spectrum (providing the real-time impedance spectrum changes with 1000 spectra per second), and does not require the complex processing to account for the electrode polarisation and other parasitic effects. Moreover, the device is well established commercially to be used on human tissues in compliance with the IEC 60601 standards. Due to bandwidth of interest for this study being 1 kHz – 2 MHz, the measurements obtained from the Quadra were fitted to a Cole model with a single dispersion region. The Cole spectrum for all the three diameters was obtained and yielded expected results as were found during the simulation study.

As is evident from the Figure 4.50, Figure 4.51 and Figure 4.52, the measurements show a decrease in the impedance spectrum with increasing diameter. This follows the results obtained from the simulation study where a similar trend was observed. However, the measured impedance magnitudes were found to be consistently different from those obtained from the simulation analysis (Figure 4.56).

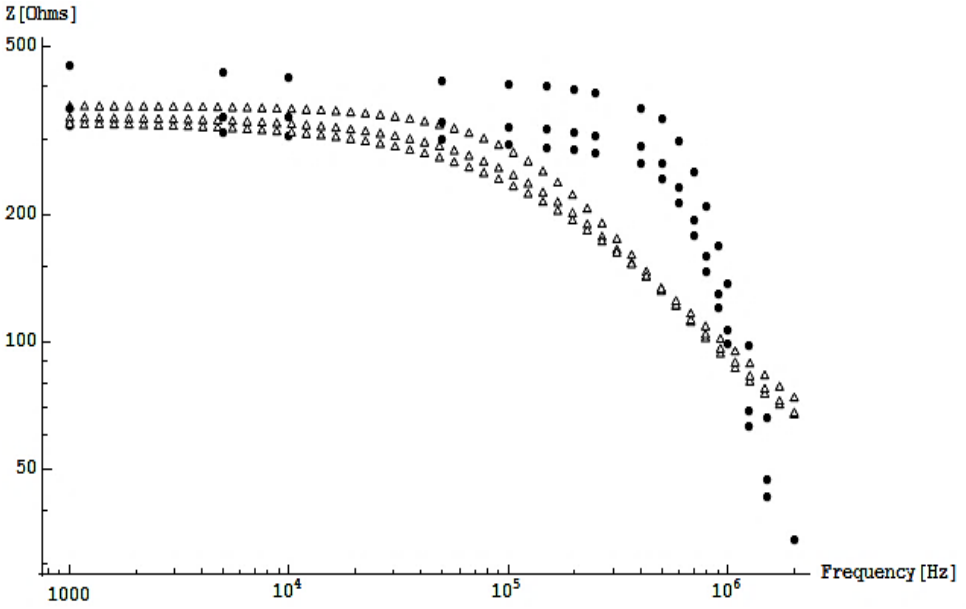

Figure 4.56: Comparison of the simulation obtained Z vs the measured Z of the forearm phantom at all three diameters (the decreasing magnitude of the curves show the increasing diameter): • Z - simulated, and ∆ Z – measured

From the above figure, it is clear that the impedance obtained from the simulation analysis exhibits a slightly different dispersion mechanism than that measured from the constructed forearm phantom. The characteristic frequency of the phantom measurements was found to be smaller than that of the simulation analysis leading to a shift in the frequency dispersion spectra of the impedance variation. The difference in the Cole-type behaviour of the phantom measurements and the Debye-type behaviour of the simulation data is clear at frequencies above 100 kHz. There is also a difference in the absolute values of the impedance between the simulation and phantom measurements at the corresponding diameters. However, there is a similar decreasing trend of the impedance magnitude with increasing artery diameter. Other differences between the simulation and forearm phantom measurements have been summarised in Table 4-10. These differences explain the contribution of factors such as the electrodes and the tissue layers on the overall measurements. The size and the configuration of electrodes contribute significantly to the overall measurements, however in this case, they were configured similarly between the phantom and simulation.

Table 4-10: Differences between the simulation analysis and Forearm phantom measurements

	Simulation Analysis	**Forearm Phantom measurements**
Electrode Interface	No contribution of the electrode-fat interface was considered in the overall measurements	The measurement device provided for an appropriate compensation for the electrode-phantom interface
Size of electrodes	The electrodes used were smaller in cross-sectional contact dimensions (1 mm diameter)	The electrodes used were commercial surface electrodes
Fat and Muscle layers	The dimensions of the fat and muscle tissue layers as modelled in the simulation geometry were relatively smaller than the forearm dimensions	The dimensions of the moulds and hence the constructed phantom were closer to the actual forearm cross-section.

A far more significant contribution to the difference in behaviour was that the simulation analysis in Chapter 3 used bulk dielectric properties of fat and muscle obtained from Gabriel's database. The forearm phantom was constructed using tissue simulants that had somewhat different properties. Considering these differences, an investigation was done to modify the simulation using the dielectric properties measured for each tissue simulant. This aimed to understand the contribution material properties to the deviations observed in dispersion. A comparison of the new simulated results with the forearm phantom measurements for all three artery diameters can be seen in Figure 4.57.

The simulation results using the new material properties agree closely with the phantom measurements for all three diameters. The overall time constants and dispersion coefficients of the systems are found to be in good agreement. The Cole-Cole plots for the three diameters for both the phantom measurements and the new simulated analysis

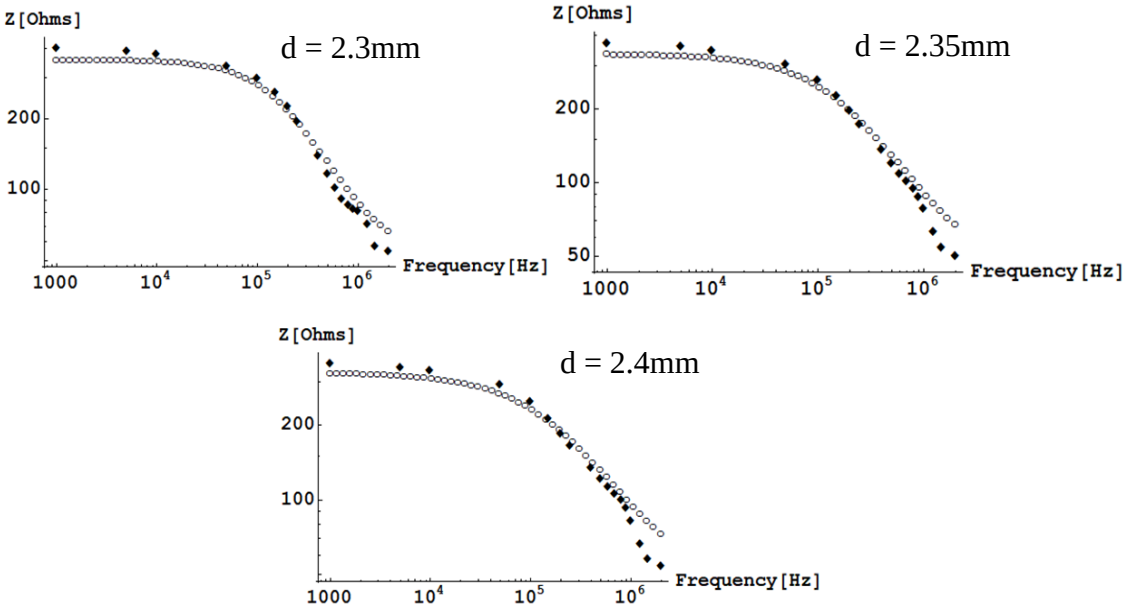

Figure 4.57: Comparison of the impedance measurements at forearm phantom and the simulation analysis with the phantom properties: ♦ Z - simulated, and ○ Z – measured

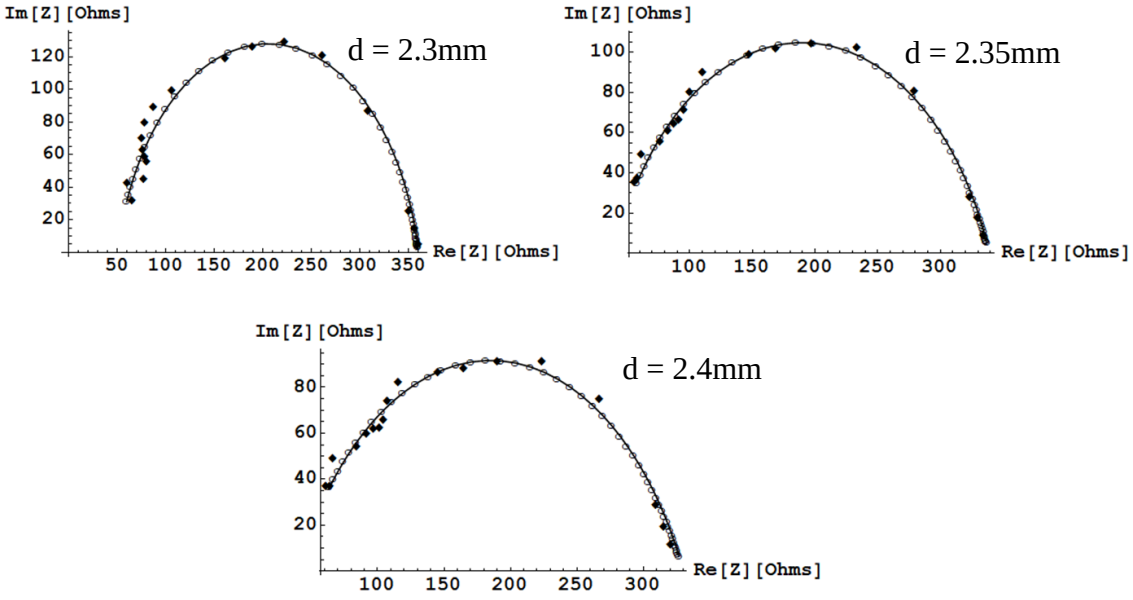

Figure 4.58: Cole plots for forearm phantom measurements and simulation analysis with phantom properties for all three diameters: ♦ Simulation results, and ⊖Phantom measurements

(shown in Figure 4.58) also verifies the good agreement in both resistive and reactive behaviour. Hence, it is fair to assume that the major contribution to the deviation in the original simulation study and the forearm measurements was provided by the shifted dispersion spectra for the dielectric properties of the tissue simulants. Although slight differences in the tissue layer geometries and the electrode contact could explain the remaining deviation, particularly at the extreme resistances (R_0 and R_∞),

The change in the impedance with arterial diameter shows potential for bioimpedance to be a prospective modality for analysing hemodynamics. The diameter of the radial artery is smaller than many other arteries but the ease of measurement procedure (using adhesive electrodes) without introducing discomfort to the test subject makes it clinically attractive. SF-BIA applications already aim at assessing hemodynamic parameters and evaluating indices like pulse wave velocity (PWV) and arterial stiffness. Single frequency measurement is common in such applications, where the frequency is chosen to be significantly above 1 kHz and within 100 kHz [66], [120]. Frequencies below 1 kHz may affect the nervous system and muscular contractions and are hence avoided [234], [235]. However, the use of MF-BIA shows potential for analysing real time spectral changes of the regional tissues and potentially could be used to more accurately measure significant physiological parameters, such as the artery diameter fluctuations. Results of the simulation and phantom analysis both indicate that the decrease in the value of R_0 is significant but is not monotonic which leads to a postulation of non-linear impedance changes with changing diameter. Moreover, the value of R_∞ is almost the same for all the three diameters indicating a constant resistive contribution with the diameter changes. An explanation of this phenomena is that fat and the muscle tissue layers do not undergo significant changes in their overall dimensions with changing diameter of the artery, and contribute invariably to both the high and low frequency behaviour. In contrast, the resistance of blood due to its constituents such as the plasma and erythrocytes is more significant at lower frequencies, and reflects arterial diameter changes. This understanding leads to identifying MF-BIA as a potential technique to monitor arterial diameter changes over the cardiac cycle.

4.8 Closure

This chapter focussed on identifying the potential materials for constructing tissue phantoms to mimic the dielectric properties of fat, muscle and blood tissues. The chapter also described experimental investigation to accurately measure conductivity and relative permittivity. The development of the blood phantom was based on identifying the potential mixtures exhibiting a Debye or Cole response along with physical properties such as density and dynamic viscosity. A mixture of 80% propylene glycol and 20% 4 M saline solution was found to replicate the properties of blood within acceptable tolerances in the β dispersion frequency range. The identification of the potential simulants for fat

and muscle involved the use of agar, gelatine and saline solution which were tested and modified to achieve the required conductivity and permittivity. An 5% agar with 0.05% saline mixture was found to mimic the properties of fat, whereas the muscle properties were mimicked through a suspension of agar, gelatine, saline and propylene glycol (Table 4-7).

The identification of the potential tissue simulants was followed by construction of the forearm phantom with three geometries to simulate the three arterial diameter instances. The measurements were performed using the Quadra® Impedance Spectroscopy device within 1 kHz – 349 kHz which were fitted to a Cole model to estimate the entire frequency spectrum within 1 kHz – 2 MHz. Once material dielectric properties were accounted for, the results showed considerable similarity between the simulation and the phantom impedance measurements.

The impedance spectra were found to decrease with increasing arterial diameter, showing prospects for using MF-BIA for estimating the blood flow induced vascular changes. The next chapter discusses the different parameters contributing to the overall impedance response at the three diameters through electrical modelling, providing further insight into the contribution of blood flow to impedance variations.

Chapter 5 ELECTRICAL MODELLING OF HUMAN FOREARM TISSUES

5.1 Introduction

Previous chapters have discussed the quantification of complex conductivity and complex permittivity of biological tissues. The type of dielectric behaviour exhibited by the tissues is explained through a dielectric relaxation phenomenon. Generally, it is justifiable to assume that the tissue electrical response can be modelled using Debye relaxation theory or Cole theory, depending upon the type of tissue. When different types of tissue are brought together into anatomical structures, dielectric relaxation phenomenon within the β dispersion region of frequencies containing most of the complex tissue properties cannot be completely described using Debye relaxation. However, it can be employed to model the system in terms of passive electrical components. Such models can provide tractable solutions for applications such as body fat estimation and impedance cardiography where a more complicated but accurate model cannot be used.

This chapter describes two different approaches to model the simulated impedance measurements. Section 5.2 describes a parametric electrical model to fit the simulation results in a Debye-type response to calculate the resistances of individual tissue domains. Section 5.3 discusses a Cole modelling approach to model the simulation results in terms of Cole parameters. The next section, 5.4, builds on the previous sections to electrically model the relation of diameter to the overall simulated impedance measurements.

5.2 Parametric Electrical Modelling of Human Forearm Simulation Model

The use of simple circuits may be adapted to describe tissue response over a single frequency. However, there is not an extensive literature on the electrical circuit modelling of tissues across all the dispersion regions. The individual dielectric behaviour of each tissue type is different, owing to different complex conductivities and permittivities and hence simple circuit models are not likely to behave well over a wider range of the β dispersion region.

Here, we describe an electrical circuit model defining the response of three layers of tissues – fat, muscle and blood, as has been considered for the simulation study in Chapter 3. A Debye-type model has been used to parametrically fit simulated bioimpedance responses. A parametric fitting approach has been used with the assumed electrical model and compared with the simulated measurements.

5.2.1 A Debye-type electrical model for tissue layers

The three layers of the tissues were considered as lumped into two domains – artery (blood) and combined fat and muscle. Each domain was individually defined through its equivalent circuit consisting of two resistors and a capacitor (Figure 5.1).

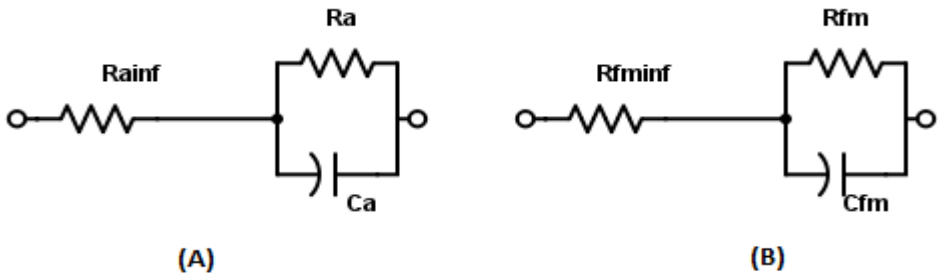

Figure 5.1: Proposed equivalent circuits for (A). Artery (Blood) domain and (B). Fat/Muscle domain

The circuit elements have been considered to be frequency independent, hence this is a Debye model. The impedance of the two domains can be defined as:

$$Z_a = R_{ainf} + \frac{R_a}{1 + j\omega R_a C_a} \tag{5.1}$$

$$Z_{fm} = R_{fminf} + \frac{R_{fm}}{1 + j\omega R_{fm} C_{fm}} \tag{5.2}$$

where Z_a and Z_{fm} are the impedances of artery and fat/muscle domains respectively, R_{ainf} and R_{fminf} represent the artery and fat/muscle resistances at infinitely high frequency, R_a and R_{fm} represent the resistances of artery and fat/muscle at zero frequency, C_a and C_{fm} represent the capacitances of artery and fat/muscle domains respectively and $\omega = 2\pi f$, with f as the frequency of operation.

The division of tissue layers into two domains was decided after analysing the current conduction pathways through all the three layers as evidenced by the simulation. The

artery (blood) possesses a higher conductivity and lower relative permittivity thereby allowing for most current flow. The artery has been modelled as passing through both muscle and fat regions, which makes it difficult to separate the conduction pathways for fat and muscle layers. Hence the fat and muscle layers have been defined here as a single domain with an impedance Z_{fm}.

The simulation results from section 3.5 were used as data sets to compute the equivalent circuit model parameters. The investigation of the electric field distribution, which also relates to the path of current distribution, revealed that the current initially entered through the fat/muscle domain and divided into the two domains as it traversed the anatomy under consideration (Figure 3.12, Figure 3.13, Figure 3.14, and Figure 3.15).

This led to the formulation of overall tissue impedance (Z_{tissue}) as:

$$Z_{tissue} = Z_{fm} + (Z_a || Z_{fm}) \tag{5.3}$$

Substituting the values from equations (5.1) and (5.2),

$$Z_{\text{tissue}} = \frac{R_{\text{fm}}}{1 + i\omega C_{\text{fm}} R_{\text{fm}}} + R_{\text{fminf}} + \frac{\left(\frac{R_a}{1 + i\omega C_a R_a} + R_{\text{ainf}}\right)\left(\frac{R_{\text{fm}}}{1 + i\omega C_{\text{fm}} R_{\text{fm}}} + R_{\text{fminf}}\right)}{\frac{R_a}{1 + i\omega C_a R_a} + R_{\text{ainf}} + \frac{R_{\text{fm}}}{1 + i\omega C_{\text{fm}} R_{\text{fm}}} + R_{\text{fminf}}} \tag{5.4}$$

The Nyquist plot can be used to help characterize the dielectric response of most biomaterials. The extreme values of the plot (R_0 and R_∞) along with the characteristic frequency (ω_c) offer enough information to reproduce the complete behaviour of the system. Therefore, these parameters were estimated and used to calculate the model parameters defined by the passive components. The real and the imaginary values of tissue impedance were related in terms of model parameters and frequency. The obtained expressions were expanded and solved to reduce to more simplistic forms by deriving different equations for real and imaginary parts at zero and infinite frequencies such as:

$$\text{Re}[Z_{\text{tissue}}][\infty] = \frac{R_{\text{fminf}}(2R_{\text{ainf}} + R_{\text{fminf}})}{R_{\text{ainf}} + R_{\text{fminf}}} \tag{5.5}$$

$$\text{Re}[Z_{\text{tissue}}][0] = \frac{(R_{\text{fm}} + R_{\text{fminf}})(2R_a + 2R_{\text{ainf}} + R_{\text{fm}} + R_{\text{fminf}})}{R_a + R_{\text{ainf}} + R_{\text{fm}} + R_{\text{fminf}}} \tag{5.6}$$

The estimation of the parameters - R_a, R_{fm}, R_{ainf} and R_{fminf}, as defined in the electrical model and included numerical simulations, was achieved by considering equations (5.5) and (5.6) for three different diameters. $\text{Re}[Z_{\text{tissue}}][\infty]$ denotes the real part of the impedance at infinite frequency (here, equivalent to 2 MHz) and $\text{Re}[Z_{\text{tissue}}][0]$ denotes the real part of impedance at zero frequency. It was assumed that no significant changes occur in the fat/muscle domain due to the diameter changes in artery, mainly due to negligible change in the artery dimensions as compared to the entire model. Hence a single value was estimated for fat/muscle domain (for both zero and infinite frequencies) as R_{fm} and R_{fminf} whereas the arterial resistances were obtained for three diameters as $R_a[d1]$, $R_a[d2]$, $R_a[d3]$, $R_{ainf}[d1]$, $R_{ainf}[d2]$ and $R_{ainf}[d3]$, where d1 = 2.3mm, d2 = 2.35mm and d3 = 2.4mm.

The simulation data was fitted to the Debye equation (equation (5.7)) with the centre of the plot assumed to be on the real axis for all the diameters over the measured frequency range.

$$Z(\omega) = R_\infty + \frac{R_o - R_\infty}{1 + j\omega\tau_D} \tag{5.7}$$

The equations relating the imaginary part of $Z(\omega)$ (X) to the real part of $Z(\omega)$ (R) were calculated to be:

$$\text{X1} = \sqrt{35701.8 - (-190.2 + \text{R1})^2} \tag{5.8}$$

$$\text{X2} = \sqrt{22173.3 - (-150.15 + \text{R2})^2} \tag{5.9}$$

$$\text{X3} = \sqrt{18066.79 - (-135.64 + \text{R3})^2} \tag{5.10}$$

where, X1, X2 and X3 are the imaginary parts of $Z(\omega)$ for diameters d1, d2 and d3 respectively and R1, R2 and R3 are their corresponding real parts. The equations (5.8), (5.9) and (5.10) were used to calculate the points of interest that included R_0 [d1, d2 and d3], R_∞ [d1, d2 and d3] (the extreme points of the Cole plot) and the characteristic frequency. The parameters for the above equations were chosen to optimize their representation of the simulation data by performing a polynomial fit, which can be seen in Figure 5.2.

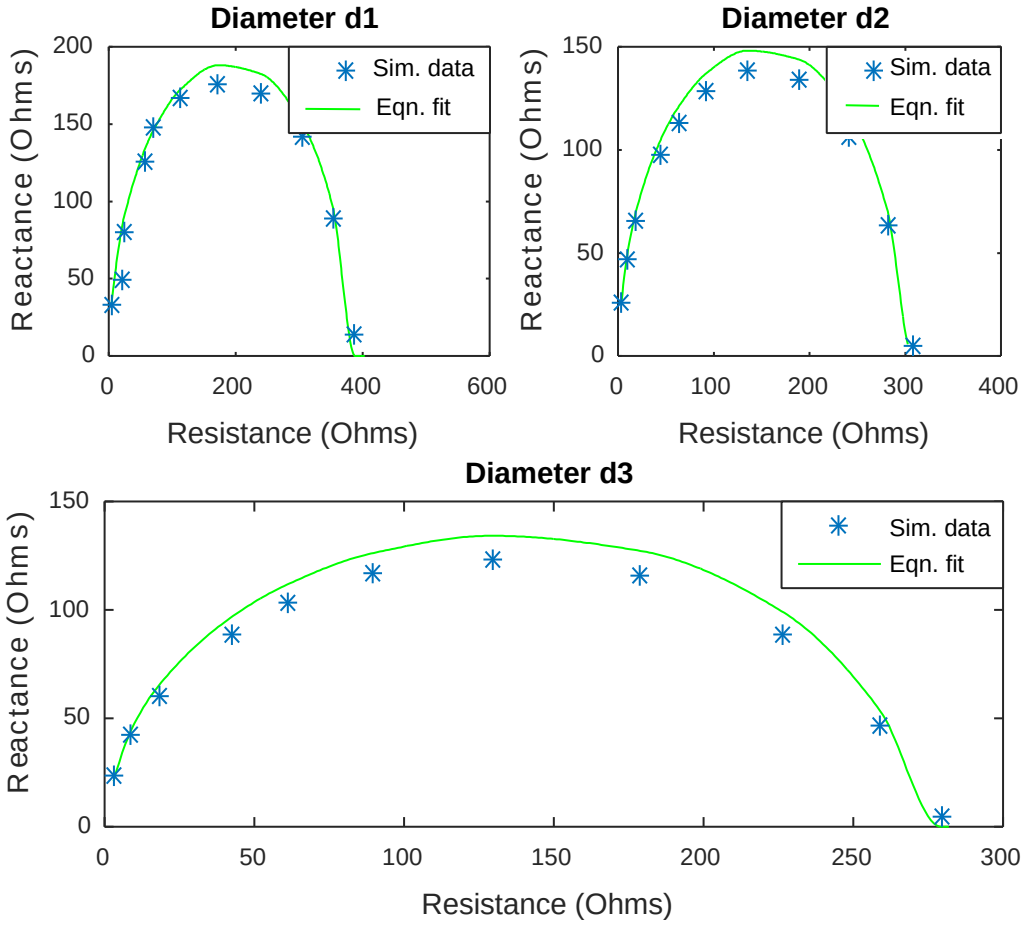

Figure 5.2: Model equations fit comparison with the simulation data for three diameters

In order to relate the different resistance values accounting for different diameters, a term called resistance ratio was introduced. It was hypothesized that the variation in the resistance at different diameters (especially for arterial volume changes) was a function of their diameter ratio. As is well established, an increase in the cross-section of a conductor decreases the resistance value (for constant length) and hence the function constitutes an inverse relation of the diameters. Hence, the resistance ratio (RR) between diameters d1 and d2 was defined as:

$$RR[d1, d2] = \frac{R_{d1}}{R_{d2}} = f\left(\frac{d2}{d1}\right) = \left(\frac{d2}{d1}\right)^{\alpha}$$

where α is the coefficient describing the relation between change in electrical resistance and change in diameter values. Using the above relation led to simplifying the complex multiple equations for different diameter parameters. The value of R_{fminf} was calculated using equation (5.11).

$$R_{\mathrm{fminf}} = \frac{\mathrm{RR_{ainf}[d1, d2] * Re}[Z_{\mathrm{tissue}}][\infty][\mathrm{d1}] - \mathrm{Re}[Z_{\mathrm{tissue}}][\infty][\mathrm{d2}]}{2(\mathrm{RR_{ainf}[d1, d2]} - 1)} \quad (5.11)$$

The values of $\mathrm{R_{ainf}}$ [d1], $\mathrm{R_{ainf}}$ [d2] and $\mathrm{R_{ainf}}$ [d3] was then calculated from equations (5.12), (5.13), and (5.14) respectively.

$$R_{\mathrm{ainf}}[\mathrm{d1}] = \frac{R_{\mathrm{fminf}} * \mathrm{Re}[Z_{\mathrm{tissue}}][\infty][\mathrm{d1}] - R_{\mathrm{fminf}}^2}{2R_{\mathrm{fminf}} - \mathrm{Re}[Z_{\mathrm{tissue}}][\infty][\mathrm{d1}]} \quad (5.12)$$

$$R_{\mathrm{ainf}}[\mathrm{d2}] = \frac{R_{\mathrm{fminf}} * \mathrm{Re}[Z_{\mathrm{tissue}}][\infty][\mathrm{d2}] - R_{\mathrm{fminf}}^2}{2R_{\mathrm{fminf}} - \mathrm{Re}[Z_{\mathrm{tissue}}][\infty][\mathrm{d2}]} \quad (5.13)$$

$$R_{\mathrm{ainf}}[\mathrm{d3}] = \frac{R_{\mathrm{fminf}} * \mathrm{Re}[Z_{\mathrm{tissue}}][\infty][\mathrm{d3}] - R_{\mathrm{fminf}}^2}{2R_{\mathrm{fminf}} - \mathrm{Re}[Z_{\mathrm{tissue}}][\infty][\mathrm{d3}]} \quad (5.14)$$

R_{fm} and consequently $R_{\mathrm{a}}[\mathrm{d1}]$, $R_{\mathrm{a}}[\mathrm{d2}]$ and $R_{\mathrm{a}}[\mathrm{d3}]$ were also calculated using similar expressions.

5.2.2 Debye model parameters for simulation response

The model equations (5.8), (5.9), and (5.10) were used to estimate the equivalent circuit model passive components and their relation in terms of frequency. Table 5-1 lists the estimated extreme value points and the characteristic frequencies for all three diameters.

Table 5-1: Estimated R_0, R_∞ and F_c values for three diameters

	R_0 (Ω)	**R_∞ (Ω)**	**F_c (kHz)**
Diameter – d1	379.198	1.3	690.75
Diameter – d2	299.064	1.255	672.9
Diameter – d3	270.056	1.23	693.6

The values of all the unknown variables were calculated using the before mentioned relations. The overall resistances as well as the individual resistance values for different domains were calculated for a heuristically determined value of α = 72, although the search was constrained so that α law within 50-100. The approach was heuristic due to scarcity of knowledge relating the distribution of electrical current between artery and fat/muscle layers in human arteries. The overall estimation of the equation variables was

followed with the estimation of the frequency response for all the three diameters. Figure 5.3 shows the plots of the calculated data along with the original simulation measurements.

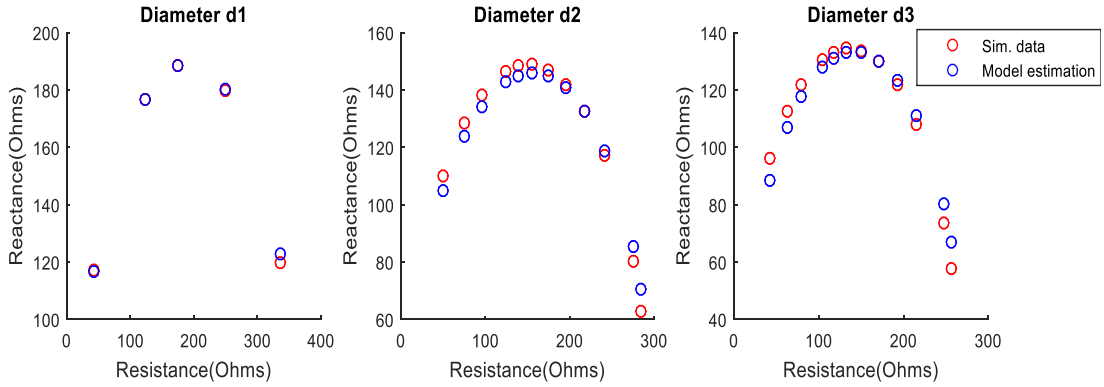

Figure 5.3: Overall model estimated tissue response in comparison with simulation response for three diameters: O Simulation data, and O Model fit

Generally, correlation as a measure of agreement between two data sets is commonplace, however it may not always be appropriate for data sampled over a large range. Instead, Bland Altman analysis [236] is more appropriate. This is done by specifying 95% limits of agreement as a measure of the similarity of two measurements, calculated as 95% confidence intervals (CI) (mean ±1.96*SD (standard deviation)) of the difference between the datasets. Figure 5.4, Figure 5.5 and Figure 5.6 show the correlation and Bland Altman plots for the three diameters respectively. The horizontal axis represents the mean of the simulation and the model impedance values (in Ω) and the vertical axis represents the difference in the impedance magnitudes of the two data sets (in Ω).

The plots show the statistical parameters 'r', 'SSE', 'RPC' and 'CV'. The Pearson's correlation coefficient (r) defines the linear interdependence between two variables or samples. It takes values between -1 and +1. It can be calculated by the formula:

$$r = \frac{\sum_{i=1}^{n}(x_i - \hat{x})(y_i - \hat{y})}{\sqrt{\sum_{i=1}^{n}(x_i - \hat{x})^2}\sqrt{\sum_{i=1}^{n}(y_i - \hat{y})^2}}$$

where x_i is the ith sample value of one dataset, y_i is the ith value of another dataset, n is the number of values in both datasets, $\hat{x} = \frac{1}{n}\sum_{i=1}^{n} x_i$ is the mean value of the first dataset and $\hat{y} = \frac{1}{n}\sum_{i=1}^{n} y_i$ is the mean of the second dataset. SSE or sum of squared errors of prediction gives a measure of errors or variability in the original and estimated model. It is calculated as:

$$SSE = \sum_{i=1}^{n} (x_{original(i)} - x_{predicted(i)})^2$$

Where n is the number of values, $x_{original(i)}$ is the known/original value at i[th] sample and $x_{predicted(i)}$ is the model estimated value at i[th] sample. RPC is the reproducibility coefficient and is calculated as 1.96*SD, and CV is the coefficient of variation and is the ratio of the SD to the mean difference expressed as a percentage.

Promising agreement was observed between the simulation and model derived data for all the three diameters with r=0.9993, 0.9953 and 0.9854 for d1, d2 and d3 respectively ($p < .001$ in all cases).

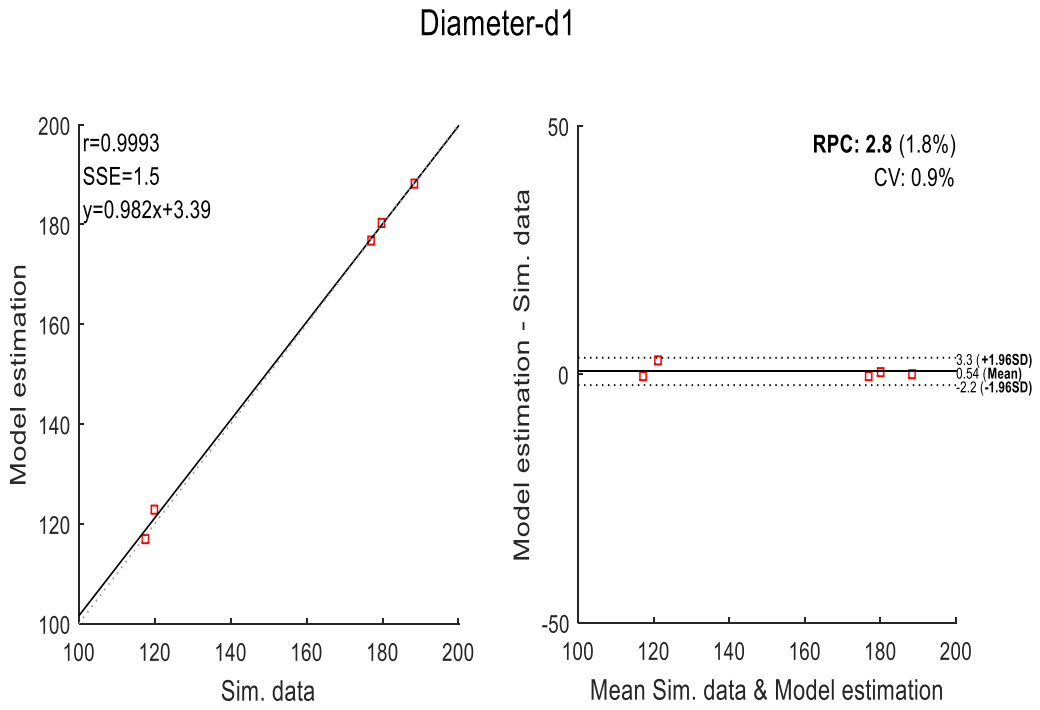

Figure 5.4: Correlation and Bland Altman plots for comparing model and simulation data for diameter d1. The horizontal axis represents the mean of the simulation and the model impedance values (in Ω) and the vertical axis represents the difference in the impedance magnitudes of the two data sets (in Ω).

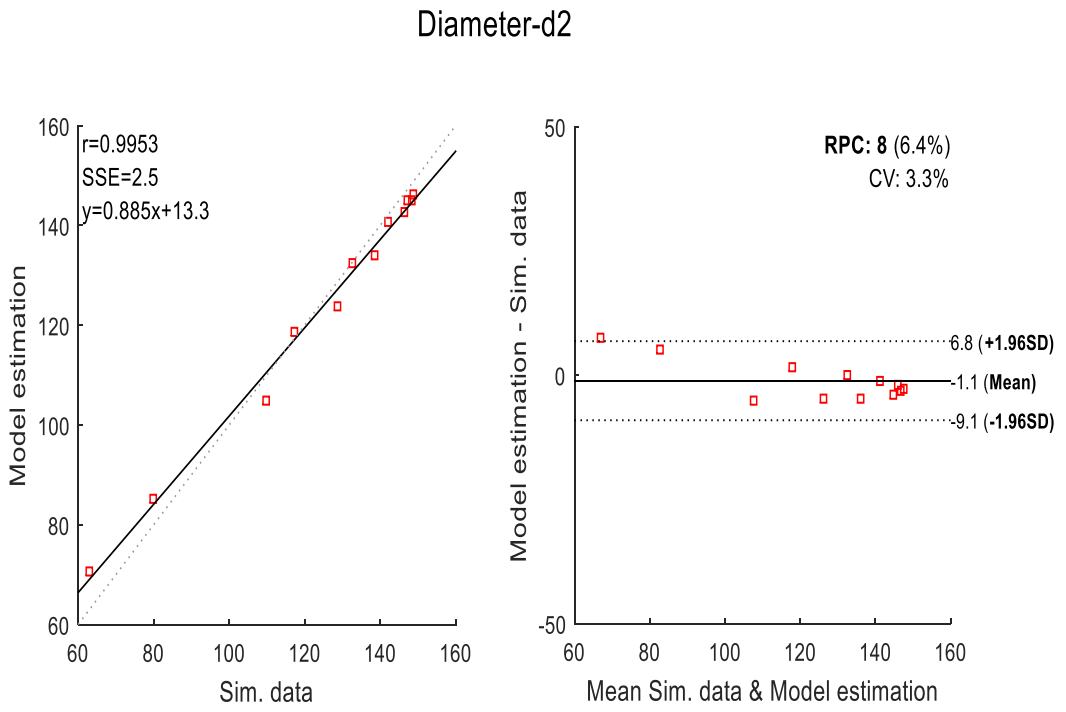

Figure 5.5: Correlation and Bland Altman plots for comparing model and simulation data for diameter d2. The horizontal axis represents the mean of the simulation and the model impedance values (in Ω) and the vertical axis represents the difference in the impedance magnitudes of the two data sets (in Ω).

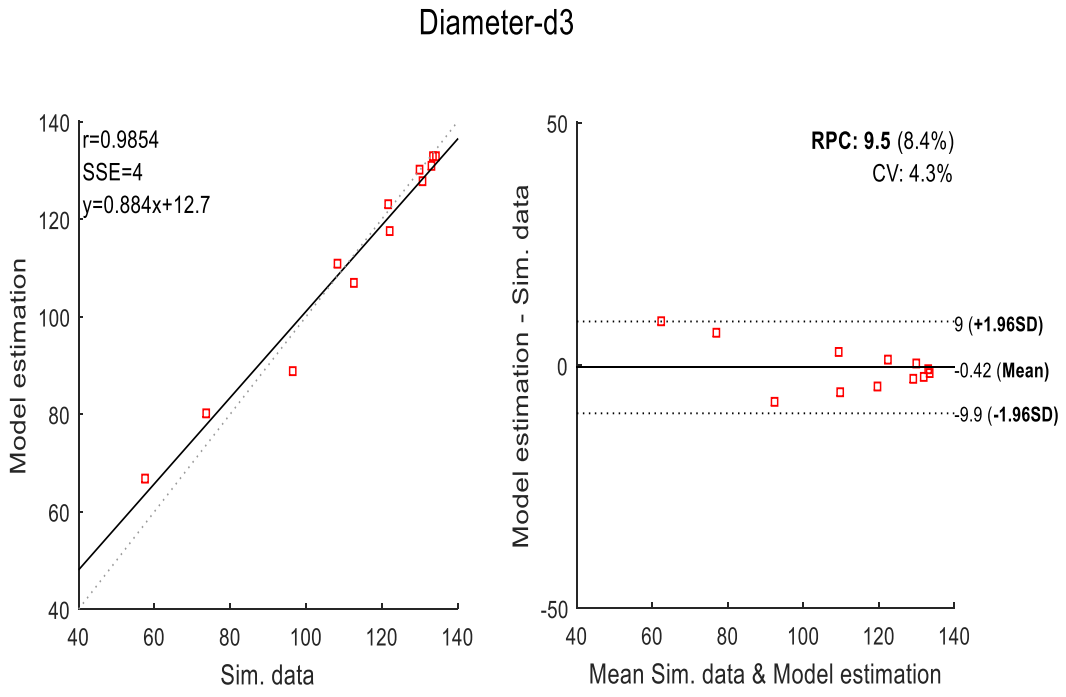

Figure 5.6: Correlation and Bland Altman plots for comparing model and simulation data for diameter d3. The horizontal axis represents the mean of the simulation and the model impedance values (in Ω) and the vertical axis represents the difference in the impedance magnitudes of the two data sets (in Ω).

On the basis of above results, the present model has been found to reproduce the original data within agreeable limits. However, the performance of the system depends on the fit parameters. Quality of fit was found to be particularly sensitive to resistance ratio and consequently on the value of α. There is much scope to signify the importance of fit parameters and the relationships amongst them in context to the physical system.

The values of R_a [d1], R_a [d2] and R_a [d3] were found to follow a decreasing trend with increasing diameters, which is expected. The consideration of R_{fm} to be constant for all the diameter changes appears reasonable in the sense that it preserves the ability of the equivalent circuit model to predict behaviour. However, a more distributed model (i.e. with more lumped parameters) could be more accurate, although harder to fit to data. The consideration of each tissue component as layered allows each domain to be represented using passive components but ignores potential changes in tissue perfusion, in practice. The equivalent circuit model also does not capture the very low-frequency response (at nearly constant reactance). This is likely to be due to the non-linear frequency dependence of the tissues, as modelled in the numerical simulation, which cannot be adequately represented by linear circuit elements.

There are various other factors like tissue anisotropy and inhomogeneity that play a vital role in accurately defining the overall response which have not been considered in this work. Nevertheless, the present study represents a multi-frequency representation of the human forearm simulation response using passive components, using a parametric approach to approximate the tissue behaviour in terms of the passive elements. It exhibits similar response to artery diameter changes as numerical simulation and measurements from tissue phantoms.

5.3 Dielectric – relaxation modelling of Human Forearm Simulation

Multi-frequency electrical bioimpedance measurements are generally fitted to a Cole-Cole model. The Cole equation is an empirical definition of the dielectricity of complex materials possessing overlapping relaxation dispersion regions. However, it has become a common way to model impedance data and define the dielectric behaviour of materials in particular, biological tissues. The Cole-Cole model is one of a few models that define

the extent of dispersion for tissue dielectric relaxation. The important general dielectric relaxation models are mentioned in Table 5-2.

Table 5-2: Different dielectric relaxation models

Dielectric Relaxation Model	**Model Equation**
Debye dielectric model [68]	$Z(\omega) = R_\infty + \frac{R_o - R_\infty}{1 + j\omega\tau_D}$
Havriliak – Negami model [237]	$Z(\omega) = R_\infty + \frac{R_o - R_\infty}{(1 + (j\omega\tau_{HN})^\alpha)^\beta}$
Cole-Davidson model [238]	$Z(\omega) = R_\infty + \frac{R_o - R_\infty}{(1 + j\omega\tau_{CD})^\beta}$
Cole-Cole model [73]	$Z(\omega) = R_\infty + \frac{R_o - R_\infty}{1 + (j\omega\tau_{CC})^\alpha}$

For each model as mentioned above, the dielectric phenomenon exhibits its own relaxation time constant: τ_D as time constant for Debye relaxation, τ_{HN} for Havriliak – Negami relaxation, τ_{CD} for Cole-Davidson model and τ_{CC} for Cole – Cole model (all other terms have their usual meaning). It is worthwhile to note that all the models and relations are empirical and essentially modified relations of Debye type relaxation to account for different types of asymmetry occurring in the overall dielectric response. The Cole – Davidson and Cole model combine to form the Havriliak – Negami relaxation model, which generalises the overall dielectric relaxation in tissues. The characteristic frequency (ω_c) can be defined as the reciprocal of the time constant. In symmetric relationships it is also the frequency of maximal loss, although that does not hold true in cases of asymmetrical relaxations [239].

Conventionally, all the coefficients in all the above mentioned models, i.e. α and β, lie within 0 and 1 and the systems are often referred to as stretched exponential systems [240]. However, the value of either of α or β greater than 1 defines a state of a compressed exponential system which has been reported in various studies [241], [242] and reflects disorder in the material properties due to heterogeneity or random atomic re-arrangements.

In this work, the modelling is carried out by fitting the equations mentioned in Table 5-2 to simulated data. The dielectric fitting can be carried out in two ways: Impedance – frequency (Z-ω) fitting or resistance – reactance (R-X) fitting. In this study, R-X fitting

was employed where the reactance (X) was fitted as a function of resistance (R) and other Cole parameters. The data considered for fitting was that obtained from the simulation study (section 3.5) for all the three diameters. Fitting was performed using a nonlinear, constrained optimisation approach using Wolfram Mathematica® to minimize the squared error between the actual data and the fitted data.

5.3.1 Mathematical model

A general Cole equation expressing the impedance, Z as a function of Cole parameters R_0, R_∞, ω_c and k is defined as:

$$Z(\omega) = R_\infty + \frac{R_o - R_\infty}{1 + (j\frac{\omega}{\omega_c})^k} \tag{5.15}$$

where R_0 and R_∞ are the resistances at D.C and very high frequency respectively, ω_c is the characteristic frequency ($\omega c = 1/\tau$, where τ is the time constant of the system) and k is the relaxation dispersion coefficient. Comparing with equation (1.12), $k = 1-\alpha$ and k $\pi/2$ defines the angle subtended by the plot at the center.

Equation (5.15) is defined for complex numbers and can be simplified by substituting the value of $(j)^k = \cos\left(k\frac{\pi}{2}\right) + j\sin(k\frac{\pi}{2})$. The equation modifies to:

$$Z(\omega) = R_\infty + \frac{R_0 - R_\infty}{1 + \omega^k \mathrm{Cos}[k\frac{\pi}{2}]\omega_c^{-k} + i\omega^k \mathrm{Sin}[k\frac{\pi}{2}]\omega_c^{-k}} \tag{5.16}$$

The real and the imaginary parts of impedance Z can be obtained as:

$$Re(Z) = R_\infty + \frac{(R_0 - R_\infty)(1 + (\frac{\omega}{\omega_c})^k \mathrm{Cos}[k\frac{\pi}{2}])}{1 + 2(\frac{\omega}{\omega_c})^k \mathrm{Cos}[k\frac{\pi}{2}] + (\frac{\omega}{\omega_c})^{2k}} \tag{5.17}$$

$$Img(Z) = -j\frac{(R_0 - R_\infty)(\frac{\omega}{\omega_c})^k \mathrm{Sin}[k\frac{\pi}{2}]}{1 + 2(\frac{\omega}{\omega_c})^k \mathrm{Cos}[k\frac{\pi}{2}] + (\frac{\omega}{\omega_c})^{2k}} \tag{5.18}$$

This can be further processed into relating the Im(Z) directly in terms of Re(Z) so as to form an expression where Im (Z) is a function of Re(Z). For ease of processing, Re (Z) can be symbolised as ‘R’ and Im (Z) can be symbolised as ‘X’. The following expression relates X and R:

$$4X + 2\cot\left[\frac{k\pi}{2}\right](R_0 - R_\infty)$$
$$= \sqrt{2}\,\mathrm{cosec}\left[\frac{k\pi}{2}\right] \tag{5.19}$$
$$* \sqrt{-4R^2 + 4RR_0 + R_0^2 + 4RR_\infty - 6R_0R_\infty + R_\infty^2 + \mathrm{Cos}[k\pi](-2R + R_0 + R_\infty)^2}$$

The methodology for the curve fitting involved choosing a general dielectric Cole model with at-least four parameters (R_0, R_∞, ω_c and k) that would define the dielectric relaxation spread in the frequency range. Moreover, a cost function was implemented to minimize the sum of squared errors between the curve fit and simulation data as:

$$RMSE = \sqrt{\frac{\sum_{i=1}^{N}\left(R_{fit}^i - R_{sim}^i\right)^2}{N}} + \sqrt{\frac{\sum_{i=1}^{N}\left(X_{fit}^i - X_{sim}^i\right)^2}{N}}$$

where RMSE is the root mean squared error, R_{fit}^i and X_{fit}^i denote the R and X fit data for ith sample, R_{sim}^i and X_{sim}^i denote the R and X simulation data for ith sample and N is the number of samples.

5.3.2 Cole parameters for simulation response

The minimization was obtained for the simulation data of all the three diameters. The least squares fitting was performed using *NMinimize* function in Mathematica to calculate the parametric values pertaining to the minimum RMSE. The number of frequency steps under consideration was chosen to be 11 between 250 kHz to 2 MHz. The obtained values of parameters for all three diameters are listed in Table 5-3.

Table 5-3: Fit obtained parameters for all three diameters

Diameter	**R_0 (Ω)**	**R_∞ (Ω)**	**ω_c (rad/s)**	**k**
D1	264.275	93.09	4.34 x 10^6	1.476
D2	204.768	76.75	4.35 x 10^6	1.487
D3	183.25	72.89	4.47 x 10^6	1.499

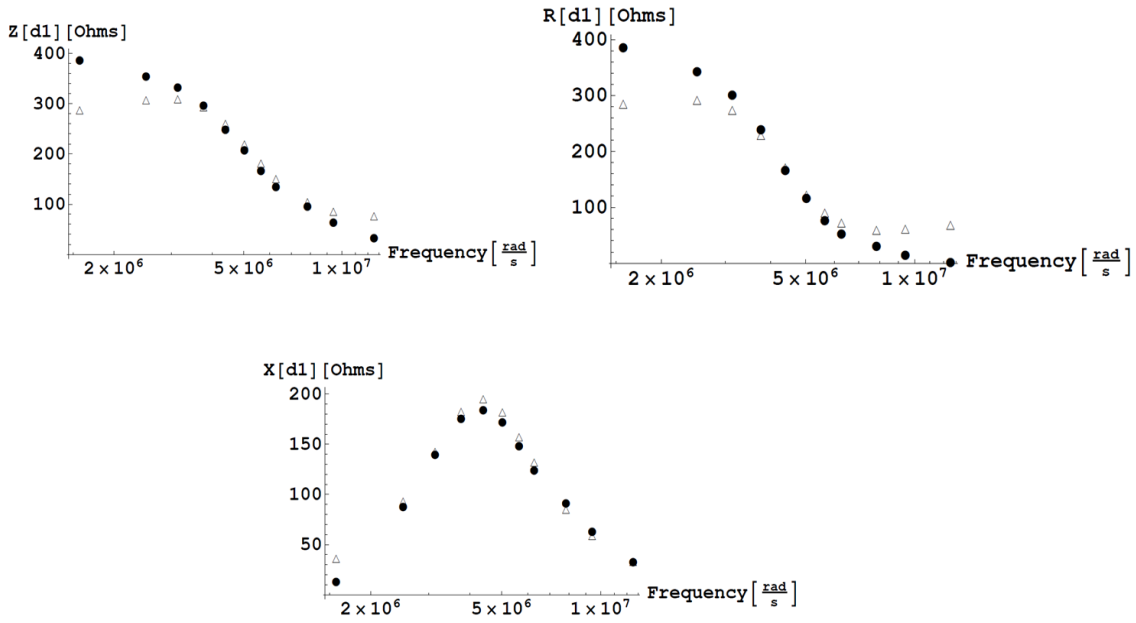

Figure 5.7: Fit and simulation plots for magnitudes of Z, R and X data versus frequency for diameter D1: • Simulation data, and ▵ Cole model fit

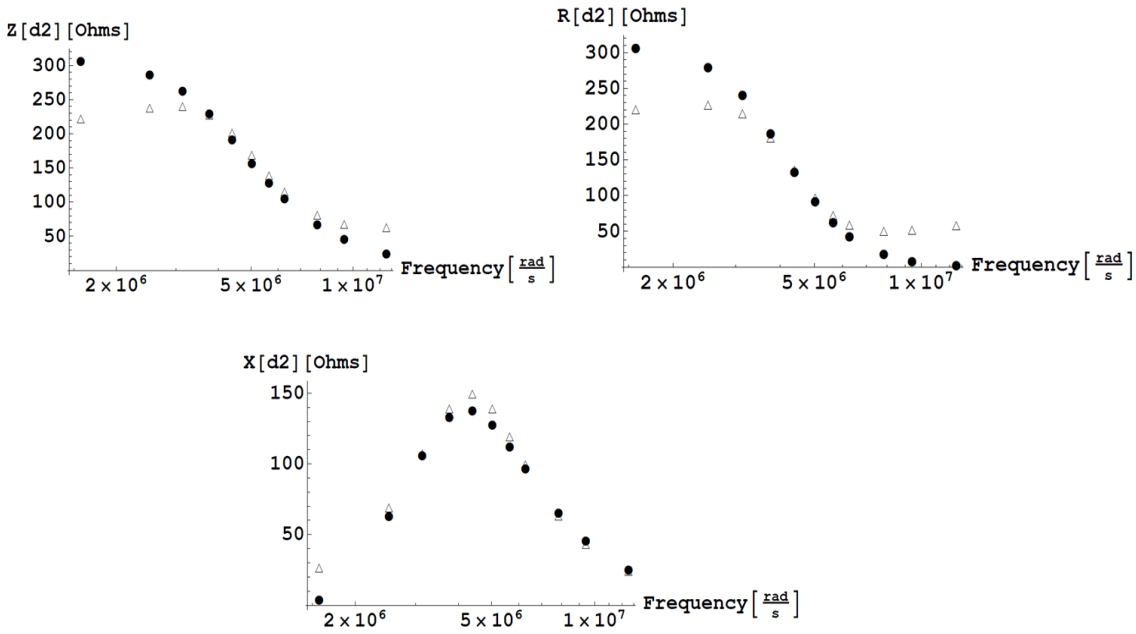

Figure 5.8: Fit and simulation plots for magnitudes of Z, R and X data versus frequency for diameter D2: • Simulation data, and ▵ Cole model fit

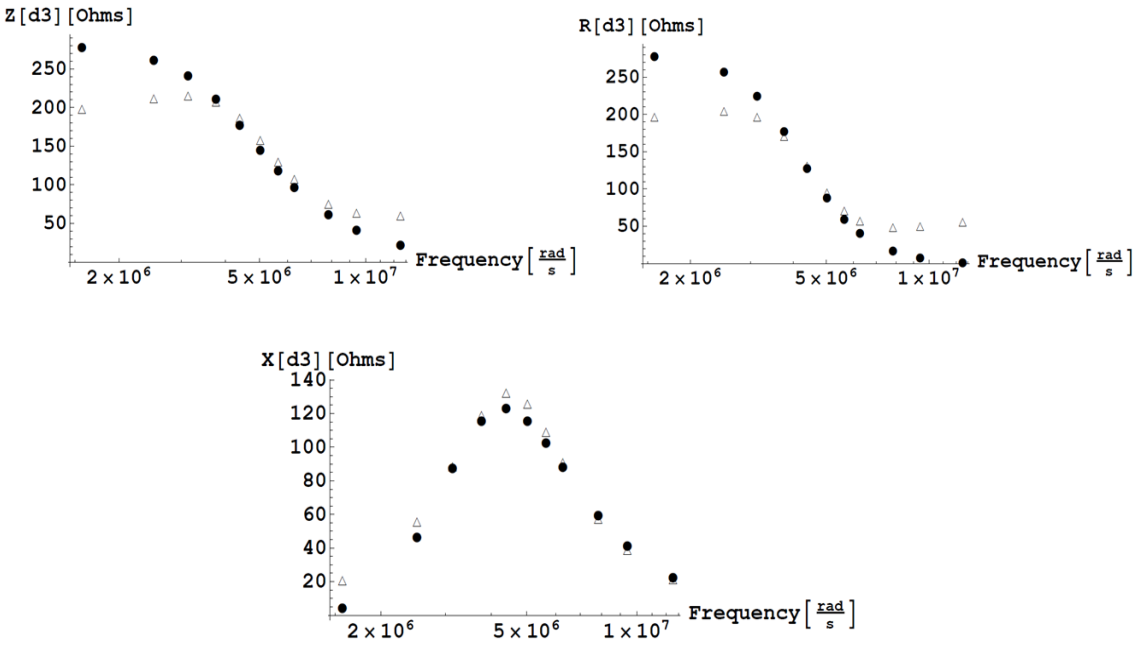

Figure 5.9: Fit and simulation plots for magnitudes of Z, R and X data versus frequency for diameter D3: • Simulation data, and ∆ Cole model fit

Figure 5.7, Figure 5.8 and Figure 5.9 indicate the quality of fit obtained for the simulation data using the Cole model through least squares fitting for diameters d1, d2 and d3, respectively. It is evident there are clear deviations observed in the magnitude of Z and the R plots for all the three diameters. However, the quality of fit was excellent for fitting the X data. It was found that, given the model, changes in the cost function did not result in significantly better fits to all of R, X and Z simulation data.

The deviation of the fitting from the simulation data, especially at the lower frequencies for real part of impedance, i.e., R can be understood by considering the contribution of the different parameters to the shape of the curve. The overall model, although being defined by four parameters, was mainly dominated by two degrees of freedom from the coefficient, k, and the frequency ratio ω/ω_c. R_0 and R_∞ contributed in scaling and determining the extremities of the plot. It was quite evident that the data seemed to fit for values of $k>1$ which was due to the dimensions, properties and characteristics of the simulation model.

5.4 Contribution of Arterial diameter to the dielectric relaxation model for Simulation response

The simulation geometry used to obtain the response included isotropic tissue domains of fat, muscle and artery (blood). In the previous section, we discussed the fitting of the impedance data obtained at three diameters – d1, d2 and d3, to their respective Cole equivalent models. The fits obtained provided acceptable Cole parameters for all the three diameters, when fitted individually. In this section, we discuss the introduction of arterial diameter, d, as a variable in the Cole dielectric model to fit the response at all the three diameters. The objective is to model the overall impedance response through a single modified Cole equation including d as a parameter along with the usual Cole parameters.

5.4.1 Mathematical modelling

The simulation model geometry provides the initial basis of understanding the effect of changing diameter of the artery to the overall impedance. From the model, the artery has been considered as a cylindrical tube of uniform diameter d which was changed to three instances- d1, d2 and d3 to mimic the diameter changes with blood flow.

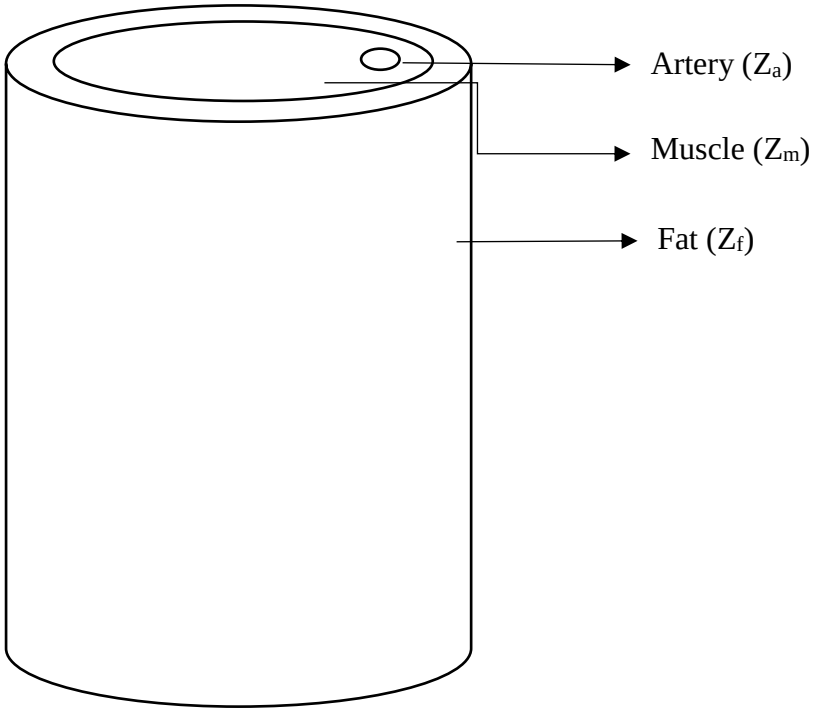

Figure 5.10: Simplified geometry of the developed forearm model showing tissue domains with their impedances represented as – artery (Z_a), muscle (Z_m) and fat (Z_f)

The developed simulation model can be simplified (for understanding) as shown in Figure 5.10.

The overall impedance can thus be defined from assumed parallel components as:

$$\frac{1}{Z} = \frac{1}{Z_a} + \frac{1}{Z_m} + \frac{1}{Z_f} \tag{5.20}$$

For a cylindrical geometry, the impedance of the artery can be defined as:

$$Z_a = \rho_a \frac{l_a}{A_a} \tag{5.21}$$

where ρ_a is the resistivity of the artery (blood), l_a is the length of the arterial section and A_a is the cross-sectional area. The area of cross section for a cylindrical artery can be defined in terms of diameter as:

$$A_a = \pi \frac{d^2}{4} \tag{5.22}$$

Hence, from equations (5.21) and (5.22), we can write:

$$Z_a = \rho_a \frac{4\, l_a}{\pi d^2} \tag{5.23}$$

Considering the dimensions of the artery are significantly smaller than the muscle and fat tissue domains, we can assume that the diameter changes in the artery will only affect the impedance of the artery and not of the muscle or fat domains. In other words, pulsatile blood flow causes a change in the arterial diameter which is reflected as an overall change in the impedance due to the change in the impedance of the arterial domain, i.e., Z_a.

Based on the above interpretation, it should be reasonable to assume the contribution of the arterial diameter changes to the overall impedance changes being related through:

$$Z \propto \frac{1}{k\, d^2}$$

The overall impedance data was described by a double relaxation Cole equation, along with the contribution of the arterial diameter, as:

$$Z = R_\infty + \frac{1}{k * d^2}\left(\frac{R_{01} - R_\infty}{1 + (I\frac{\omega}{\omega_{c1}})^{\alpha_1}} + \frac{R_{02} - R_\infty}{1 + (I\frac{\omega}{\omega_{c2}})^{\alpha_2}} \right) \tag{5.24}$$

where R_{01} and R_{02} are the two resistances at zero frequency, R_∞ is the resistance at high frequency, ω_{c1} and ω_{c2} are the respective characteristic frequencies of the two dispersion regions, α_1 and α_2 are the corresponding dispersion coefficients for the two relaxation

mechanisms, k is a proportionality constant and d is the arterial diameter. The fitting was performed as in the previous section by constructing a similar cost function to minimize the sum of root mean squared errors.

5.4.2 Cole parameters for simulation response varying with diameter

The simulation data for impedance was obtained for three diameters (as mentioned previously in section 3.5) and was used for fitting of the model defined by equation (5.24). The fit parameters obtained are listed in Table 5-4.

Table 5-4: Parameters obtained after fitting simulation data in equation (5.24)

R_{01} (Ω)	R_{02} (Ω)	R_{∞} (Ω)	ωc1 (rad/s)	ωc2 (rad/s)	k	α1	α2
464.58	100.13	7.15	3.13×10^6	1.24×10^6	324749	1.395	1.636

The obtained fit for all the three diameters can be seen in Figure 5.11. The comparison of the obtained fit data with the simulation data was analysed by performing a Bland-Altman analysis.

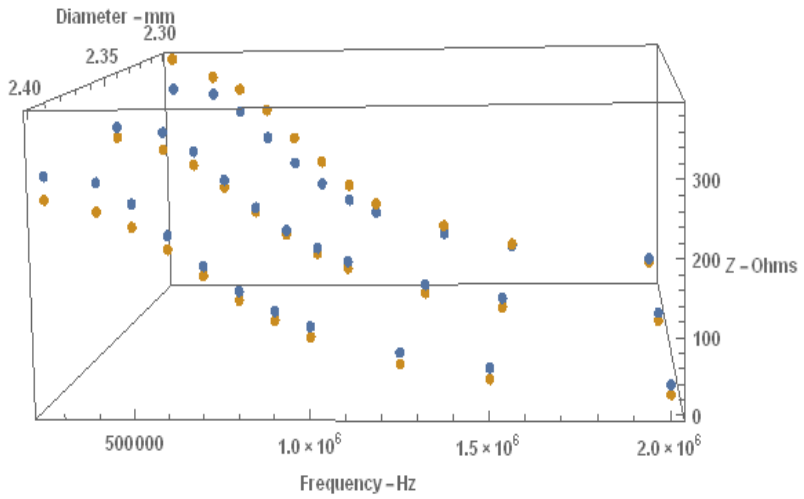

Figure 5.11: 3D plot showing the comparison of simulation data with fit data computed at the three diameters – 2.3mm, 2.35mm and 2.4mm: ● Fit data, and ● Simulation data

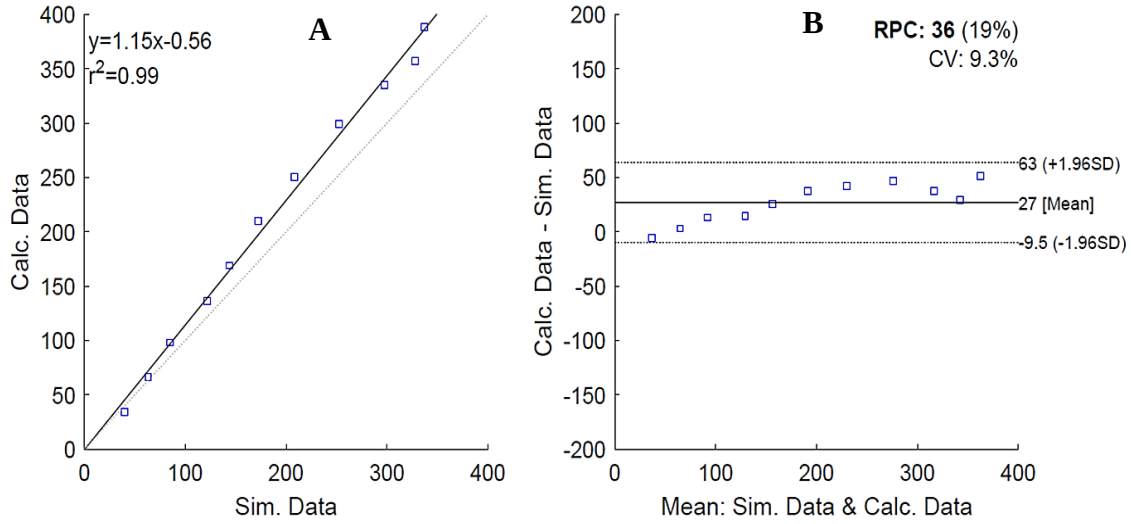

Figure 5.12: (A): Correlation plot and (B): Bland Altman plot for the fit performance of Z for diameter d1 = 2.3mm. The horizontal axis represents the mean of the simulation and the calculated impedance values (in Ω) and the vertical axis represents the difference in the impedance magnitudes of the two data sets (in Ω).

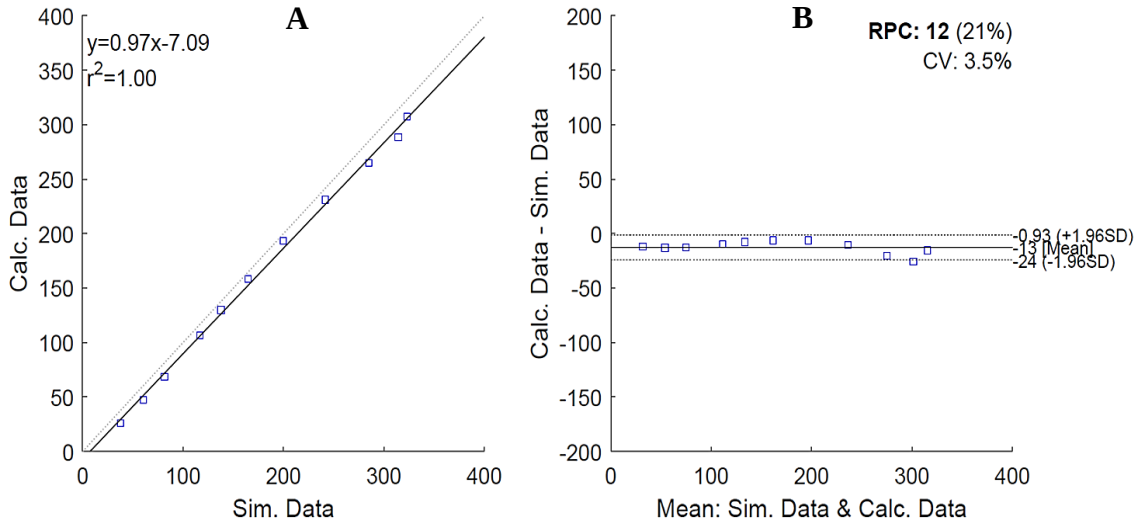

Figure 5.13: (A): Correlation plot and (B): Bland Altman plot for the fit performance of Z for diameter d2 = 2.35mm. The horizontal axis represents the mean of the simulation and the calculated impedance values (in Ω) and the vertical axis represents the difference in the impedance magnitudes of the two data sets (in Ω).

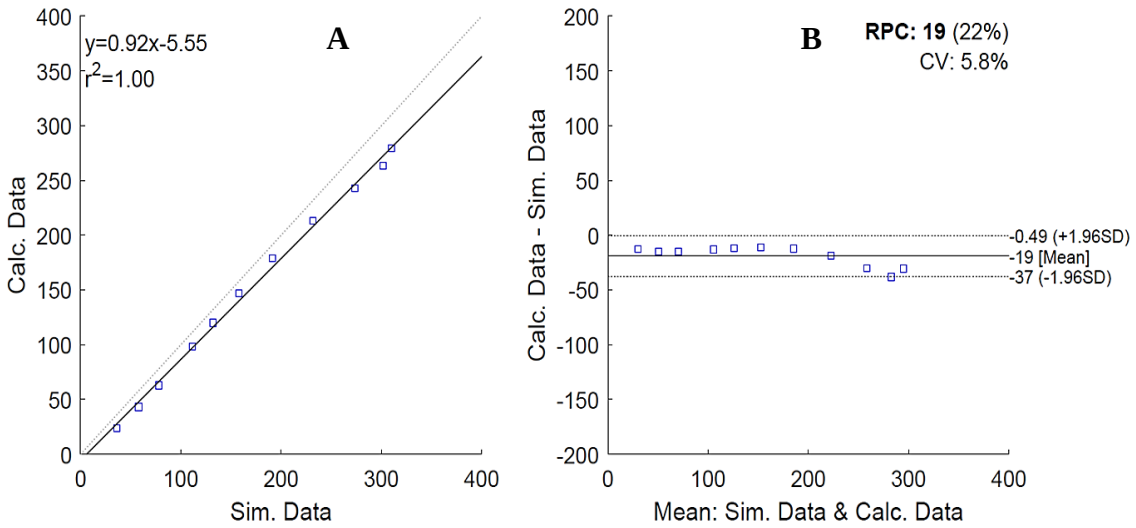

Figure 5.14: (A): Correlation plot and (B): Bland Altman plot for the fit performance of Z for diameter d3 = 2.4mm. The horizontal axis represents the mean of the simulation and the calculated impedance values (in Ω) and the vertical axis represents the difference in the impedance magnitudes of the two data sets (in Ω).

As can be seen from Figure 5.12, Figure 5.13 and Figure 5.14, the correlation plot (A) and Bland Altman plot (B) verify a good fit performance for the three diameters 2.3mm, 2.35mm and 2.4mm respectively. The r squared correlation coefficients obtained were 0.99, 1.00 and 1.00 for the three diameters. The agreement of the simulated and fit values for the three diameters was found to be within 95% confidence intervals (no outliers) as an acceptable criterion for a good fit. However, there are deviations of the fit data from the simulated data at lower frequencies where the fit was larger in magnitude for the first diameter and slightly lower in the other two. This is also evident from the slope of the correlation plot being greater than 1 for the first diameter and less than 1 for the other two. One of the reasons for this might be the dissimilarity between the consideration of the artery as a uniform cylinder and its curved geometry in the simulation model. Also, the double relaxation Cole model used for fitting does not itself fully reflect the dispersion spectra.

The acceptable fit to a double relaxation Cole equation implies two dispersion mechanisms which can be interpreted as one for the arterial (blood) domain and the other for fat/muscle domain. Based on the difference in the R_0 values for the first and the second part of equation (5.24) it appears that the first relating to the fat/muscle (higher R_0) and the second relating to the artery (lower R_0).

The consideration of a diameter variable in the Cole equation for defining the dielectric response of the forearm section has implications for understanding hemodynamics using

impedance measurements. Although the magnitude of the impedance of a tissue volume such as the forearm is dependent on many factors, changes in the impedance reflect the contribution of pulsatile blood flow and may be useful in clinical applications.

5.5 Closure

This chapter discussed the electrical modelling perspective for the measured impedance of the simulation study. The chapter was divided into three sections – the first introduced a parametric electrical circuit model for the simulation analysis performed in Chapter 3, the second section highlighted a Cole model for the same and the third section focussed on modelling the effect of diameter changes on the overall impedance spectra. The parametric modelling of the simulation response aimed at characterising the obtained impedance response in terms of passive resistance and capacitance values of the fat, muscle and artery tissue domains. A Debye type modelling approach was followed to relate the impedance spectra at three arterial diameters considering an unknown contribution of the arterial dimensions to the overall response. The second section employed a more realistic Cole – Cole model approach characterising the impedance response in terms of Cole parameters (R_0, R_∞, ω_c and k). The two sections provide two different electrical modelling perspectives where the first approach aims at quantifying the contribution of each tissue layer to the overall impedance and the second section quantifies the system in terms of resistances at extreme frequencies and dispersion coefficient.

The third section highlights the effects of diameter to the overall impedance response. The impedance spectra at different arterial diameters were modelled using diameter as a variable. The quality of the fit obtained points to the potential of employing MF-BIA to identify the diameter changes in the artery.

Chapter 6 PILOT STUDY IN HUMAN FOREARM SECTION

6.1 Introduction

The primary objective of this study has been to investigate MF-BIA as a means to estimate diameter changes in the radial artery. The simulation study in Chapter 3 yielded three impedance spectra within 1 kHz to 2 MHz for three instances of arterial diameter. The behaviour was verified by realising similar tissue properties through a forearm phantom at the same diameters. The results obtained clearly showed decreased magnitude of impedance spectra with increasing diameter. In section 5.4, a parametric relationship was developed relating artery diameter with curves fitted to impedance spectra from simulation.

This chapter describes a pilot study performed on the left human forearm section of three human subjects to estimate the radial artery diameter in response to pulsatile blood flow, from impedance measurements in combination with the previously developed models. This study is not intended to be a complete validation of the technique, but instead show that estimation of radial artery diameter using impedance spectroscopy is feasible. The estimated diameter were compared with measurements from an ultrasound device.

6.2 Experimental Setup and Procedure

6.2.1 Impedance Measurements

The experimental procedure was set up to measure the impedance response of the ventral side of the forearm section spanning within 10 cm from the wrist. The placement of electrodes was chosen to mimic the configuration used in the simulation study. The separation was 1cm between each electrode, where the outer pair was used to feed the input current and the inner pair to measure the voltage, as can be seen in Figure 6.1.

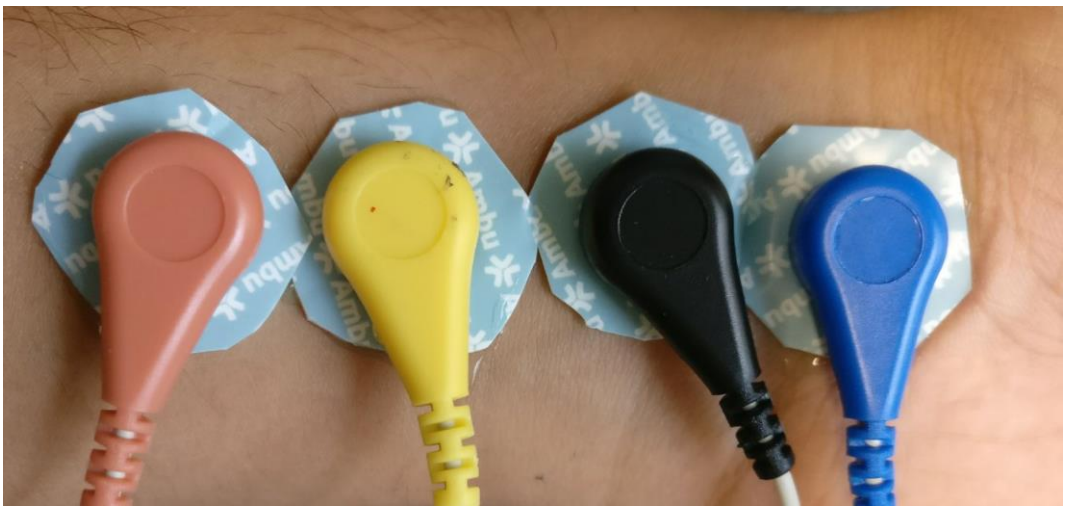

Figure 6.1: Electrode setup for impedance measurements at forearm section

The electrode setup was connected to the Quadra® impedance spectroscopy device under a similar configuration as used for the phantom experiments. The frequency range of measurements was 1 kHz – 349 kHz.

The impedance measurements were taken under conditions of normal blood flow and artery occlusion. The artery was occluded by using a sphygmanometer (Accoson^{TM} MK2 BS 2744, Accoson, UK) with the maximum cuff pressure of 200 mmHg. The cuff was placed over the electrodes. Two sets of measurements were performed – with occlusion and without occlusion. The measurements without occlusion were performed to reflect the total impedance response of the blood flow in the radial artery and the fat and muscle tissues surrounding it. The artery occlusion was performed to squeeze the blood out of the artery at the measurement site and reflect the impedance of only the fat/muscle tissues. This was intended to acquire two sets of measurements to separate the contribution of blood flow from the overall impedance response. This procedure was performed in 3 subjects - all males (aged 26, 42 and 67) under normal resting conditions.

The impedance spectra obtained using the Quadra® impedance spectroscopy device was collected and analysed using MATLAB.

6.2.2 Ultrasound Measurements

The diameter for the left radial artery was measured for all the three subjects by ultrasound (Acuson Sequoia^{TM} C512, Siemens Healthcare, Germany) using a 17L5 HD probe, within 1 minute to the impedance measurements. The high-resolution probe (17L5) was

employed with frequency capabilities up to 15 MHz and was suitable for obtaining high resolution M-mode images at the superficial depths (up to 2 cm). The probe was placed transverse to the arterial to acquire cross-sectional images and the diameter changes with the blood flow. The ultrasound measurements were performed under the condition of no arterial occlusion by the cuff along with the impedance measurements, as can be seen in Figure 6.2.

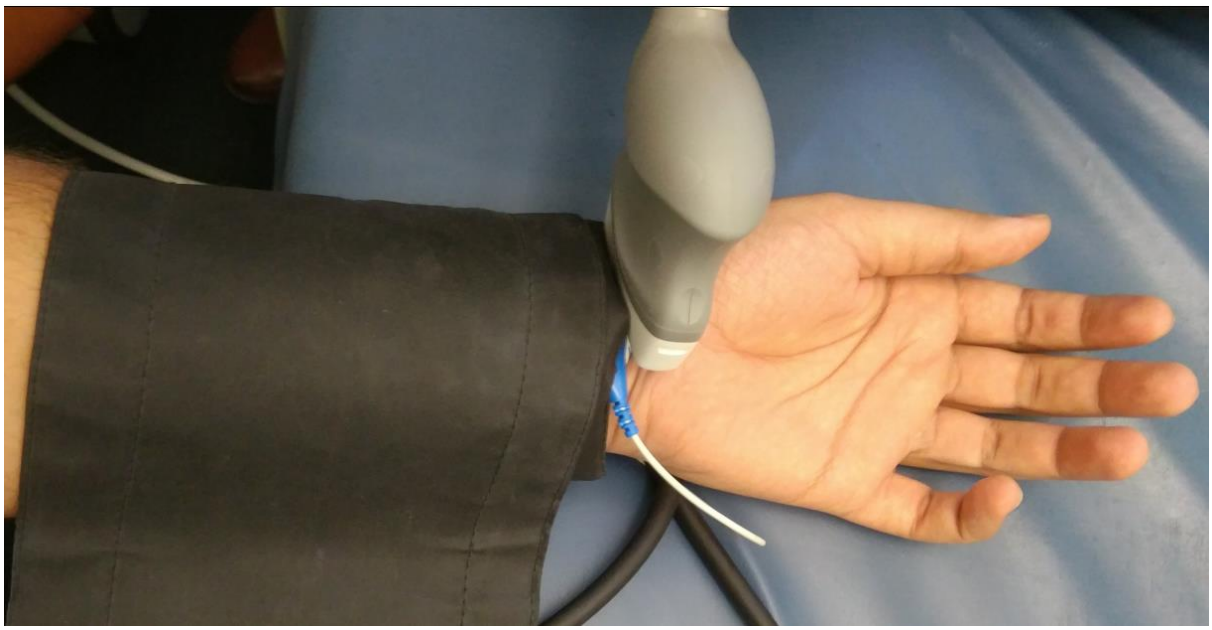

Figure 6.2: Ultrasound and Impedance measurement setup with cuff pressure at 200 mmHg

6.3 Impedance Measurement Results

The measurements obtained under normal conditions and the artery occluded with the cuff pressure at 200 mmHg have been shown in Figure 6.3.

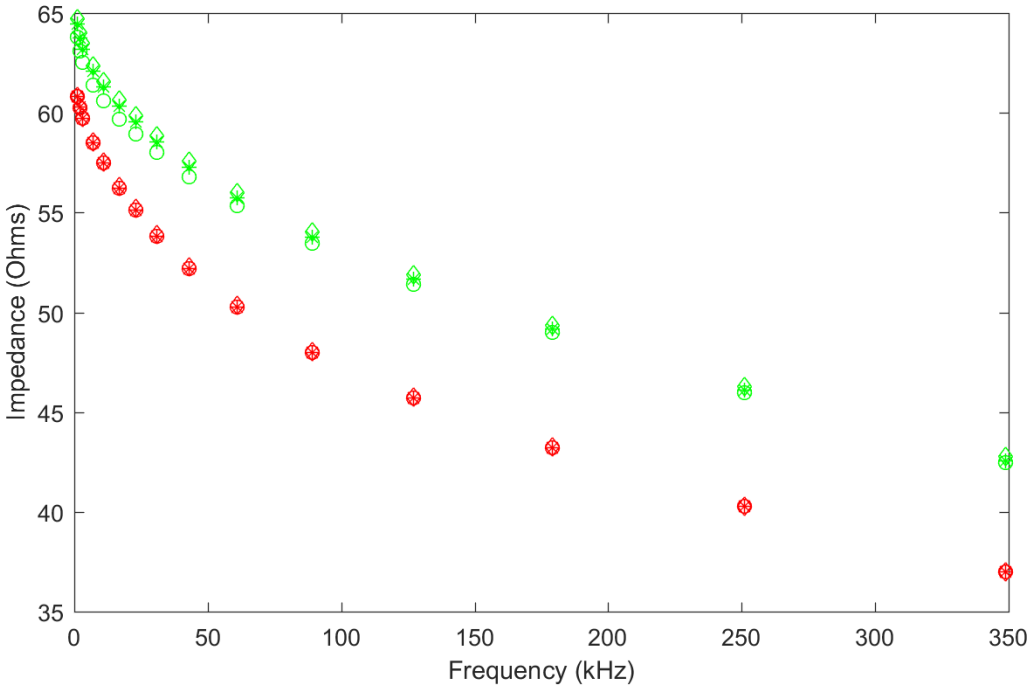

Figure 6.3: Impedance measurements for subjects 1,2 and 3 as measured by Quadra® impedance spectroscopy device, with and without the application of cuff pressure: ✳ Subject 1 – with cuff, ✳ Subject 1 – without cuff, ○ Subject 2 – with cuff, ○ Subject 2 – without cuff, ◇ Subject 3 – with cuff, and ◇ Subject 3 – without cuff

Figure 6.3 shows a significant difference in the impedance of the forearm under the two conditions. The overall magnitude of impedance was found to be larger in the case of occluded artery (shown in green) than the normal conditions (shown in red). This is expected due to the relatively low impedance of blood compared to other tissue.

The Quadra® impedance spectroscopy device measured the impedance spectra at a rate of 1000 samples/second. This facilitated the time domain analysis of the impedance values. The impedance spectra samples for each subject were recorded for 10 seconds which were analysed for each frequency. The collected samples were processed to extract the impedance contributions due to blood flow by passing time series through a low pass filter with cut-off 7.5 Hz followed by high pass filtering above 0.7 Hz to remove baseline wander. The resultant signals obtained can be seen in Figure 6.4, Figure 6.5 and Figure 6.6 for subjects 1, 2 and 3 respectively.

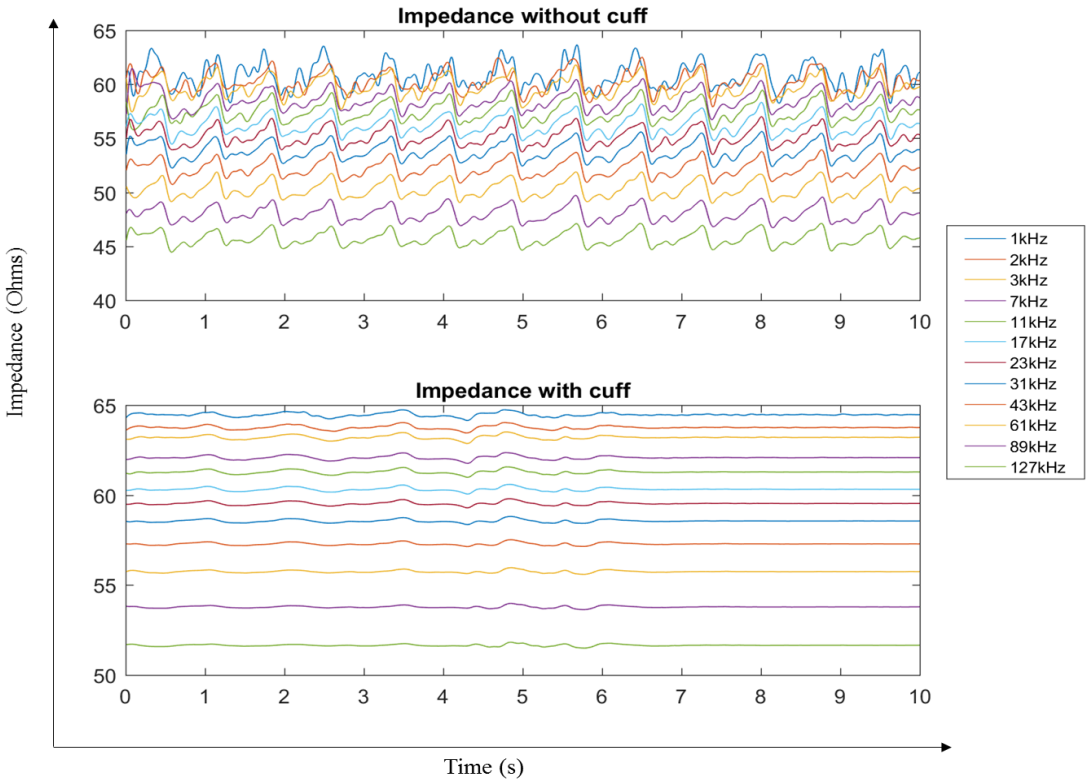

Figure 6.4: Impedance waveforms measured within 1 kHz – 127 kHz for subject 1, without and with cuff application

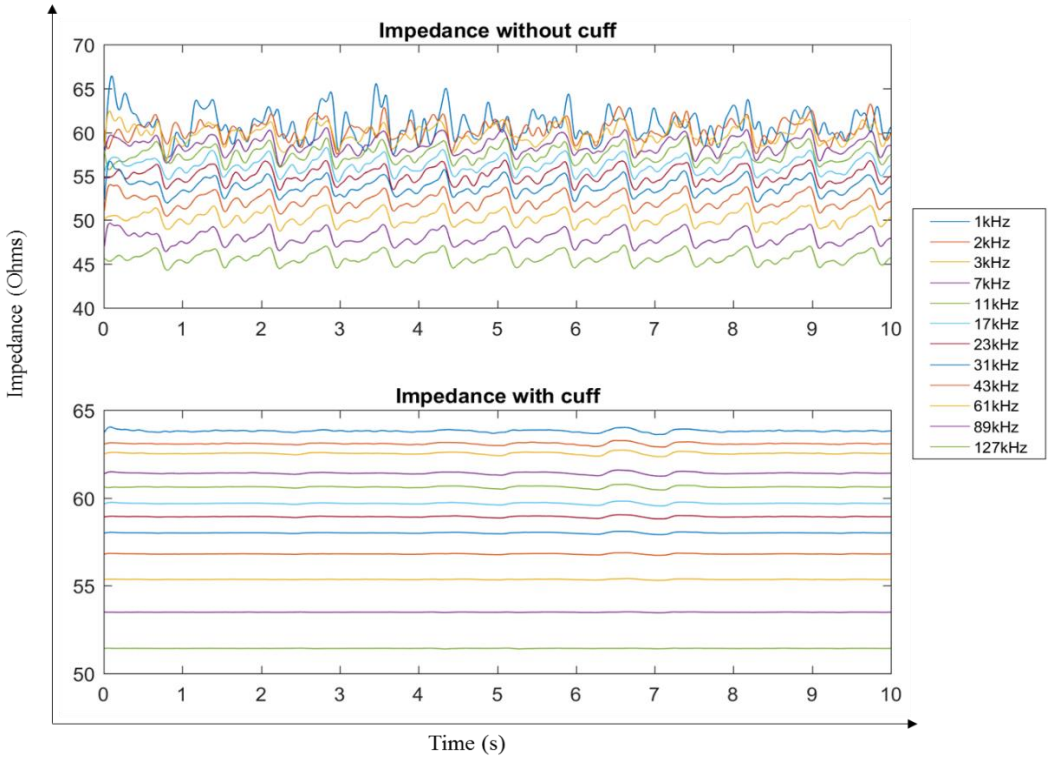

Figure 6.5: Impedance waveforms measured within 1 kHz – 127 kHz for subject 2, without and with cuff application

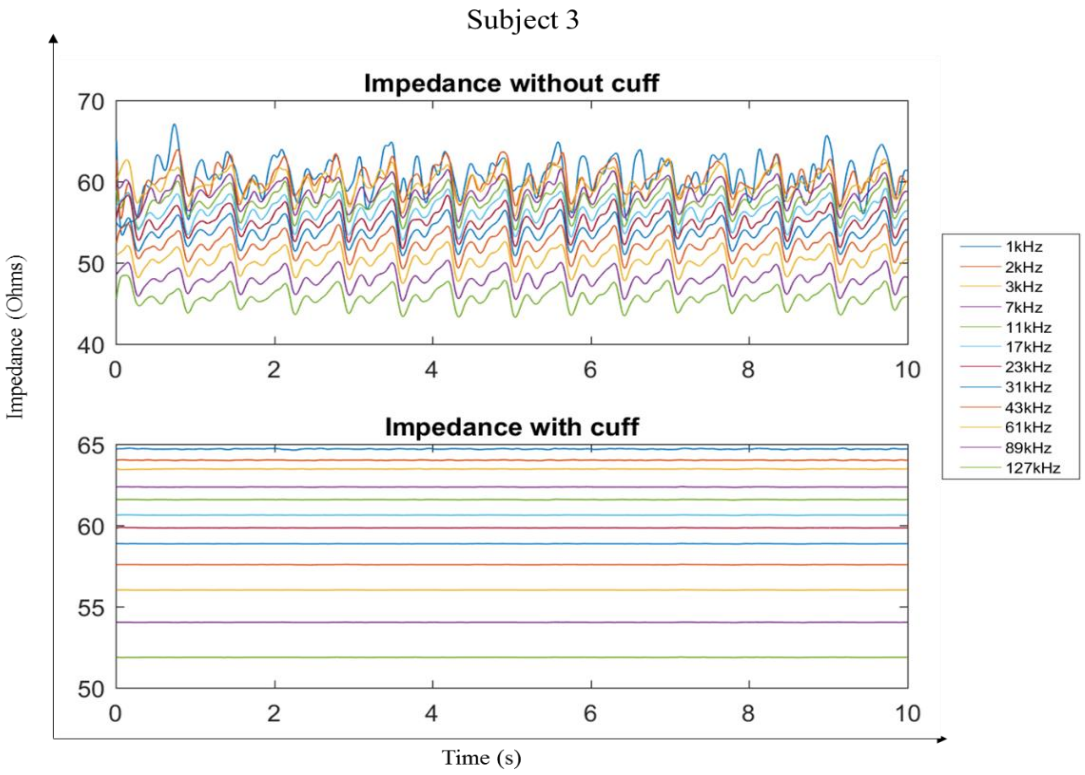

Figure 6.6: Impedance waveforms measured within 1 kHz – 127 kHz for subject 3, without and with cuff application

As can be seen in the obtained impedance signals, the application of cuff pressure was reflected in negligible variations in signal amplitudes as compared to quite significant and periodic waves in the other case. The acquired impedance waveforms can be seen to be noisy at lower frequencies of 1 – 3 kHz. Also, the impedance for the frequencies 179 kHz, 251 kHz and 349 kHz were too noisy to be considered. Hence, only the signals up to 127 kHz were considered for further analysis.

To separate the impedance contribution of blood flow in the radial artery from the combined impedance measurement of the forearm (impedance without artery occlusion), a parallel combination of the impedance of the artery and the remaining tissue layers of fat and muscle was assumed. The applicability of this model (with separate fat and muscle domains) is described in section 5.4 and supported by the obtained results. Considering the impedance of pulsating radial artery to be Z_a and of the fat/muscle layers to be $Z_{f/m}$, it was assumed that:

$$\frac{1}{Z_t} = \frac{1}{Z_a} + \frac{1}{Z_{f/m}} \tag{6.1}$$

where Z_t is the total impedance of the forearm. Hence, the impedance of artery can be calculated as:

$$Z_a = \frac{1}{\frac{1}{Z_t} - \frac{1}{Z_{f/m}}} \tag{6.2}$$

From the above measurement procedure, the impedance measurement without the cuff was considered to be Z_t and the measurement with the artery occluded considered as $Z_{f/m}$.

Moreover, by considering the radial artery to be cylindrical in section leads to a relation between the impedance and the arterial diameter, stated as:

$$Z_a = \frac{1}{\sigma} * \frac{l}{A} = \frac{1}{\sigma} * \frac{l}{\pi d^2/4} \tag{6.3}$$

where σ is the conductivity of blood (0.7 S m^{-1}), l is the length of the section of the artery under consideration, A is the area of cross-section of the radial artery ($A = \pi d^2/4$, where d is the arterial diameter). In this case, l = 0.01m and hence the diameter of the artery can be calculated as:

$$d\ (in\ mm) = 135 * \sqrt{\frac{1}{Z_a}} \tag{6.4}$$

Following the above expression (equation (6.4)), the obtained diameter waveforms for each subject can be seen in Figure 6.7.

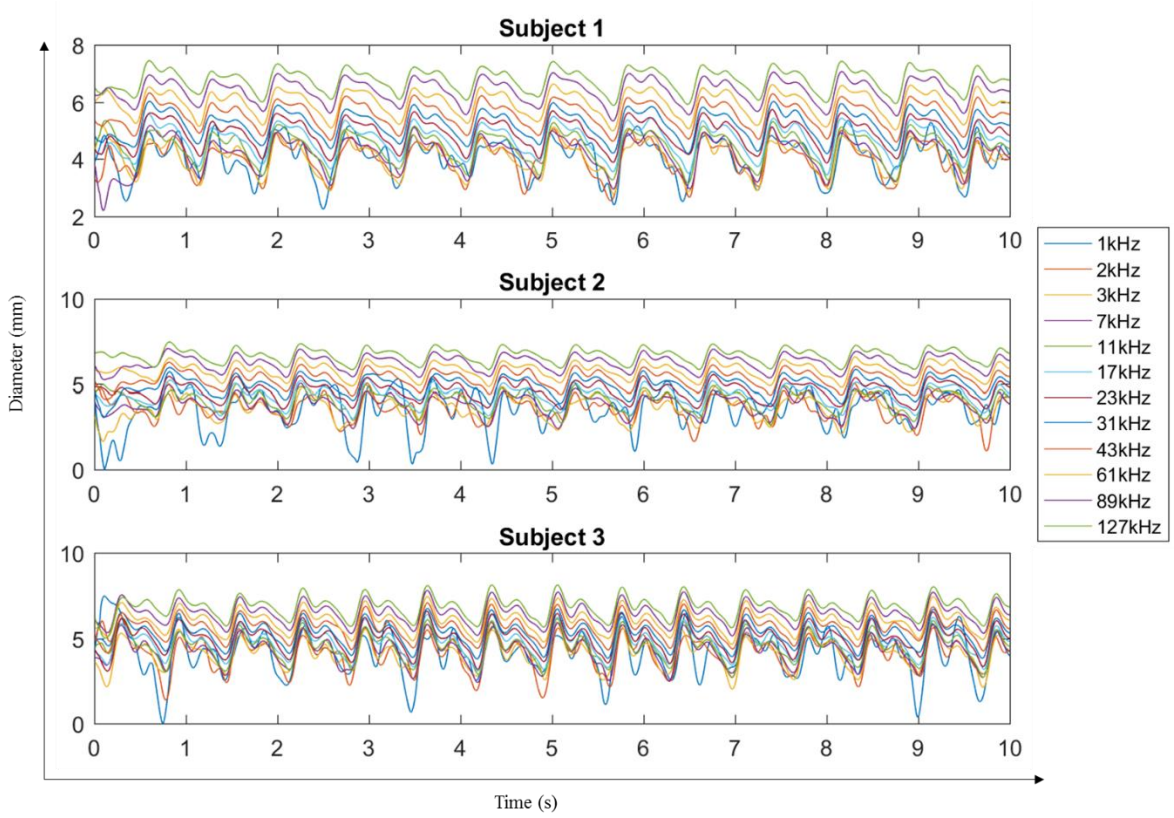

Figure 6.7: Diameter waveforms calculated from impedance measurements for each subject using equation (6.4)

To relate the calculated diameter values more closely to the actual diameter of the radial artery, equation (6.4) was modified to:

$$d(in\ mm) = k * 135 * \sqrt{\frac{1}{Z_a}} + c \tag{6.5}$$

where k is the proportionality constant and c is the offset. This linear scaling is thought to compensate for two aspects. Firstly, when the cuff is inflated, blood is removed not only from the artery under consideration but from the venous system and other perfused tissue. Therefore, the impedance being measured using the method above represents both the volumetric changes due to blood flow and also a component of non-pulastile blood (from veins and other perfused tissues). Secondly, as observed from the distribution of the electric field inside the tissue domains during the simulation study, the conduction path was identified to be normal to the forearm fat and muscle layers before and after traversing through the arterial section, which cannot be exactly represented as a parallel combination of tissue domains. These two unmodelled considerations do not change with time and are taken into account by considering the above mentioned correction factors (k and c), although it is recognised that more investigation into these effects is warranted.

The values for best fit were found to be 0.15 for k and 1.5 for c. Hence the modified relation of arterial diameter to the impedance was taken to be:

$$d(in\ mm) = 20.25 * \sqrt{\frac{1}{Z_a}} + 1.5 \tag{6.6}$$

The diameters of the radial artery for all three subjects within the frequencies 1k – 127 kHz were obtained using equation (6.6) as seen in Figure 6.8. Also, Figure 6.9 shows the diameter waveform for subject 1 between the 3rd and 8th second to indicate more clearly the morphology of the diameter changes due to blood flow as obtained from the measured impedance.

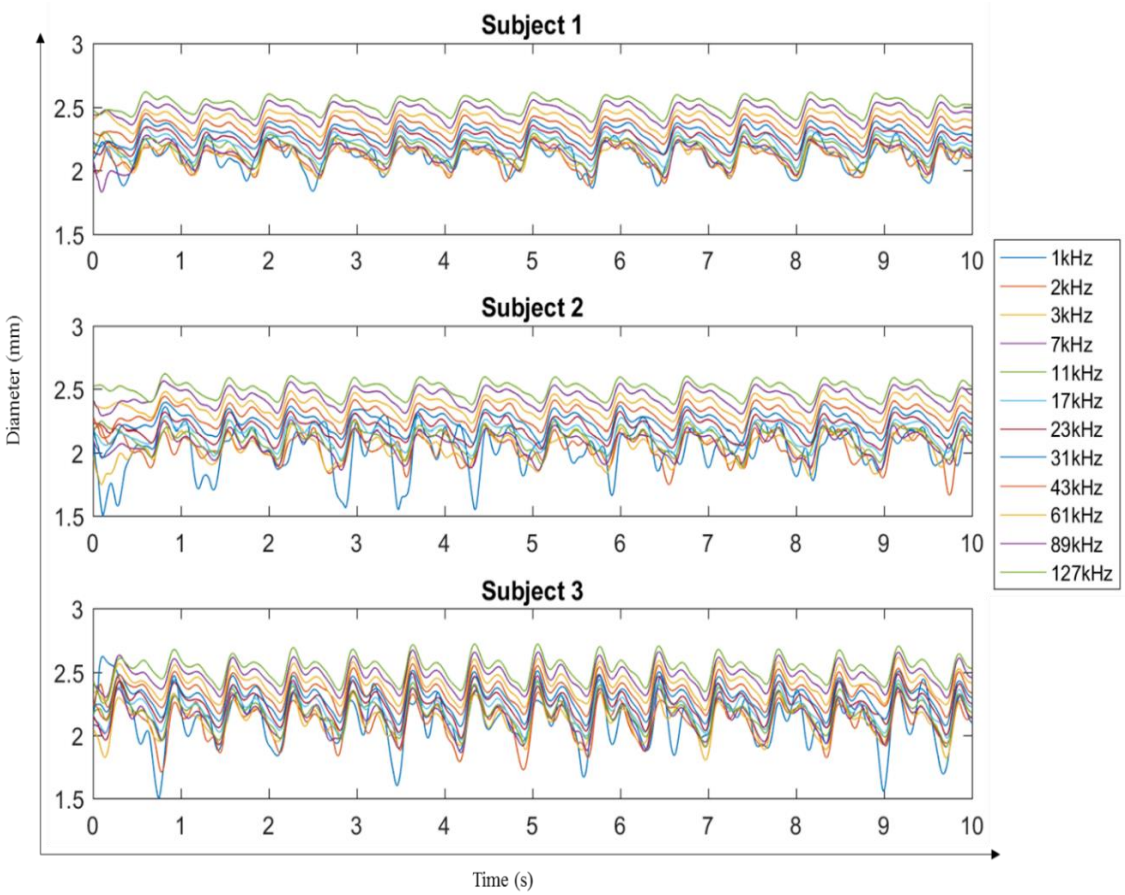

Figure 6.8: Diameter waveforms calculated from impedance measurements for each subject using equation (6.6)

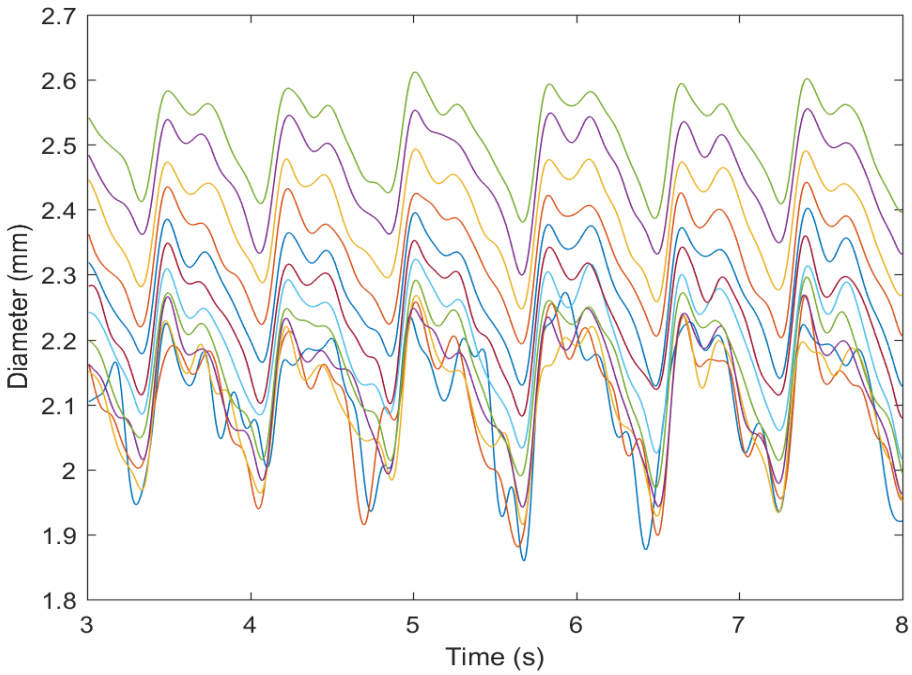

Figure 6.9: Diameter waveform for subject 1 for 5 seconds showing wave morphology for frequencies within 1 kHz – 127 kHz

6.4 Ultrasound Measurements for Radial Artery diameter

As a reference, ultrasound measurements to estimate the diameter of the left radial artery were performed on all three subjects, at the same time as the impedance measurements. Initially, the probe was adjusted to correctly locate the cross-section of the artery for M-mode analysis. Figure 6.10, Figure 6.11 and Figure 6.12 show the obtained cross-sectional diameter changes in the left radial artery for subjects 1, 2 and 3 respectively.

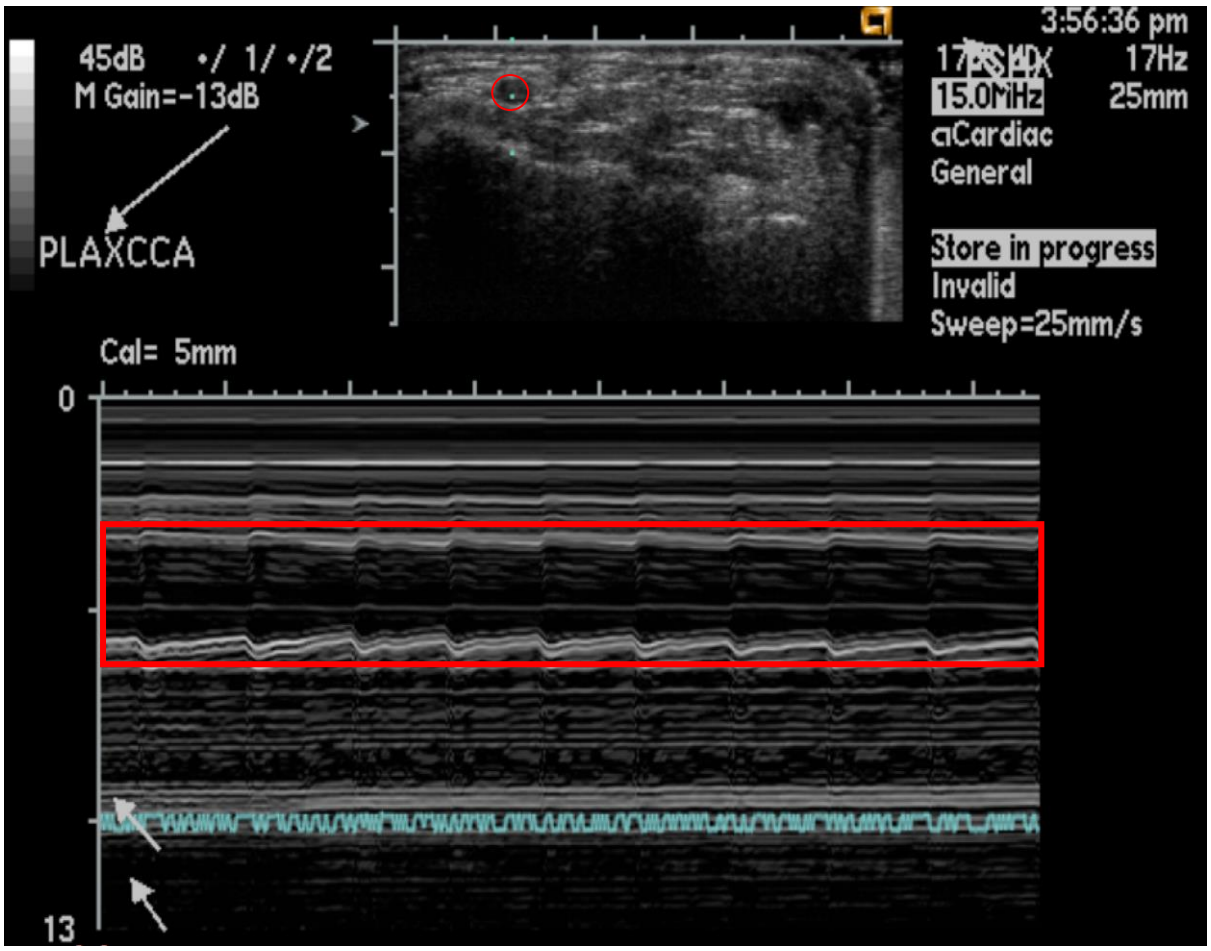

Figure 6.10: Radial artery diameter changes measured using ultrasound for subject 1. The artery is outlined by a red circle and the corresponding M-mode diameter wave is outlined using a red rectangle.

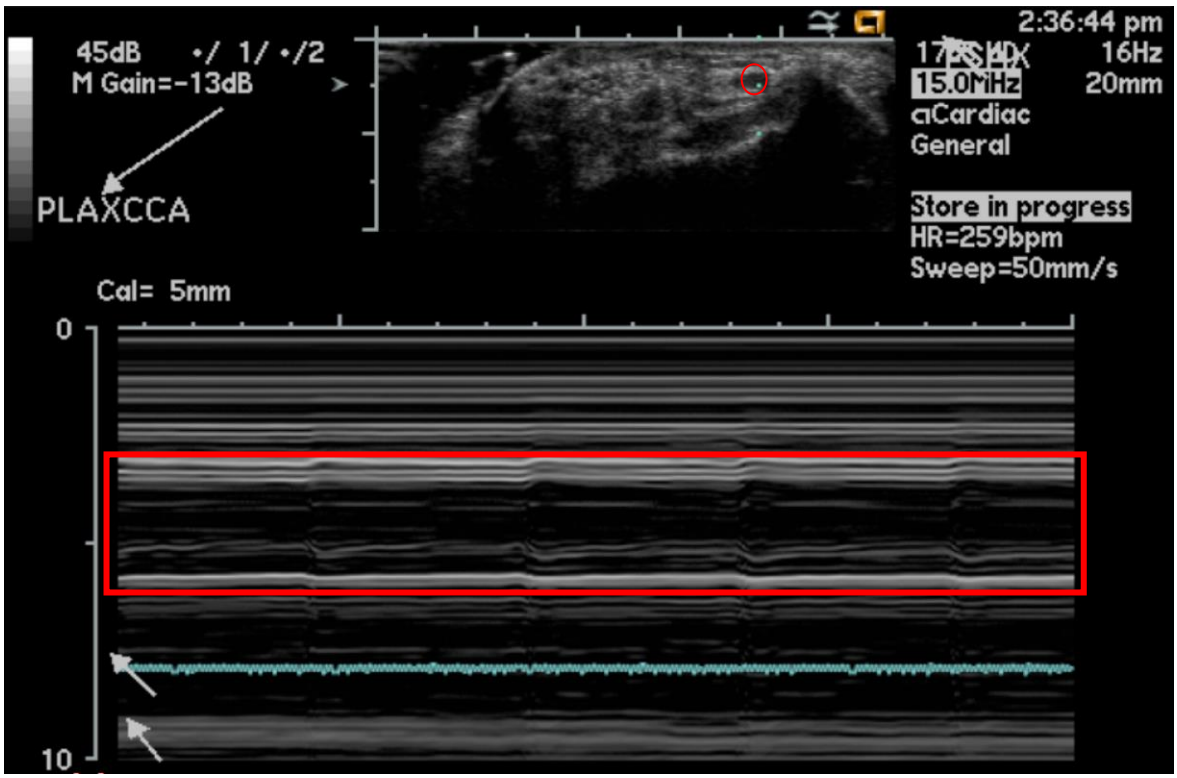

Figure 6.11: Radial artery diameter changes measured using ultrasound for subject 3. The artery is outlined by a red circle and the corresponding M-mode diameter wave is outlined using a red rectangle.

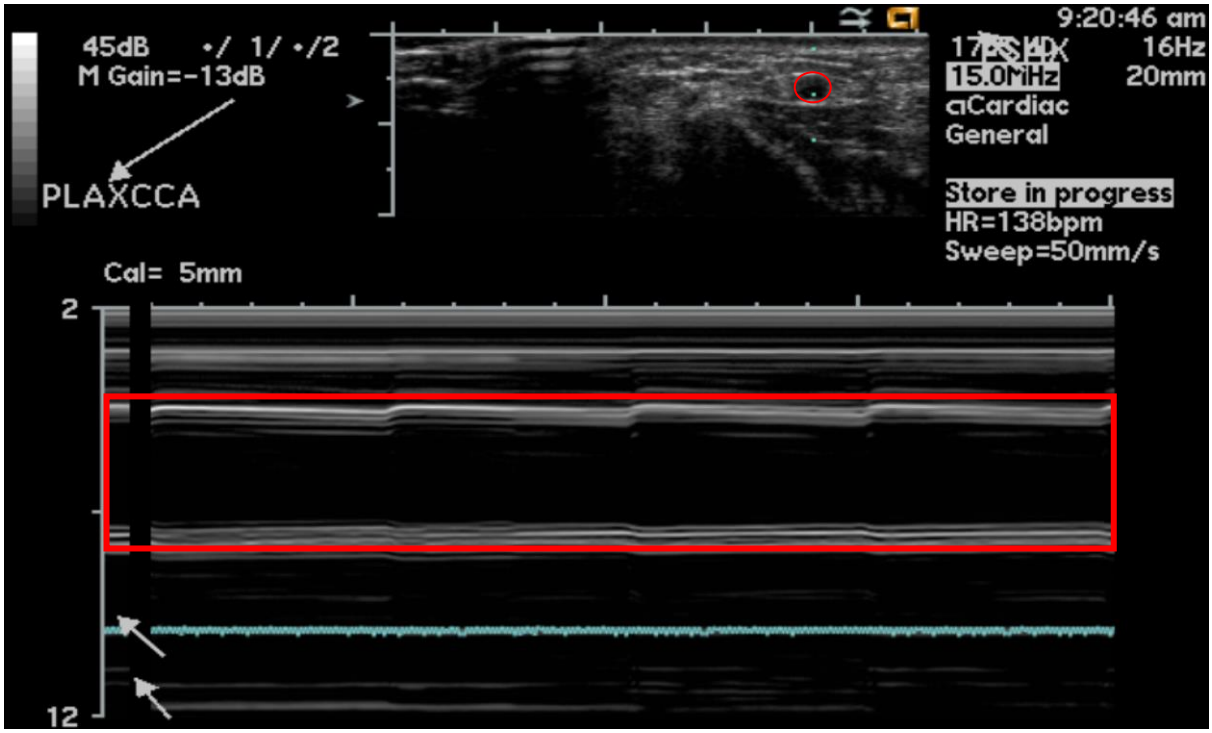

Figure 6.12: Radial artery diameter changes measured using ultrasound for subject 3. The artery is outlined by a red circle and the corresponding M-mode diameter wave is outlined using a red rectangle.

Extraction of the diameter waveform was performed using image processing in MATLAB. Each ultrasound image was smoothened and contours were extracted containing the information of each related pixel. The contours for the near and far artery walls (on the probe) were identified and the overall diameter waveform was obtained as a difference between the two. The extracted diameter waveform from the above ultrasound images for all the subjects can be seen in Figure 6.13, Figure 6.14 and Figure 6.15 respectively.

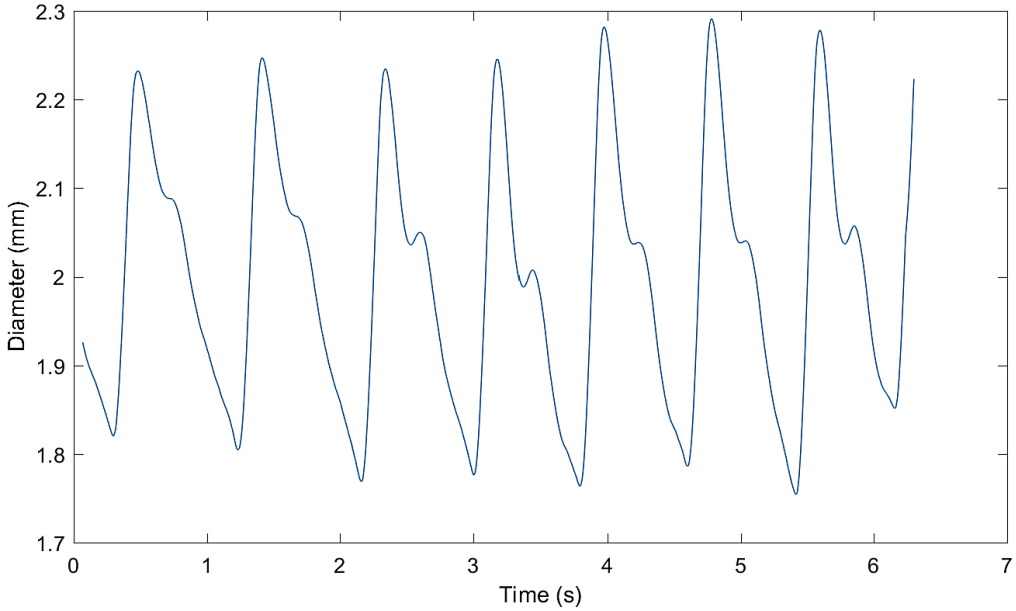

Figure 6.13: Diameter waveform for subject 1 from the ultrasound measurement

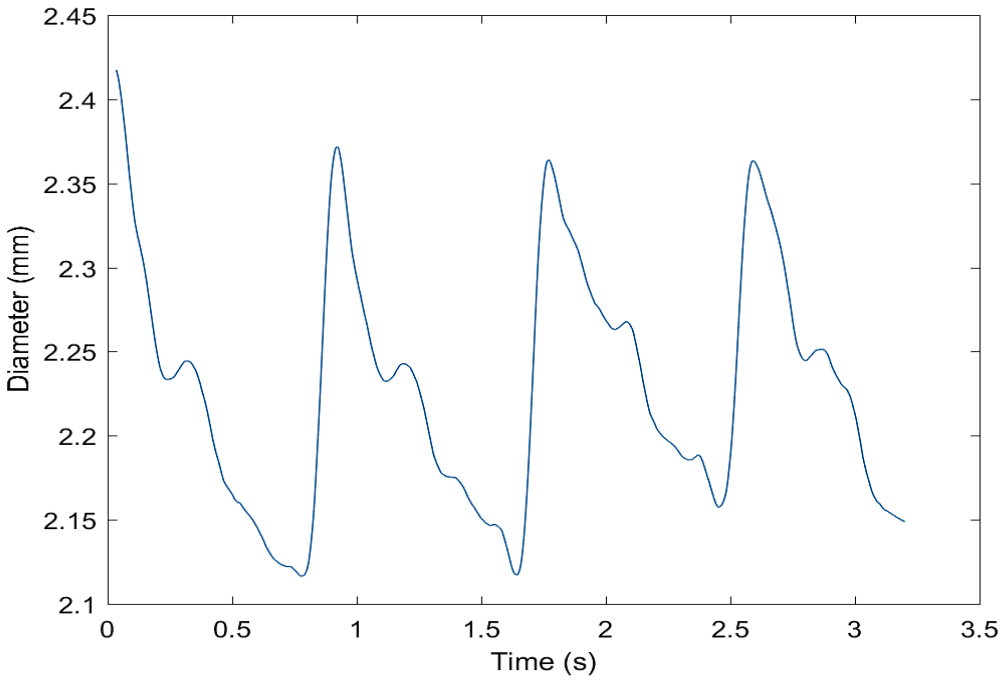

Figure 6.14: Diameter waveform for subject 2 from the ultrasound measurement

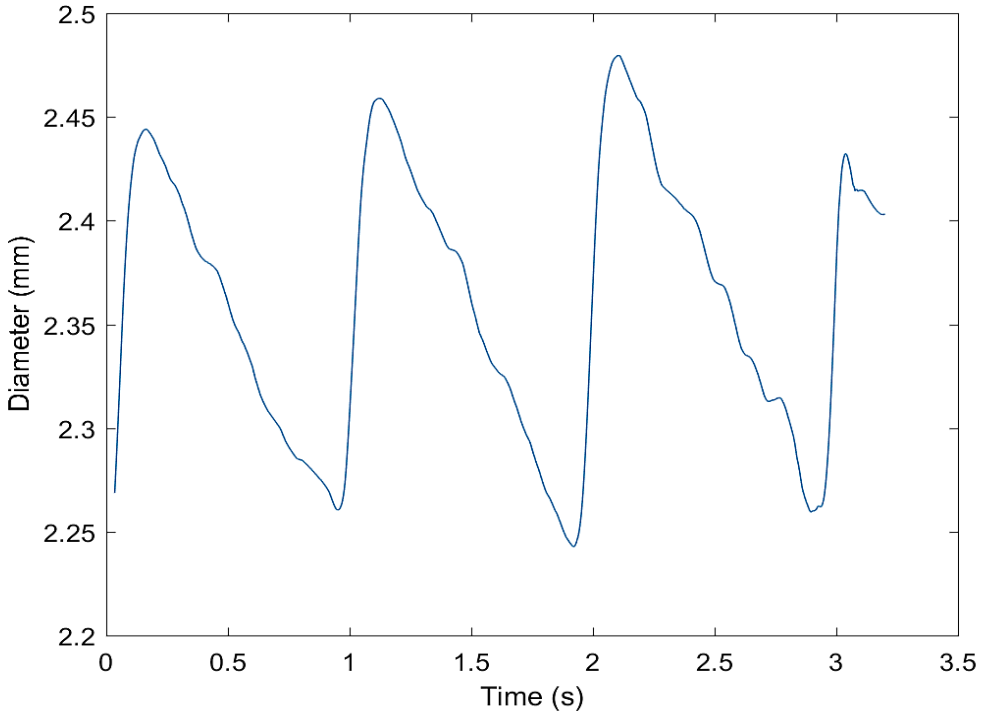

Figure 6.15: Diameter waveform for subject 3 from the ultrasound measurement

6.5 Comparison of the Simulation study with Impedance and Ultrasound calculated diameter results

The diameter calculated from the impedance measurements were different for different frequencies but possessed the similar waveform morphology to that measured by ultrasound. Also, the magnitude of changes in calculated diameters with each pulse (0.1 – 0.2 mm) was found to be similar to ultrasound (0.1 – 0.3 mm), thus showing the potential of impedance measurements for estimating arterial diameter changes.

The simulation study resulted in impedance spectra for three different diameters within the frequency range of 1 kHz – 2 MHz. These results explain why diameter varies when estimated from impedance at different frequencies. In this section, this relationship is investigated to explain the difference in diameter estimated from measured impedance at different frequencies using equation (6.6).

Figure 6.16 shows the diameters calculated using equation (6.6) from the simulation response using subject 1 as the reference ultrasound diameter. (That is, the ultrasound-measured diameters of subject 1 were used to interpolate the impedance spectra from the simulation described in Chapter 3) The morphology of each of the diameter waves follows that of the ultrasound measured diameter. However, the mean magnitudes and the peak-to-trough amplitudes of the estimated diameters increase with increasing frequency. This is due to the decreasing magnitudes of the impedance at higher frequencies and very small differences in the impedance spectra at frequencies around 2 MHz as is clear from the simulation results. The trend of the increasing diameter values with simulation frequency can be seen in Figure 6.17 and is symmetrically opposite to that observed for the impedance spectra (Figure 3.16) as impedance is inversely proportional to artery diameter. However, the increasing trend is not so significant at lower frequencies (1 – 250 kHz). The comparison of these diameters with the reference ultrasound diameter has been more clearly represented in Figure 6.18.

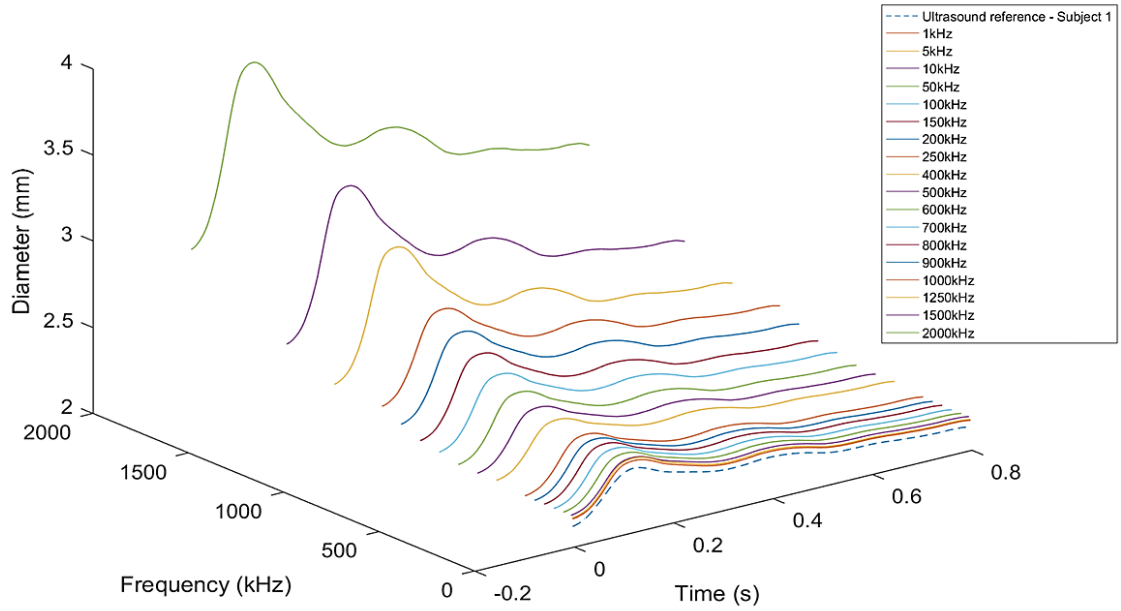

Figure 6.16: 3-D plot showing the diameters obtained using simulation response for frequencies 1 kHz – 2 MHz compared with the ultrasound measured diameter for subject 1 (dashed line)

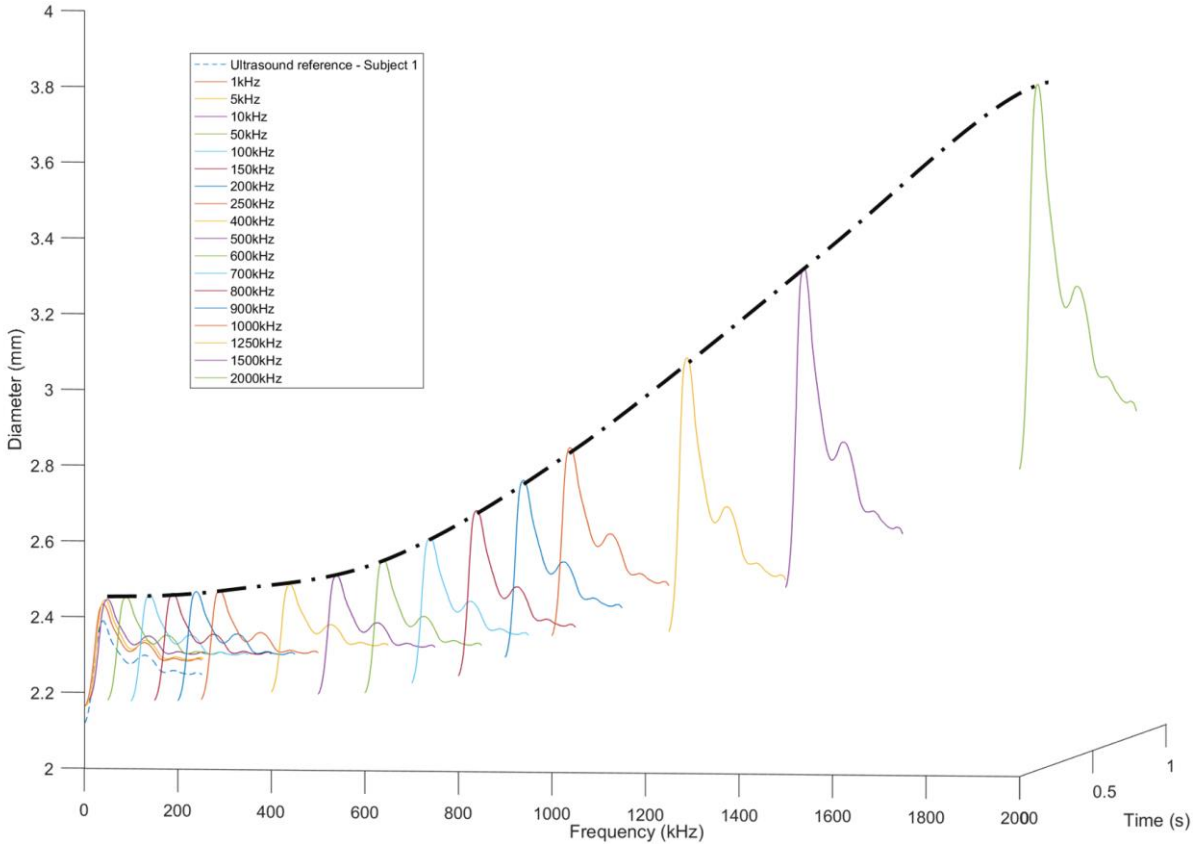

Figure 6.17: Diameters obtained from simulation following an increasing trend with frequency

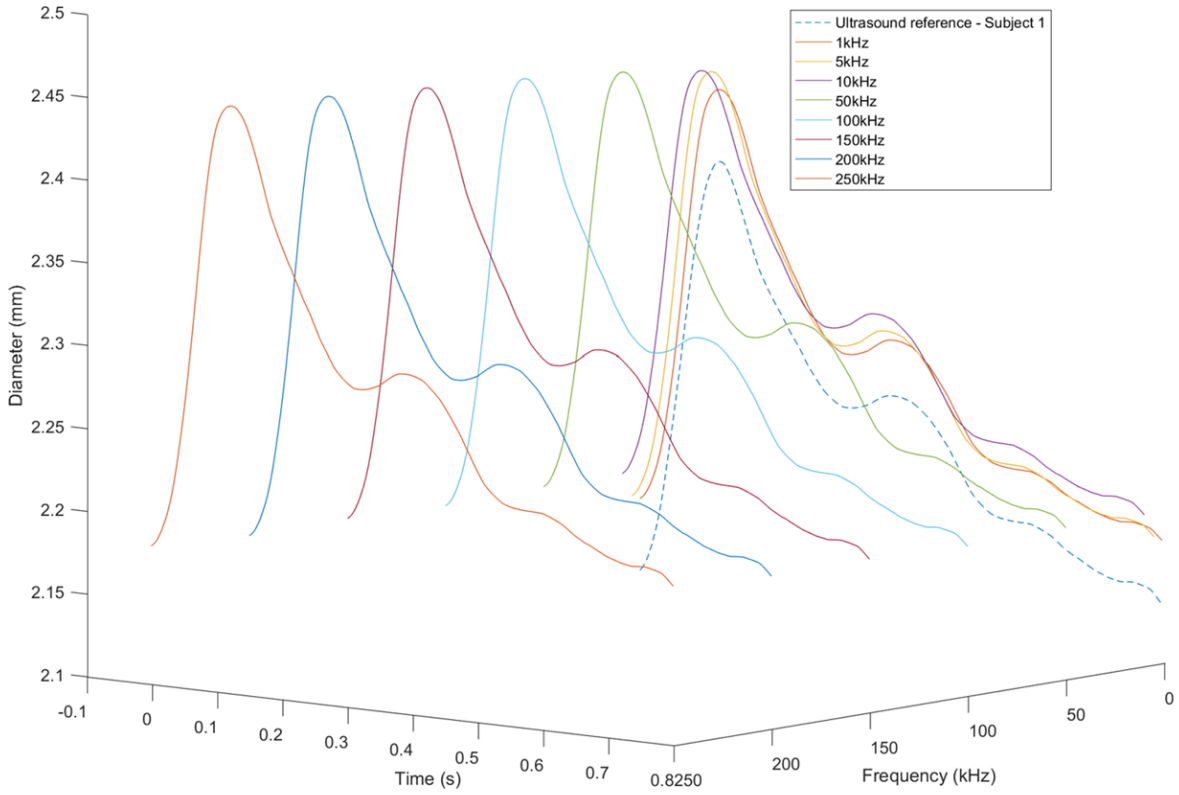

Figure 6.18: Simulation obtained diameters within 1 kHz – 250 kHz with same magnitude and in constant proportion with the reference ultrasound measured diameter (dashed line)

The multi-frequency results presented so far have utilised impedance spectra obtained from the simulation. Diameters were also calculated from the impedance measured using the Quadra® impedance spectroscopy device and compared with the ultrasound reference diameter, as can be seen in Figure 6.19 for subject 1. Similar behaviour was observed in case of other two subjects. Figure 6.20 shows the trend of the diameters with increasing frequency.

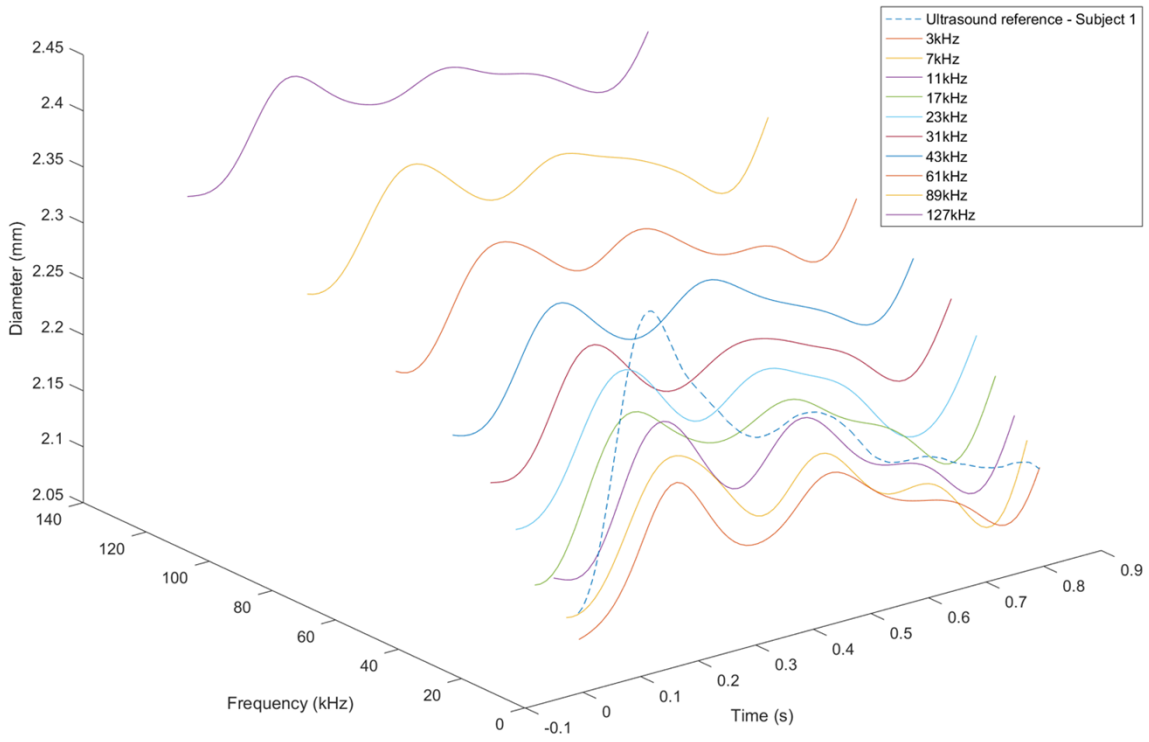

Figure 6.19: 3-D plot showing the diameters obtained from Quadra® impedance spectroscopy impedance measurements compared with the ultrasound measured diameter for subject 1 (dashed line)

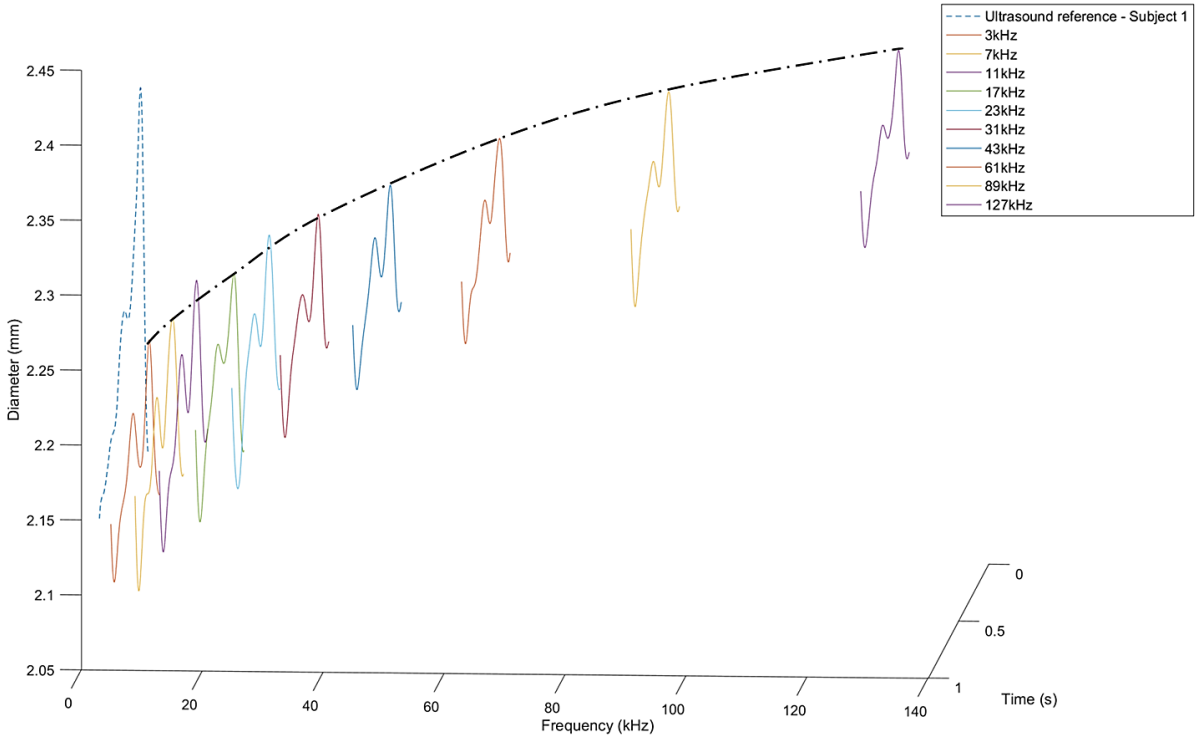

Figure 6.20: Diameters obtained from Quadra® impedance spectroscopy impedance measurements following an increasing trend with frequency

The diameters derived from measured impedance show a similar increase in the trend of the diameter values as obtained by the simulation derived diameters. However, the trend tends to converge at a frequency of 127 kHz in the latter case as compared to 2 MHz in the former case. This difference is possibly due to differences between the dispersion behaviour of the simulation study and the impedance measurements on human subjects. For the simulation and phantom studies, the three tissue layers – fat, muscle and the artery – were clearly separated domains and the dielectric properties for the model and the phantom were defined to be isotropic. In real human forearm tissues, the tissue layers are all perfused to some extent with blood, and anisotropic tissue properties are expected.

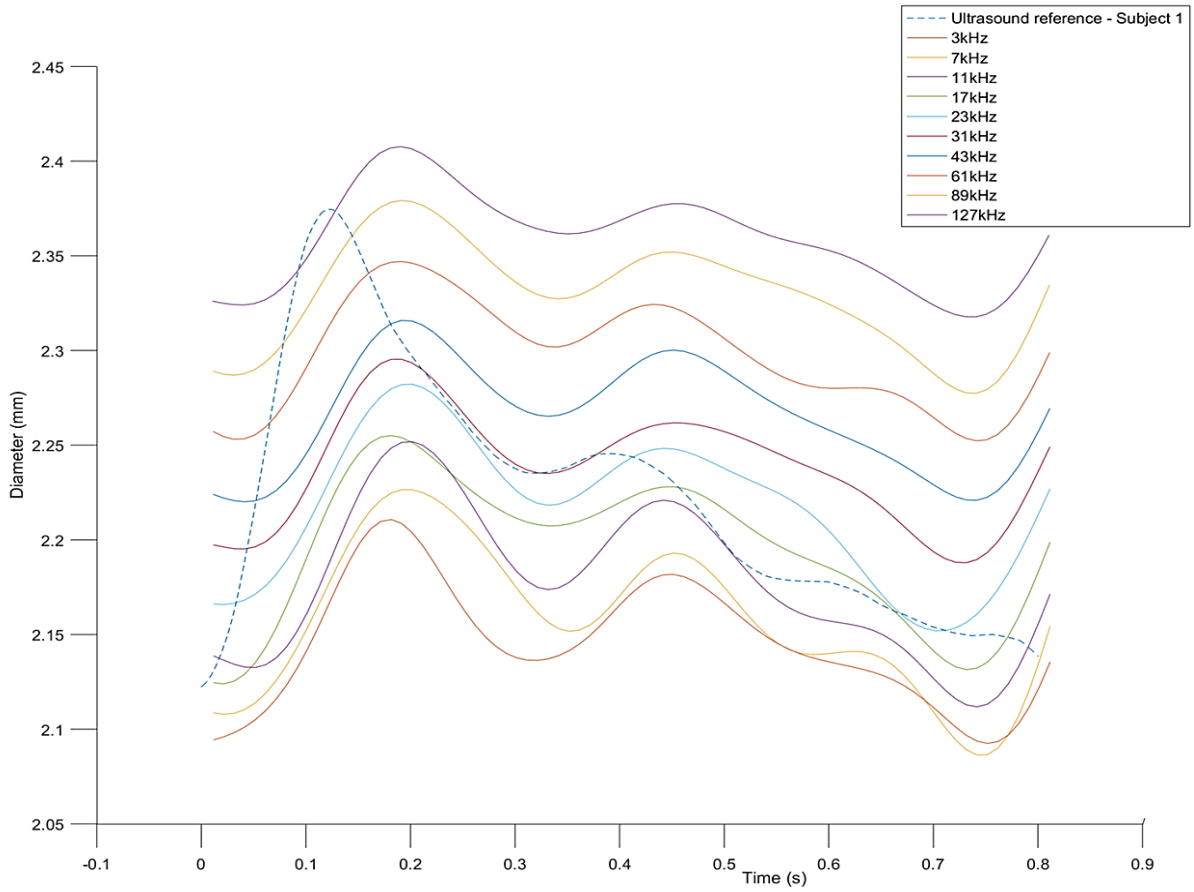

Figure 6.21: Comparison of the amplitudes of impedance derived diameters with the ultrasound diameter for subject 1

The peak-to-trough amplitudes of the impedance obtained diameters were significantly different from the ultrasound measurements. This can also be explained by differences between dielectric properties of the human forearm compared to the values used in the simulation.

With regards to the morphology, impedance and ultrasound diameter waveforms are similar but show some apparent phase changes, as seen in Figure 6.21. This may partly

be due to the pulse wave and pulse rate changing between the time of the impedance and ultrasound measurements. However, some of the differences in shape are likely to indicate a need for further improvement in the impedance derived diameters reflecting the pulsatile blood flow. One focus should be on efficiently determining the constants k and c in equation (6.5), which have been arbitrarily selected for this initial investigation.

6.6 Closure

This pilot study aimed at investigating the prospects of using MF-BIA for estimating the changes in left radial artery due to pulsatile blood flow. The objective was to identify whether the simulation, phantom and analytical models discussed in previous chapters bear any resemblance to real life.

The results obtained indicate that the use of multiple frequency measurements may aid in improving the accuracy of the otherwise conventionally employed SF-BIA approach adopted for hemodynamic monitoring. Here, we have compared the simulated impedance response at three artery diameter instances and the diameter calculated from the impedance measurements on three human subjects with the diameter measurements from the ultrasound. In case of the simulation, the obtained diameter values at frequencies up to 250 kHz were found to be of the same order of magnitude and peak-to-trough amplitude as the ultrasound diameters for subject 1. However, diameters derived from impedance measurements differed in the magnitude and peak amplitudes from the ultrasound reference, probably due to different dielectric properties of the tissues under test.

These results lay a foundation for using MF-BIA in estimating accurate diameter changes. The main challenge will be to effectively determine the relative contributions of the artery and surrounding tissue domains.

Chapter 7 CONCLUSION AND FUTURE WORK

This research investigated the dielectric response of forearm tissues to understand the contribution of the changing diameter of the radial artery to the overall impedance spectrum. This study focused on three aspects:

1. Simulation analysis of a human forearm section with fat, muscle and blood as the three tissue domains. The simulation was performed at three different artery dimensions to quantify the resulting difference in the impedance response within the β dispersion range of frequencies. This approach to investigate the dielectric behavior of human forearm tissues has not previously been reported in the literature.
2. Construction and analyzing the dielectric behavior of a forearm section phantom to verify the results and behavior observed in the simulation response.
3. Analytical, electrically modeling the change in the impedance spectra with diameter regarding passive tissue parameters and Cole parameters.

Also, a pilot study was undertaken to identify whether the results from these aspects related to measurements from human subjects.

7.1 Simulation Analysis

The simulation study was performed to gain a detailed insight into the behaviour of the individual and overall dielectric tissue domains in the human forearm. The simulation study was carried out through quantifying the electrical response of modelled tissue layers (fat, muscle and radial artery) using an electromagnetic finite element analysis. The frequency range of interest was chosen within 1 kHz – 2 MHz (β dispersion).

One of the limitations of the simulation study was that it only focussed on the compositional dielectric properties of the three tissue layers. Any dynamic and non-linear effects were neglected, although the blood flow was mimicked by simulating at three instances of arterial diameters which allowed analysis of the corresponding changes in the impedance spectra. Also, the study only focussed on one forearm geometry, with one artery (radial artery), without the inclusion of bone, skin and other blood vessels.

The outcomes and conclusions of this study were:

a. The overall impedance of the simulation model was found to exhibit Cole-type behavior, which was expected since the tissues have been found to exhibit complex dielectric properties showing multiple and distributed dispersions within the β dispersion frequency range. The Cole-type impedance response validated the simulation approach and methodology to model the tissue layers for measuring their overall impedance.
b. The impedance spectra were found to be different for different arterial diameters. This verified the contribution of blood flow-induced arterial cross-sectional changes to the overall impedance measurements. However, the observed decrease in the impedance magnitude with increasing diameter was non-linear. Also, the difference in the impedance spectra was found to be prominent at lower frequencies and almost negligible at the higher frequency end of the spectra. This has not been discussed previously in the literature and indicates that the contribution of the blood flow to the Cole-type behavior is only prominent at lower frequencies, verifying the majority of this contribution as being resistive.
c. The contribution of the bone tissue to the overall impedance behavior was found to be negligible. There was a decrease in the impedance magnitude with including bone in the simulation geometry, however, no change in the dielectric response was observed. This finding can aid in simplifying the future investigations to measure diameter changes by optimizing the choice of tissue domains to be considered.

7.2 Human Forearm phantom

The simulation results provided important insights into the electrical response of the tissues. This was verified by constructing a human forearm phantom to mimic the simulation model. Tissue simulants were designed to exhibit the dielectric properties of the three tissue domains. These materials were characterized based on their conductivity and relative permittivity. This was followed by the construction of the human forearm phantom to mimic the simulation geometry at the three arterial diameters and estimating their response.

This investigation was limited to investigating the impedance response of bulk, isotropic electrical properties of the tissue simulants. The tissue simulants approximated the

dielectric properties of tissues as modeled by Gabriel but exhibited a shifted dielectric dispersion mechanism. Also, the tissue simulants did not mimic the physical properties and were limited to only fat, muscle, and blood as in the simulation study.

The outcomes and conclusions of this investigation were:

a. A coaxial cylindrical sensor was constructed and calibrated to approximate the dielectric properties of liquids. A measurement analysis procedure was developed to mitigate the erroneous effects due to electrodes and polarization for the precise calculation of conductivity and relative permittivity of the liquid medium.
b. This research has identified mixtures of readily available constituents that can be used to mimic blood in the β dispersion range. Previously published research has primarily evaluated phantom properties in higher frequency ranges. A mixture of 80% propylene glycol with 20% 4 M NaCl solution was found to approximate the bulk conductivity and relative permittivity of blood within 1 kHz – 2 MHz. There is potential for such a mixture to also approximate density and dynamic viscosity of blood, but this was not studied in detail.
c. The surveyed literature identified mimicking the physical properties of muscle and fat tissues using gelatine-water and agar-water/oil suspensions, respectively. However, there was not enough investigation into the dielectric properties of these tissues in the β dispersion range. In this study, a suspension of 5% agar in 0.05% NaCl solution was found to mimic the dielectric parameters of fat tissue in the β dispersion range. The dielectricity of the muscle tissue was found to be simulated using 3.77% agar and 1.88% gelatine suspended in 0.3% NaCl solution with 18.8% propylene glycol. This supports the use of such constituents to both physically and electrically simulate the properties of muscle and fat tissues.
d. The forearm phantom was constructed using the above-identified simulants and a Cole-type response was observed. The simulation analysis was re-investigated with the measured properties of the tissue simulants, and the phantom was found to replicate the impedance spectra with excellent agreement. It is concluded that material, electrical properties in the forearm will significantly affect the measured impedance values, although the spectral behavior is similar. This can assist in providing a better alternative to experimentally investigate the electrical properties of the forearm tissues, especially within the β dispersion range which is lacking in the literature.

7.3 Electrical Modelling

The results of the simulation analysis were modeled electrically to understand the interpretation of the response in terms of existing bioimpedance theories.

The electrical modeling only aimed at approximating the dielectric response of the simulation study while neglecting other affecting parameters. Each of the adopted modeling approaches was based on some assumptions. The parametric modeling assumed the relation between the resistances of the artery at two diameter instances as an arbitrary function of the ratio of the diameters. The initial Cole modeling assumed only a single dispersion model and a two-dispersion model was assumed while assuming the impedance of the artery to be equivalent to that of a cylindrical section.

The following outcomes were obtained:

a. A parametric fitting of simulation data was performed to calculate the individual resistances of the fat/muscle and arterial domains. The model fitted to a Debye-type response for each diameter where the relation between the parameters for two diameters was defined by assuming resistance ratios (RR) as an arbitrary power function of the diameter ratios. The model implemented a new circuit analog for the forearm tissue layers and provided an understanding of the significance of modeling artery as other than a cylindrical conductor. Also, the model proposed a new analytical method of parameter estimation defining individual tissue domains.
b. A Cole modeling approach was used to represent the simulation data in terms of Cole parameters. The model analyzed the mathematical implementation of the Cole-type behavior of the forearm tissues. It was found to simultaneously fit the complex impedance, real (resistive) and imaginary (reactive) values for each diameter with excellent agreement, except at lower frequencies.
c. The relation of diameter to the simulation measurements was modelled and found to fit to an inverse square relationship with a two dispersion Cole model. This can help in developing models and algorithms for estimating arterial diameters from impedance measurements.

Moreover, a pilot study was performed to investigate a more practical application of MF-BIA measurements on human forearm to estimate the changes in radial artery diameter. No comparable study has been found in the existing literature. The methods employed in

this study, including using an inflatable cuff to take measurements in perfused and un-perfused tissue states for analysis with the models presented, have not been reported previously.

The simulation and the phantom impedance results indicate the importance of the actual dielectric properties of the concerned tissues. The results showed that the simulation and the phantom forearm geometries including the fat, muscle and blood domains proved to be reasonable representations of the actual behaviour of the human forearm section, particularly the effect of blood flow induced diameter changes. Also, the significant variations in frequency and the Cole-type response confirmed the choice of frequency range of interest to be within β dispersion, hence making the analysis at very high frequencies not so relevant for the applications considered by this research.

7.4 Future Directions

In summary, this study provided evidence of good potential for using MF-BIA to estimate diameter changes in the radial artery. This was validated against the measurements from the ultrasound and simulation and forearm phantom results.

Further directions of research are suggested to address the limitations of the work presented here.

1. This work assumes a lumped model for the three tissue layers in the simulation analysis. Future work could investigate the need for a more distributed model for forearm tissues layers. For example, in this study, blood (along with fat and muscle) has been considered as a separate tissue layer with isotropic properties. This can be further investigated by considering blood perfusion in the adjacent tissues, microcirculation, the venous system and other arteries in simulation, phantom, and analytical modeling.

2. The effect of blood flow on electrical impedance properties is still the subject of controversy. Future analysis of dielectric response should investigate the significance of these dynamic effects, which can be performed coupled with the associated fluid dynamics due to blood flow.

3. The electrical modeling for the obtained simulation results can be further investigated to better approximate the multiple dielectric dispersion behavior of tissues in the forearm geometry. More sophisticated models could be investigated to relate model parameters, such as the contribution of Cole parameters, with radial diameters.

4. The pilot study demonstrated that MF-BIA has the potential for estimation of arterial diameter changes. However, any practical system would require much more robust validation in a wider range of participants and under varying physiological conditions.

The human tissues work in conjunction with each other, and most of them are perfused with blood. This indicates employing a multi-frequency analysis of the overall dielectric behavior of the tissues. If MF-BIA can be used to measure arterial diameter changes, it could provide itself as an easy, low-cost and comfortable alternative to the standard ultrasound procedure. Further analysis and improvements could help place this technology in mainstream clinical practice for hemodynamic monitoring.

REFERENCES

[1] E. Atzler and G. Lehmann, *Anatomie und physiologie der arbeit*, vol. 1. C. Marhold, 1930.

[2] J. Nyboer, S. Bango, A. Barnett, and R. H. Halsey, "Radiocardiograms: Electrical impedance changes of the heart in relation to electrocardiograms and heart sounds," *J Clin Invest*, vol. 19, p. 963, 1940.

[3] R. Y. T. Sung, P. Lau, C. W. Yu, P. K. W. Lam, and E. A. S. Nelson, "Measurement of body fat using leg to leg bioimpedance," *Arch. Dis. Child.*, vol. 85, no. 3, pp. 263–267, 2001.

[4] H. D. McCarthy, T. J. Cole, T. Fry, S. A. Jebb, and A. M. Prentice, "Body fat reference curves for children," *Int. J. Obes.*, vol. 30, no. 4, pp. 598–602, 2006.

[5] M. Lintsi, H. Kaarma, and I. Kull, "Comparison of hand-to-hand bioimpedance and anthropometry equations versus dual-energy X-ray absorptiometry for the assessment of body fat percentage in 17–18-year-old conscripts," *Clin. Physiol. Funct. Imaging*, vol. 24, no. 2, pp. 85–90, 2004.

[6] S. A. Jebb, M. Siervo, P. R. Murgatroyd, S. Evans, G. Frühbeck, and A. M. Prentice, "Validity of the leg-to-leg bioimpedance to estimate changes in body fat during weight loss and regain in overweight women: a comparison with multi-compartment models," *Int. J. Obes.*, vol. 31, no. 5, pp. 756–762, 2007.

[7] F. R. Faria *et al.*, "Body Fat Equations and Electrical Bioimpedance Values in Prediction of Cardiovascular Risk Factors in Eutrophic and Overweight Adolescents," *Int. J. Endocrinol.*, vol. 2013, p. e501638, 2013.

[8] J. C. Denniston, J. T. Maher, J. T. Reeves, J. C. Cruz, A. Cymerman, and R. F. Grover, "Measurement of cardiac output by electrical impedance at rest and during exercise," *J. Appl. Physiol.*, vol. 40, no. 1, pp. 91–95, 1976.

[9] M. T. Allen, J. Fahrenberg, R. M. Kelsey, W. R. Lovallo, L. J. Doornen, and others, "Methodological guidelines for impedance cardiography," *Psychophysiology*, vol. 27, no. 1, pp. 1–23, 1990.

[10] W. G. Kubicek, R. P. Patterson, and D. A. Witsoe, "Impedance Cardiography as a Noninvasive Method of Monitoring Cardiac Function and Other Parameters of the Cardiovascular System*," *Ann. N. Y. Acad. Sci.*, vol. 170, no. 2, pp. 724–732, Jul. 1970.

[11] R. P. Patterson, “Fundamentals of impedance cardiography,” *IEEE Eng. Med. Biol. Mag.*, vol. 8, no. 1, pp. 35–38, Mar. 1989.

[12] M. Cheney, D. Isaacson, and J. C. Newell, “Electrical Impedance Tomography,” *SIAM Rev.*, vol. 41, no. 1, pp. 85–101, 1999.

[13] C. J. Kotre, “Electrical Impedance Tomography,” *Br. J. Radiol.*, vol. 70, no. Special-Issue-1, pp. S200–S205, Nov. 1997.

[14] R. H. Bayford, “Bioimpedance Tomography (electrical Impedance Tomography),” *Annu. Rev. Biomed. Eng.*, vol. 8, no. 1, pp. 63–91, 2006.

[15] D. S. Holder, *Electrical impedance tomography: methods, history and applications*. CRC Press, 2010.

[16] T. E. Kerner, K. D. Paulsen, A. Hartov, S. K. Soho, and S. P. Poplack, “Electrical impedance spectroscopy of the breast: clinical imaging results in 26 subjects,” *IEEE Trans. Med. Imaging*, vol. 21, no. 6, pp. 638–645, Jun. 2002.

[17] J. R. Mager, S. D. Sibley, T. R. Beckman, T. A. Kellogg, and C. P. Earthman, “Multifrequency bioelectrical impedance analysis and bioimpedance spectroscopy for monitoring fluid and body cell mass changes after gastric bypass surgery,” *Clin. Nutr.*, vol. 27, no. 6, pp. 832–841, Dec. 2008.

[18] “Electrical impedance spectroscopy (EIS)-based evaluation of biological tissue phantoms to study multifrequency electrical impedance tomography (Mf-EIT) systems,” *springerprofessional.de*. [Online]. Available: https://www.springerprofessional.de/electrical-impedance-spectroscopy-eis-based-evaluation-of-biolog/11832464. [Accessed: 03-Apr-2017].

[19] C. V. Parmar, D. L. Prajapati, V. V. Chavda, P. A. Gokhale, and H. B. Mehta, “A Study of Cardiac Parameters using Impedance Plethysmography (IPG) in Healthy Volunteers,” *J. Physiol. Pharmacol. Adv.*, vol. 2, no. 11, pp. 365–379, 2012.

[20] C. Corciova, R. Ciorap, D. Zaharia, and D. Matei, “On using impedance plethysmography for estimation of blood flow,” in *2011 IEEE International Workshop on Medical Measurements and Applications Proceedings (MeMeA)*, 2011, pp. 84–87.

[21] J. J. Oliver and D. J. Webb, “Noninvasive assessment of arterial stiffness and risk of atherosclerotic events,” *Arterioscler. Thromb. Vasc. Biol.*, vol. 23, no. 4, pp. 554–566, 2003.

[22] R. D. Allison, E. L. Holmes, and J. Nyboer, “Volumetric dynamics of respiration as measured by electrical impedance plethysmography,” *J. Appl. Physiol.*, vol. 19, no. 1, pp. 166–173, Jan. 1964.

[23] E. C. Hoffer, C. K. Meador, and D. C. Simpson, “Correlation of whole-body impedance with total body water volume.,” *J. Appl. Physiol.*, vol. 27, no. 4, pp. 531–534, 1969.

[24] P. S. Kurtin, A. C. Shapiro, H. Tomita, and D. Raizman, “Volume Status and Body Composition of Chronic Dialysis Patients: Utility of Bioelectric Impedance Plethysmography,” *Am. J. Nephrol.*, vol. 10, no. 5, pp. 363–367, 1990.

[25] B. M. Eyüboğlu, “Electrical Impedance Plethysmography,” in *Wiley Encyclopedia of Biomedical Engineering*, John Wiley & Sons, Inc., 2006.

[26] A. C. Bhuta, “Technical aspects of impedance plethysmography.,” *J. Postgrad. Med.*, vol. 36, no. 2, p. 64, Apr. 1990.

[27] A. Adler, R. Amyot, R. Guardo, J. H. T. Bates, and Y. Berthiaume, “Monitoring changes in lung air and liquid volumes with electrical impedance tomography,” *J. Appl. Physiol.*, vol. 83, no. 5, pp. 1762–1767, 1997.

[28] R. V. Luepker, J. R. Michael, and J. R. Warbasse, “Transthoracic electrical impedance: quantitative evaluation of a non-invasive measure of thoracic fluid volume,” *Am. Heart J.*, vol. 85, no. 1, pp. 83–93, 1973.

[29] J. Hatlestad, B. Moon, J. W. Hartley, and J. E. Stahmann, *Calibration of impedance monitoring of respiratory volumes using thoracic DC impedance*. Google Patents, 2009.

[30] F. G. Spinale, H. D. Reines, M. C. Cook, and F. A. Crawford, “Noninvasive estimation of extravascular lung water using bioimpedance,” *J. Surg. Res.*, vol. 47, no. 6, pp. 535–540, 1989.

[31] M. Pomerantz, F. Delgado, and B. Eiseman, “Clinical evaluation of transthoracic electrical impedance as a guide to intrathoracic fluid volumes.,” *Ann. Surg.*, vol. 171, no. 5, p. 686, 1970.

[32] H. Heijboer, H. R. Buller, A. Lensing, A. Turpie, L. P. Colly, and J. W. ten Cate, “A comparison of real-time compression ultrasonography with impedance plethysmography for the diagnosis of deep-vein thrombosis in symptomatic outpatients,” *N. Engl. J. Med.*, vol. 329, no. 19, pp. 1365–1369, 1993.

[33] R. D. Hull *et al.*, “Diagnostic efficacy of impedance plethysmography for clinically suspected deep-vein thrombosis,” *Ann Intern Med*, vol. 102, no. 2, p. 28, 1985.

[34] P. S. Wells *et al.*, “Value of assessment of pretest probability of deep-vein thrombosis in clinical management,” *The Lancet*, vol. 350, no. 9094, pp. 1795–1798, 1997.

[35] P. Wells *et al.*, “Accuracy of clinical assessment of deep-vein thrombosis,” *The Lancet*, vol. 345, no. 8961, pp. 1326–1330, 1995.

[36] R. P. Patterson, W. G. Kubicek, E. Kinnen, D. A. Witsoe, and G. Noren, “Development of an electrical impedance plethysmography system to monitor cardiac output,” in *Proc of the First Ann Rocky Mountain Bioengineering Symposium*, 1964, pp. 56–71.

[37] E. Kinnen, W. Kubicek, and R. Patterson, “Thoracic cage impedance measurements. Impedance plethysmographic determination of cardiac output (a comparative study),” DTIC Document, 1964.

[38] R. W. Gotshall, V. C. Wood, and D. S. Miles, “Comparison of two impedance cardiographic techniques for measuring cardiac output,” *Ann. Biomed. Eng.*, vol. 17, no. 5, pp. 495–505, 1989.

[39] M. Muzi, D. C. Jeutter, and J. J. Smith, “Computer-Automated Impedance-Derived Cardiac Indexes,” *IEEE Trans. Biomed. Eng.*, vol. BME-33, no. 1, pp. 42–47, Jan. 1986.

[40] K. E. Bloch and E. W. Russi, “Comparison of impedance cardiography to invasive techniques for measurement of cardiac output.,” *Am. J. Cardiol.*, vol. 79, no. 6, pp. 846–846, 1997.

[41] W. V. Judy, D. J. Powner, K. Parr, R. Demeter, C. Bates, and S. Marshall, “COMPARISON OF ELECTRICAL IMPEDANCE AND THERMAL DILUTION MEASURED CARDIAC OUTPUT IN THE CRITICAL CARE SETTING.,” *Crit. Care Med.*, vol. 13, no. 4, p. 305, 1985.

[42] W. C. SHOEMAKER, P. L. APPEL, H. B. KRAM, R. C. NATHAN, and J. L. THOMPSON, “Multicomponent noninvasive physiologic monitoring of circulatory function,” *Crit. Care Med.*, vol. 16, no. 5, pp. 482–490, 1988.

[43] N. J. Secher, A. Thomsen, and P. Arnsbo, “Measurement of rapid changes in cardiac stroke volume. An evaluation of the impedance cardiography method,” *Acta Anaesthesiol. Scand.*, vol. 21, no. 5, pp. 353–358, 1977.

[44] A. T. Edmunds, S. Godfrey, and M. Tooley, “Cardiac output measured by transthoracic impedance cardiography at rest, during exercise and at various lung volumes,” *Clin Sci*, vol. 63, no. 2, pp. 107–13, 1982.

[45] Y. Miyamoto, M. Takahashi, T. Tamura, T. Nakamura, T. Hiura, and M. Mikami, “Continuous determination of cardiac output during exercise by the use of impedance plethysmography,” *Med. Biol. Eng. Comput.*, vol. 19, no. 5, pp. 638–644, 1981.

[46] K.-K. Teo, M. D HETHERINGTON, R. G. HAENNEL, P. V. GREENWOOD, R. E. ROSSALL, and T. KAPPAGODA, “Cardiac output measured by impedance cardiography during maximal exercise tests,” *Cardiovasc. Res.*, vol. 19, no. 12, pp. 737–743, 1985.

[47] Y. Zhang, M. Qu, J. G. Webster, W. J. Tompkins, B. A. Ward, and D. R. Bassett, “Cardiac Output Monitoring by Impedance Cardiography During Treadmill Exercise,” *IEEE Trans. Biomed. Eng.*, vol. BME-33, no. 11, pp. 1037–1042, Nov. 1986.

[48] E. Enghoff and O. Lovheim, “A comparison between the transthoracic electrical impedance method and the direct Fick and the dye dilution methods for cardiac output measurements in man,” *Scand. J. Clin. Lab. Invest.*, vol. 39, no. 6, pp. 585–590, 1979.

[49] I. C. Henry, D. P. Bernstein, and M. J. Banet, “Stroke volume obtained from the brachial artery using transbrachial electrical bioimpedance velocimetry,” in *2012 Annual International Conference of the IEEE Engineering in Medicine and Biology Society (EMBC)*, 2012, pp. 142–145.

[50] H. Keren, D. Burkhoff, and P. Squara, “Evaluation of a noninvasive continuous cardiac output monitoring system based on thoracic bioreactance,” *Am. J. Physiol.-Heart Circ. Physiol.*, vol. 62, no. 1, p. H583, 2007.

[51] N. Y. Raval, P. Squara, M. Cleman, K. Yalamanchili, M. Winklmaier, and D. Burkhoff, “Multicenter evaluation of noninvasive cardiac output measurement by bioreactance technique,” *J. Clin. Monit. Comput.*, vol. 22, no. 2, pp. 113–119, 2008.

[52] Y. Ballestero *et al.*, “Measurement of cardiac output in children by bioreactance,” *Pediatr. Cardiol.*, vol. 32, no. 4, pp. 469–472, 2011.

[53] B. Benomar, A. Ouattara, P. Estagnasie, A. Brusset, and P. Squara, “Fluid responsiveness predicted by noninvasive bioreactance-based passive leg raise test,” *Intensive Care Med.*, vol. 36, no. 11, pp. 1875–1881, 2010.

[54] H. Keren, D. Burkhoff, and P. Squara, “Evaluation of a noninvasive continuous cardiac output monitoring system based on thoracic bioreactance,” *Am. J. Physiol. - Heart Circ. Physiol.*, vol. 293, no. 1, pp. H583–H589, Jul. 2007.

[55] B. H. Brown, “Medical impedance tomography and process impedance tomography: a brief review,” *Meas. Sci. Technol.*, vol. 12, no. 8, p. 991, 2001.

[56] B. H. Brown, “Electrical impedance tomography (EIT): a review,” *J. Med. Eng. Technol.*, vol. 27, no. 3, pp. 97–108, 2003.

[57] D. Holder, “Biomedical applications of electrical impedance tomography,” *Physiol. Meas.*, vol. 23, no. 1, 2002.

[58] T. Dowrick, C. Blochet, and D. Holder, “In vivo bioimpedance measurement of healthy and ischaemic rat brain: implications for stroke imaging using electrical impedance tomography,” *Physiol. Meas.*, vol. 36, no. 6, p. 1273, 2015.

[59] T. A. T. Hughes, P. Liu, H. Griffiths, B. W. Lawrie, and C. M. Wiles, “Simultaneous electrical impedance tomography and videofluoroscopy in the assessment of swallowing,” *Physiol. Meas.*, vol. 17, no. 2, p. 109, 1996.

[60] V. Cherepenin *et al.*, “A 3D electrical impedance tomography (EIT) system for breast cancer detection,” *Physiol. Meas.*, vol. 22, no. 1, p. 9, 2001.

[61] Y. Zou and Z. Guo, “A review of electrical impedance techniques for breast cancer detection,” *Med. Eng. Phys.*, vol. 25, no. 2, pp. 79–90, 2003.

[62] M. H. Choi, T.-J. Kao, D. Isaacson, G. J. Saulnier, and J. C. Newell, “A reconstruction algorithm for breast cancer imaging with electrical impedance tomography in mammography geometry,” *IEEE Trans. Biomed. Eng.*, vol. 54, no. 4, pp. 700–710, 2007.

[63] H. P. Schwan, “Electrical properties of tissue and cell suspensions.,” *Adv. Biol. Med. Phys.*, vol. 5, p. 147, 1957.

[64] J. R. Matthie, “Bioimpedance measurements of human body composition: critical analysis and outlook,” 2008.

[65] A. D. Lorenzo, A. Andreoli, J. Matthie, and P. Withers, “Predicting body cell mass with bioimpedance by using theoretical methods: a technological review,” *J. Appl. Physiol.*, vol. 82, no. 5, pp. 1542–1558, May 1997.

[66] J. Malmivuo and R. Plonsey, *Bioelectromagnetism: principles and applications of bioelectric and biomagnetic fields*. New York: Oxford University Press, 1995.

[67] D. B. Geselowitz, “An application of electrocardiographic lead theory to impedance plethysmography,” *Biomed. Eng. IEEE Trans. On*, no. 1, pp. 38–41, 1971.

[68] P. Debye, “Zur Theorie der anomalen Dispersion im Gebiete der langwelligen elektrischen Strahlung,” *Ber Dt Phys Ges*, vol. 15, pp. 777–793, 1913.

[69] K. W. Wagner, “Erklärung der dielektrischen Nachwirkungsvorgänge auf Grund Maxwellscher Vorstellungen,” *Arch. Für Elektrotechnik*, vol. 2, no. 9, pp. 371–387.

[70] R. W. Sillars, “The properties of a dielectric containing semiconducting particles of various shapes,” *J. Inst. Electr. Eng.*, vol. 80, no. 484, pp. 378–394, Apr. 1937.

[71] L. K. H. Van Beek, “The Maxwell-Wagner-Sillars effect, describing apparent dielectric loss in inhomogeneous media,” *Physica*, vol. 26, no. 1, pp. 66–68, 1960.

[72] K. S. Cole, “Permeability and impermeability of cell membranes for ions,” in *Cold Spring Harbor Symposia on Quantitative Biology*, 1940, vol. 8, pp. 110–122.

[73] K. S. Cole and R. H. Cole, “Dispersion and absorption in dielectrics I. Alternating current characteristics,” *J. Chem. Phys.*, vol. 9, no. 4, pp. 341–351, 1941.

[74] W. G. Kubicek, *Minnesota impedance cardiograph model 303. Univ*. of Minnesota press, Minneapolis, 1968.

[75] S. N. Mohapatra, *Non-invasive cardiovascular monitoring by electrical impedance technique*. Pitman Medical, 1981.

[76] P. Bertemes Filho, “Tissue Characterisation Using an Impedance Spectrosopy Probe,” 2002.

[77] H. Griffiths and A. Ahmed, “A dual-frequency applied potential tomography technique: computer simulations,” *Clin. Phys. Physiol. Meas.*, vol. 8, no. 4A, p. 103, 1987.

[78] A. Lozano, J. Rosell, and R. Pallas-Areny, “Two-frequency impedance plethysmograph: real and imaginary parts,” *Med. Biol. Eng. Comput.*, vol. 28, no. 1, pp. 38–42, 1990.

[79] P. M. Record, R. Gadd, and F. Vinther, “Multifrequency electrical impedance tomography,” *Clin. Phys. Physiol. Meas.*, vol. 13, no. A, p. 67, 1992.

[80] A. R. Waterworth, P. Milnes, R. H. Smallwood, and B. H. Brown, “Cole equation modelling to measurements made using an impulse driven transfer impedance system,” *Physiol. Meas.*, vol. 21, no. 1, p. 137, 2000.

[81] M. E. Valentinuzzi, “Bioelectrical impedance techniques in medicine. Part I: Bioimpedance measurement. First section: general concepts.,” *Crit. Rev. Biomed. Eng.*, vol. 24, no. 4–6, pp. 223–255, 1995.

[82] B. H. Brown, P. V. Lawford, R. H. Smallwood, D. R. Hose, and D. C. Barber, *Medical Physics and Biomedical Engineering. 1999*. Institute of Physics Publishing, London.

[83] B. H. Brown, J. Tidy, K. Boston, A. D. Blackett, and F. Sharp, “Tetrapolar measurement of cervical tissue structure using impedance spectroscopy,” in *Proceedings of the 20th Annual International Conference of the IEEE Engineering in Medicine and Biology Society, 1998*, 1998, vol. 6, pp. 2886–2889 vol.6.

[84] C. GONZÁLEZ-CORREA *et al.*, “Virtual biopsies in Barrett’s esophagus using an impedance probe,” *Ann. N. Y. Acad. Sci.*, vol. 873, no. 1, pp. 313–321, 1999.

[85] U. M. Moissl *et al.*, “Body fluid volume determination via body composition spectroscopy in health and disease,” *Physiol. Meas.*, vol. 27, no. 9, p. 921, 2006.

[86] C. W. Denyer, F. J. Lidgey, Q. S. Zhu, and C. N. McLeod, “High output impedance voltage controlled current source for bio-impedance instrumentation,” in *Proceedings of the 15th Annual International Conference of the IEEE Engineering in Medicine and Biology Society, 1993*, 1993, pp. 1026–1027.

[87] C. W. Denyer, F. J. Lidgey, Q. S. Zhu, and C. N. McLeod, “A high output impedance current source,” *Physiol. Meas.*, vol. 15, no. 2A, p. A79, 1994.

[88] C. W. Denyer, F. J. Lidgey, C. N. McLeod, and Q. S. Zhu, “Current source calibration simplifies high-accuracy current source measurement,” *Innov. Technol. En Biol. Médecine*, vol. 15, pp. 47–55, 1994.

[89] B. Blad, K. Lindstrom, L. Bertenstam, B. R. Persson, and N.-G. Holmer, “A current injecting device for electrical impedance tomography,” *Physiol. Meas.*, vol. 15, no. 2A, p. A69, 1994.

[90] J. Li, C. Joppek, and U. Faust, “An isolated wideband current source used in multifrequency electrical impedance tomography,” *Innov. Technol. En Biol. Médecine*, vol. 15, pp. 62–68, 1994.

[91] L. Lu and B. H. Brown, “The electrode and electronic interface in an EIT spectroscopy system,” *Innov. Technol. En Biol. Médecine*, vol. 15, pp. 97–103, 1994.

[92] J. Jossinet, G. Tourtel, and R. Jarry, “Performance and operation of a set of wide band current generators for eit,” *Innov. Technol. En Biol. Médecine*, vol. 15, pp. 40–46, 1994.

[93] T. R. Qureshi, C. Chatwin, and W. Wang, “Bio-impedance Excitation System: A Comparison of Voltage Source and Current Source Designs,” *APCBEE Procedia*, vol. 7, pp. 42–47, 2013.

[94] R. W. M. Smith, I. Freeston, and B. H. Brown, “A real-time electrical impedance tomography system for clinical use-design and preliminary results,” *IEEE Trans. Biomed. Eng.*, vol. 42, no. 2, pp. 133–140, Feb. 1995.

[95] G. Cusick, D. S. Holder, A. Birkett, and K. Boone, “A system for impedance imaging epilepsy in ambulatory human subjects,” *Innov. Technol. En Biol. Médecine*, vol. 15, pp. 33–39, 1994.

[96] J. Jossinet, C. Tourtel, and R. Jarry, “Active current electrodes for in vivo electrical impedance tomography,” *Physiol. Meas.*, vol. 15, no. 2A, p. A83, 1994.

[97] O. Casas, J. Rosell, R. Bragós, A. Lozano, and P. J. Riu, “A parallel broadband real-time system for electrical impedance tomography,” *Physiol. Meas.*, vol. 17, no. 4A, p. A1, 1996.

[98] P. J. Riu, J. Rosell, A. Lozano, and R. Pallàs-Areny, “A broadband system for multifrequency static imaging in electrical impedance tomography,” *Clin. Phys. Physiol. Meas.*, vol. 13, no. A, p. 61, 1992.

[99] J. C. Márquez Ruiz, “Sensor-Based Garments that Enable the Use of Bioimpedance Technology: Towards Personalized Healthcare Monitoring,” 2013.

[100] J.-J. Wang, W.-C. Hu, T. Kao, C.-P. Liu, and S.-K. Lin, “Development of forearm impedance plethysmography for the minimally invasive monitoring of cardiac pumping function.,” *J. Biomed. Sci. Eng.*, vol. 4, no. 2, 2011.

[101] L.-Y. Shyu, C.-Y. Chiang, C.-P. Liu, and W.-C. Hu, “Portable impedance cardiography system for real-time noninvasive cardiac output measurement,” *J. Med. Biol. Eng.*, vol. 20, no. 4, pp. 193–202, 2000.

[102] B. E. Hurwitz, L.-Y. Shyu, C.-C. Lu, S. P. Reddy, N. Schneiderman, and J. H. Nagel, “Signal fidelity requirements for deriving impedance cardiographie measures of cardiac function over a broad heart rate range,” *Biol. Psychol.*, vol. 36, no. 1–2, pp. 3–21, Aug. 1993.

[103] K. R. Aroom, M. T. Harting, C. S. Cox Jr., R. S. Radharkrishnan, C. Smith, and B. S. Gill, “Bioimpedance Analysis: A Guide to Simple Design and Implementation,” *J. Surg. Res.*, vol. 153, no. 1, pp. 23–30, May 2009.

[104] S. Grimnes and Ø. G. Martinsen, “Bioimpedance,” in *Wiley Encyclopedia of Biomedical Engineering*, John Wiley & Sons, Inc., 2006.

[105] Y. David, W. W. von Maltzahn, M. R. Neuman, and J. D. Bronzino, *Clinical Engineering*. CRC Press, 2003.

[106] Y. N. Zhou and M. D. Breyen, *Joining and Assembly of Medical Materials and Devices*. Elsevier, 2013.

[107] “Surface chemistry of neural implants,” *Wikipedia*. 17-May-2017.

[108] “Cardiac Monitoring and Cardiopulmonary Resuscitation,” *Clinical Gate*, 12-Jun-2015. .

[109] M. Jaffrin, H. Morel, and Y. Lavielle, “Body composition measurements in limbs using eight-electrodes bioimpedance,” in *13th International Conference on Electrical Bioimpedance and the 8th Conference on Electrical Impedance Tomography*, 2007, pp. 771–774.

[110] T. Nakamura, Y. Yamamoto, T. Yamamoto, and H. Tsuji, “Fundamental characteristics of human limb electrical impedance for biodynamic analysis,” *Med. Biol. Eng. Comput.*, vol. 30, no. 5, pp. 465–472, 1992.

[111] S. C. Kim, K. C. Nam, D. W. Kim, C. Y. Ryu, Y. H. Kim, and J. C. Kim, “Optimum electrode configuration for detection of arm movement using bio-impedance,” *Med. Biol. Eng. Comput.*, vol. 41, no. 2, pp. 141–145, Mar. 2003.

[112] S. Köppä, V. Savolainen, and J. Hyttinen, “Modelling Approach for Assessment of Electrode Configuration and Placement in Bioimpedance Measurements of Skin Irritation,” in *5th European Conference of the International Federation for Medical and Biological Engineering*, Á. Jobbágy, Ed. Springer Berlin Heidelberg, 2012, pp. 1238–1241.

[113] T. Vuorela, J. Hännikäinen, K. Vähäkuopus, and J. Vanhala, “Textile electrode usage in a bioimpedance measurement,” in *In: Talvenmaa, P.(ed.). Ambience 05, International Scientific Conference, Intelligent Ambience and Well-Being, 19-20 September 2005, Tampere, Finland*, 2005.

[114] G. Medrano, N. Zimmermann, T. Gries, and S. Leonhardt, “Bioimpedanz-Spektroskopie (BIS) mit textilen Elektroden,” *Dreiländertagung BMT*, 2006.

[115] G. Medrano, A. Ubl, N. Zimmermann, T. Gries, and S. Leonhardt, “Skin electrode impedance of textile electrodes for bioimpedance spectroscopy,” in *13th International Conference on Electrical Bioimpedance and the 8th Conference on Electrical Impedance Tomography*, 2007, pp. 260–263.

[116] J. C. Marquez, F. Seoane, E. Valimaki, and K. Lindecrantz, “Textile electrodes in electrical bioimpedance measurements #x2013; a comparison with conventional Ag/AgCl electrodes,” in *Annual International Conference of the IEEE Engineering in Medicine and Biology Society, 2009. EMBC 2009*, 2009, pp. 4816–4819.

[117] S. Rush and D. A. Driscoll, “EEG electrode sensitivity-an application of reciprocity,” *Biomed. Eng. IEEE Trans. On*, no. 1, pp. 15–22, 1969.

[118] D. C. Barber, B. H. Brown, and I. L. Freeston, “Imaging spatial distributions of resistivity using applied potential tomography—APT,” in *Information Processing in Medical Imaging*, 1984, pp. 446–462.

[119] L. A. Geddes and C. Sadler, “The specific resistance of blood at body temperature,” *Med. Biol. Eng.*, vol. 11, no. 3, pp. 336–339, 1973.

[120] S. Rush, J. A. Abildskov, and R. McFee, “Resistivity of body tissues at low frequencies,” *Circ. Res.*, vol. 12, no. 1, pp. 40–50, 1963.

[121] B. R. Epstein and K. R. Foster, “Anisotropy in the dielectric properties of skeletal muscle,” *Med. Biol. Eng. Comput.*, vol. 21, no. 1, pp. 51–55, 1983.

[122] H. P. SCHWAN and C. F. KAY, “Specific resistance of body tissues,” *Circ. Res.*, vol. 4, no. 6, pp. 664–670, 1956.

[123] L. A. Geddes and L. E. Baker, “The specific resistance of biological material—a compendium of data for the biomedical engineer and physiologist,” *Med. Biol. Eng.*, vol. 5, no. 3, pp. 271–293, 1967.

[124] S. Saha and P. A. Williams, “Electric and dielectric properties of wet human cortical bone as a function of frequency,” *Biomed. Eng. IEEE Trans. On*, vol. 39, no. 12, pp. 1298–1304, 1992.

[125] R. Pethig, “Dielectric properties of biological materials: Biophysical and medical applications,” *Electr. Insul. IEEE Trans. On*, no. 5, pp. 453–474, 1984.

[126] D. Miklavčič, N. Pavšelj, and F. X. Hart, “Electric Properties of Tissues,” in *Wiley Encyclopedia of Biomedical Engineering*, John Wiley & Sons, Inc., 2006.

[127] H. Fricke, “A mathematical treatment of the electric conductivity and capacity of disperse systems II. The capacity of a suspension of conducting spheroids surrounded by a non-conducting membrane for a current of low frequency,” *Phys. Rev.*, vol. 26, no. 5, p. 678, 1925.

[128] J. Lario-Garc?a and R. Pall?s-Areny, “Constant-phase element identification in conductivity sensors using a single square wave,” *Sens. Actuators Phys.*, vol. 132, no. 1, pp. 122–128, Nov. 2006.

[129] H. Fricke, “XXXIII. The theory of electrolytic polarization,” *Lond. Edinb. Dublin Philos. Mag. J. Sci.*, vol. 14, no. 90, pp. 310–318, 1932.

[130] F. Zhu and N. W. Levin, “An electrical resistivity model of segmental body composition using bioimpedance analysis,” in *Proceedings of the 25th Annual International Conference of the IEEE Engineering in Medicine and Biology Society, 2003*, 2003, vol. 3, p. 2679–2682 Vol.3.

[131] J. R. Cook, R. R. Bouchard, and S. Y. Emelianov, “Tissue-mimicking phantoms for photoacoustic and ultrasonic imaging,” *Biomed. Opt. Express*, vol. 2, no. 11, pp. 3193–3206, 2011.

[132] T. J. Hall, M. Bilgen, M. F. Insana, and T. A. Krouskop, “Phantom materials for elastography,” *Ieee Trans. Ultrason. Ferroelectr. Freq. Control*, vol. 44, no. 6, pp. 1355–1365, 1997.

[133] J. Garrett and E. Fear, “Stable and flexible materials to mimic the dielectric properties of human soft tissues,” *IEEE Antennas Wirel. Propag. Lett.*, vol. 13, pp. 599–602, 2014.

[134] K. Kawabata, Y. Waki, T. Matsumura, and S. Umemura, “Tissue mimicking phantom for ultrasonic elastography with finely adjustable elastic and echographic properties,” in *Ultrasonics Symposium, 2004 IEEE*, 2004, vol. 2, pp. 1502–1505.

[135] D. W. Davidson and R. H. Cole, “Dielectric relaxation in glycerol, propylene glycol, and n-propanol,” *J. Chem. Phys.*, vol. 19, no. 12, pp. 1484–1490, 1951.

[136] A. Yilmaz, O. Javed, and M. Shah, “Object tracking: A survey,” *Acm Comput. Surv. CSUR*, vol. 38, no. 4, p. 13, 2006.

[137] C. Marchal, M. Nadi, A. J. Tosser, C. Roussey, and M. L. Gaulard, “Dielectric properties of gelatine phantoms used for simulations of biological tissues between 10 and 50 MHz,” *Int. J. Hyperthermia*, vol. 5, no. 6, pp. 725–732, 1989.

[138] Y. Liu, S. Maruvada, R. L. King, B. A. Herman, and K. A. Wear, “Development and characterization of a blood mimicking fluid for high intensity focused ultrasound,” *J. Acoust. Soc. Am.*, vol. 124, no. 3, pp. 1803–1810, 2008.

[139] K. V. Ramnarine, D. K. Nassiri, P. R. Hoskins, and J. Lubbers, “Validation of a new blood-mimicking fluid for use in Doppler flow test objects,” *Ultrasound Med. Biol.*, vol. 24, no. 3, pp. 451–459, 1998.

[140] M. Y. Yousif, D. W. Holdsworth, and T. L. Poepping, “A blood-mimicking fluid for particle image velocimetry with silicone vascular models,” *Exp. Fluids*, vol. 50, no. 3, pp. 769–774, 2011.

[141] C. Gabriel, “Compilation of the Dielectric Properties of Body Tissues at RF and Microwave Frequencies.,” DTIC Document, 1996.

[142] C. Gabriel, S. Gabriel, and E. Corthout, “The dielectric properties of biological tissues: I. Literature survey,” *Phys. Med. Biol.*, vol. 41, no. 11, p. 2231, 1996.

[143] S. Gabriel, R. W. Lau, and C. Gabriel, “The dielectric properties of biological tissues: II. Measurements in the frequency range 10 Hz to 20 GHz,” *Phys. Med. Biol.*, vol. 41, no. 11, pp. 2251–2269, Nov. 1996.

[144] S. Gabriel, R. W. Lau, and C. Gabriel, “The dielectric properties of biological tissues: III. Parametric models for the dielectric spectrum of tissues,” *Phys. Med. Biol.*, vol. 41, no. 11, p. 2271, 1996.

[145] R. J. Sengwa, R. Chaudhary, and S. C. Mehrotra, “Dielectric behaviour of propylene glycol-water mixtures studied by time domain reflectometry,” *Mol. Phys.*, vol. 99, no. 21, pp. 1805–1812, 2001.

[146] P. Petong, R. Pottel, and U. Kaatze, “Water-ethanol mixtures at different compositions and temperatures. A dieletric relaxation study,” *J. Phys. Chem. A*, vol. 104, no. 32, pp. 7420–7428, 2000.

[147] R. J. Sengwa, R. Chaudhary, and S. C. Mehrotra, “The study of dielectric relaxation in propylene glycol–poly (propylene glycol) mixtures,” *Polymer*, vol. 43, no. 4, pp. 1467–1471, 2002.

[148] R. Behrends, K. Fuchs, U. Kaatze, Y. Hayashi, and Y. Feldman, “Dielectric properties of glycerol/water mixtures at temperatures between 10 and 50 C,” *J. Chem. Phys.*, vol. 124, no. 14, p. 144512, 2006.

[149] A. W. Guy, “Analyses of Electromagnetic Fields Induced in Biological Tissues by Thermographic Studies on Equivalent Phantom Models,” *IEEE Trans. Microw. Theory Tech.*, vol. 19, no. 2, pp. 205–214, Feb. 1971.

[150] K. Ito, K. Furuya, Y. Okano, and L. Hamada, “Development and characteristics of a biological tissue-equivalent phantom for microwaves,” *Electron. Commun. Jpn. Part Commun.*, vol. 84, no. 4, pp. 67–77, Apr. 2001.

[151] M. Lazebnik, E. L. Madsen, G. R. Frank, and S. C. Hagness, “Tissue-mimicking phantom materials for narrowband and ultrawideband microwave applications,” *Phys. Med. Biol.*, vol. 50, no. 18, p. 4245, 2005.

[152] L. Fomundam and J. Lin, “Multi-layer low frequency tissue equivalent phantoms for noninvasive test of shallow implants and evaluating antenna-body interaction,” in *Engineering in Medicine and Biology Society (EMBC), 2016 IEEE 38th Annual International Conference of the*, 2016, pp. 2353–2356.

[153] T. Dec, C. Snooks, S. Nelson, J. Schoneman, A. Connelly, and J. Song, “Human Dielectric Equivalent Phantom.”

[154] A. M. R. Pinto, P. Bertemes-Filho, and A. Paterno, “Gelatin: a skin phantom for bioimpedance spectroscopy,” *Biomed. Phys. Eng. Express*, vol. 1, no. 3, p. 035001, 2015.

[155] T. Sunaga *et al.*, “Development of a dielectric equivalent gel for better impedance matching for human skin,” *Bioelectromagnetics*, vol. 24, no. 3, pp. 214–217, Apr. 2003.

[156] M. P. Robinson, M. J. Richardson, J. L. Green, and A. W. Preece, “New materials for dielectric simulation of tissues,” *Phys. Med. Biol.*, vol. 36, no. 12, p. 1565, 1991.

[157] S. N. Mohapatra, “Impedance cardiography,” *Encycl. Med. Devices Instrum.*, pp. 1622–1632, 1988.

[158] F. G. Hirsch *et al.*, “THE ELECTRICAL CONDUCTIVITY OF BLOOD I. RELATIONSHIP TO ERYTHROCYTE CONCENTRATION,” *Blood*, vol. 5, no. 11, pp. 1017–1035, 1950.

[159] S. Graff, A. B. Voorhees, and A. H. Blakemore, “Electrical resistance of whole blood,” *Science*, vol. 106, no. 2742, pp. 68–69, 1947.

[160] R. L. Rosenthal and C. W. Tobias, “Measurement of the electric resistance of human blood; use in coagulation studies and cell volume determinations,” *J Lab Clin Med*, vol. 33, pp. 1110–1122, 1948.

[161] S. N. Mohapatra and D. W. Hill, “The changes in blood resistivity with haematocrit and temperature,” *Eur. J. Intensive Care Med.*, vol. 1, no. 4, pp. 153–162, 1975.

[162] H. Fricke, “A mathematical treatment of the electric conductivity and capacity of disperse systems I. The electric conductivity of a suspension of homogeneous spheroids,” *Phys. Rev.*, vol. 24, no. 5, p. 575, 1924.

[163] L. L. Hause, F. . Gayon, and M. E. Aleksza, “Impedance measurements during simulated blood flow,” in *Engineering in Medicine and Biology Society, 1989. Images of the Twenty-First Century., Proceedings of the Annual International Conference of the IEEE Engineering in*, 1989, p. 1232 vol.4-vol.

[164] E. Sigman, A. Kolin, L. Katz, and K. Jochim, “Effect of motion on the electrical conductivity of the blood,” *Am. J. Physiol. Content*, vol. 118, no. 4, pp. 708–719, 1937.

[165] K. Tanaka, H. Kanai, K. Nakayama, and N. Ono, “The impedance of blood: the effects of red cell orientation and its application,” *Jpn J Med Eng*, vol. 8, pp. 436–443, 1970.

[166] K. Sakamoto and H. Kanai, “Electrical Characteristics of Flowing Blood,” *IEEE Trans. Biomed. Eng.*, vol. BME-26, no. 12, pp. 686–695, Dec. 1979.

[167] H. Kanai, K. Sakamoto, and M. Miki, “Impedance of blood; the effects of red cell orientation,” *Proc. Llth ICMBE Ott. Can.*, pp. 238–239, 1976.

[168] M. Niwa, K. Sakamoto, and H. Kanai, “Optical reflection by whole blood—the effects of erythrocytes orientation,” *Dig. 11th ICMBE Ott. Can.*, vol. 74, 1976.

[169] J. W. Dellimore and R. G. Gosling, “Use of electrical conductance measurements in studies of the orientation of microscopic particles in stationary and flowing suspensions,” *J. Appl. Phys.*, vol. 44, no. 12, pp. 5599–5606, 1973.

[170] R. H. Edgerton, “Conductivity of sheared suspensions of ellipsoidal particles with application to blood flow,” *Biomed. Eng. IEEE Trans. On*, no. 1, pp. 33–43, 1974.

[171] S. C. Brooks, “Conductivity as a measure of the permeability of suspended cells,” *J. Gen. Physiol.*, vol. 7, no. 3, pp. 349–362, 1925.

[172] G. N. Stewart, “The conductivity of erythrocytes compared with that of serum,” *Am. J. Physiol. Content*, vol. 90, no. 1, pp. 194–209, 1929.

[173] J. Wtorek and A. Polinski, “The contribution of blood-flow-induced conductivity changes to measured impedance,” *Biomed. Eng. IEEE Trans. On*, vol. 52, no. 1, pp. 41–49, 2005.

[174] K. Visser, R. Lamberts, H. Korsten, and W. Zijlstra, “Observations on blood flow related electrical impedance changes in rigid tubes,” *Pflüg. Arch.*, vol. 366, no. 2–3, pp. 289–291, 1976.

[175] J. W. Dellimore and R. G. Gosling, “Change in blood conductivity with flow rate,” *Med. Biol. Eng.*, vol. 13, no. 6, pp. 904–913, Nov. 1975.

[176] I. K. R. Visser, “Electric properties of flowing blood and impedance cardiography,” *Ann. Biomed. Eng.*, vol. 17, no. 5, pp. 463–473, Sep. 1989.

[177] R. A. Peura, B. C. Penney, J. Arcuri, F. A. A. Jr, and H. B. Wheeler, “Influence of erythrocyte velocity on impedance plethysmographic measurements,” *Med. Biol. Eng. Comput.*, vol. 16, no. 2, pp. 147–154, Mar. 1978.

[178] T. M. R. Shankar, J. G. Webster, and S. Shao, “The Contribution of Vessel Volume Change and Blood Resistivity Change to the Electrical Impedance Pulse,” *IEEE Trans. Biomed. Eng.*, vol. BME-32, no. 3, pp. 192–198, Mar. 1985.

[179] R. L. Gaw, B. H. Cornish, and B. J. Thomas, “The Electrical Impedance of Pulsatile Blood Flowing Through Rigid Tubes: A Theoretical Investigation,” *IEEE Trans. Biomed. Eng.*, vol. 55, no. 2, pp. 721–727, Feb. 2008.

[180] P. De Vries, J. W. G. Langendijk, and P. M. Kouw, “The influence of alternating current frequency on flow related admittance changes of blood: a concept for improvement of impedance cardiography,” *Physiol. Meas.*, vol. 16, no. 1, p. 63, 1995.

[181] F. M. Liebman, J. Pearl, and S. Bagno, “The electrical conductance properties of blood in motion,” *Phys. Med. Biol.*, vol. 7, no. 2, p. 177, 1962.

[182] F. M. Liebman and S. Bagno, “The behavior of the red blood cells in flowing blood which accounts for conductivity changes.,” *Biomed. Sci. Instrum.*, vol. 4, pp. 25–35, 1967.

[183] K. R. Visser, “Electric conductivity of stationary and flowing human blood at low frequencies,” in *Engineering in Medicine and Biology Society, 1989. Images of the*

Twenty-First Century., Proceedings of the Annual International Conference of the IEEE Engineering in, 1989, pp. 1540–1542 vol.5.

[184] A. E. Hoetink, T. J. C. Faes, K. R. Visser, and R. M. Heethaar, "On the flow dependency of the electrical conductivity of blood," *IEEE Trans. Biomed. Eng.*, vol. 51, no. 7, pp. 1251–1261, Jul. 2004.

[185] G. N. Jager, N. Westerhof, and A. Noordergraaf, "Oscillatory Flow Impedance in Electrical Analog of Arterial System: Representation of Sleeve Effect and Non-Newtonian Properties of Blood," *Circ. Res.*, vol. 16, no. 2, pp. 121–133, Feb. 1965.

[186] A. L. Kunz and N. A. Coulter Jr., "Non-Newtonian Behavior of Blood in Oscillatory Flow," *Biophys. J.*, vol. 7, no. 1, pp. 25–36, Jan. 1967.

[187] J. R. Womersley, *An elastic tube theory of pulse transmission and oscillatory flow in mammalian arteries*. Wright Air Development Center, 1957.

[188] K. Kumin, "Bestimmung des Zahigkeitskoeffizienten[mu] fur Rinderblut bei Newton'schen Stromungen in verschieden weiten Rohren und Kapillaren bei physiologischer Temperatur," Bern, 1949.

[189] L. E. Bayliss, *Rheology of blood and lymph*, vol. 355. North-Holland, Amsterdam, 1952.

[190] L. E. Bayliss, "The anomalous viscosity of blood," *Flow Prop. Blood*, pp. 29–62, 1960.

[191] M. G. Taylor, "The influence of the anomalous viscosity of blood upon its oscillatory flow," *Phys. Med. Biol.*, vol. 3, no. 3, p. 273, 1959.

[192] "ANSYS HFSS - High Frequency Electromagnetic Field Simulation." [Online]. Available: http://www.ansys.com/products/electronics/ANSYS-HFSS. [Accessed: 06-Oct-2016].

[193] S. Grimnes and O. G. Martinsen, *Bioimpedance and Bioelectricity Basics*. Academic Press, 2014.

[194] V. Mooser *et al.*, "Non-invasive measurement of internal diameter of peripheral arteries during the cardiac cycle," *J. Hypertens.*, vol. 6, no. 4, Dec. 1988.

[195] S. Trazzi, S. Omboni, C. Santucciu, G. Parati, and G. Mancia, "Variability in arterial diameter and compliance: compliance modulation reserve," *J. Hypertens.*, Aug. 1992.

[196] "IEC 60601," *Wikipedia, the free encyclopedia*. 16-Oct-2015.

[197] "ANSYS Meshing: Mesh Analysis." ANSYS, 28-Apr-2009.

[198] W. H. Olson, "Electrical safety," *Med. Instrum. Appl. Des.*, 1978.

[199] M. Frydrysiak, J. Zięba, L. Tęsiorowski, and M. Tokarska, “Textronic system to muscle electrostimulation,” *PES*, vol. 149, pp. 0–41, 2012.

[200] M. Savegnago *et al.*, “Determinación de composición corporal mediante análisis de impedancia segmentada: consideraciones y aplicaciones prácticas,” *Rev. Chil. Nutr.*, vol. 37, no. 3, pp. 262–268, 2010.

[201] J. Alastruey, K. H. Parker, and S. J. Sherwin, “Arterial pulse wave haemodynamics,” in *Anderson. 11th International Conference on Pressure Surges*, 2012, pp. 401–442.

[202] “Moens–Korteweg equation,” *Wikipedia, the free encyclopedia*. 20-Feb-2015.

[203] J. K.-J. Li, *Comparative Cardiovascular Dynamics of Mammals*. CRC Press, 1995.

[204] R. Asmar *et al.*, “Assessment of Arterial Distensibility by Automatic Pulse Wave Velocity Measurement Validation and Clinical Application Studies,” *Hypertension*, vol. 26, no. 3, pp. 485–490, Sep. 1995.

[205] I. B. Wilkinson *et al.*, “Reproducibility of pulse wave velocity and augmentation index measured by pulse wave analysis,” *J. Hypertens.*, vol. 16, no. 12, pp. 2079–2084, 1998.

[206] P. Salvi, G. Lio, C. Labat, E. Ricci, B. Pannier, and A. Benetos, “Validation of a new non-invasive portable tonometer for determining arterial pressure wave and pulse wave velocity: the PulsePen device,” *J. Hypertens.*, vol. 22, no. 12, pp. 2285–2293, 2004.

[207] Y. W. Brans and W. W. Hay, *Physiological Monitoring and Instrument Diagnosis in Perinatal and Neonatal Medicine*. CUP Archive, 1995.

[208] A. L. Pauca, “The second peak of the radial artery pressure wave represents aortic systolic pressure in hypertensive and elderly patients,” *Br. J. Anaesth.*, vol. 92, no. 5, pp. 651–657, Mar. 2004.

[209] A. Shmulewitz and A. A. Wallace, “Apparatus and methods of bioelectrical impedance analysis of blood flow,” US6095987 A, 01-Aug-2000.

[210] G. N. Reddy and S. Saha, “Electrical and dielectric properties of wet bone as a function of frequency,” *Biomed. Eng. IEEE Trans. On*, no. 3, pp. 296–303, 1984.

[211] S. L. Schiefelbein, N. A. Fried, K. G. Rhoads, and D. R. Sadoway, “A high-accuracy, calibration-free technique for measuring the electrical conductivity of liquids,” *Rev. Sci. Instrum.*, vol. 69, no. 9, pp. 3308–3313, 1998.

[212] M. L. Zahn, “Electromagnetic field theory,” 1979.

[213] J. K. K. Carver and J. D. Kraus, *Electromagnetics*. New York: McGraw-Hill, 1973.

[214] H. P. Schwan, “Electrode polarization impedance and measurements in biological materials,” *Ann. N. Y. Acad. Sci.*, vol. 148, no. 1, pp. 191–209, 1968.

[215] “Wolfram Mathematica: Modern Technical Computing.” [Online]. Available: https://www.wolfram.com/mathematica/. [Accessed: 24-Mar-2017].

[216] A. D. Hollingsworth and D. A. Saville, “A broad frequency range dielectric spectrometer for colloidal suspensions: cell design, calibration, and validation,” *J. Colloid Interface Sci.*, vol. 257, no. 1, pp. 65–76, Jan. 2003.

[217] A. Szypłowska, A. Nakonieczna, A. Wilczek, B. Paszkowski, G. Solecki, and W. Skierucha, “Application of a Coaxial-Like Sensor for Impedance Spectroscopy Measurements of Selected Low-Conductivity Liquids,” *Sensors*, vol. 13, no. 10, pp. 13301–13317, Sep. 2013.

[218] “Compact and Fast Impedance Spectroscopy Platform - Quadra,” *Eliko*. .

[219] J. Kendall and K. P. Monroe, “THE VISCOSITY OF LIQUIDS. II. THE VISCOSITY-COMPOSITION CURVE FOR IDEAL LIQUID MIXTURES. 1,” *J. Am. Chem. Soc.*, vol. 39, no. 9, pp. 1787–1802, 1917.

[220] D. J. Vitello, R. M. Ripper, M. R. Fettiplace, G. L. Weinberg, and J. M. Vitello, “Blood Density Is Nearly Equal to Water Density: A Validation Study of the Gravimetric Method of Measuring Intraoperative Blood Loss,” *J. Vet. Med.*, vol. 2015, p. e152730, Jan. 2015.

[221] W. L. Chandler and G. Schmer, “Evaluation of a new dynamic viscometer for measuring the viscosity of whole blood and plasma.,” *Clin. Chem.*, vol. 32, no. 3, pp. 505–507, 1986.

[222] L.-M. Wang and R. Richert, “Dynamics of glass-forming liquids. IX. Structural versus dielectric relaxation in monohydroxy alcohols,” *J. Chem. Phys.*, vol. 121, no. 22, pp. 11170–11176, 2004.

[223] H. Weingärtner *et al.*, “The dielectric response of room-temperature ionic liquids: effect of cation variation,” *J. Phys. Chem. B*, vol. 111, no. 18, pp. 4775–4780, 2007.

[224] M. A. Floriano and C. A. Angell, “On the relaxation between Debye and nonexponential relaxation in supercooled monohydric alcohols and water: A solution study,” *J. Chem. Phys.*, vol. 91, no. 4, pp. 2537–2543, 1989.

[225] E. L. Mertz and L. I. Krishtalik, “Low dielectric response in enzyme active site,” *Proc. Natl. Acad. Sci.*, vol. 97, no. 5, pp. 2081–2086, 2000.

[226] R. Bergman, H. Jansson, and J. Swenson, “Slow Debye-type peak observed in the dielectric response of polyalcohols,” *J. Chem. Phys.*, vol. 132, no. 4, p. 044504, 2010.

[227] R. H. Cole, “Evaluation of dielectric behavior by time domain spectroscopy. I. Dielectric response by real time analysis,” *J. Phys. Chem.*, vol. 79, no. 14, pp. 1459–1469, 1975.

[228] P. Dutta, S. Biswas, and S. K. De, “Dielectric relaxation in polyaniline–polyvinyl alcohol composites,” *Mater. Res. Bull.*, vol. 37, no. 1, pp. 193–200, 2002.

[229] D. Bertolini, M. Cassettari, and G. Salvetti, “The dielectric properties of alcohols–water solutions. I. The alcohol rich region,” *J. Chem. Phys.*, vol. 78, no. 1, pp. 365–372, 1983.

[230] J. B. Hasted, *Water: a comprehensive treatise*. Plenum Press, New York, 1972.

[231] U. Kaatze, “Complex permittivity of water as a function of frequency and temperature,” *J. Chem. Eng. Data*, vol. 34, no. 4, pp. 371–374, 1989.

[232] J. Barthel, K. Bachhuber, R. Buchner, and H. Hetzenauer, “Dielectric spectra of some common solvents in the microwave region. Water and lower alcohols,” *Chem. Phys. Lett.*, vol. 165, no. 4, pp. 369–373, 1990.

[233] S. Sudo, N. Shinyashiki, Y. Kitsuki, and S. Yagihara, “Dielectric Relaxation Time and Relaxation Time Distribution of Alcohol−Water Mixtures,” *J. Phys. Chem. A*, vol. 106, no. 3, pp. 458–464, Jan. 2002.

[234] B. Lenaerts and R. Puers, *Omnidirectional inductive powering for biomedical implants*. Springer, 2009.

[235] “Guidelines for limiting exposure to time-varying electric, magnetic, and electromagnetic fields (up to 300 GHz). International Commission on Non-Ionizing Radiation Protection,” *Health Phys.*, vol. 74, no. 4, pp. 494–522, Apr. 1998.

[236] J. M. Bland and D. Altman, “STATISTICAL METHODS FOR ASSESSING AGREEMENT BETWEEN TWO METHODS OF CLINICAL MEASUREMENT,” *The Lancet*, vol. 327, no. 8476, pp. 307–310, Feb. 1986.

[237] S. Havriliak and S. Negami, “A complex plane representation of dielectric and mechanical relaxation processes in some polymers,” *Polymer*, vol. 8, pp. 161–210, Jan. 1967.

[238] D. W. Davidson and R. H. Cole, “Dielectric relaxation in glycerine,” *J. Chem. Phys.*, vol. 18, no. 10, pp. 1417–1417, 1950.

[239] F. Kremer and A. Schönhals, *Broadband Dielectric Spectroscopy*. Springer Science & Business Media, 2002.

[240] R. Kohlrausch, “Theorie des elektrischen Rückstandes in der Leidener Flasche,” *Ann. Phys.*, vol. 167, no. 2, pp. 179–214, 1854.

[241] R. Bandyopadhyay *et al.*, “Evolution of particle-scale dynamics in an aging clay suspension,” *Phys. Rev. Lett.*, vol. 93, no. 22, p. 228302, 2004.

[242] Y.-H. Hwang, J.-A. Seo, H.-J. Kwon, and H. K. Kim, “Relaxation Dynamics of Sugar Glasses,” *Rep Inst. Fluid Sci.*, vol. 19, pp. 27–34, 2007.

APPENDICES

Appendix I	List of publications
Appendix II	CAD Drawings for mould preparation
Appendix III	Device Specifications – Keysight® E4980A Precision LCR Meter
Appendix IV	Device Specifications - Quadra® Impedance Spectroscopy

Appendix I: List of publications

1. G. Anand, A. Lowe, and A. M. Al-Jumaily, “Simulation of impedance measurements at human forearm within 1 kHz to 2 MHz,” *J. Electr. Bioimpedance*, vol. 7, no. 1, p. 20, May 2016.

2. G. Anand, A. Lowe, and A. M. Al-Jumaily, “Parametric Electrical Modelling of Human Forearm Simulation Response Using Multi-Frequency Electrical Bioimpedance,” *J. Biosens. Bioelectron.*, vol. 7, no. 2, 2016.

Appendix II: CAD Drawings for mould preparation

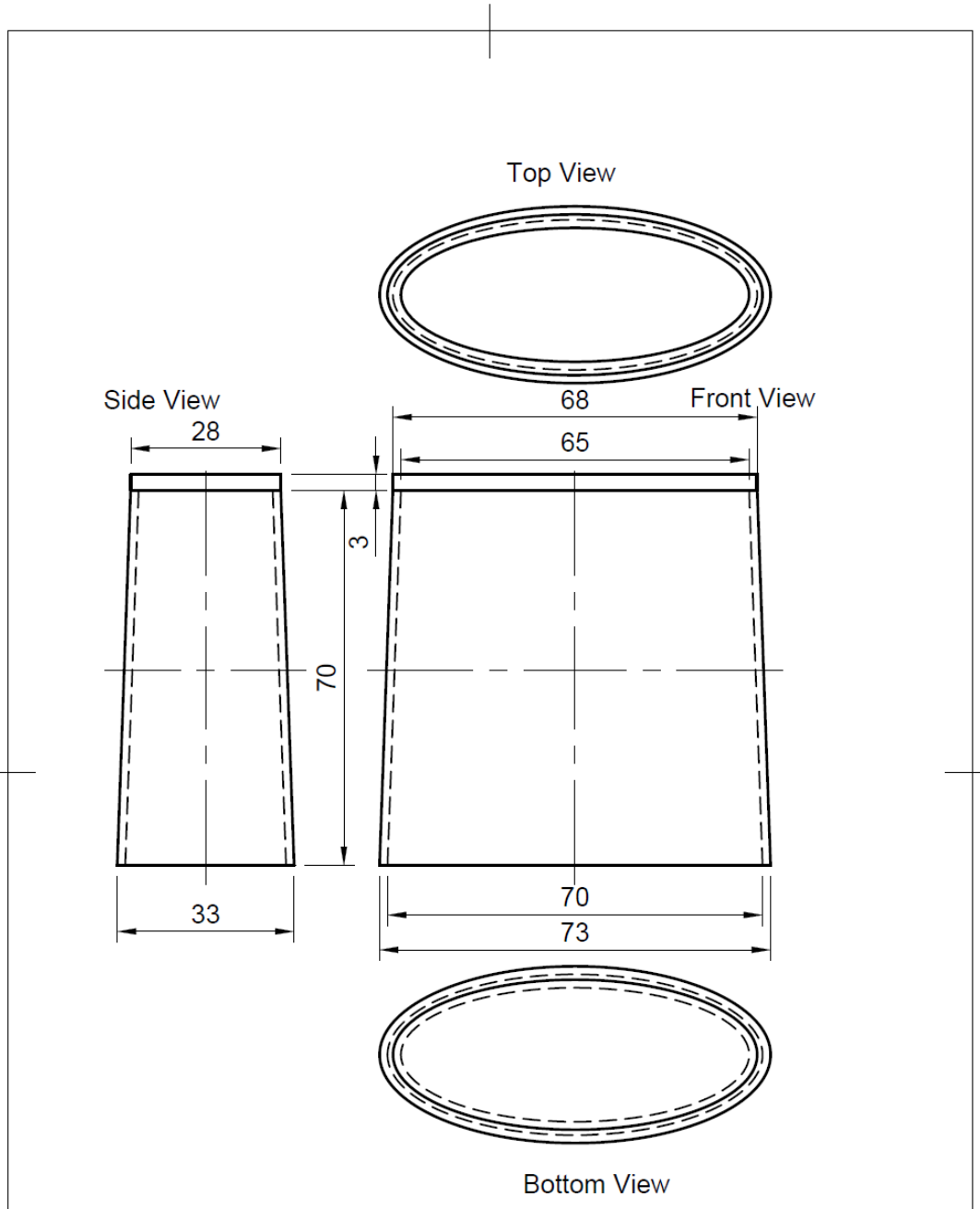

Dept.	Technical reference	Created by	Approved by
	Units: mm	Gautam Anand 7/05/2017	
		Document type: CAD Specification sheet	Document status
		Title: Foreram Phantom Fat Mould	DWG No.
			Rev. / Date of issue / Sheet: 1/1

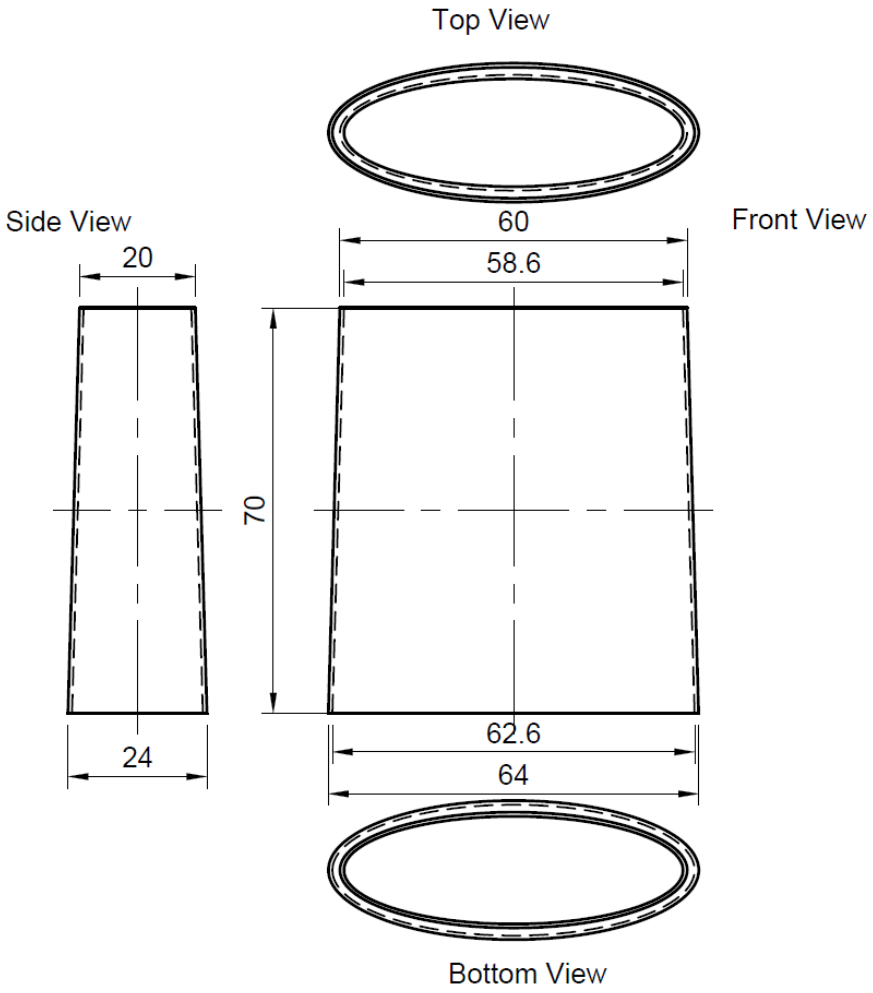

Dept.	Technical reference	Created by	Approved by
	Units: mm	Gautam Anand 7/05/2017	
		Document type: CAD Specification sheet	Document status
		Title: Forearm Phantom Muscle Mould	DWG No.
			Rev. / Date of issue / Sheet: 1/1

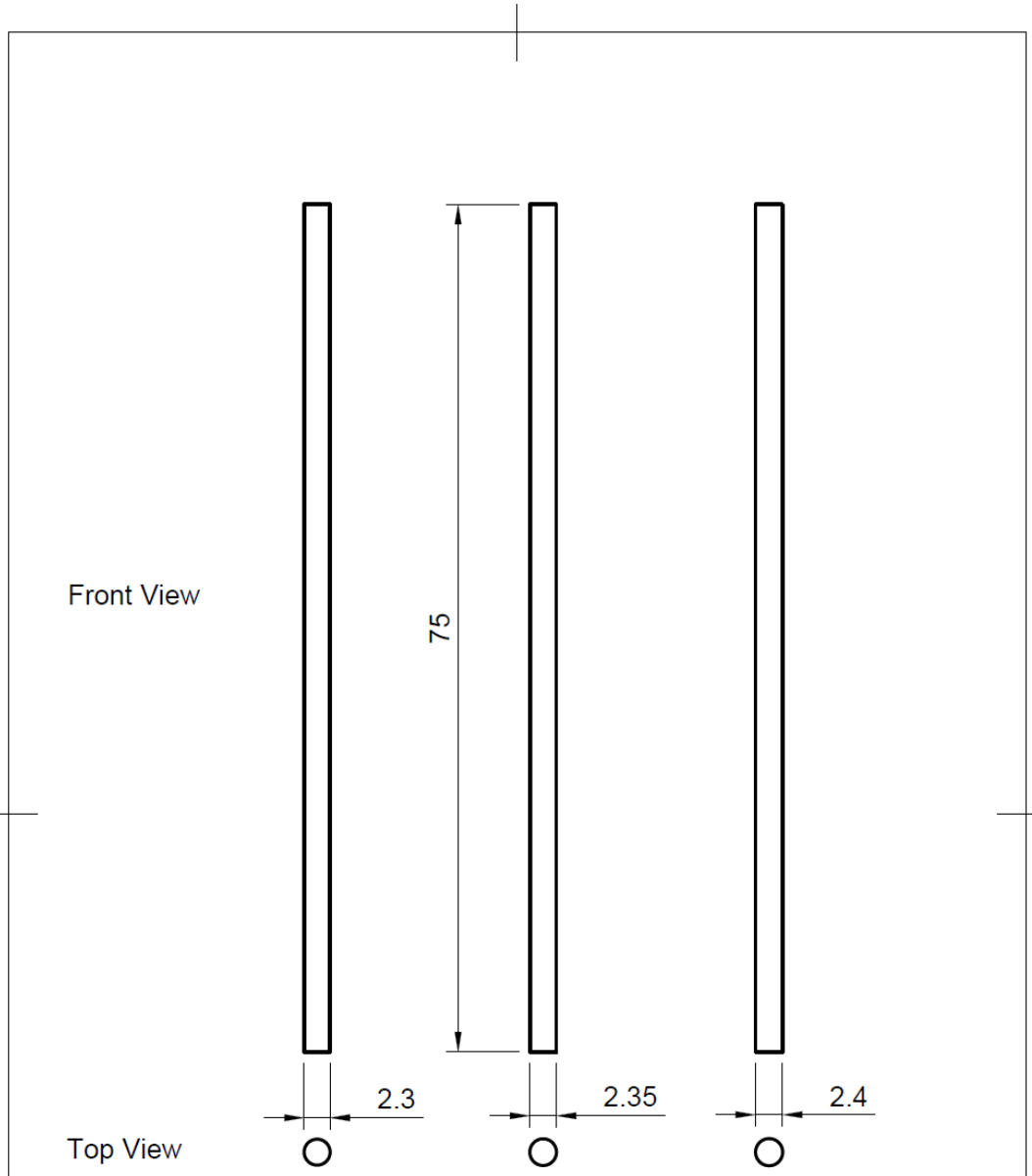

Dept.	Technical reference	Created by	Approved by
	Units: mm	Gautam Anand 7/05/2017	
		Document type: CAD Specification sheet	Document status:
		Title: Foreram Phantom Artery Moulds	DWG No.
			Rev. / Date of issue / Sheet: 1/1

Appendix III: Device Specifications - Keysight® E4980A Precision LCR Meter

General Specifications

Table 48. Power source

Voltage	90 VAC - 264 VAC
Frequency	47 Hz - 63 Hz
Power consumption	Max. 150 VA

Table 49. Operating environment

Temperature	0 - 55 °C
Humidity (≤ 40 °C, no condensation)	15% - 85% RH
Altitude	0 m - 2000 m

Table 50. Storage environment

Temperature	–20 - 70 °C
Humidity (≤ 60 °C, no condensation)	0% - 90% RH
Altitude	0 m - 4572 m

Outer dimensions: 375 (width) x 105 (height) × 390 (depth) mm (nominal)

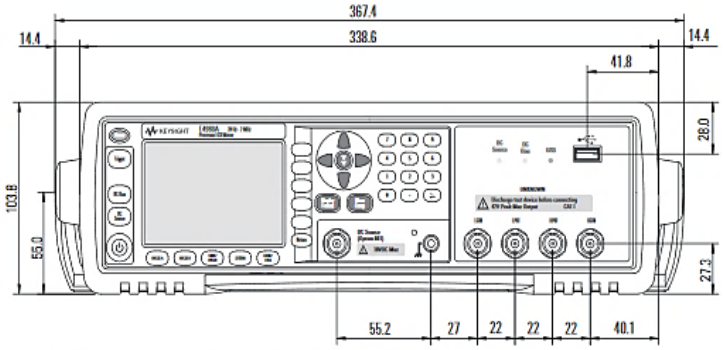

Figure 2. Dimensions (front view, with handle and bumper, in millimeters, nominal)

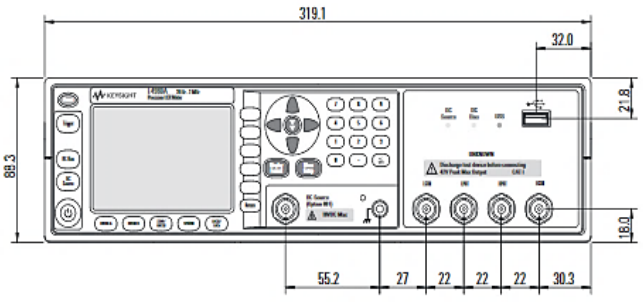

Figure 3. Dimensions (front view, without handle and bumper, in millimeters, nominal)

Basic Specifications

Measurement functions

Measurement parameters

- Cp-D, Cp-Q, Cp-G, Cp-Rp
- Cs-D, Cs-Q, Cs-Rs
- Lp-D, Lp-Q, Lp-G, Lp-Rp, Lp-Rdc
- Ls-D, Ls-Q, Ls-Rs, Ls-Rdc
- R-X
- Z-θd, Z-θr
- G-B
- Y-θd, Y-θr
- Vdc-Idc[1]

Definitions

Cp	Capacitance value measured with parallel-equivalent circuit model
Cs	Capacitance value measured with series-equivalent circuit model
Lp	Inductance value measured with parallel-equivalent circuit model
Ls	Inductance value measured with series-equivalent circuit model
D	Dissipation factor
Q	Quality factor (inverse of D)
G	Equivalent parallel conductance measured with parallel-equivalent circuit model
Rp	Equivalent parallel resistance measured with parallel-equivalent circuit model
Rs	Equivalent series resistance measured with series-equivalent circuit model
Rdc	Direct-current resistance
R	Resistance
X	Reactance
Z	Impedance
Y	Admittance
θd	Phase angle of impedance/admittance (degree)
θr	Phase angle of impedance/admittance (radian)
B	Susceptance
Vdc	Direct-current voltage
Idc	Direct-current electricity

Deviation measurement function: Deviation from reference value and percentage of deviation from reference value can be output as the result.

Equivalent circuits for measurement: Parallel, Series

Impedance range selection: Auto (auto range mode), manual (hold range mode)

Trigger mode: Internal trigger (INT), manual trigger (MAN), external trigger (EXT), GPIB trigger (BUS)

Measurement display ranges

Table 10 shows the range of measured value that can be displayed on the screen. For the effective measurement ranges, refer to Figure 1 impedance measurement accuracy example.

Table 10. Allowable display ranges for measured values

Parameter	Measurement display range
Cs, Cp	± 1.000000 aF to 999.9999 EF
Ls, Lp	± 1.000000 aH to 999.9999 EH
D	± 0.000001 to 9.999999
Q	± 0.01 to 99999.99
R, Rs, Rp, X, Z, Rdc	± 1.000000 aΩ to 999.9999 EΩ
G, B, Y	± 1.000000 aS to 999.9999 ES
Vdc	± 1.000000 aV to 999.9999 EV
Idc	± 1.000000 aA to 999.9999 EA
θr	± 1.000000 arad to 3.141593 rad
θd	± 0.0001 deg to 180.0000 deg
Δ%	± 0.0001 % to 999.9999 %

a: 1 x 10^{-18}, E: 1 x 10^{18}

Appendix IV: Device Specifications - Quadra® Impedance Spectroscopy

Device Specifications

Table 1 Measurement Parameters

Parameter	Value(s)
Impedance	Relative value of impedance. Module in units of ohms and phase in units of degrees.
Number of Frequencies in Spectrogram	15
Spectrogram Acquisition Period	1ms , 1.8s during Minimum Spectrogram Frequencies configuration
Maximum Spectrogram Frequencies	1.0000kHz, 2.0000kHz, 3.0000kHz, 7.0000kHz, 11.0000kHz, 17.0000kHz, 23.0000kHz, 31.0000kHz, 43.0000kHz, 61.0000kHz, 89.0000kHz, 127.0000kHz, 179.0000kHz, 251.0000kHz, 349.0000kHz
Minimum Spectrogram Frequencies	0.5580Hz, 1.1160Hz, 1.6741Hz, 3.9062Hz, 6.1383Hz, 9.4866Hz, 12.8348Hz, 17.2991Hz, 23.9955Hz, 34.0401Hz, 49.6651Hz, 70.8705Hz, 99.8883Hz, 140.06697Hz, 194.7544Hz
Repeatability, Resolutions	0.1%, 12-Bit ADC's, 16-Bit DFT references

Table 2 Technical Parameters

Parameter	Value(s)
Excitation Waveform	Binary Multi Frequency
Number of Excitation Channels	1
Excitation Channel Type	Differential, 50Ω
Excitation Channel Voltage Level, Offset	0.4Vpp ... 7.5Vpp, DC Offset 0V
Number of Excitation Channel Voltage Level Steps	255
Number of Measurement Channels	2
Measurement Channels Type, Input Impedance	Differential, > 10MΩ
Measurement Channels Input Range	3Vpp @ PGA G=1
Measurement Channels Preamplifier Gains	1x, 2x, 5x, 10x
USB Bus Speed Settings, Standards	12Mbps, Full Speed, USB 1.0, USB 2.0, USB 3.0
Power Consumption from USB Bus, Battery Duration	500mA 2.5W, 8 hour
Synchronization IO SMA Levels, Output Syncro Type	3.3V CMOS, Output 1ms Toggle, 5V Tolerant, 50Ω
Analog Front End Digital IO	3x GPIO, I2C (400kHz)
Analog Front End Digital IO Levels	3.3V CMOS, Not 5V tolerant
Analog Front End Digital & Analog Supply	3.3V 150mA, +5V 150mA, -5V 100mA

Mäealuse 2/1
Tallinn, 12618
Estonia

Tel: +372 6599 881
Fax: +372 6599 880

info@eliko.ee
www.eliko.ee